In compliance with the
Canadian Privacy Legislation
some supporting forms
may have been removed from
this dissertation.

While these forms may be included
in the document page count,
their removal does not represent
any loss of content from the dissertation.

University of Alberta

The Acoustic Reflectivity and Transmissivity of Liquid Saturated Porous Media: Experimental Tests of Theoretical Concepts

by

Youcef Bouzidi ©

A thesis submitted to the Faculty of Graduate Studies and Research in partial fulfillment of the requirements for the degree of Doctor of Philosophy in Geophysics

Department of Physics

Edmonton, Alberta

Fall, 2003

National Library
of Canada

Acquisitions and
Bibliographic Services

395 Wellington Street
Ottawa ON K1A 0N4
Canada

Bibliothèque nationale
du Canada

Acquisisitons et
services bibliographiques

395, rue Wellington
Ottawa ON K1A 0N4
Canada

Your file Votre référence
ISBN: 0-612-87942-9
Our file Notre référence
ISBN: 0-612-87942-9

The author has granted a non-exclusive licence allowing the National Library of Canada to reproduce, loan, distribute or sell copies of this thesis in microform, paper or electronic formats.

The author retains ownership of the copyright in this thesis. Neither the thesis nor substantial extracts from it may be printed or otherwise reproduced without the author's permission.

L'auteur a accordé une licence non exclusive permettant à la Bibliothèque nationale du Canada de reproduire, prêter, distribuer ou vendre des copies de cette thèse sous la forme de microfiche/film, de reproduction sur papier ou sur format électronique.

L'auteur conserve la propriété du droit d'auteur qui protège cette thèse. Ni la thèse ni des extraits substantiels de celle-ci ne doivent être imprimés ou aturement reproduits sans son autorisation.

Canadä

University of Alberta

Library Release Form

NAME OF AUTHOR: Youcef Bouzidi

TITLE OF THESIS: The Acoustic Reflectivity and Transmissivity of Liquid Saturated Porous Media: Experimental Tests of Theoretical Concepts

DEGREE: Doctor of Philosophy

YEAR THIS DEGREE GRANTED: 2003

Permission is hereby granted to the University of Alberta Library to reproduce single copies of this thesis and to lend or sell such copies for private, scholarly or scientific research purposes only.

The author reserves all other publication and other rights in association with the copyright in the thesis, and except as hereinbefore provided neither the thesis nor any substantial portion thereof may be printed or otherwise reproduced in any material form whatever without the author's prior written permission.

Date : 09/30/2003

To

My family and especially my mother

University of Alberta

Faculty of Graduate Studies and Research

The undersigned certify that they have read, and recommend to the Faculty of Graduate Studies and Research for acceptance, a thesis entitled **The Acoustic Reflectivity and Transmissivity of Liquid Saturated Porous Media: Experimental Tests of Theoretical Concepts** submitted by **Youcef Bouzidi** in partial fulfillment of the requirements for the degree of Doctor of Philosophy in Geophysics.

Dr. D. R. Schmitt (Supervisor)
Department of Physics

Dr. J. Beamish (Chair)
Department of Physics

Dr. R. O'Connell (External)
Department of Earth and Planetary Science
Harvard University

Dr. J. T. Spanos
Department of Physics

Dr. J. K. Szymanski
Department of Civil and Environmental Engineering

Dr. M. Heimpel
Department of Physics

DATE: 09/29/2003

Abstract

Acoustic wave propagation, reflectivity and transmissibility in porous media are presented. A new experimental method of probing various materials was developed. It utilizes a large ultrasonic source and a near-point receiver. The effects of geometrical spreading and averaging at the point of observation are minimized.

The calibration of the method on elastic materials immersed in water revealed a large amplitude drop at the so-called Rayleigh angle of incidence. Extensive modelling has shown that the phase of the reflection coefficient is solely responsible for this energy drop and the apparent shift of the wave-field is attributed to a "spatial dispersion effect" and not a leaky Rayleigh wave in the solid as previously suggested in the literature. This was supported by experimental measurements. The method was sufficiently understood to be used in more complex materials.

In addition to the compressional and shear wave modes, a transmission experiment conducted on a thin water-saturated porous plate definitively detected the highly attenuated slow P-wave. Further, an additional mode that may be the porosity wave was observed. Further modelling is necessary to confirm this fourth wave. Measured velocities and attenuations of the transmitted waves are in agreement with the theory. Further, the reflectivity experiment revealed conversions of both P and S-waves to slow P-waves. To the author's knowledge, this is the first reported observation of such conversion modes in a reflectivity experiment.

Reflectivity curves were acquired from water-saturated thick porous plates im-

mersed in water. These plates exhibit a low degree of sintering and large thickness, and consequently large "dry" P and S-attenuations and not all required parameters could acceptably be obtained. A numerical approach is employed instead yielding satisfactory reflectivity results. However, some features were not modelled properly.

Both the Biot and the de la Cruz/Spanos theories were reviewed, employed in the modelling, and compared in the context of the present experiments. When water is considered both theories adequately explained the observations but similarities break down for higher viscosity fluids.

Zoeppritz's equations are found to disagree with the observations at ultrasonic frequencies. Extrapolation to seismic frequencies is left to future work.

Acknowledgements

A special acknowledgement goes to my wife, Hayette, for all the support she provided and for taking care of our family and making my accomplishments during my tenure at the University of Alberta possible. I am also grateful to my son Lounis for giving up so many things children of his age love to do and who never (almost never!) disturbed the course of my studies. This surely helped me focus on my studies.

I am grateful to my supervisor Dr. D. R. Schmitt for all the support, continuous guidance, and the confidence he showed in my accomplishments.

A special thank goes to Dr. E. R. Kanasewich who guided me in my first years at the University of Alberta while working on the Depth Imaging Project. Rest in peace Ernie! I am also grateful to M. J. A. Burianyk for his support in the Lithoprobe project and it was a pleasure working with him.

I am grateful to Dr. R. A. Burwash for all the contributions he provided in the Depth Imaging Project. I have learned so much about the structure of the Alberta basement and the underlying crust from him.

I would like also to thank Dr. V. de la Cruz, Dr. T. J. T. Spanos, Dr. E. Krebes, Dr. J. Beamish, and Dr. M. Sacchi for all the discussions which were of great help in understanding many issues related to my project. Thank you for keeping your office door open any time I needed help.

I would like to thank the members of my defense committee, Dr. D. R. Schmitt, Dr. J. Beamish, Dr. R. O'Connell, Dr. T. J. T. Spanos, Dr. J. K. Szymanski, Dr. M. Heimpel, and the guest Dr. R. A. Burwash for reviewing my thesis.

I would like to thank the Physics Machine Shop personnel, G. Lachat, P. Zimmermann, T. Walford, T. Paget, D. Helm, and M. Reidner for the construction of the equipment used in my experiments. I also thank the Glass Blowing Shop personnel for letting me use their equipment in the construction of the synthetic sandstones.

A special thank goes to L. Tober who always answers present when I needed help in the Rock Physics Laboratory. Thanks go also to J. Mackinnon and J. Haverstock

for all the computing resources they maintained and to the Computing Network Services for providing the parallel processing clusters employed in the Depth Imaging Project.

I would like to thank my colleagues at the department for all the fruitful scientific discussions we had together particularly M. Mah and J. Molyneux. I also appreciate the help M. Welz offered to me in being my permanent connection to the University while I was away. Thank you Marek!

The financial support provided by the Seismic Heavy Oil Consortium, the Lithoprobe project, NSERC, the Petroleum Research Fund administered by the American Chemical Society, and the department of physics is greatly appreciated. Further, many other support personnel in the department assisted me greatly and many are deserving of thanks.

Table of Contents

Abstract

Acknowledgements

Table of Contents

List of Tables

List of Figures

1 Introduction 1

2 Waves in isotropic media 9

- 2.1 Introduction 9
  - 2.1.1 Geometry of the problem 10
- 2.2 Wave propagation in real fluids 11
  - 2.2.1 Plane waves in fluids 12
  - 2.2.2 Effect of fluid viscosity on acoustic plane waves 13
- 2.3 Plane waves in non-attenuating media 19
  - 2.3.1 Solutions to the dilatational wave equation 19
  - 2.3.2 Transverse wave 22
- 2.4 Reflection-transmission of acoustic waves at a liquid-solid interface. . 23
  - 2.4.1 Boundary conditions at a fluid-solid boundary 24
  - 2.4.2 Displacement and velocity potentials 24
  - 2.4.3 Stress tensor for an isotropic solid 25
  - 2.4.4 Stress tensor in a real fluid 26
  - 2.4.5 Monochromatic plane wave reflection-transmission coefficients 27
  - 2.4.6 Boundary conditions 27

2.4.7 Solution 28
2.5 Numerical results for monochromatic plane wave reflectivity 31
2.5.1 Water-copper alloy 32
2.6 Phase distortion of the reflected monochromatic plane wave field . . . 36
2.7 Monochromatic bounded acoustic beams 44
2.7.1 Fourier components 46
2.8 Bounded acoustic pulses 51
2.9 Modelling of bounded acoustic beams 53
2.9.1 Monochromatic flat acoustic beams 53
2.9.2 Monochromatic Gaussian beams 55
2.10 Modelling of bounded acoustic pulses 65
2.10.1 Propagation 67
2.10.2 Bounded acoustic pulse reflectivity 70
2.11 Discussion 75
2.12 Conclusions 78

3 Reflectivity calibration **80**
3.1 Experimental equipment and setup 81
3.1.1 Transmitter 82
3.1.2 Receiver 83
3.1.3 Three dimensional acoustic scanner 84
3.2 Acoustic goniometer 86
3.3 Source and receiver characterization results 88
3.4 Reflectivity results and discussion 95
3.4.1 Material property measurements 107
3.4.2 Summary of the results 110
3.5 Conclusions 111

4 Waves in fluid-saturated porous media **113**
4.1 Introduction 113
4.2 Biot theory 114
4.2.1 Propagation of dilatational waves 115
4.2.2 Rotational waves 117
4.3 de la Cruz/Spanos theory 119
4.3.1 Propagation of dilatational waves 119

4.3.2 Rotational waves 121
4.4 Porosity-pressure wave propagation 122
4.5 Porous media parameters 124
4.5.1 Parameters for the Biot theory 125
4.5.2 Parameters for the de la Cruz/Spanos theory 128
4.6 Comparison between Biot's theory and de la Cruz/Spanos theory . . 129
4.7 Modelling wave propagation in porous media 134
4.8 Influence of the solid skeleton properties on wave propagation 150
4.9 Choice of parameters to model fluid-saturated porous materials . . . 156
4.10 Conclusions 159

5 Reflection-transmission in porous media 161

5.1 Introduction 161
5.2 Wave equations 162
5.3 Stress components 164
5.4 Boundary conditions for a fluid-porous material interface 166
5.4.1 Deresiewicz and Skalak boundary conditions in porous media . 166
5.4.2 de la Cruz/Spanos boundary conditions in porous media . . . 167
5.4.3 Comparison of the two boundary condition sets 168
5.5 Plane wave solutions 169
5.6 Modelling with plane waves in porous media 173
5.6.1 Amplitudes versus angle of incidence 175
5.6.2 Phase angle versus angle of incidence 176
5.7 Bounded acoustic pulses in porous media 181
5.8 Bounded acoustic pulse modelling in porous media 181
5.9 Conclusions 182

6 Porous media parameters 185

6.1 Introduction 185
6.2 Tortuosity measurement 186
6.2.1 Experimental setup 186
6.2.2 Tortuosity derivation 188
6.3 Permeability measurements 189
6.3.1 Experimental setup 189
6.3.2 Permeability derivation 191

6.4 Phase velocity measurement 192
6.4.1 Methodology 192
6.5 Attenuation measurements 193
6.5.1 Methodology 193
6.6 Solid skeleton characterization 195
6.6.1 Methodology 195
6.7 Conclusions 197

7 Porous media transmission experiment 198
7.1 Introduction 198
7.2 Synthetic sample description 199
7.3 Experimental procedure 201
7.4 Experimental observations 204
7.5 Phase velocities of the observed waves 207
7.6 Attenuations of the observed waves 211
7.7 Conclusions 214

8 Porous media reflectivity experiments 215
8.1 Introduction 215
8.2 Experimental reflectivity from water and a water-saturated thin porous synthetic sample 216
8.3 Discussion 230
8.4 Conclusions 230

9 Weakly consolidated porous materials 232
9.1 Introduction 232
9.2 Porous synthetic samples 233
9.2.1 Sample construction 233
9.2.2 Porosity measurements 236
9.2.3 Tortuosity measurements 236
9.2.4 Permeability measurements 238
9.2.5 Phase velocity and attenuation measurements of the solid skeleton 239
9.3 Reflectivity observations and modelling 241
9.3.1 Numerical approach 241

9.3.2 Observed and modelled results 243
9.4 Conclusions 243

10 Conclusions 250

A Acoustic beam with a cosine taper 255

B Review of the Biot theory 258
B.1 Introduction 258
B.2 Determination of Biot parameters 259
B.2.1 Jacketed compressibility test 259
B.2.2 Unjacketed compressibility test 261
B.2.3 Determination of the coefficient of fluid content 263
B.3 Wave propagation 264
B.3.1 Equations of motion 264
B.3.2 Longitudinal waves 266
B.3.3 Rotational waves 267
B.3.4 Frequency limitations 269

C Review of the de la Cruz/Spanos theory 272
C.1 Wave propagation 272
C.2 de la Cruz/Spanos parameters 275
C.2.1 Drained compressibility tests 277
C.2.2 A continuous family of compressibilities 277
C.2.3 Coefficient of fluid content 278

References 280

List of Tables

2.1 Physical and mechanical properties of water and glycerol at 20^0C . . 15

2.2 Physical and mechanical properties copper and water 32

2.3 Physical and mechanical properties of water and glass 57

2.4 Laboratory measured properties of the fluid (water) and the copper alloy sample used in the numerical example 65

3.1 Properties of the materials used in the reflectivity experiments on the glass, aluminium, and copper 97

3.2 P and S critical angles, Rayleigh angle, and calculated Rayleigh wave velocity 97

3.3 Parameters calculated using the properties of the materials listed in table 3.1 98

3.4 The Rayleigh angle θ_R measured from the reflectivity measurements and the inferred Rayleigh wave velocity V_R 108

3.5 The observed critical angle θ_p^c, and the inferred P-wave velocity V_P for the glass, aluminium, and copper 108

3.6 The inferred S-wave velocities from the observed Rayleigh angles given in table 3.1 109

3.7 Inferred and measured densities of the glass, copper, and aluminium from the reflectivity of the bounded acoustic pulse 110

3.8 Summary of the inferred materials properties from the reflectivity response of a bounded acoustic pulse from a water-solid boundary . . 111

4.1 Properties of glycerol used in the present example 135

4.2 Properties of the water-saturated porous material used as an illustrative example 135

4.3 P and S wave phase velocities and attenuations of the "dry" solid skeleton . . . 136
4.4 The complex bulk and shear moduli of the solid skeleton, the mass transfer ρ_{12}, and the assumed characteristic length Δ of the pore size of the porous material . . . 136
4.5 The derived parameters A, Q, R, δ_f, and δ_s of the water-saturated porous material and a glycerol-saturated porous material . . . 138
4.6 The inferred ρ_{12}, and Δ from the S-wave velocity and attenuation of the fluid-saturated porous sample . . . 159

7.1 Measured porous sample S082 characteristics and properties . . . 201
7.2 Measured "dry" dynamic properties of the porous sample S082 . . . 201
7.3 The measured phase velocities of the fast P, the slow P, and the converted S waves . . . 208
7.4 Inferred dynamic mass transfer ρ_{12}, the viscosity correction factor $F(\omega)$, and the characteristic length Δ at the frequency 0.78 MHz . . . 212

9.1 Porous samples characteristics . . . 236
9.2 Measured porosities of the porous synthetic samples used in this study 236
9.3 Measured electrical potentials for the saline solution . . . 236
9.4 Measured electrical potentials for the porous sample S060 saturated with the same saline solution as that in table 9.3 . . . 237
9.5 Measured tortuosities . . . 237
9.6 Measured permeabilities . . . 238
9.7 Estimated P and S wave velocities on thin porous samples cored from the large original ones . . . 241
9.8 μ_M, A, Q, R, and Δ resulting from the numerical calculations to find the best set that leaded to a best match of the observed and calculated reflectivities . . . 242
9.9 Calculated P and S wave velocities and attenuations using the parameters of table 9.8 . . . 243

List of Figures

2.1 The two dimensional reference frame used in all 2D problems 11
2.2 P-wave attenuation and quality factor in water 16
2.3 P-wave attenuation and quality factor in glycerol 16
2.4 S-wave attenuation and quality factor in water 17
2.5 S-wave attenuation and quality factor in glycerol 18
2.6 Phase velocity of transverse plane waves in water and glycerol 18
2.7 Waves generated at an interface between a liquid and a solid by an incident P-wave 24
2.8 Normalized energy distribution at a water-copper alloy boundary . . 33
2.9 Amplitudes of the generated waves at a water-copper alloy boundary 34
2.10 Phase angles of the generated waves at a water-copper alloy boundary 35
2.11 Phase angles of the waves generated at a water-copper alloy boundary and far from the boundary 35
2.12 Plane wave front with a given intensity distribution on the plane $z = 0$ 38
2.13 Lateral displacement as a function of incidence angle 40
2.14 The displacement along the $\hat{x}$ axis is null if the reflection coefficient is real 41
2.15 Geometrical shift Δ_1 and the displacement Δ_2 due the phase change of the reflection coefficient at the boundary 42
2.16 Lateral displacement Δ as a function of wavelength in the case of a water-copper boundary at incidence angles near the Rayleigh angle . 43
2.17 Lateral displacement Δ as a function of frequency near the Rayleigh angle 43
2.18 Lateral displacement Δ as a function of wavelength at Rayleigh angle 44
2.19 Bounded acoustic beam formed by a plane wave incident on a screen containing a slit 47

2.20 Bounded acoustic beam in the frequency domain 50

2.21 Example of a bounded acoustic pulse 51

2.22 Downward continuation along $\hat{z}$ direction of a monochromatic bounded flat beam wave field 54

2.23 Normalized amplitude of the bounded acoustic beam of figure 2.22 . . 54

2.24 Normalized amplitude of the bounded acoustic beam along the axis of propagation 55

2.25 Downward continuation of a bounded Gaussian acoustic beam 56

2.26 Normalized amplitude of the bounded Gaussian acoustic beam of figure 2.25 56

2.27 Amplitude along the axis of propagation of the bounded Gaussian acoustic beam of figure 2.25 57

2.28 Amplitude envelope of a monochromatic Gaussian beam at 0.5 MHz, and a width of 8 cm. Angle of incidence 10^o 58

2.29 Amplitude envelope of a monochromatic Gaussian beam at 0.5 MHz and a width of 8 cm. Angle of incidence 20^o 59

2.30 Amplitude envelope of a monochromatic Gaussian beam at 0.5 MHz and a width of 8 cm. Angle of incidence 35^o 60

2.31 Amplitude envelope of a monochromatic Gaussian beam at 3 MHz and a width of 8 cm. Incidence at Rayleigh angle of 28.1^o 61

2.32 Amplitude envelope of a monochromatic Gaussian beam at 2 MHz and a width of 8 cm. Incidence at Rayleigh angle of 28.1^o 62

2.33 Amplitude envelope of a monochromatic Gaussian beam at 1 MHz and a width of 8 cm. Incidence at Rayleigh angle of 28.1^o 62

2.34 Amplitude envelope of a monochromatic Gaussian beam at 0.5 MHz and a width of 8 cm. Incidence at Rayleigh angle of 28.1^o 63

2.35 Amplitude envelope of a monochromatic Gaussian beam at 0.2 MHz and a width of 8 cm. Incidence at angle of 28.1^o 63

2.36 Amplitude envelope of a monochromatic Gaussian beam with 0.1 MHz and a width of 8 cm. Incidence at Rayleigh angle of 28.1^o 64

2.37 Amplitude envelope of a monochromatic Gaussian beam similar to that of figure 2.35 but with a width of 24 cm 64

2.38 Amplitude envelope of a monochromatic Gaussian beam similar to that of figure 2.36 but with a width of 24 cm 65

2.39 Amplitude envelope of the source generated bounded acoustic pulse . 66
2.40 F-k spectrum of the acoustic bounded pulse of figure 2.39 66
2.41 The maximum of the amplitude envelope of the cross-section of a propagating bounded acoustic pulse at the far field 67
2.42 The maximum amplitude envelope of a propagating bounded acoustic pulse at near field 68
2.43 The maximum amplitude along the axis of a propagating bounded acoustic pulse 68
2.44 Forward continuation to 20 cm and 40 cm of the wave field of figure 2.39 69
2.45 Reflection coefficient of a reflected bounded acoustic pulse from a copper plate immersed in water in contrast with a plane wave reflectivity response 71
2.46 Snap shots of a reflected bounded acoustic pulse from a water-copper interface at an angle of 30^o 72
2.47 Snap shots of a reflected bounded acoustic pulse from a water-copper interface at the Rayleigh angle of 43.1^o 73

3.1 Cut-away schematic view drawn to scale of transmitting acoustic source 82
3.2 The near-point receiver with a preamplifier 83
3.3 The acoustic scanner used to characterize the source and the receiver 84
3.4 Setup for recording of a bounded acoustic pulse at a given distance away from the source 85
3.5 Photograph of the reflectivity experiment from a soda-lime glass sample in water using an acoustic goniometer 86
3.6 Diagram of the reflectivity experiment corresponding to the photograph of figure 3.5 87
3.7 Waveform and frequency spectrum of the source signal 89
3.8 Vertical scan of the source wave field recorded at 2 cm from the source 90
3.9 Observed and modelled vertical wave field at a distance of 35 cm . . . 92
3.10 Observed and modelled normalized amplitude envelope at 2 cm and 35 cm 93
3.11 Forward continuation of the observed wave field to a distance of 40 cm 94
3.12 The three isotropic blocks used in the experiments 95

3.13 Water velocity during each reflectivity experiment on the isotropic blocks . . . 96
3.14 Observed reflectivity from a water-glass interface . . . 100
3.15 Observed reflectivity from a water-aluminium interface . . . 101
3.16 Observed reflectivity from a water-copper interface . . . 102
3.17 The direct arrivals in the water-copper reflectivity experiment at large angles of incidence . . . 103
3.18 Water-glass reflectivity experiment: Observed data near the Rayleigh angle . . . 104
3.19 Water-aluminium reflectivity experiment: Observed data near the Rayleigh angle . . . 105
3.20 Water-copper reflectivity experiment: Observed data near the Rayleigh angle . . . 106

4.1 The coefficient of fluid content γ against the unjacketed bulk modulus K_{un} . . . 133
4.2 The real and imaginary parts of the viscosity correction factor . . . 137
4.3 Calculated phase velocities of the fast P, the slow P, and the S waves at frequencies 0-20 kHz . . . 139
4.4 The phase velocities of the fast P, the slow P, and the converted S waves at frequencies 0-2 MHz . . . 140
4.5 The attenuations of the fast P, the slow P, and the converted S waves at frequencies 0-20 kHz . . . 141
4.6 The attenuations of the fast P, the slow P, and the converted S waves at frequencies 0-2 MHz . . . 142
4.7 The relative amplitudes (solid over fluid) of the fast P, the slow P, and the converted S waves at frequencies 0-20 kHz . . . 143
4.8 The relative amplitudes (solid over fluid) of the fast P, the slow P, and the converted S waves at frequencies 0-2 MHz . . . 144
4.9 The relative phase (solid over fluid) of the fast P, the slow P, and the converted S waves at frequencies 0-20 kHz . . . 145
4.10 The relative phase (solid over fluid) of the fast P-wave, the slow P-wave, and the converted S waves at frequencyies 0-2 MHz . . . 146

4.11 The phase velocity, the attenuation, and relative amplitudes (solid over fluid components) the the slow S-wave in de la Cruz/Spanos theory at frequencies 0-20 kHz 147

4.12 The phase velocity, the attenuation, and relative amplitudes (solid over fluid components) of the slow S-wave in de la Cruz/Spanos theory at frequencies 0-2 MHz 148

4.13 The phase velocity and the attenuation of the slow P-wave in a glycerol-saturated porous material at a frequency range 0-2 MHz 149

4.14 The phase velocity and the attenuation, of the slow S-wave (de la Cruz/Spanos theory) at a frequency range of 0-2 MHz 150

4.15 Influence of permeability on the attenuation of the fast P, slow P, and S waves. Low permeability materials 152

4.16 Influence of permeability on the attenuation of the fast P, slow P, and S waves. High permeability materials 153

4.17 Influence of the P-wave attenuation of the solid skeleton on the overall attenuation in a water-saturated porous material 154

4.18 Influence of the S-wave attenuation of the solid skeleton on the overall attenuation in a water-saturated porous material 155

5.1 Normalized energy fluxes normal to the boundary of all generated wave modes 174

5.2 Signed values of normalized energy fluxes normal to the boundary of all generated wave modes 175

5.3 Normalized amplitudes in the solid skeleton of all generated wave modes 175

5.4 Normalized amplitudes in the fluid component of all generated wave modes 176

5.5 The phase of the fluid component for all generated wave modes at a boundary between a fluid and a fluid-saturated porous material . . . 177

5.6 The phase of the solid component for all generated wave modes at a boundary between a fluid and a fluid-saturated porous material . . . 177

5.7 The phase of the reflected wave at a boundary between a fluid and a fluid-saturated porous material 178

5.8 The reflectivity-transmission at the boundary between water and an elastic medium replacing the water-saturated porous material. Zoeppritz's equations . . . 179
5.9 The reflectivity-transmission at the boundary between water and a water-saturated porous material . . . 180
5.10 Plane wave of a narrow (2 cm) bounded acoustic pulse and a wide (8 cm) bounded acoustic pulse reflectivity responses from a boundary between water and a water-saturated porous material . . . 183

6.1 Setup for electrical conductivity measurement through porous media . 187
6.2 Photograph of the electrical conductivity experiment apparatus . . . 188
6.3 Schematic of the apparatus used to measure permeability . . . 190
6.4 Photograph of the apparatus used to measure permeability . . . 190
6.5 Two snap shots showing a difference in the water columns of 7 cm within 11 minutes time difference . . . 191

7.1 Photograph of the porous synthetic sandstone S082 used in the transmission experiment . . . 200
7.2 S.E.M photograph of the surface of the porous synthetic sandstone S082 used in the transmission experiment . . . 200
7.3 Wave transmission through a water-saturated synthetic porous plate using an acoustic scanner . . . 202
7.4 A cartoon of the transmission experiment showing the three wave modes 203
7.5 Travel distances and arrival times of the various waves that are transmitted through a thin water-saturated porous plate immersed in water 205
7.6 Observed transmitted bounded pulse through a thin water-saturated porous plate immersed in water . . . 206
7.7 Measured phase velocity of the fast P-wave . . . 208
7.8 Measured phase velocity of the S-wave . . . 208
7.9 Measured phase velocity of the slow P-wave . . . 209
7.10 Calculated arrival times via Snell's law . . . 209
7.11 4 main events, fast P, S, slow P, and the "porosity" waves corrected to normal incidence . . . 210
7.12 Measured attenuation of the fast P-wave . . . 213
7.13 Measured attenuation of the S-wave . . . 213

7.14 Measured attenuation of the slow P-wave 214

8.1 Setup diagram of the acoustic goniometer (to scale) for the reflectivity measurement 217
8.2 Uninterpreted observed data using the setup of figure 8.1 218
8.3 Observed data using the setup of figure 8.1 overlayed by arrival times from the source edge S1 219
8.4 Observed data using the setup of figure 8.1 overlayed by arrival times from the source edge S2 220
8.5 Observed data using the setup of figure 8.1 overlayed by arrival times from the source area S3 221
8.6 Identification of events detected by the reflectivity setup of figure 8.1 224
8.7 Displays of the recorded reflectivity from a water and a water-saturated porous plate normalized to the input signal 225
8.8 Observed and modelled reflectivity from water and a 2.46 cm thick porous synthetic sample saturated by water 226
8.9 Observed and modelled phase angle 227
8.10 The reflectivity-transmission of the water-saturated porous material . 228
8.11 The reflectivity-transmission of an elastic medium replacing the water-saturated porous material of figure 8.10 229

9.1 S.E.M photographs of the surface of the porous synthetic sandstones used in this study (Samples S040, S060, and S081) 234
9.2 S.E.M photographs of the surface of the porous synthetic sandstones used in this study (Samples S082, S100, and S130) 235
9.3 Tortuosity results for the porous samples described in table 9.1 237
9.4 Measured permeability for the porous samples described in table 9.1 . 238
9.5 Measured permeability for the porous sample S082 239
9.6 Transmission wave forms and estimated P-wave velocities of the "Dry" solid skeletons of the porous samples described in table 9.1 240
9.7 Observed and modelled reflectivity from a boundary between water and a water-saturated 7 cm thick synthetic porous plate (S130) . . . 244
9.8 Observed and modelled reflectivity from a boundary between water and a water-saturated 7 cm thick synthetic porous plate (S100) . . . 245

9.9 Observed and modelled reflectivity from a boundary between water and a water-saturated 7 cm thick synthetic porous plate (S081) . . . 246
9.10 Observed and modelled reflectivity from a boundary between water and a water-saturated 7 cm thick synthetic porous plate (S060) . . . 247
9.11 Observed and modelled reflectivity from a boundary between water and a water-saturated 7 cm thick synthetic porous plate (S040) . . . 248

B.1 Jacketed compressibility test setup 260
B.2 Unjacketed compressibility test setup 261
B.3 *ber* and *bei* functions 270
B.4 The real and imaginary parts of the viscosity correction factor 270

Chapter 1

Introduction

During my tenure at the University of Alberta, it is important to note that additional contributions in the field of deep crustal seismology were made. The author has accomplished another project begun with Dr. E. R. Kanasewich on depth migration. The map of the topography of the Mohorovičič discontinuity in Alberta was revised using 1900 km of reanalyzed reflection profiles acquired as part of the Lithoprobe Alberta Basement Transect. These data were depth migrated using a parallelized algorithm that accounts for steeply dipping structures and an improved crustal velocity model based on rock physics measurements was employed. This work was published elsewhere and one paper (Bouzidi et al., 2002) was dedicated to the memory of E. R. Kanasewich, a pioneer in deep crustal seismology. However, to maintain the theme of the present research the author has chosen not to include this material in the thesis.

The ultimate goal of the present work is to conduct experiments on wave propagation, reflectivity, and transmission in water-saturated porous materials on one hand and to model and test theoretical concepts on the other. It is important to study this problem, as Zoeppritz's equations do not describe properly the reflectivity and transmission in fluid-saturated materials. However Zoeppritz's equations are commonly used in Amplitude Variation with Offset (AVO) studies and assume that the media involved are elastic. The present work will address this problem.

In this thesis experimental reflectivity and transmission tests on porous materials of various properties are conducted. The modelling of theoretical concepts are presented along the experimental results.

The thesis is divided into two parts. The first part will deal with the calibration and characterization of the ultrasonic source-receiver pair; the primary equipment developed and used in these experiments. This process is conducted on well known isotropic and elastic materials. The second part will be devoted to experimental measurements of wave propagation, reflection, and transmission in fluid-saturated porous materials.

In order to properly conduct laboratory acoustic reflectivity measurements, the source-receiver pair must be well characterized and calibrated. In chapter 2 the fundamental theory on wave propagation and reflection from fluid-solid boundaries will be reviewed with an emphasis on the phase angle that plays a major role as will be demonstrated later in the reflectivity of bounded wave fields. This theory is then extended to bounded acoustic beams and to bounded acoustic pulses with an extensive numerical modelling to illustrate the role of the phase of the reflection coefficient in the reflected wave field. These type of wave fields will be treated both theoretically and numerically in details in this chapter. This work was necessitated by the first observations of reflectivity where an unexpected behaviour of the reflectivity curve was found.

In general, laboratory experiments are usually conducted with acoustic sources and receivers of non-negligible size compared to the dimensions of the experiment. If the source and receiver are considered as point source-receiver pair, errors will be induced on any measurement and must be corrected for. Many times this is not easily achievable without many approximations. On the other hand using very small transducers as sources adds complications to laboratory measurements. The energy transmitted by a point source is usually not intense enough to discern weak events from the background noise. Furthermore, diffractions from the equipment can be problematic. To overcome these problems a new laboratory method is developed. The idea is to use as large a source as possible combined with as small a receiver as possible. A large transmitting source was constructed from a large piezo-electric ceramic sheet; this produces a stable wave field with the amplitude along the main axis of propagation remaining constant to large distances. The measurements acquired with this type of wave field are much closer to a hypothetical plane wave. However, despite the efforts in the present work to obtain a plane wave, this type of wave field is still bounded both spatially and temporally; these realities must be taken into account in any modelling calculation. The receiver on the other hand is made as small as possible to avoid any averaging around the point of observation.

The receiver that is used in this study is very small compared to the source, with an area 0.046% of that of the source. This reduces drastically the averaging effects of signals detected by the receiver. This source-receiver pair is highly directional, a feature that ensures lateral arrivals are very weak relative to those whose wave fronts are parallel to the receiver surface. This source-receiver pair will be used in most of the experimental work presented in this study. Chapter 3 is devoted to experimental results and calculated models in the calibration process of the source-receiver pair. The experimental reflectivity calibration will be conducted on 3 solid materials, a copper alloy, a soda-lime glass, and an aluminium block.

An acoustic goniometer was developed. The experimental calibration of the reflectivity from water and the three elastic solid interfaces revealed an unexpected energy drop near the S-wave critical angle of incidence. The horizontal velocity of the reflected wave coincides with that of a Rayleigh wave that would propagate at the surface of the solid in the absence of the fluid medium *at exactly the angle of minimum reflectivity*. This angle is referred as the Rayleigh angle and the phenomenon itself as the Rayleigh angle effect in earlier literature. This complicates experimental analysis, but makes it more interesting. Several authors studied this effect and proposed theories to explain the behaviour of the reflected wave field at this particular angle of incidence. This effect is also known in the optics literature as the Goos-Hänchen shift. It was first experimentally observed by Goos and Hänchen (1947). Schoch (1950) has experimentally observed this phenomena in acoustic experiments and presented photographs of a displaced acoustic beam upon reflection from a fluid-solid interface using schlieren photograph. He has also explained the effect and gave an approximation for the displacement of the reflected beam along the reflecting boundary (Schoch, 1952a; Schoch, 1952b). Brekhovskikh (1960) has followed the work of Schoch and approximated the energy distribution of the displaced reflected beam. He also pointed out that the displacement is analogous to the theory of propagation of a pulse in a dispersive medium. Since then, however, many authors proposed alternate explanations. Diachok and Mayer (1970) observed a pronounced minimum reflectivity at the so-called Rayleigh angle in a reflectivity experiment from a fluid and a solid medium and attributed this phenomena to a conversion of the incident wave to a Rayleigh-type wave at the interface. Horowitz and Tamir (1971) argued at that time that the beam displacement was not well understood. They proposed an analytical formulation for the displacement of a reflected Gaussian beam for electromagnetic waves. A theory was proposed by Tamir and Bertoni (1973) that attributes this effect to a leaky surface wave for electromagnetic waves. A similar theory was proposed for the observed phenomenon for a reflected acoustic beam at the Rayleigh angle and was attributed to a leaky surface wave (Bertoni and Tamir, 1973). Experimental measurements were also acquired near the Rayleigh angle and were used to measure the beam displacement (Breazeale and Adler, 1974; Breazeale et al., 1977) and material properties (Neubauer and Dragonette, 1974). Recently an experimental study on a water-porous material interface at the Rayleigh angle was presented by Guo-Zhen et al. (2001) where the displacement is also photographed. However it is important to note that their experiment is conducted on a porous material with large bulk and shear moduli which makes the case study close to the ones performed on elastic media by others as mentioned above.

Most publications related to the Rayleigh angle focus on the displacement of Gaussian beams and earlier experimental work focused around this particular angle of incidence. In this study an extensive modelling of the reflectivity of bounded acoustic beams and bounded acoustic pulses from water-solid interfaces will be presented and supported by experimental results for a wide range of angles of incidence. In this study the observed phenomenon at the Rayleigh angle is explained by what will be called "spatial dispersion" and not to a leaky Rayleigh wave as suggested in earlier work despite the existence of surface waves at post P and S critical angles of incidence.

In chapters 4 and 5 the fundamental plane wave theory of wave propagation, reflection-transmission at interfaces between fluid and fluid-saturated porous materials will be given. The plane wave theory is extended to bounded acoustic pulses with an emphasise on the phase of the reflection coefficient that plays an important role in the reflected wave field. As experimental measurements and interpretation of reflectivity from water and water-saturated porous material interfaces are the ultimate goal of the present work it is important to review the literature in this domain. This review will be presented with a focus on fluid-solid skeleton interaction, a manner somewhat different from the literature in this domain. The theoretical concepts will be illustrated by modelling examples.

A large part of published work of wave propagation and reflection-transmission in fluid-saturated porous media is theoretical. Interest in acoustic wave propagation in porous media became more important for many scientists after the publication of two classical papers in this topic by Biot (1956a; 1956b). However there exists work prior to that of Biot on wave propagation in porous materials such as the work of Frenkel (1944) on seismoelectric phenomena in moist soils and the work of Morse (1952) on wave propagation in granular media. In his theory Biot demonstrated that two dilatational waves and one shear wave can propagate in such media. This theory requires several elastic coefficients to be measured. An experimental methodology to measure these parameters was proposed later by Biot and Willis (1957). In this theory only viscous losses due to fluid movement relative to the solid skeleton were included in the attenuation of the wave modes that can propagate in fluid-saturated porous materials. Later the theory was generalized to include other processes such as anisotropy and viscoelasticity (Biot, 1962a; Biot, 1962b). A set of boundary conditions for boundary value problems involving porous media was developed by Deresiewicz and Skalak (1963).

Since then many authors developed alternative theories. Among these, that developed by de la Cruz/Spanos (1985) is based on a different physical background. The equations of motion were derived at the microscopic scale then averaged to obtain the macroscopic equations of motion. This is in contrast with the Biot theory that treated the problem directly at the macroscopic scale and neglected the existence of viscous stress in the fluid. In de la Cruz/Spanos's theory the viscous stress of the fluid was included in the formulation of the problem, consequently, a second S-wave was also found to propagate in such media. The authors have refined the theory to include thermomechanical coupling (de la Cruz and Spanos, 1989b; Hickey et al., 1991; de la Cruz et al., 1993) which allows 4 P-waves and two S-waves to exist. However the attenuation of these extra waves is extreme and consequently they would be difficult to observe in nature. With respect to reflectivity, de la Cruz/Spanos (1989b) proposed a set of boundary conditions based on different physical background from that of Deresiewicz and Skalak (1963). Hickey et al. (1995) suggested a set of experimental tests for the measurements of the elastic coefficients involved in the theory of de la Cruz/Spanos. The reflection-transmission boundary value problem was solved by de la Cruz et al. (1992) according to their theory and boundary conditions for hypothetical materials and conditions.

In the present work both Biot's and de la Cruz/Spanos's theories will be investigated and used to model the experimental observations of wave propagation and reflectivity-transmission at water and water-saturated porous material interfaces.

A theoretical study of reflectivity of acoustic waves at a water-sediment interface (ocean bottom) was given by Stoll and Kan (1981) where the loss in the solid skeleton was taken into account. However, the description of the boundary value problem and the choice of parameters was not supported by experimental measurements. Another purely theoretical calculation of the reflection coefficients in fluid-saturated porous media was given by Santos et al. (1992). The debate on the boundary conditions related to porous media is still not completely settled as some experiments do not always conform with the proposed models. The boundary conditions revisited by Gurevich and Schoenberg (1999) were derived from the Biot's equations of poroelasticity. These conditions are similar to those of Deresiewicz and Skalak (1963) with a variant for the open pore conditions at the interface. A recent publication by Denneman et al. (2002) deals with theoretical reflectivity and transmission at fluid-porous medium interface with both open pore boundary conditions and sealed pore boundary conditions. The authors considered fluid-saturated porous media filled with air and with water and found remarkable differences between the open pore conditions and the sealed pore conditions. These results have implications for the interpretation of observations of reflectivity versus angle of incidence in the field.

In the experimental domain, Wu et al. (1990) showed measurements of transmitted fast P, slow P, and S waves through porous media. However the authors have treated the boundary value problem as an elastic case as considered by Biot in the low frequency limit (Biot, 1956a) and therefore attenuation was not included. In this paper none of the observed wave forms were shown. Beamish et al. (1983) have measured longitudinal and transverse sound velocity in liquid ^{4}He-filled porous Vycor as a function of temperature and pressure and found that Biot theory applies well to the results. They were also able to observe the transition from the low to high frequency limits that agrees well with the Biot theory. Warner and Beamish (1988) applied the velocity measurements successfully in ^{4}He-filled porous materials to measure the surface area of such materials. The measurement of the S-wave velocity and attenuation in ^{4}He-filled porous material can also be used to calculate the parameters that characterizes the porous medium geometry (Warner and Beamish, 1994).

The first successful observation of the slow P-wave predicted by Biot theory was made by Plona (1980) in sintered glass spheres. A more recent observation of this wave was made in a water-saturated Nivelsteiner sandstone by Kedler and Smeulders (1997). A numerical simulation of the Biot slow P-wave in a water-saturated Nivelsteiner sandstone was recently presented by Arntsen and Carcione (2001). Discrepancies in the amplitudes of the events between the observation and the predictions were attributed, without hard evidence, to non-Biot attenuation mechanisms.

The slow P-wave has a large attenuation and is consequently not easily observable. In most cases (Plona, 1980; Kedler and Smeulders, 1997), it was observed as a low amplitude event relative to the stronger P and S observed wave modes. These earlier experiments used small source-receiver pairs in which the transducers of the sources and receivers were of the same size. In the present study, definitive evidence of the existence of the slow P-wave with a relatively strong amplitude will be presented in a transmission experiment through a thin (2.46 cm) water-saturated porous sample constructed from sintered glass beads. Moreover, other converted modes related to the slow P-wave will also be observed in a reflectivity experiment using the same porous sample. To the author's knowledge this is the first time that hard evidence of converted modes involving the slow P-wave have been reported in a reflectivity experiment. This was made possible by the use of a large acoustic source in the experiments. Geerits and Kedler (1997) have presented mainly theoretical work along with some experimental results of a transmission through a porous medium. Their measurements were made for the fast P, the slow P, and S waves at only angles of incidence of 24^o, 54^o, and 45^o respectively. During their experiment scanning with the receiver to search for the maximum energy of the arrivals was used. In the present experimental transmission test, the source and the receiver remain fixed during measurements for all angles of incidence, only the sample orientation is changed.

In chapter 6 the experimental methodology for measurements of the required parameters describing porous materials is highlighted. The experiments used in this study were also described.

In chapter 7 and chapter 8 a complete experimental and modelling study on a reflectivity-transmission was conducted on a thin synthetic porous plate. In the transmission experiment the slow P-wave is observed strongly at all angles of incidence. In the reflectivity experiments several converted waves were observed. Converted fast P and S-wave modes to a slow P-wave were observed. Reiterating again here, to the author's knowledge this is the first time such wave conversions were observed experimentally. It was also possible to measure wave speeds and attenuations of all the transmitted waves. This makes the study complete as all relevant parameters and measurements were made in this experiment. The reflectivity calculated from the set of measured parameters is found to agree with theory.

In chapter 9 reflectivity observations were acquired at the interfaces between water and water-saturated synthetic thick (7 cm) samples with a wide range of permeability and pore sizes. Not all parameters could be measured on these due to the thickness and the high attenuation related to the solid skeleton for both P and S waves. In these cases numerical modelling was used instead to find the best set of parameters that would give the closest reflectivity to the observed one. The reflectivity curves agree well with calculations but disagreement in the detail is noticeable particularly at post P-critical angle of incidence. Discrepancies between the full elastic Zoeppritz's (Zoeppritz, 1919) and porous media theory solutions are substantial at the frequency range used in this study. Therefore Zoeppritz's equations cannot be applied to laboratory reflectivity measurements from fluid-saturated porous media.

Concluding remarks, a summary of the results, and suggestions for future work are given in chapter 10.

Chapter 2

Plane waves, bounded acoustic beams, and bounded acoustic pulses in isotropic media

2.1 Introduction

The laboratory method used in the forthcoming experimental investigation of the reflectivity of porous media uses a large source transducer that generates a broad "bounded" acoustic pulse in a water filled tank. The pulse is referred to as bounded because it is both spatially and temporally limited. In order to properly describe the behaviour of the acoustic wave field generated by this source, the field is decomposed into its Fourier components. Each Fourier component represents a plane wave with an angular frequency and a direction of propagation defined by its wave number vector. It is therefore important to first briefly review plane wave propagation and the partitioning of energy at a fluid-solid interface. There are as well some interesting effects when acoustic beams are reflected at post-critical angles of incidence that are useful to review. One of these that occurs most strongly at what has been called the Rayleigh angle (Schoch, 1950; Brekhovskikh, 1960) is of particular significance to experimental observations.

A review of wave propagation in isotropic media is first given followed by the solution to the reflection-transmission problem at a fluid-solid boundary. The phase of the reflection coefficient will be studied in detail as it plays a dominant role in the understanding of bounded acoustic beams and bounded acoustic pulses reflected from a fluid-solid boundary. An example of a water-glass interface will be given as an illustration that will show the importance the phase of the reflection coefficient plays in the reflectivity response of a fluid-solid boundary. Finally numerical reflectivity results will be given for both bounded acoustic beams and bounded acoustic pulses.

In this thesis a "bounded acoustic pulse" refers to a wave field limited in both time and space whereas a "bounded acoustic beam" is only bounded in space and is monochromatic. These two type of wave field are distinguished because the phase shift that these experience will depend on frequency even though the reflectivity of a plane wave has a frequency independent reflection coefficient when isotropic and elastic media are involved. This substantially complicates, but also makes more interesting, the experimental observations.

In achieving these results a great deal of computational effort was made. Many codes were developed for forward modelling, migration, and reflectivity of both bounded acoustic beams and bounded acoustic pulses. Some of these programs involve significant running time to accomplish the results that will be presented, particularly for preparing the data for each angle of incidence in the reflectivity models of the bounded acoustic pulses.

2.1.1 Geometry of the problem

The reference frame that will be used at all time is the ($\hat{x}$, $\hat{z}$) cartesian coordinate system where $\hat{x}$ and $\hat{z}$ are the horizontal and vertical directions respectively (Fig. 2.1). This coordinate system will be used in all two dimensional problems and the third dimension $\hat{y}$ if needed is normal to the plane of the paper. The reflection and transmission coefficients are all written in terms of the vertical and horizontal wave numbers. This will allow a better understanding of the reflectivity of bounded acoustic beams and particularly of bounded acoustic pulses. Indeed, the development of the theory here was necessitated by the earliest observations of the acoustic reflectivity tests. It was anticipated, perhaps naïvely, that the experimental reflectivity curves would be easily interpretable using plane wave theory as occurs often in experimental geophysics. This was not the case and a more realistic description of the bounded acoustic pulse was required.

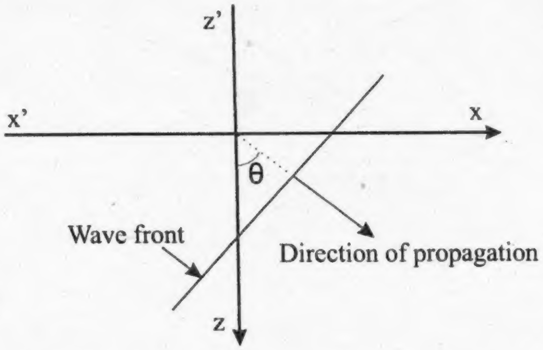

Figure 2.1: The two dimensional reference frame used in all 2D problems. The third dimension $\hat{y}$ is normal to the plane $(\hat{x}, \hat{z})$.

To the author's knowledge bounded acoustic pulses have not been investigated in detail in the literature. It is therefore crucial to give a complete description of these wave fields as they are used exclusively in the experiments. The present analysis is based on the theoretical work described in Brekhovskikh (1960) but likely first developed by Schoch (1950). This work is reviewed and then applied to model the response of reflected bounded acoustic pulses. Initially, however, we begin with an overview of wave propagation in fluids, this material exists in many texts but it is included in order to introduce the reader to the nomenclature and mathematical methods employed.

2.2 Wave propagation in real fluids

The fluid used in the forthcoming experiments is water. In this section plane waves propagating in real fluids with viscosity are first considered. Viscous fluids can support a shear stress and consequently S-waves can propagate although in reality they are highly attenuated. Attenuation and dispersion of both longitudinal and shear waves vary with viscosity. Here the propagation of both longitudinal and shear waves in real fluids will be considered.

All bounded acoustic beams and bounded acoustic pulses can be decomposed onto plane waves. These basic concepts presented will demonstrate that in the frequency range used here one can ignore completely transverse waves and attenuation of P-waves in water. Such plane waves are then used in constructing bounded acoustic beams and bounded acoustic pulses. It is important to understand the behaviour of bounded acoustic beams and bounded acoustic pulses to properly interpret and support the later experimental observations, the unusual characteristics of which were not expected when this work was began.

2.2.1 Plane waves in fluids

The derivation of the equations that describe wave propagation in fluids below is a shortened version of that found in many texts which will follow the work of Bhatia and Singh (1986). The wave equation in real fluids is given by the acoustic approximation to the Navier-Stokes equation for small displacements. In the absence of body forces this equation is given by Bhatia and Singh (1986)

$$\rho_0 \frac{\partial \vec{v}}{\partial t} = -\vec{\nabla} p + \left(b + \frac{1}{3}\eta \right) \vec{\nabla}\vec{\nabla} \cdot \vec{v} + \eta \nabla^2 \vec{v} \tag{2.1}$$

where ρ_0 represents the unperturbed fluid mass density, $\vec{v}$ the particle velocity, t time, p pressure, b bulk viscosity, and η the shear viscosity. η is the quantity more commonly known as viscosity, it can be easily experimentally measured (Gray, 1963). The bulk viscosity is a dynamic parameter that depends on the time rate of change of the density of the fluid as it is perturbed by the wave. Bulk viscosity is very difficult to measure directly and it must be inferred from ultrasonic wave attenuation (Bhatia and Singh, 1986).

To develop the approximation, expand the pressure p in a Taylor's series and retain terms of first order

$$p(\rho) = p(\rho_0 + \delta\rho) = p(\rho_0) + \left(\frac{\delta p}{\delta \rho} \right)_{\rho=\rho_0} (\rho - \rho_0) \tag{2.2}$$

where ρ_0 and ρ are the unperturbed and perturbed densities respectively. Equation 2.2 can be rewritten as

$$\vec{\nabla} p = \left(\frac{\delta p}{\delta \rho} \right) \vec{\nabla} \rho \tag{2.3}$$

The equation of continuity is given by

$$\frac{\partial \rho}{\partial t} + \rho_0 \vec{\nabla} \cdot \vec{v} = 0 \tag{2.4}$$

Combining equations 2.3 and 2.4 allows equation 2.1 to be rewritten as

$$\rho_0 \frac{\partial^2 \vec{v}}{\partial t^2} = \rho_0 V_0^2 \vec{\nabla} \vec{\nabla} \cdot \vec{v} + \frac{\partial}{\partial t} \left[\left(b + \frac{1}{3} \eta \right) \vec{\nabla} \vec{\nabla} \cdot \vec{v} + \eta \nabla^2 \vec{v} \right] \tag{2.5}$$

where $V_0 = \left(\frac{\delta p}{\delta \rho} \right)^{\frac{1}{2}}$ is constant and is the speed of sound in the fluid. Now, using Helmhotz decomposition we express the particle velocity $\vec{v}$ in terms of a scalar potential ϕ and a vector potential $\vec{\psi}$

$$\vec{v} = \frac{\partial}{\partial t} \left(\vec{\nabla} \phi + \vec{\nabla} \times \vec{\psi} \right) \tag{2.6}$$

Substituting equation 2.6 into equation 2.5 we obtain

$$\rho_0 \frac{\partial^2 \phi}{\partial t^2} = \left[\rho_0 V_0^2 + \left(b + \frac{4}{3} \eta \right) \frac{\partial}{\partial t} \right] \nabla^2 \phi \tag{2.7}$$

for longitudinal waves and

$$\rho_0 \frac{\partial^2 \vec{\psi}}{\partial t^2} = \eta \frac{\partial}{\partial t} \nabla^2 \vec{\psi} \tag{2.8}$$

for transverse waves.

2.2.2 Effect of fluid viscosity on acoustic plane waves

Real fluids can support shear stress which is, of course, highly dependent on viscosity. Shear waves thus can propagate in real fluid due to viscosity although in practice one may never actually be able to observe this, particularly for low viscosity fluids.

First consider longitudinal waves, specifically an $\hat{x}$ propagating plane wave with particle velocity in the $\hat{x}$ direction. Then equation 2.7 becomes

$$\rho_0 \frac{\partial^2 \phi}{\partial t^2} = \left[\rho_0 V_0^2 + \left(b + \frac{4}{3} \eta \right) \frac{\partial}{\partial t} \right] \frac{\partial^2 \phi}{\partial x^2} \tag{2.9}$$

Using plane wave solutions of the form

$$\phi = \phi_0 e^{i(kx - \omega t)} \tag{2.10}$$

where k is the wave number, which is in general complex, and ω is the angular frequency, we get the dispersion relation

$$k^2 = \frac{\rho_0 \omega^2}{\left[\rho_0 V_0^2 + i\omega \left(b + \frac{4}{3} \eta \right) \right]} \tag{2.11}$$

Let $\vec{k} = \vec{k_1} + i\vec{k_2}$ where $\vec{k_1}$ represents the propagation vector perpendicular to lines of constant phase, and $\vec{k_2}$ represents the attenuation vector, perpendicular to the lines of constant amplitude. In general, $\vec{k_1}$ and $\vec{k_2}$ need not be parallel. The scalar potential can then be rewritten as

$$\phi = \phi_0 e^{-k_2 x} e^{i(k_1 x - \omega t)} \tag{2.12}$$

The phase velocity and the attenuation can be derived from equation 2.11. First rewrite this equation as

$$k_1^2 - k_2^2 - 2ik_1k_2 = \frac{\omega^2}{V_0^2}\frac{1}{1 + i\frac{\omega}{\omega_\eta}} \tag{2.13}$$

Let $\omega << \omega_\eta$ where $\omega_\eta = \frac{\rho_0 V_0^2}{b+\frac{4}{3}\eta}$ often known as the viscosity relaxation frequency (Bhatia and Singh, 1986). In the low frequency limit (10^7 Hz) solving for k_1 and k_2 and keeping only terms of first order in $\frac{\omega}{\omega_\eta}$ we get

$$V = V_0 \tag{2.14}$$

Thus there is no dispersion in the phase velocity of longitudinal waves as can be seen through equation 2.14 where the velocity of the propagation V remains constant. The attenuation in the other hand increases with viscosity and is given by

$$k_2(\omega) = \frac{\omega^2}{2\rho_0 V_0^3}\left(b + \frac{4}{3}\eta\right) \tag{2.15}$$

Equation 2.15 can be used to infer the bulk viscosity b (Bhatia and Singh, 1986). In the absence of bulk viscosity equation 2.15 reduces to Stokes attenuation formula given by

$$k_2^{Stokes}(\omega) = 2\frac{\omega^2\eta}{3\rho_0 V_0^3} \tag{2.16}$$

Using equation 2.15 and equation 2.16 we obtain

$$b = \frac{4}{3}\left(\frac{k_2 - k_2^{Stokes}}{k_2^{Stokes}}\right)\eta \tag{2.17}$$

In the formula above k_2 is the total observed attenuation that includes attenuation due to both the shear and bulk viscosities. k_2^{Stokes} is found using the shear viscosity η, the unperturbed fluid mass density ρ_0, and the velocity of sound in the fluid V_0. Therefore at any given frequency the bulk viscosity can be inferred from the measurement of the total attenuation and the Stokes attenuation.

A more common way to describe attenuation is by the dimensionless quality factor Q (see e.g. Aki and Richards (1980), Guéguen and Palciauskas (1994), and O'Connell and Budiansky (1978)) that is given by

$$Q = \frac{2\pi E}{\Delta E} \tag{2.18}$$

where E is the total energy in a wave cycle and ΔE is the dissipated energy during a wave cycle. For a plane wave we have

$$Q(\omega) = \frac{\omega}{2k_2 V_0} \tag{2.19}$$

where k_2 is the attenuation, V_0 is the phase velocity at the angular frequency ω. In the case of a viscous fluid we have

$$Q(\omega) = \frac{\rho_0 V_0^2}{\omega(b + \frac{4}{3}\eta)} . \tag{2.20}$$

The attenuation is illustrated by two examples, water (low viscosity) and glycerol (high viscosity). The properties of these two fluids are given in table 2.1. These data are from Bhatia and Singh (1986), after Litovitz (1960). The attenuation and the quality factor are plotted against frequency in figure 2.2 for water and in figure 2.3 for glycerol. We see that the quality factor is very high (very low attenuation) for water (in the order of 10^5 at 1 MHz). Therefore within the displayed frequency range one can safely neglect attenuation of P-waves in water. Glycerol in the other hand has a lower quality factor than water, in the order of 190 at 1 MHz. Thus in glycerol the attenuation is not negligible at the considered frequency range.

Fluid	V_0 m/s	η Pa.s	$\frac{b}{\eta}$ –	ρ_0 kg/m^3
Water	1500	0.001	2.5	1000
Glycerol	1923	1.499	1.1	1261.3

Table 2.1: Properties of water and glycerol at 20^0C. V_0 is the velocity of sound, η the shear viscosity, b the bulk viscosity, and ρ_0 the unperturbed density. Data from Bhatia and Singh (1986), after Litovitz (1960).

Now consider transverse waves propagating in the $\hat{x}$ direction and let the particle motion be in the $\hat{z}$ direction. Because the displacement (or velocity) is derived

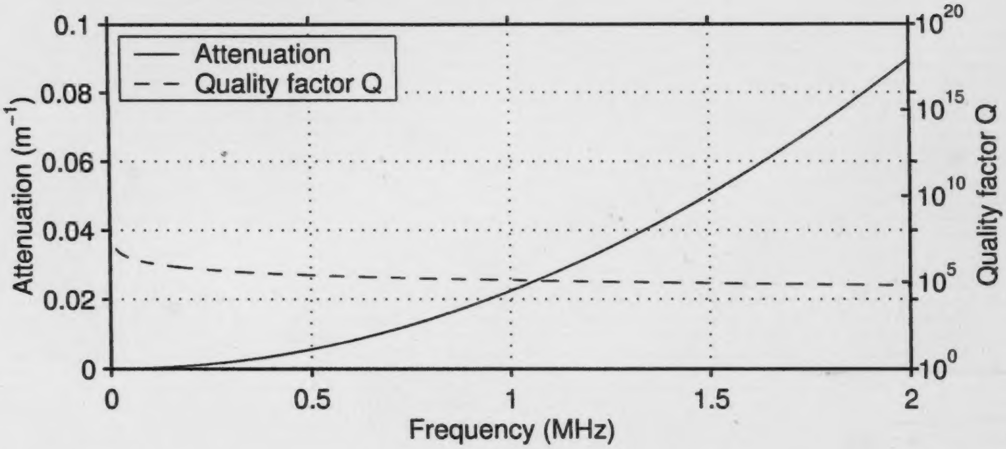

Figure 2.2: Attenuation and quality factor Q of longitudinal plane waves in water. The quality factor is very high and is of the order of 10^5 at 1 MHz.

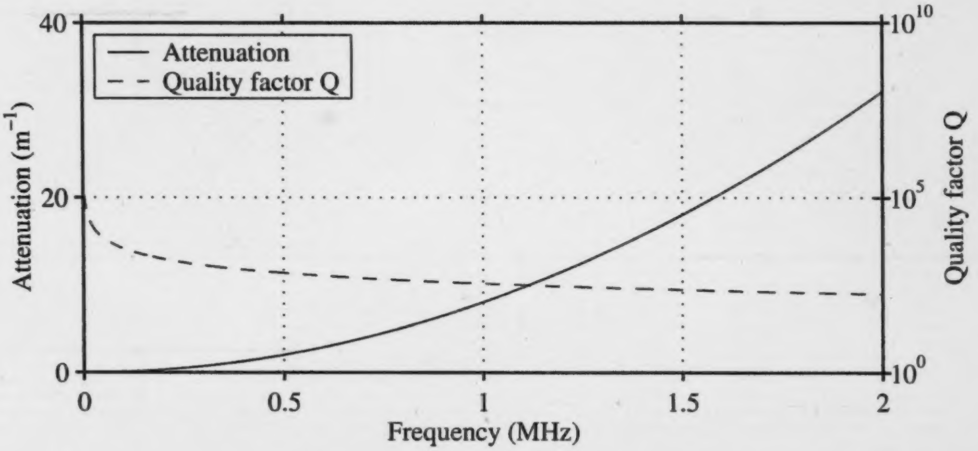

Figure 2.3: Attenuation and quality factor Q of longitudinal planes wave in glycerol. The quality factor is low and is of the order of 190 at 1 MHz.

from the curl of the vector potential, the latter must be in the $\hat{y}$ direction to be perpendicular to both the velocity and the wave number vector $\vec{k}$. In this case equation 2.8 becomes

$$\rho_0 \frac{\partial^2 \psi_y}{\partial t^2} = \eta \frac{\partial}{\partial t} \nabla^2 \psi_y \qquad (2.21)$$

Using a plane wave solution of the form

$$\vec{\psi} = \hat{y}\psi_0 e^{i(kx-\omega t)} \tag{2.22}$$

we get the dispersion relation

$$k^2 = i\omega\frac{\rho_0}{\eta} \tag{2.23}$$

Letting $\vec{k} = \vec{k_1} + i\vec{k_2}$ as for longitudinal waves, the vector potential $\vec{\psi}$ can be rewritten as

$$\vec{\psi} = \hat{y}\psi_0 e^{-k_2 x} e^{i(k_1 x-\omega t)} \tag{2.24}$$

From the dispersion relation 2.23 we have $k_1 = k_2$. The phase velocity and the attenuation of the viscous waves are then given by

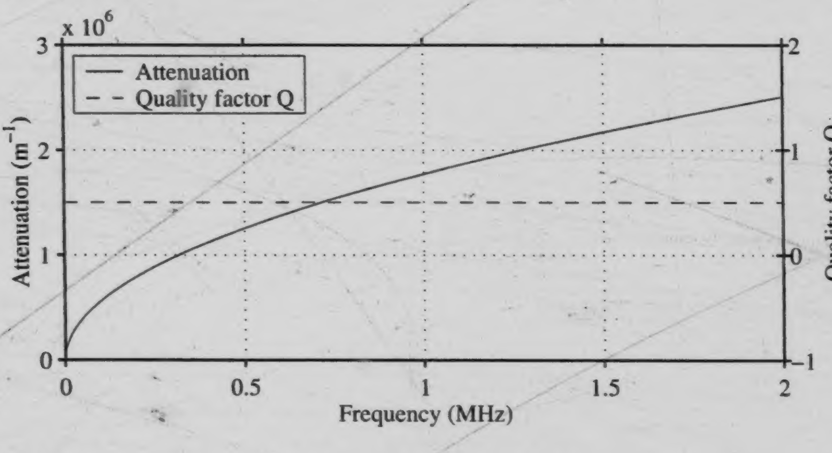

Figure 2.4: Attenuation and quality factor Q of transverse plane waves in water.

$$V(\omega) = \left(\frac{2\eta\omega}{\rho_0}\right)^{\frac{1}{2}} \tag{2.25}$$

$$k_1(\omega) = \left(\frac{\omega\rho_0}{2\eta}\right)^{\frac{1}{2}} \tag{2.26}$$

$$Q(\omega) = 0.5 \tag{2.27}$$

Note that for transverse waves both the phase velocity and the attenuation depend on frequency. The phase velocity increases whereas the attenuation decreases with increasing viscosity. The quality factor is constant (0.5) and is independent of the fluid properties for all frequencies and is very low (Figs. 2.4-2.5). The attenuation

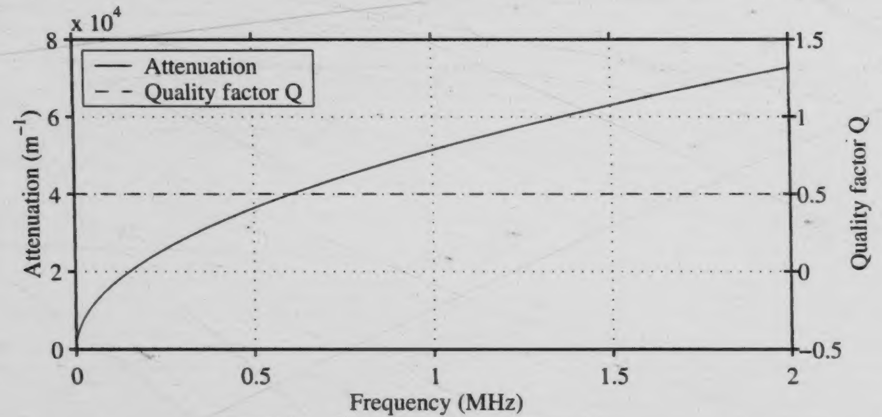

Figure 2.5: Attenuation and quality factor Q of transverse plane waves in glycerol. The quality factor factor is very low.

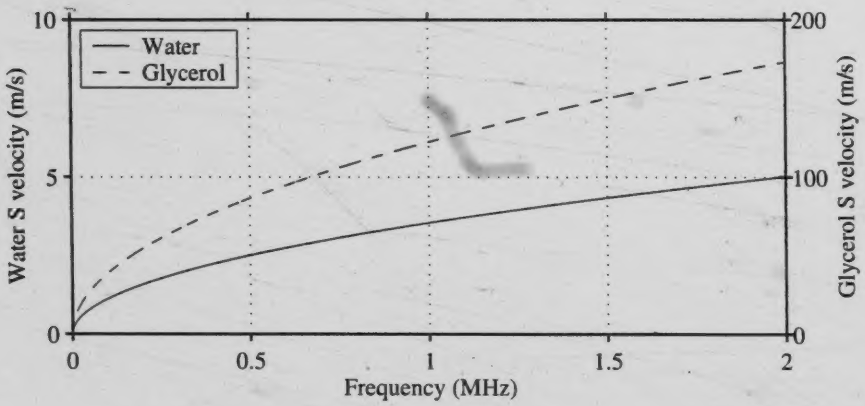

Figure 2.6: Phase velocity of transverse plane waves in water and glycerol.

is very high for water and moderate for glycerol. The phase velocities of transverse waves in water and glycerol are shown in figures 2.6. These velocities are very low for water and reach the value of 175 m/s at 2 MHz for glycerol. In light of these results we can safely neglect the transverse waves in water in the forthcoming experiments. To carry the experimental work which will be described and discussed in this study a frequency bandwidth limited signal will be used (0.2-1.2 MHz). All experiments will be conducted in a water filled tank.

2.3 Plane waves in non-attenuating media

In this section we first investigate the type of waves that can propagate in an isotropic, homogeneous, and non-attenuating medium. This review will follow the work of Bedford et al. (2000). Create a Cartesian space ($\hat{x}$,$\hat{y}$,$\hat{z}$) that contains an isotropic, homogeneous, and non-attenuating medium (Fig. 2.1), the $\hat{y}$ axis points outwards perpendicular to the plane of the paper. Let the particle motions for all possible wave modes that can propagate in such media lie in the $(\hat{x}, \hat{z})$ plane. Subscripts $_x$, and $_z$ indicate components in the corresponding direction. The wave equations are given in terms of potentials by

$$\frac{\partial^2 \phi}{\partial t^2} = V_p^2 \left(\frac{\partial^2 \phi}{\partial x^2} + \frac{\partial^2 \phi}{\partial z^2} \right) \tag{2.28}$$

$$\frac{\partial^2 \vec{\psi}}{\partial t^2} = V_s^2 \left(\frac{\partial^2 \vec{\psi}}{\partial x^2} + \frac{\partial^2 \vec{\psi}}{\partial z^2} \right) \tag{2.29}$$

for dilatational and rotational waves respectively. As is shown in many texts the dilatational wave velocity V_p and the S-wave velocity V_s are given in terms of material parameters by

$$V_p = \left(\frac{\lambda + \mu}{\rho} \right)^{\frac{1}{2}} \tag{2.30}$$

$$V_s = \left(\frac{\mu}{\rho} \right)^{\frac{1}{2}} \tag{2.31}$$

where λ and μ are the Lamé constants.

2.3.1 Solutions to the dilatational wave equation

Assume solutions to equation 2.28 of the form

$$\phi = f(z) e^{i(k_x x - \omega t)} \tag{2.32}$$

The potential for compressional waves as given by equation 2.32 assumes that the wave propagates in the $\hat{x}$ direction with a real wave number $\vec{k_x}$ but with no restrictions in the $\hat{z}$ direction. By substituting this solution into the equation of motion 2.28 we get

$$\frac{d^2 f(z)}{dz^2} + \left(\frac{\omega^2}{V_p^2} - k_x^2 \right) f(z) = 0 \tag{2.33}$$

Equation 2.33 has solutions of the form

$$f(z) = Ae^{ik_z z} + Be^{-ik_z z} \tag{2.34}$$

where A and B are arbitrary complex numbers and k_z is the vertical wave number given by

$$k_z = \left(\frac{\omega^2}{V_p^2} - k_x^2\right)^{\frac{1}{2}} \tag{2.35}$$

Note that here k_z can either be real or pure imaginary according to the sign of the quantity under the square root.

2.3.1.1 Case where k_z is a real number

If $k_x^2 < \frac{\omega^2}{V_p^2}$ then k_z is real and the solution given by equation 2.32 becomes

$$\phi = Ae^{i(k_x x + k_z z - \omega t)} + Be^{i(k_x x - k_z z - \omega t)} \tag{2.36}$$

The first term of equation 2.36 represents waves travelling with a component in the positive $\hat{z}$ direction whereas the second term represents waves travelling with a component in the negative $\hat{z}$ direction. k_x and k_z represent the projections of the wave number $\vec{k}$ in the direction $\hat{x}$ and $\hat{z}$ respectively. Equation 2.36 can be rewritten as

$$\phi = Ae^{i(k\sin\theta x + k\cos\theta z - \omega t)} + Be^{i(k\sin\theta x - k\cos\theta z - \omega t)} \tag{2.37}$$

where θ is the angle between the wave number $\vec{k}$ and the $\hat{z}$ direction (Fig. 2.1). Now let the wave be travelling with a component in the positive $\hat{z}$ direction ($B = 0$). The displacement is then given by

$$\vec{u} = \frac{\partial\phi}{\partial x}\hat{x} + \frac{\partial\phi}{\partial z}\hat{z} \tag{2.38}$$

Using the solution given by equation 2.37 we get

$$\vec{u} = \left[\hat{x}ikA\sin\theta + \hat{z}ikA\cos\theta\right] e^{i(k\sin\theta x + k\cos\theta z - \omega t)} \tag{2.39}$$

which can be rewritten as

$$\vec{u} = i\vec{k}Ae^{i(\vec{k}\cdot\vec{x} - \omega t)} \tag{2.40}$$

The physical displacement is then given by the real part of equation 2.40 and is

$$\vec{u_r} = \vec{k} \mid A \mid \cos(\vec{k}\cdot\vec{x} - \omega t + arg(A) + \frac{\pi}{2}) \tag{2.41}$$

The amplitude of the wave is $k \mid A \mid$. These are longitudinal waves that propagate with a real wave number.

2.3.1.2 Case where k_z is a pure imaginary number

If k_z is a pure imaginary number (case where $k_x^2 > \frac{\omega^2}{V_p^2}$) then equation 2.34 becomes

$$f(z) = Ae^{-hz} + Be^{hz} \tag{2.42}$$

where A and B are arbitrary complex numbers and h is a real positive number given by

$$h = \left(k_x^2 - \frac{\omega^2}{V_p^2}\right)^{\frac{1}{2}} \tag{2.43}$$

In this case we have

$$\phi = Ae^{-hz}e^{i(k_x x-\omega t)} + Be^{hz}e^{i(k_x x-\omega t)} \tag{2.44}$$

The first term of equation 2.44 represents waves travelling in the $\hat{x}$ direction with amplitudes decaying exponentially with increasing z and increasing exponentially with decreasing z. The second term represents waves travelling in the $\hat{x}$ direction with amplitudes increasing exponentially with increasing z and decreasing exponentially with decreasing z. Now let the wave be travelling with amplitudes increasing in the positive $\hat{x}$ direction and decaying with increasing z ($B = 0$). The other direction ($A = 0$) can be treated similarly. Equation 2.44 can then be rewritten as

$$\phi = Ae^{i(k_x x+k_z z-\omega t)} \tag{2.45}$$

where k_z is

$$k_z = ih \tag{2.46}$$

Thus equation 2.45 can be rewritten as

$$\phi = Ae^{i(\vec{k}\cdot\vec{x}-\omega t)} \tag{2.47}$$

with $\vec{k}$ given by

$$\vec{k} = \vec{k_x} + i\vec{h} \tag{2.48}$$

where $\vec{k_x}$ and $\vec{h}$ are the components of the wave number $\vec{k}$ in the direction $\hat{x}$ and $\hat{z}$ respectively. Furthermore we have

$$\begin{aligned} k^2 &= k_x^2 - h^2 & (2.49) \\ k &= \frac{\omega}{V_p} & (2.50) \end{aligned}$$

The displacement is given by equation 2.38. Using the solution given by equation 2.44 we get

$$\vec{u} = iA\vec{k}e^{i(k_x x - \omega t)}e^{-hz} \tag{2.51}$$

The physical displacement is then given by the real part of equation 2.51

$$\vec{u_r} = \mid A \mid \left[\hat{x}k_x \cos(k_x x - \omega t + arg(A) + \frac{\pi}{2}) - \hat{z}h \sin(k_x x - \omega t + arg(A) + \frac{\pi}{2})\right] e^{-hz} \tag{2.52}$$

These type of waves are a special case of the general inhomogeneous waves that can propagate in attenuating media (and will be discussed again later in the porous media study in chapter 4). Here these waves propagate with a pure imaginary wave number k_z in the $\hat{z}$ direction and a real wave number k_x in the $\hat{x}$ direction. The amplitude increases exponentially in the negative $\hat{z}$ direction and decays exponentially in the positive $\hat{z}$ direction.

2.3.2 Transverse wave

Consider transverse waves travelling in the $\hat{x}$ direction. Let the physical displacement be in the $(\hat{x}, \hat{z})$ plane and the vector potential $\vec{\psi}$ be in the $\hat{y}$ direction. In this case equation 2.29 becomes

$$\frac{\partial^2 \psi_y}{\partial t^2} = V_s^2 \left(\frac{\partial^2 \psi_y}{\partial x^2} + \frac{\partial^2 \psi_y}{\partial z^2}\right) \tag{2.53}$$

This equation has the same form as equation 2.28 and can be treated in a manner similar to that for longitudinal waves described above. The vector potential can be written as

$$\psi_y = Ce^{i(\vec{k}\cdot\vec{x} - \omega t)} \tag{2.54}$$

where $k = \frac{\omega}{V_s}$. The displacement is given by

$$\vec{u} = \vec{\nabla} \times \vec{\psi} \tag{2.55}$$

using equation 2.54 in equation 2.55 we get

$$\vec{u} = -iC\left[k_z\hat{x} - k_x\hat{z}\right]e^{i\left(\vec{k}\cdot\vec{x} - \omega t\right)} \tag{2.56}$$

The physical displacement is given by the real part of equation 2.56 and is

$$\vec{u_r} = \mid C \mid \left[k_z\hat{x} - k_x\hat{z}\right]\cos(\vec{k}\cdot\vec{x} - \omega t + arg(C) - \frac{\pi}{2}) \tag{2.57}$$

and the amplitude of the wave is $\mid C \mid k$. In the case where $\vec{k} = \vec{k_x} + i\vec{h}$ equation 2.57 becomes

$$\vec{u} = C\left[h\hat{x} + ik_x\hat{z}\right]e^{-hz}e^{i(k_x x-\omega t)} \tag{2.58}$$

and the physical displacement is then

$$\vec{u_r} = \left[\hat{x} \mid C \mid h\cos(k_x x - \omega t + arg(C)) - \hat{z} \mid C \mid k_x \sin(k_x x - \omega t + arg(C))\right]e^{-hz} \tag{2.59}$$

with the amplitude of the wave $\mid C \mid ke^{-hz}$. These waves are of the same type as those described above for inhomogeneous dilatational waves.

2.4 Reflection-transmission of acoustic waves at a liquid-solid interface.

Even though the following two-dimensional boundary value problem has been solved in many texts, but often only partially treated for particular needs, it is essential to give here the solutions for the reflection-transmission coefficients as it is the framework upon which the experiments will build. The treatment will be given in terms of wave numbers as this will be found useful in describing propagation of bounded acoustic beams and bounded acoustic pulses in elastic media. Furthermore it will help understand the reflection-transmission problem in porous media that will be treated later. A spatial shift in the experimental reflected pulses will be discussed in great detail. It will turn out that understanding this unexpected phenomenon is central to the interpretation of the experimental results.

Consider a steady state dilatational plane wave be incident on a plane boundary between a fluid and a solid. Let the two isotropic media (a) and (b) be in perfect contact at the plane $z = 0$. Let the medium (a) be a liquid (with negligible viscosity) and the medium (b) be an elastic solid. A monochromatic plane wave (frequency ω) travelling in the liquid at an angle θ with respect to the $\hat{z}$ axis strikes the boundary between the liquid and the isotropic solid. In this case three waves are generated at the boundary, a reflected P-wave, a transmitted P-wave, and a transmitted S-wave (Fig. 2.7). Let the incident and reflected P-wave potentials be denoted by superscripts ^{i} and ^{r} respectively and the transmitted P-wave and S-wave potentials be denoted by a superscript ^{t}. Subscripts $_x$ and $_z$ will denote the components of the considered vectors and subscripts $_p$ and $_s$ will denote P and S transmitted waves respectively.

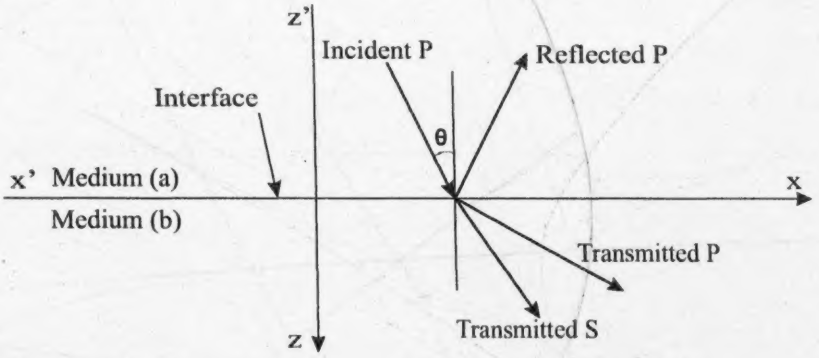

Figure 2.7: Waves generated at an interface between a liquid (medium (a)) and a solid (medium (b)) by an incident P-wave.

2.4.1 Boundary conditions at a fluid-solid boundary

The general boundary conditions at an interface between a fluid (a) and a solid (b) are

- continuity of normal stress across the boundary
- continuity of tangential stress across the boundary
- continuity of the normal particle displacement (or particle velocity) across the boundary

The first two conditions can be combined to

$$\sigma^{a}_{ij} n_i = \sigma^{b}_{ij} n_i \tag{2.60}$$

where n_i are components of the normal unit vector $\vec{n}$ to the boundary. To satisfy these conditions three waves must be generated at the interface (Fig. 2.7).

2.4.2 Displacement and velocity potentials

This boundary value problem is approached by using scalar and vector potentials and writing the boundary conditions given above in terms of the components of these quantities. Let ϕ and $\vec{\psi}$ be the scalar and vector potentials respectively. Using Helmhotz decomposition of a vector field, the particle displacement $\vec{u}$ and the particle velocity $\vec{v}$ can be written as

$$\vec{u} = \vec{\nabla}\phi + \vec{\nabla} \times \vec{\psi} \tag{2.61}$$

$$\vec{v} = \frac{\partial}{\partial t}\left(\vec{\nabla}\phi + \vec{\nabla} \times \vec{\psi}\right) \tag{2.62}$$

where ϕ describes the potential field created by a longitudinal particle motion and $\vec{\psi}$ describes the potential field created by a rotational particle motion. The combination of the two fields form the total potential field of the acoustic wave propagation.

2.4.3 Stress tensor for an isotropic solid

Let x_i be the $\hat{x}$, $\hat{y}$, and $\hat{z}$ directions for $i = 1, 2, 3$ respectively. For an isotropic solid material the stress tensor is given by

$$\sigma = \begin{bmatrix} \sigma_{11} & \sigma_{12} & \sigma_{13} \\ \sigma_{21} & \sigma_{22} & \sigma_{23} \\ \sigma_{31} & \sigma_{32} & \sigma_{33} \end{bmatrix}$$

We also have $\sigma_{21} = \sigma_{12}$, $\sigma_{31} = \sigma_{13}$, and $\sigma_{32} = \sigma_{23}$. The general stress components are given by

$$\sigma_{ij} = \mu\frac{\partial}{\partial x_j}\left(\vec{\nabla}\phi + \vec{\nabla} \times \vec{\psi}\right)_i + \mu\frac{\partial}{\partial x_i}\left(\vec{\nabla}\phi + \vec{\nabla} \times \vec{\psi}\right)_j + \lambda\delta_{ij}\nabla^2\phi \tag{2.63}$$

where μ and λ are the Lamé constants and i and j take the values $1, 2, 3$, and x_i are the Cartesian coordinates and

$$\delta_{ij} = \begin{cases} 1 & : \quad i = j \\ 0 & : \quad i \neq j \end{cases}$$

For a stress generated by a longitudinal wave ($\vec{\nabla} \times \vec{\psi} = 0$) equation 2.63 becomes

$$\sigma_{ij} = 2\mu\frac{\partial^2\phi}{\partial x_i \partial x_j} + \lambda\delta_{ij}\nabla^2\phi \tag{2.64}$$

and for a stress generated by a transverse wave ($\vec{\nabla}\phi = 0$) equation 2.64 becomes

$$\sigma_{ij} = \mu\left(\frac{\partial(\vec{\nabla} \times \vec{\psi})_i}{\partial x_j} + \frac{\partial(\vec{\nabla} \times \vec{\psi})_j}{\partial x_i}\right) \tag{2.65}$$

Using the longitudinal and transverse wave phase velocities

$$V_p = \left(\frac{\lambda + 2\mu}{\rho}\right)^{\frac{1}{2}} \tag{2.66}$$

$$V_s = \left(\frac{\mu}{\rho}\right)^{\frac{1}{2}} \tag{2.67}$$

equations 2.64 and 2.65 become

$$\sigma_{ij} = 2\rho V_s^2 \left(\frac{\partial^2 \phi}{\partial x_i \partial x_j} - \delta_{ij} \nabla^2 \phi\right) + \rho V_p^2 \delta_{ij} \nabla^2 \phi \tag{2.68}$$

$$\sigma_{ij} = \rho V_s^2 \left(\frac{\partial(\vec{\nabla} \times \vec{\psi})_i}{\partial x_j} + \frac{\partial(\vec{\nabla} \times \vec{\psi})_j}{\partial x_i}\right) \tag{2.69}$$

Evaluating the stress components we have explicitly for a longitudinal wave

$$\sigma_{zz} = \rho V_p^2 \frac{\partial^2 \phi}{\partial z^2} + \rho(V_p^2 - 2V_s^2)\frac{\partial^2 \phi}{\partial x^2} \tag{2.70}$$

in the $\hat{z}$ direction and

$$\sigma_{xz} = 2\rho V_s^2 \frac{\partial^2 \phi}{\partial x \partial z} \tag{2.71}$$

in the $\hat{x}$ direction. For a transverse wave we have

$$\sigma_{zz} = 2\rho V_s^2 \frac{\partial^2 \psi_y}{\partial z \partial x} \tag{2.72}$$

in the $\hat{z}$ direction and

$$\sigma_{xz} = \rho V_s^2 \left[\frac{\partial^2 \psi_y}{\partial x^2} - \frac{\partial^2 \psi_y}{\partial z^2}\right] \tag{2.73}$$

in the $\hat{x}$ direction.

2.4.4 Stress tensor in a real fluid

The general stress tensor (Bhatia and Singh, 1986) for a real fluid with non-negligible viscosity is given by

$$\begin{aligned}\sigma_{ij} = {} & -p\delta_{ij} + \eta^{'} \vec{\nabla} \cdot \frac{\partial}{\partial t}\left(\vec{\nabla}\phi + \vec{\nabla} \times \vec{\psi}\right)\delta_{ij} + \\ & 2\eta \frac{\partial}{\partial t}\left[\frac{\partial}{\partial x_i}\left(\vec{\nabla}\phi + \vec{\nabla} \times \vec{\psi}\right)_j + \frac{\partial}{\partial x_j}\left(\vec{\nabla}\phi + \vec{\nabla} \times \vec{\psi}\right)_i\right]\end{aligned} \tag{2.74}$$

where p is the fluid pressure, η is the shear viscosity, and $\eta^{'} = b + \frac{2}{3}\eta$ where b is the bulk viscosity. In the limit of vanishing viscosity equation 2.74 approaches

$$\sigma_{ij} = -p\delta_{ij} \tag{2.75}$$

and the vector potential $\vec{\psi} = 0$. All stress components vanish save for the principal stress $-p$ which may be written as

$$p = \rho V^2 \nabla^2 \phi \tag{2.76}$$

In the fluid we will neglect the viscosity and write the non-zero stress component as

$$\sigma_{zz} = -\rho V^2 \nabla^2 \phi \tag{2.77}$$

that is also equal to σ_{xx} and σ_{yy}.

2.4.5 Monochromatic plane wave reflection-transmission coefficients

The potentials of the incident, the reflected, and transmitted waves are described by

$$\begin{aligned}
\phi^i &= e^{i(k_{iz}z + k_{ix}x - \omega t)} \\
\phi^r &= Ae^{i(k_{rz}z + k_{rx}x - \omega t)} \\
\phi^t &= Be^{i(k_{pz}z + k_{px}x - \omega t)} \\
\vec{\psi}^t &= C\hat{y}e^{i(k_{sz}z + k_{sx}\cdot x - \omega t)}
\end{aligned} \tag{2.78}$$

where A, B, and C are complex amplitudes, and $\vec{k}$ is the wave number. Complex potentials are considered here for purely mathematical purposes as this will simplify greatly the problem. The actual potentials are the real parts of equations 2.78. All potentials are normalized with respect to the incident wave.

2.4.6 Boundary conditions

The boundary conditions in the case of a two dimensional problem are

$$\begin{aligned}
\sigma^a_{zz} &= \sigma^b_{zz} \\
\sigma^a_{xz} &= \sigma^b_{xz} \\
v^a_z &= v^b_z
\end{aligned} \tag{2.79}$$

There are no constraints on v_x, σ_{xy}, and σ_{yy}. In the solid medium (b) the normal stress is given by

$$\sigma^b_{zz} = \rho^b {V_p}^2 \frac{\partial^2 \phi^t}{\partial z^2} + \rho^b ({V_p}^2 - 2{V_s}^2) \frac{\partial^2 \phi^t}{\partial x^2} + 2\rho^b {V_s}^2 \frac{\partial^2 \psi^t_y}{\partial z \partial x} \tag{2.80}$$

and the tangential stress is given by

$$\sigma^b_{zx} = 2\rho^b {V_s}^2 \frac{\partial^2 \phi^t}{\partial z \partial x} + \rho^b {V_s}^2 \left(\frac{\partial^2 \psi^t_y}{\partial x^2} - \frac{\partial^2 \psi^t_y}{\partial z^2} \right) \tag{2.81}$$

In the fluid medium (a) the normal and tangential stresses are respectively

$$\sigma^a_{zz} = -\rho^a V^2 \nabla^2 (\phi^i + \phi^r) \tag{2.82}$$

$$\sigma^a_{xz} = 0 \tag{2.83}$$

In equations 2.79 through 2.83 upper case V and lower case v designate the wave speed and the particle velocity in the fluid respectively.

2.4.7 Solution

Using the potentials given in equations 2.78 in the boundary conditions 2.79 we get

$$\begin{aligned}
&\rho^b V_p^2 k_{pz}^2 \phi^t + \rho^b \left[V_p^2 - 2V_s^2\right] k_{px}^2 \phi^t + \\
&2\rho^b V_s^2 k_{sx} k_{sz} \psi^t_y - \rho^a V^2 \left[{k_{rx}}^2 + {k_{rz}}^2\right] \phi^r - \\
&\rho^a V^2 \left[{k_{ix}}^2 + {k_{iz}}^2\right] \phi^i &= 0 \\
&2k_{px}k_{pz}\phi^t + \left[k_{sx}^2 - k_{sz}^2\right] \psi^t_y &= 0 \\
&k_{pz}\phi^t + k_{sx}\psi^t_y - k_{rz}\phi^r - k_{iz}\phi^i &= 0
\end{aligned} \tag{2.84}$$

In order for equations 2.84 to hold for all x at all times on the plane $z = 0$ we must have all the exponential terms equal. Therefore we must have

$$k_{ix} = k_{rx} = k_{px} = k_{sx} \tag{2.85}$$

which is simply the generalized Snell's law. The fact that these horizontal wave numbers components remain real valued is important as will be seen in the discussion later. Let the $\hat{x}$ component for all wave numbers in both media be simply k_x and let $\rho = \frac{\rho^a}{\rho^b}$. We also have $k_{iz} = -k_{rz}$. Rearranging equation 2.84 we get

$$\begin{bmatrix} -\rho V^2 k^2 & [V_p^2 k_p^2 - 2V_s^2 k_x^2] & 2V_s^2 k_x k_{sz} \\ 0 & 2k_x k_{pz} & [2k_x^2 - k_s^2] \\ k_{iz} & k_{pz} & k_x \end{bmatrix} \begin{bmatrix} A \\ B \\ C \end{bmatrix} = \begin{bmatrix} \rho V^2 k^2 \\ 0 \\ k_{iz} \end{bmatrix} \tag{2.86}$$

Replacing V^2, V_p^2, and V_s^2 by $\frac{\omega^2}{k^2}$, $\frac{\omega^2}{k_p^2}$, and $\frac{\omega^2}{k_s^2}$ respectively we have

$$\begin{bmatrix} -\rho k_s^2 & [k_s^2 - 2k_x^2] & 2k_{sz} k_x \\ 0 & 2k_x k_{pz} & [2k_x^2 - k_s^2] \\ k_{iz} & k_{pz} & k_x \end{bmatrix} \begin{bmatrix} A \\ B \\ C \end{bmatrix} = \begin{bmatrix} \rho k_s^2 \\ 0 \\ k_{iz} \end{bmatrix} \tag{2.87}$$

where $k_{iz} = [k^2 - k_x^2]^{\frac{1}{2}}$, $k_{pz} = [k_p^2 - k_x^2]^{\frac{1}{2}}$, and $k_{sz} = [k_s^2 - k_x^2]^{\frac{1}{2}}$. Solving the system of equations 2.87 we get the complex amplitudes A, B, and C of the reflected scalar potential ϕ^r, the transmitted scalar potential ϕ^t, and the transmitted vector potential $\vec{\psi}^t$ respectively. Explicitly:

$$A = \frac{(2k_x^2 - k_s^2)^2 + 4[k_p^2 - k_x^2]^{\frac{1}{2}}[k_s^2 - k_x^2]^{\frac{1}{2}}k_x^2 - \rho k_s^4[k_p^2 - k_x^2]^{\frac{1}{2}}[k^2 - k_x^2]^{-\frac{1}{2}}}{(2k_x^2 - k_s^2)^2 + 4[k_p^2 - k_x^2]^{\frac{1}{2}}[k_s^2 - k_x^2]^{\frac{1}{2}}k_x^2 + \rho k_s^4[k_p^2 - k_x^2]^{\frac{1}{2}}[k^2 - k_x^2]^{-\frac{1}{2}}} \tag{2.88}$$

$$B = -\frac{2\rho k_s^2(2k_x^2 - k_s^2)}{(2k_x^2 - k_s^2)^2 + 4[k_p^2 - k_x^2]^{\frac{1}{2}}[k_s^2 - k_x^2]^{\frac{1}{2}}k_x^2 + \rho k_s^4[k_p^2 - k_x^2]^{\frac{1}{2}}[k^2 - k_x^2]^{-\frac{1}{2}}} \tag{2.89}$$

$$C = \frac{4\rho k_x[k_p^2 - k_x^2]^{\frac{1}{2}}k_s^2}{(2k_x^2 - k_s^2)^2 + 4[k_p^2 - k_x^2]^{\frac{1}{2}}[k_s^2 - k_x^2]^{\frac{1}{2}}k_x^2 + \rho k_s^4[k_p^2 - k_x^2]^{\frac{1}{2}}[k^2 - k_x^2]^{-\frac{1}{2}}} \tag{2.90}$$

The complex amplitudes A, B, and C describe the maximum amplitudes of the potentials at the interface $z = 0$. When $z \neq 0$ the amplitudes of the reflected and transmitted waves depend on the complex wave numbers in the $\hat{z}$ direction beyond the P and S critical angles. Using equations 2.78 in equation 2.61 we get the complex displacements

$$\begin{aligned} u^r &= iA\left[k_{rx}\hat{x} + k_{rz}\hat{z}\right]e^{i(k_{rz}z + k_{rx}x - \omega t)} \\ u_p^t &= iB\left[k_{px}\hat{x} + k_{pz}\hat{z}\right]e^{i(k_{pz}z + k_{px}x - \omega t)} \\ u_s^t &= iC\left[-k_{sz}\hat{x} + k_{sx}\hat{z}\right]e^{i(k_{sz}z + k_{sx}\cdot x - \omega t)} \end{aligned} \tag{2.91}$$

The normalized complex amplitudes are A, $\frac{Bk_p}{k}$, and $\frac{Ck_s}{k}$ for the reflected P, the transmitted P, and the transmitted S waves respectively. It is also important to note that the physical displacements are given by the real parts of equations 2.91. The particle velocity is the derivative of equations 2.91 with respect to time. It is very important to notice that the normalized amplitude for the reflected wave remains the same for the potential, the displacement, particle velocity, pressure, and particle acceleration. No matter what is measured in a reflected wave experiment we obtain the same value as long as we normalize the reflected wave to the measured direct arrival.

Another quantity that is important to verify is the energy balance of the boundary. This energy balance of the boundary is calculated through the total energy flux normal to the boundary of the incident wave and all reflected and transmitted waves. The energy flux is given by the complex Poynting vector (Auld, 1973)

$$\vec{J} = -\frac{1}{2}\left[\vec{v^*} \cdot \vec{\sigma}\right] \tag{2.92}$$

where $\vec{v^*}$ is the complex conjugate of the particle velocity field, and $\vec{\sigma}$ is the stress tensor of the wave field. The energy flux normal to the boundary is then

$$J_z = -\frac{1}{2}\left[v_z^*\sigma_{zz} + v_x^*\sigma_{xz}\right] \tag{2.93}$$

The average power flow density is the real part of equation 2.93. For a plane longitudinal wave of complex amplitude A in an isotropic elastic medium we have

$$\begin{aligned}
\sigma_{zz} &= -A\rho\left[V_p^2k^2 - 2V_s^2k_x^2\right]e^{i(k_{pz}z+k_xx-\omega t)} && (2.94)\\
\sigma_{xz} &= -2A\rho V_s^2k_xk_{pz}e^{i(k_{pz}z+k_xx-\omega t)} && (2.95)\\
v_z &= A\omega k_{pz}e^{i(k_{pz}z+k_xx-\omega t)} && (2.96)\\
v_x &= A\omega k_xe^{i(k_{pz}z+k_xx-\omega t)} && (2.97)
\end{aligned}$$

Using equations 2.94 through 2.97, equation 2.93 leads to

$$J_{pz} = \frac{1}{2} \mid A \mid^2 \rho \mid k_{pz} \mid \omega\left[V_p^2k_p^2 - 4V_s^2\right]e^{iArg(k_{pz})} \tag{2.98}$$

where J_{pz} is the $\hat{z}$ component of the energy flux of the P-wave. For a plane transverse wave of complex amplitude A in an isotropic elastic medium we have

$$\begin{aligned}
\sigma_{zz} &= -2A\rho V_s^2k_xk_{sz}e^{i(k_{sz}z+k_xx-\omega t)} && (2.99)\\
\sigma_{xz} &= -A\rho V_s^2\left[k_x^2 - k_{sz}^2\right]e^{i(k_{sz}z+k_xx-\omega t)} && (2.100)\\
v_z &= A\omega k_xe^{i(k_zz+k_xx-\omega t)} && (2.101)\\
v_x &= -A\omega k_{sz}e^{i(k_{sz}z+k_xx-\omega t)} && (2.102)
\end{aligned}$$

Using equations 2.99 through 2.102 equation 2.93 leads to

$$J_{sz} = \frac{1}{2} \mid A \mid^2 \rho \mid k_{sz} \mid \omega^3e^{iArg(k_{sz})} \tag{2.103}$$

where J_{sz} is the $\hat{z}$ component of the energy flux of the S-wave. The energy fluxes J_{iz}, J_{rz}, J_{pz}, and J_{sz} of the incident P, reflected P, transmitted P, and transmitted S waves respectively are

$$\begin{aligned}
J_{iz} &= \frac{1}{2}\rho^{(a)}k_z\omega^3 && (2.104)\\
J_{rz} &= -\frac{1}{2} \mid A \mid^2 \rho^{(a)}k_z\omega^3 && (2.105)\\
J_{pz} &= \frac{1}{2} \mid B \mid^2 \rho^{(b)} \mid k_{pz} \mid \omega^3e^{iArg(k_{pz})} && (2.106)\\
J_{sz} &= \frac{1}{2} \mid C \mid^2 \rho^{(b)} \mid k_{sz} \mid \omega^3e^{iArg(k_{sz})} && (2.107)
\end{aligned}$$

The above equations take into account the fact that k_z, and k_{rz} of the incident P-wave, and the reflected P-wave are real and of opposite sign. Let $\rho = \frac{\rho^{(b)}}{\rho^{(a)}}$. The normalized energy fluxes to the incident energy are

$$
\begin{aligned}
J_{rz} &= - \mid A \mid^2 && (2.108)\\
J_{pz} &= \rho \mid B \mid^2 \frac{\mid k_{pz} \mid}{k_z} e^{iArg(k_{pz})} && (2.109)\\
J_{sz} &= \rho \mid C \mid^2 \frac{\mid k_{sz} \mid}{k_z} e^{iArg(k_{sz})} && (2.110)
\end{aligned}
$$

It is important to emphasize here that the energy fluxes that enter into the energy balance of the boundary, given above, are normal to the fluid-solid interface. The physical energy fluxes are given by the real parts of the above equations. We note that the reflected energy flux is always real whereas the energy fluxes of the transmitted P and S waves can be complex beyond the corresponding critical angle of incidence. Furthermore, beyond the P and S critical angles of incidence, k_{pz} and k_{sz} are pure imaginary, respectively. Consequently the corresponding energy fluxes are purely imaginary and thus the physical energy fluxes vanish. On the other hand below the critical angles the $\hat{z}$ components of the wave numbers are real thus the energy fluxes are real. In the light of these results the transmitted P and S waves beyond the P and S critical angles of incidence respectively do not contribute to the energy balance of the boundary.

Because the reflectivity of a diversity of materials is the main objective of this study, the reflection coefficient given by equation 2.88 in the next section on numerical modelling will be examined in some detail.

2.5 Numerical results for monochromatic plane wave reflectivity

In this section we will give numerical models of the partitioning of monochromatic plane wave energy incident to a fluid-solid interface. We will emphasize the reflection coefficient as many of the forthcoming experiments will deal with reflectivity using a bounded acoustic pulse as a source signal. These examples highlight some of the important aspects of amplitude and phase of reflected and transmitted waves. Such information is crucial to the later understanding of the bounded acoustic beams and bounded acoustic pulses.

2.5.1 Water-copper alloy

The case of the acoustic reflectivity from the interface between water and copper alloy has relevance to later reflectivity calibration tests. The material properties as measured in the laboratory using a conventional ultrasonic pulse transmission methods are listed in table 2.2. In this table all physical properties are taken from laboratory measurements. This example is for illustration and therefore no error estimates are given here. The partitioning of energy using the energy flux equations given in the previous section at the water-copper boundary is given in figure 2.8. This shows the energy balance at the boundary as the incident wave normal energy flux equals the sum of the normal energy fluxes of the reflected and transmitted waves. Note that beyond the P and S critical angles of incidence the transmitted P and S waves, respectively, do not contribute to the energy balance at the boundary. However these waves do exist as evanescent surface waves travelling along the boundary and decaying exponentially in the $\hat{z}$ direction. The calculated amplitudes of the potentials at the boundary are given in figure 2.9. The amplitudes beyond the critical angle for each wave mode have only a meaning near the boundary as these waves become evanescent, decaying exponentially away from the boundary in the positive $\hat{z}$ direction. These waves propagate as surface waves but do not contribute to the energy balance of the boundary as the normal energy flux beyond the critical angles is zero (Fig. 2.8). Below the P-critical angle of incidence the energy is partitioned mainly between the reflected and the transmitted P-waves. The reflected P-wave as the angle of incidence exceeds the P critical angle loses energy to the profit of the transverse wave which reaches maximum energy between the P and S

Material	P velocity m/s	S velocity m/s	Density kg/m^3
Copper	4789	2300	8901
Water	1493	-	995

Table 2.2: Laboratory measured material parameters used in the numerical example.

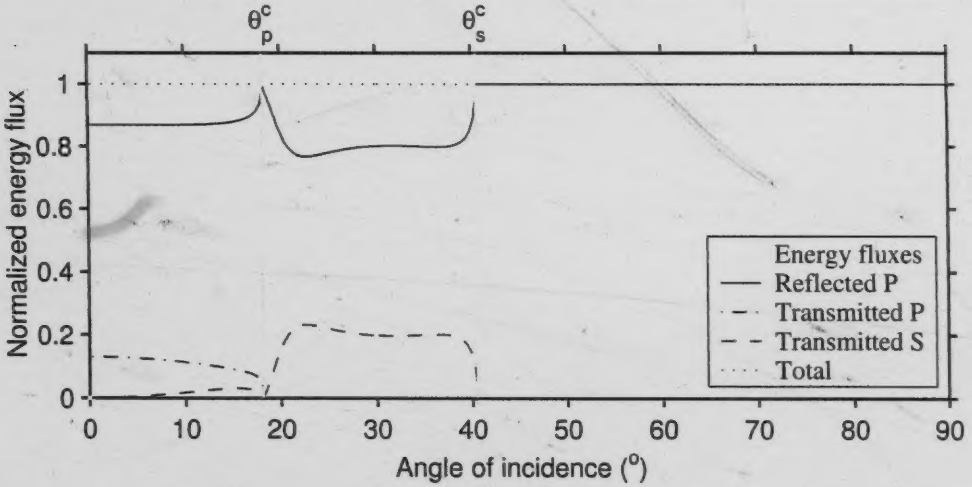

Figure 2.8: The normalized energy distribution normal to a water-copper alloy boundary. The properties of the materials used are listed in table 2.2.

critical angles. Beyond the S-critical angle total reflection occurs and all the energy is reflected as a P-wave. Other changes occur to the waves past the critical angles as will be demonstrated below.

The phase of the reflection-transmission coefficients are given in figure 2.10. Beyond the P critical incidence angle all wave modes are phase shifted. The transmitted P-wave has a zero phase angle below the P-critical angle of incidence. Far away from the boundary (Fig. 2.11) we are interested in the phase of the reflected P-wave and transmitted S-wave. Below the S-critical angle of incidence the phase of the reflected P-wave is nearly zero (or equivalently 2π) and nearly no apparent phase change is observable. However we notice that the reflected P-wave experiences an abrupt phase shift from 2π to a small value of approximately 0.35π just after the S-critical angle of incidence. The maximum phase shift in this region is 180^o at the so-called Rayleigh angle; an angle that will become important to later observations. This particular angle of incidence coincides with the angle of incidence (or emergence) at which the apparent horizontal velocity of the reflected wave is equal to that of a Rayleigh wave that would travel in the solid in the absence of the fluid. For the example described in this section for a fluid-copper alloy boundary the maximum phase shift occurs at an angle of incidence of approximately 43.97^o. This particu-

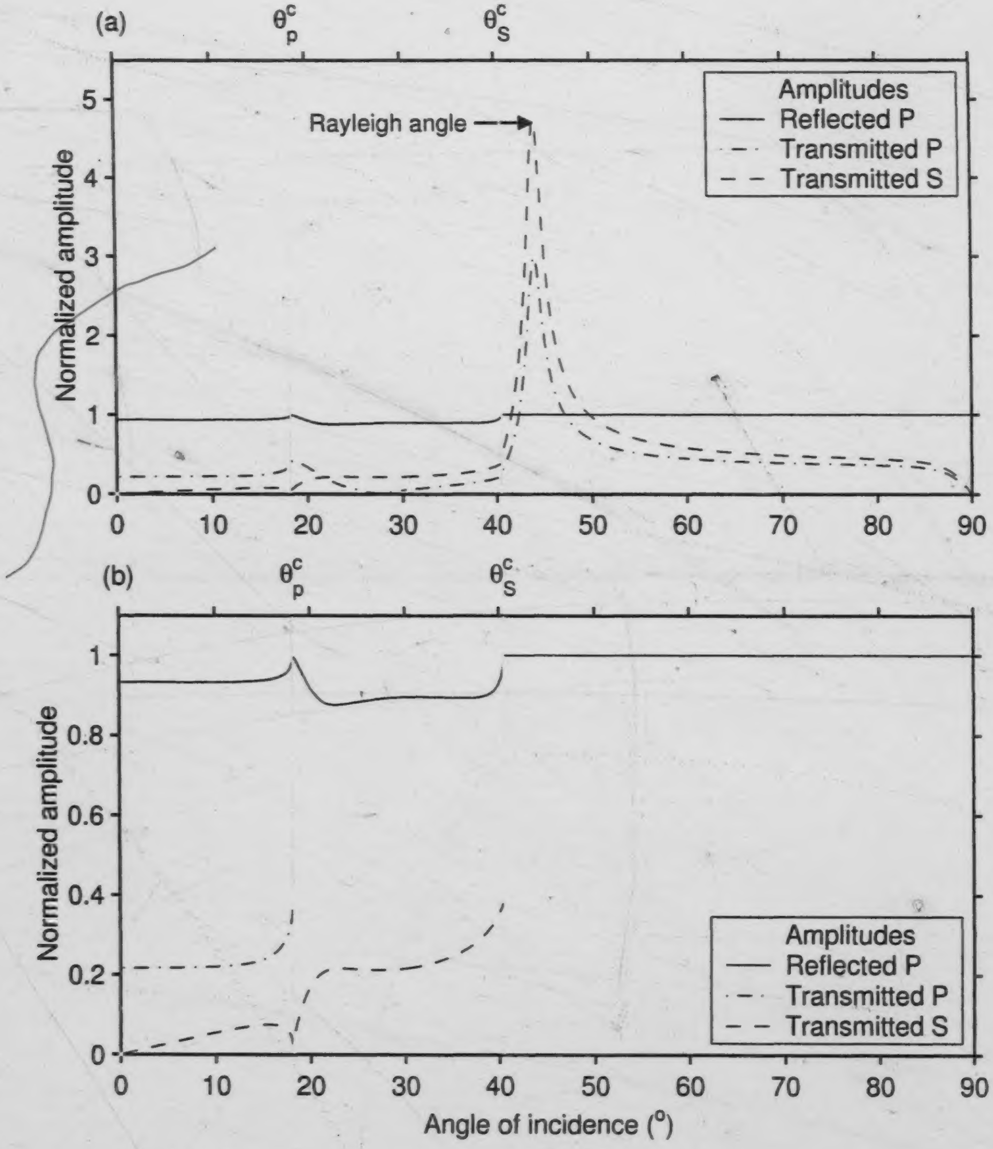

Figure 2.9: (a) The amplitudes of the potential for the three wave modes generated at the boundary. These amplitudes have a meaning only near the boundary. Beyond the critical angle the transmitted waves become evanescent waves travelling as surface waves along the boundary. (b) The amplitudes of the potentials far from the boundary, i.e. removed from the influence of the evanescent waves.

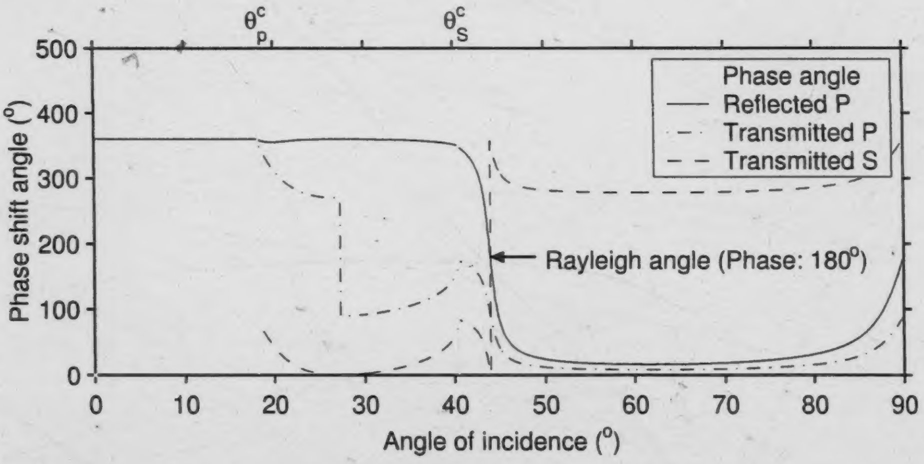

Figure 2.10: The phase angle of the reflected P, transmitted P, and transmitted S waves. Phase angles of all wave modes are given relative to 2π (360^o), thus all angles are > 0. θ_P^c and θ_S^c are critical angles for the P and S waves respectively.

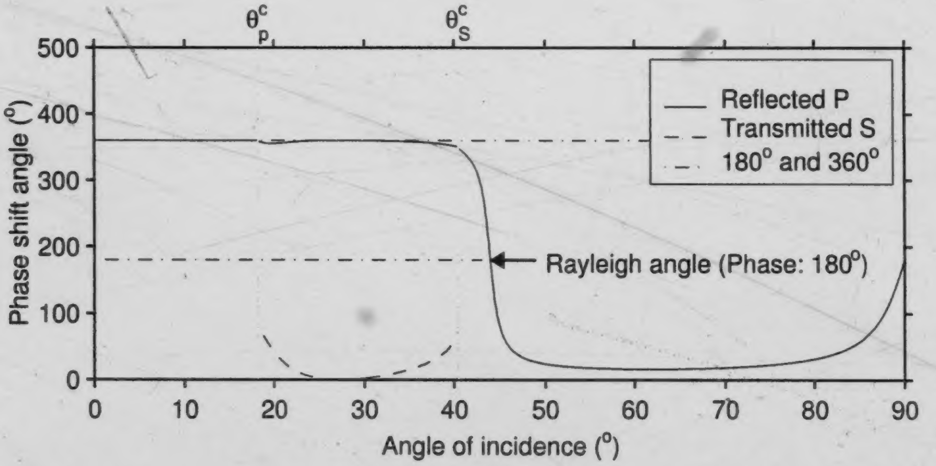

Figure 2.11: The phase angle of the reflected P, and transmitted S waves far from the boundary. The phase of the transmitted P-wave is zero. Waves beyond corresponding P and S critical angles are neglected. θ_P^c and θ_S^c are critical angles for the P and S waves respectively. Phase angles of all wave modes are given relative to 2π (360^o), thus all angles are > 0.

lar angle of incidence will be of great interest when dealing with bounded acoustic beams and bounded acoustic pulses.

2.6 Phase distortion of the reflected monochromatic plane wave field

In this section, the effects of phase shifts of post-critical incidence angle reflections are first brought to the reader's attention. The apparent shift, or displacement, of a reflected acoustic beam from the normally expected geometric reflection point will be highlighted and the angle at which this effect is greatest: the so-called and perhaps inappropriately named, Rayleigh angle is discussed. This effect will impact the experimental measurements and will reappear as we continue through to successive levels of acoustic beam complexity. The phase angle from the reflection coefficient given in equation 2.88 can be subdivided onto three regions delimited by θ_p^c and θ_s^c the P and S critical angles of incidence respectively. Region I is where the angle of incidence is below the P-wave critical angle ($\theta < \theta_p^c$), region II is where the angle of incidence is between the P-wave and S-wave critical angles $\theta_S^c > \theta > \theta_P^c$, and region III is where the angle of incidence is beyond the S-wave critical angle ($\theta > \theta_S^c$). In region I the reflection coefficient is real and thus the phase shift is zero. In region II nearly all terms of the reflection coefficient in equation 2.88 are real except for that which contains a purely imaginary wave number in the $\hat{z}$ direction of the P-wave in the solid. In this case we can write for purposes of brevity

$$\begin{aligned} a &= \left(2k_x^2 - k_s^2\right)^2 && (2.111) \\ b &= 4\left(k_x^2 - k_p^2\right)^{\frac{1}{2}} \left(k_s^2 - k_x^2\right)^{\frac{1}{2}} k_x^2 && (2.112) \\ c &= \rho k_s^4 \left(k_x^2 - k_p^2\right)^{\frac{1}{2}} \left(k^2 - k_x^2\right)^{-\frac{1}{2}} && (2.113) \end{aligned}$$

where a, b, and c are always real. Using equations 2.111 to 2.113 in equation 2.88 we get for incidence angles in region II

$$A = \frac{a + i\,(b - c)}{a + i\,(b + c)} \qquad (2.114)$$

The phase shift φ is then given by

$$\varphi = \tan^{-1}\left[\frac{-2\rho k_s^4\left(2k_x^2-k_s^2\right)^2\left(k_x^2-k_p^2\right)^{\frac{1}{2}}\left(k^2-k_x^2\right)^{\frac{1}{2}}}{\left(2k_x^2-k_s^2\right)^4+16\left(k_x^2-k_p^2\right)\left(k_s^2-k_x^2\right)\left(k^2-k_x^2\right)k_x^4-\rho^2k_s^8\left(k_x^2-k_p^2\right)}\right] \tag{2.115}$$

For incidence angles in region III the wave number components in $\hat{z}$ direction of P and S waves are both pure imaginary numbers. Consequently we have

$$\begin{aligned} a &= \left(2k_x^2-k_s^2\right)^2 && (2.116)\\ b &= -4\left(k_x^2-k_p^2\right)^{\frac{1}{2}}\left(k_x^2-k_s^2\right)^{\frac{1}{2}}k_x^2 && (2.117)\\ c &= \rho k_s^4\left(k_x^2-k_p^2\right)^{\frac{1}{2}}\left(k^2-k_x^2\right)^{-\frac{1}{2}} && (2.118)\end{aligned}$$

where a, b, and c are always real. Using equations 2.116 to 2.118 in equation 2.88 we get for incidence angles in region III

$$A = \frac{a+b-ic}{a+b+ic} \tag{2.119}$$

The phase φ is then given by

$$\varphi = \tan^{-1}\left[\frac{-2\rho k_s^4\left(k_x^2-k_p^2\right)^{\frac{1}{2}}\left(k^2-k_x^2\right)^{\frac{1}{2}}\left[\left(2k_x^2-k_s^2\right)^2-4\left(k_x^2-k_p^2\right)^{\frac{1}{2}}\left(k_x^2-k_s^2\right)^{\frac{1}{2}}k_x^2\right]}{\left[\left(2k_x^2-k_s^2\right)^2-4\left(k_x^2-k_p^2\right)^{\frac{1}{2}}\left(k_x^2-k_s^2\right)^{\frac{1}{2}}k_x^2\right]^2\left(k^2-k_x^2\right)-\rho^2k_s^8\left(k_x^2-k_p^2\right)}\right] \tag{2.120}$$

The phase angle for all incidence angles is given by

$$\varphi = \begin{cases} 0 & : \quad k_x \leq k_p \\ \tan^{-1}\left[\frac{-2\rho k_s^4\left(2k_x^2-k_s^2\right)^2\left(k_x^2-k_p^2\right)^{\frac{1}{2}}\left(k^2-k_x^2\right)^{\frac{1}{2}}}{\left(2k_x^2-k_s^2\right)^4+16\left(k_x^2-k_p^2\right)\left(k_s^2-k_x^2\right)\left(k^2-k_x^2\right)k_x^4-\rho^2k_s^8\left(k_x^2-k_p^2\right)}\right] & : \quad k_x \geq k_p \leq k_s \\ \tan^{-1}\left[\frac{-2\rho k_s^4\left(k_x^2-k_p^2\right)^{\frac{1}{2}}\left(k^2-k_x^2\right)^{\frac{1}{2}}\left[\left(2k_x^2-k_s^2\right)^2-4\left(k_x^2-k_p^2\right)^{\frac{1}{2}}\left(k_x^2-k_s^2\right)^{\frac{1}{2}}k_x^2\right]}{\left[\left(2k_x^2-k_s^2\right)^2-4\left(k_x^2-k_p^2\right)^{\frac{1}{2}}\left(k_x^2-k_s^2\right)^{\frac{1}{2}}k_x^2\right]^2\left(k^2-k_x^2\right)-\rho^2k_s^8\left(k_x^2-k_p^2\right)}\right] & : \quad k_x \geq k_s \end{cases} \tag{2.121}$$

Although it is not obvious, equation 2.121 is a continuous function.

Now let a plane wave be incident onto a fluid-solid boundary at an angle θ. Let a steady state wave field be $\phi(x) = I(x)e^{ik_{\theta x}x}$ on the plane $z = 0$ (Fig. 2.12). Here, $k_{\theta x}$ is the projection of the wave number k on the $\hat{x}$ axis. Following Brekhovskikh (1960) we can express the wave field on the plane $z = 0$ in Fourier domain and extend it to

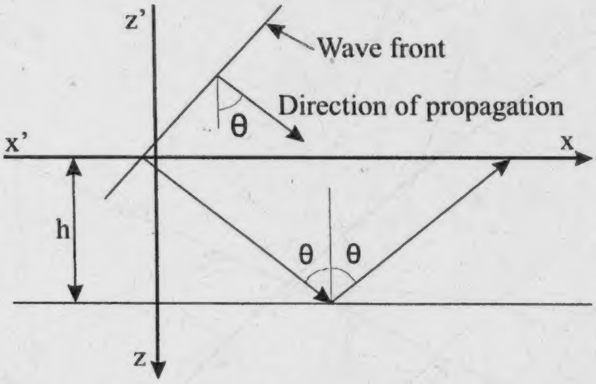

Figure 2.12: Plane wave front with a given intensity distribution on the plane $z = 0$. The wave is reflected at a boundary located at $z = h$ between two media of different material properties.

any point in the space $(\hat{x}, \hat{z})$. We have

$$\Phi(k_x) = \int_{-\infty}^{+\infty} \phi(x,0)e^{-ik_x x}dx = \int_{-\infty}^{+\infty} I(x,0)e^{ik_{\theta x}x}e^{-ik_x x}dx \tag{2.122}$$

The wave field on the plane $z = 0$ is given by the inverse Fourier transform

$$\phi(x,0) = \frac{1}{2\pi}\int_{-\infty}^{+\infty} \Phi(k_x)e^{ik_x x}dk_x \tag{2.123}$$

To describe the wave field at any point (x, z) in the space $(\hat{x}, \hat{z})$ it is sufficient to write

$$\phi(x,z) = \frac{1}{2\pi}\int_{-\infty}^{+\infty} \Phi(k_x)e^{i(k_x x + k_z z)}dk_x \tag{2.124}$$

because equation 2.124 satisfies the wave equation. Thus to find the incident wave field at the plane $z = h$ we write

$$\phi_{inc}(x,h) = \frac{1}{2\pi}\int_{-\infty}^{+\infty} \Phi(k_x)e^{i(k_x x + k_z h)}dk_x \tag{2.125}$$

The reflected wave field at $z = h$ can be written as

$$\phi_{ref}(x,h) = \frac{1}{2\pi}\int_{-\infty}^{+\infty} R(k_x)\Phi(k_x)e^{i(k_x x + k_z h)}dk_x \tag{2.126}$$

where $R(k_x)$ is the reflection coefficient at the boundary. Replacing $\Phi(k_x)$ by its quantity from equation 2.122 into equation 2.126 we obtain

$$\phi_{ref}(x,h) = \frac{1}{2\pi}\int_{-\infty}^{+\infty}\int_{-\infty}^{+\infty} R(k_x)I(x',0)e^{i(k_{\theta x}x' - k_x x' + k_x x + k_z h)}dx'dk_x \tag{2.127}$$

where x' and x are used for the space coordinate $\hat{x}$ to differentiate between the forward and the inverse Fourier transforms. Now we can write the reflection coefficient as

$$R(k_x) = \mid R(k_x) \mid e^{i\varphi(k_x)} \tag{2.128}$$

and replace it in equation 2.127 we obtain

$$\phi_{ref}(x,h) = \frac{1}{2\pi} \int_{-\infty}^{+\infty} \int_{-\infty}^{+\infty} \mid R(k_x) \mid I(x') e^{i(k_{\theta x}x' - k_x x' + k_x x + k_z h + \varphi(k_x))} dx' dk_x \tag{2.129}$$

Introducing a change of variable $\kappa = k_x - k_{\theta x}$ equation 2.129 becomes

$$\phi_{ref}(x,h) = \frac{1}{2\pi} \int_{-\infty}^{+\infty} \int_{-\infty}^{+\infty} \mid R(\kappa) \mid I(x') e^{i[\kappa(x-x') + k_{\theta x}x + \varphi(\kappa) + k_z h]} dx' d\kappa \tag{2.130}$$

Expanding $\varphi(\kappa)$ around $k_{\theta x}$ we have

$$\varphi(\kappa) = \varphi(k_{\theta x}) + \varphi'(k_{\theta x})\kappa + \frac{1}{2}\varphi''(k_{\theta x})\kappa^2 + \cdots \tag{2.131}$$

where $\varphi'(k_{\theta x}) = -\left[\frac{\partial \varphi(k_x)}{\partial k_x}\right]_{k_x = k_{\theta x}}$. If $I(x)$ is large enough such that κ is small we take into account only the first two terms of equation 2.131 and equation 2.130 becomes

$$\phi_{ref}(x,h) = \frac{1}{2\pi} e^{i\varphi(k_{\theta x})} \int_{-\infty}^{+\infty} \int_{-\infty}^{+\infty} \mid R(\kappa) \mid I(x') e^{i[\kappa(x-x'+\varphi'(k_{\theta x})) + k_{\theta x}x + k_z h]} dx' d\kappa \tag{2.132}$$

Schoch (1950) was the first to introduce this expansion and give an approximation to the displacement. The incident wave field can also be written as

$$\phi_{inc}(x,h) = \frac{1}{2\pi} \int_{-\infty}^{+\infty} \int_{-\infty}^{+\infty} I(x') e^{i\kappa[(x-x') + k_{\theta x}x + k_z h]} dx' d\kappa \tag{2.133}$$

It is important to compare carefully the incident and reflected wave-fields as there is an important point that relates to the phase. If we compare the incident wave field in equation 2.132 to that of the reflected wave field in equation 2.133 we notice each plane wave present in the decomposition will be

- shifted along the $\hat{x}$ direction by an amount equal to $-\varphi'(k_{\theta x})$
- modulated by the absolute amplitude of the reflection coefficient

This is somewhat unanticipated and not well known consequence of plane wave reflectivity at a fluid-solid boundary. This will lead to a new intensity distribution

$I(x)$. As a result, the reflected wave field will exhibit various patterns and shapes depending on the wavelength and the width of the intensity distribution $I(x)$. As all planes waves are shifted with a different amount dependent upon the wavelength this is essentially a spatial dispersion effect. This will be shown below for a plane wave and numerically later when reviewing bounded acoustic beams. The spatial displacement along the boundary is (Schoch, 1950; Brekhovskikh, 1960)

$$\Delta = -\left[\frac{\partial \varphi(k_x)}{\partial k_x}\right]_{k_x = k_{\theta x}} \tag{2.134}$$

This shift will be important when the phase angle of the reflection coefficient changes

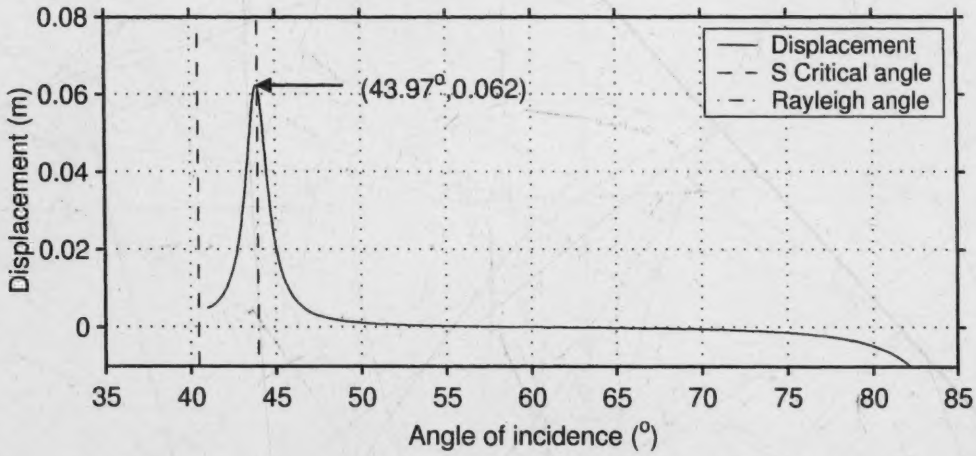

Figure 2.13: Displacement as a function of incidence angle calculated via equation 2.134 for a water-copper alloy interface. The wavelength in the fluid is approximately 1.9 mm.

abruptly such as in the case of post shear critical angle θ_S^c reflection from a fluid-solid boundary (Fig. 2.13). In this figure the displacement is calculated at post S-critical angle of incidence (43.97^o) shown by the dashed line, that is at total reflection. We notice that the maximum shift, or displacement, is at the so-called Rayleigh angle with a value of approximately 6.2 cm. At this angle the phase is exactly 180^o and near this angle it varies abruptly. It is worthwhile noting that the displacement can be negative, that is in the $-x$ reverse direction along the boundary when the angle of incidence is at grazing angles and approaches 90^o. Consider that particular angle of 43.97^o and let $I(x) = 1$ for all x. If the wave field does not contain wave numbers below the S-critical angle we have $\mid R(k_{\theta x}) \mid= 1$ and $\varphi(k_{\theta x}) = \pi$. In this case the displacement is given by equation 2.134 with the phase shift φ given by equation 2.121 for $k_x \geq k_s$.

At the angle where the phase is exactly 180^o the displacement is considerable (nearly 6.2 cm for a wavelength of 1.9 mm). This is readily observed as will be demonstrated later by numerical modelling and supported by experimental results with bounded acoustic pulses. To explain the spatial shift given above Brekhovskikh (1960), who followed the work of Schoch (1950), has considered a plane wave and a perfect reflector (Reflection coefficient of unity and zero phase). Here we will consider a plane wave travelling at an arbitrary angle θ with respect to the $\hat{z}$ direction (Figs. 2.14-2.15) and take into account the reflection coefficient for the reflected wave. Let the incident plane wave be $\phi_{inc}(x,0) = e^{i(k_x x)}$ at $z = 0$. Then the incident plane wave at $z = h$ can be written as

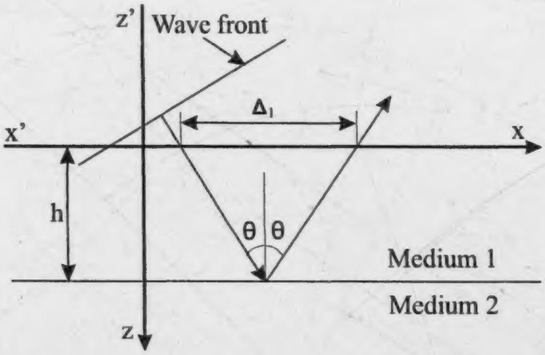

Figure 2.14: The displacement along the $\hat{x}$ axis is null if the reflection coefficient is real. Δ_1 that is shown here corresponds to the geometrical ray theory.

$$\phi_{inc}(x,h) = e^{i(k_x x+k_z h)} \tag{2.135}$$

where $k_z = (k^2 - k_x^2)^{\frac{1}{2}}$. The reflected wave as it travels back from the boundary $z = h$ to $z = 0$ is

$$\phi_{ref}(x,0) = R(k_x)e^{i(k_x x+2k_z h)} \tag{2.136}$$

where $R(k_x)$ is the reflection coefficient at the boundary located at $z = 0$. If the reflection coefficient is real then equation 2.136 becomes

$$\phi_{ref}(x,0) =\mid R(k_x) \mid e^{i(k_x x+2k_z h)} \tag{2.137}$$

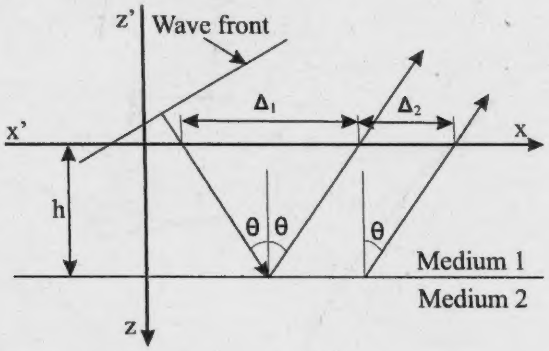

Figure 2.15: Besides the normal geometrical shift Δ_1 we have an extra displacement Δ_2 due the phase change of the reflection coefficient at the boundary.

The ratio between the reflected and incident waves at $z = 0$ is

$$R'(k_x) = | R(k_x) | e^{2ik_z h} \tag{2.138}$$

Here $R'(k_x)$ can be regarded as a virtual reflection coefficient of the plane wave from the plane $z = 0$. $\varphi(k_x) = 2k_z h$ represents the phase change as the wave has travelled from $z = 0$ to $z = h$ and back to $z = 0$. Using equation 2.134 the displacement along the plane $z = 0$ can be calculated. For a given angle of incidence θ we have

$$\Delta_1 = 2k_{\theta x}(k^2 - k_{\theta x}^2)^{-\frac{1}{2}} h = 2h \tan\theta \tag{2.139}$$

which is exactly what is expected from the ray geometry and used by Brekhovskikh (1960) in his example.

Now consider the case where $R(k_x)$ is complex. Then equation 2.138 becomes

$$R'(k_x) = | R(k_x) | e^{i(2k_z h + \varphi(k_x))} \tag{2.140}$$

where $\varphi(k_x)$ is the phase of the reflection coefficient $R(k_x)$. The displacement Δ in this case is

$$\Delta = 2k_{\theta x}(k^2 - k_{\theta x}^2)^{-\frac{1}{2}} h + \varphi'(k_{\theta x}) \tag{2.141}$$

or

$$\Delta = 2h \tan\theta + \left[\frac{\partial \varphi(k_x)}{\partial k_x}\right]_{k_x = k_{\theta x}} \tag{2.142}$$

Thus the wave field is displaced along the plane $z = 0$ by $\Delta_1 = 2h\tan\theta$ plus $\Delta_2 = \left[\frac{\partial \varphi(k_x)}{\partial k_x}\right]_{k_x = k_{\theta x}}$ (Fig. 2.15). Thus there is an extra shift in the $\hat{x}$ direction due

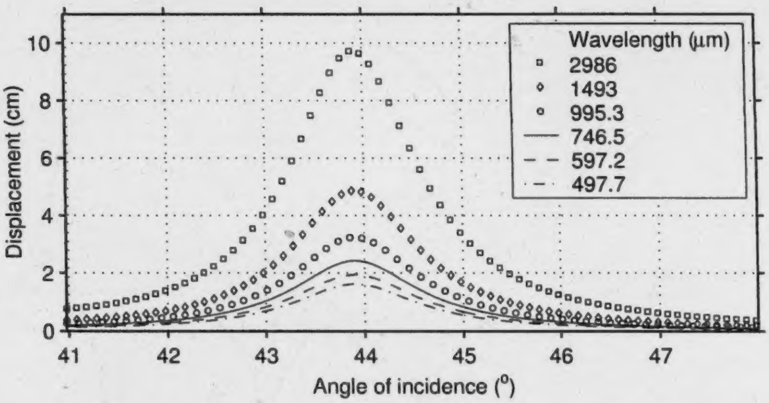

Figure 2.16: Lateral displacement Δ as a function of wavelength in the case of a water-copper boundary at incidence angles near the Rayleigh angle of 43.97°.

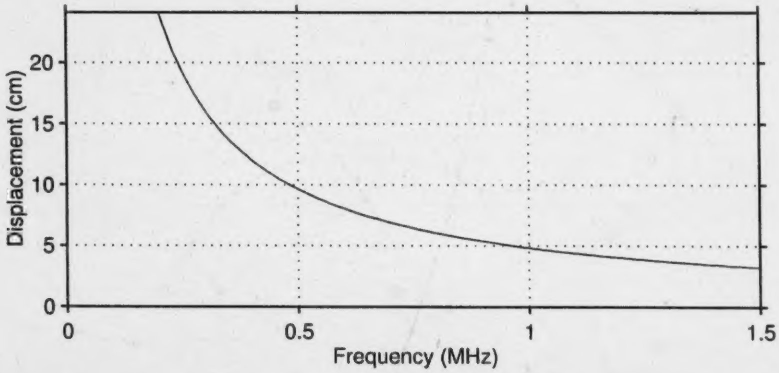

Figure 2.17: Lateral displacement Δ as a function of frequency in the case of a water-copper boundary at the Rayleigh angle of incidence (43.97°) and in the frequency range of 0.2-1.5 MHz.

to the phase change at the boundary $z = h$. This phase shift of a plane wave is the basis in considering any wave field with an arbitrary (smooth) intensity distribution at the reflecting boundary. Each plane wave present in the Fourier decomposition of the considered field will be displaced by a different amount and thus the reflected intensity distribution will be of various shapes that depend on the properties of the materials considered and the frequency content of the source signal. In figures 2.16, 2.17, and 2.18 the displacement as a function of frequency and wavelength is given. This shows a great dependence of the displacement Δ on the frequency and

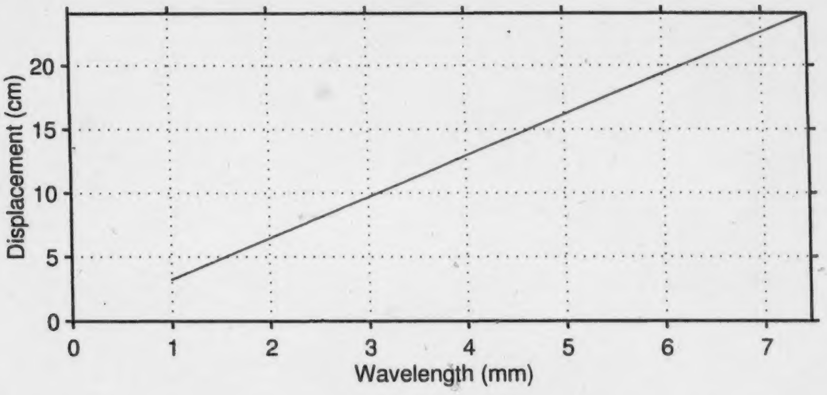

Figure 2.18: Displacement Δ as a function of wavelength in the case of a water-copper boundary at the Rayleigh angle of incidence (43.97^o) and in the frequency range of 0.2-1.5 MHz.

wavelength.

2.7 Monochromatic bounded acoustic beams

Now that the basic theory behind plane wave propagation and reflectivity has been discussed it is important to move to the next step of describing monochromatic but spatially bounded acoustic beams. The final goal will be a description of the bounded acoustic pulses used in the forthcoming experiments.

A monochromatic acoustic beam is a steady state plane wave bounded in space. An acoustic beam will exhibit various patterns of intensity distribution upon reflection from a fluid-solid boundary near the so-called Rayleigh angle existing a few degrees beyond the S-critical angle of incidence as described in the previous section. At this angle the phase of the reflection coefficient is exactly 180^o. The reflected beam is apparently displaced a considerable distance, compared to wavelength, along the boundary when reflected near this particular angle. This effect is also known in the optics literature as the Goos-Hänchen shift because it was first experimentally observed by Goos and Hänchen (Goos and Hänchen, 1947). In acoustics Schoch (1950) has first observed and photographed, using schlieren photograph (see Schoch (1950), figure 22, page 185), in), a displaced reflected ultrasonic beam and was able to measure the shift Δ. He was the first to develop a theory and give the first order displacement in a detailed theory of the reflectivity at the Rayleigh angle (Schoch, 1952a; Schoch, 1952b).

Following the work of Schoch (1950) as mentioned earlier, Brekhovskikh (1960) had included the second order term in the expansion of the reflection coefficient phase to approximate the intensity distribution across the reflected acoustic beam. The schlieren photographs presented in his book for a xylene-aluminium interface show a displaced reflected bounded beam (see Brekhovskikh (1960), figure 32-33, page 109).

Since then many workers have studied reflection at this particular angle of incidence both theoretically and experimentally. Diachok and Mayer (1970) observed a pronounced minimum reflectivity at a water-brass interface. They have used 7 MHz transducers of unspecified size to generate and record the reflected signal. They suggested that the incident energy is converted into a Rayleigh-type wave on the fluid-solid interface rather than being totally reflected back into a longitudinal wave in the fluid. Tamir and Bertoni (1973) have associated the beam displacement of electromagnetic (or light) waves to leaky waves that are excited at the boundary by the incident wave field. The displacement in the case of acoustic waves is also associated to leaky waves (Bertoni and Tamir, 1973). Becker (1971) studied theoretically the influence of the material properties, including attenuation, on the reflectivity at the Rayleigh angle and found that the observed magnitude of the minimum reflectivity varied substantially with material properties.

The Rayleigh angle and velocity have also been measured by the means of acoustic beam displacement where a null strips appear on the schlieren photographs (Neubauer and Dragonette, 1974). Their experiments were conducted using 5.3 MHz transducers. They presumed this effect was associated with the interference of the excited Rayleigh wave and a reflected wave that are 180^o out of phase. They have also found that the calculated Schoch displacement is inadequate to explain the observations. Their measurements of Rayleigh wave velocity were based on the observation of the minimum reflectivity at the dark strip shown in the schlieren photographs.

Similar work has bean carried by Breazeale et al. (1977) and Ngoc et al. (1980) using a Gaussian beam and an analytical solution was proposed. The experimental measurement (Breazeale et al., 1977) of the displacement was found to be too large compared to that predicted by Schoch. However it is in good agreement to that proposed by Bertoni and Tamir (1973). Other applications of this phenomena have also been tested in other media such as in a multilayered viscoelastic medium (Schmidt and Jensen, 1985).

2.7.1 Fourier components

As the introductory material shows, there are a number of explanations for the apparent shift. However, in this thesis the experimental results will be found to be explained by the analytic solution given in part by Brekhovskikh (1960). A summary of this approach is given here. Specifically a spatially bounded acoustic beam of infinite time extent will be described using Fourier methods.

Brekhovskikh (1960) has represented a bounded acoustic beam as a superposition of plane waves. Here a bounded acoustic beam means spatially bounded but of infinite temporal extent. This theory assumes that if a wave field is known at a given time on one plane in the considered space of constant velocity it can be extended to the whole space at later time. First consider a plane wave propagating at an angle θ with respect to the $\hat{z}$ direction as shown in figure 2.19. The wave strikes a screen containing an open slit with an opening of $2a$ (cc'). As a result a beam, shown by the dashed lines, is formed. This acoustic beam does satisfy the wave equation as will be shown below. The slit width must be much larger than the wavelength. Suppose that the field is zero behind the screen except at the slit. Suppose that in the plane of the slit the field behaves as if the screen did not exist. The field is then completely determined by the wave equation and the boundary conditions. The angle of incidence is important to consider here as the reflectivity of the wave field from a boundary will depend on this. The field in back of the screen is then a beam with a propagation angle θ between the direction of propagation and the $\hat{z}$ axis. It is sufficient to know the field at the slit and the wave number in order to determine the wave field at any point in the $(\hat{x}, \hat{z})$ space. The potential field ϕ of the incident plane wave in front of the screen is assumed to be of the form

$$\phi = e^{i(k_{\theta x}x+k_z-i\omega t)} \tag{2.143}$$

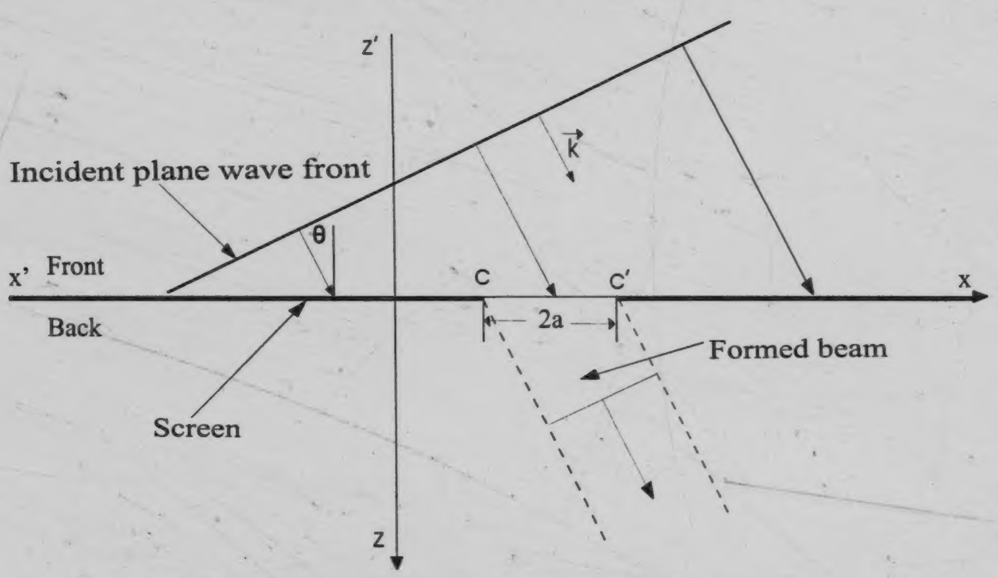

Figure 2.19: Bounded acoustic beam formed by a plane wave with wave number $\vec{k}$ at an angle θ with respect to the $\hat{z}$ direction incident on a screen containing an open slit of width $2a$. After Schoch (1950) and Brekhovskikh (1960)

where

$$k_{\theta x} = k \sin\theta \tag{2.144}$$

$$k_z = k \cos\theta \tag{2.145}$$

where k is the wave number in the medium. After it passes through the slit we have at $z = 0$ (omitting the time dependence)

$$\phi(x,0) = \begin{cases} e^{ik_{\theta x}x} & : \quad -a \leq x \geq a \\ 0 & : \quad |\, x \,| > a \end{cases} \tag{2.146}$$

$\phi(x)$ can be generalized by writing and dropping out the time dependence

$$\phi(x,0) = F(x)e^{ik_{\theta x}x}, \; -\infty < x < +\infty \tag{2.147}$$

where $F(x)$ is a slowly varying function of x. The field at the plane $z = 0$ is represented by the Fourier integral

$$\phi(x,0) = \int_{-\infty}^{+\infty} \Phi(k_x)e^{ik_x x}dk_x \tag{2.148}$$

The function $\Phi(k_x)$ is given by

$$\begin{aligned} \Phi(k_x) &= \frac{1}{2\pi}\int_{-\infty}^{+\infty} \phi(x,0)e^{-ik_x x}dx \\ &= \frac{1}{2\pi}\int_{-\infty}^{+\infty} F(x)e^{i(k_{\theta x}-k_x)x}dx \end{aligned} \tag{2.149}$$

In the case of a beam formed by a plane wave passing through a slit we have

$$\begin{aligned} F(x) &= 1, \ -a < x < a, \\ F(x) &= 0, \ \mid x \mid > a \end{aligned} \tag{2.150}$$

leading to

$$\begin{aligned} \Phi(k_x) &= \frac{1}{2\pi}\int_{-a}^{+a} e^{i(k_{\theta x}-k_x)x}dx \\ &= \frac{\sin(k_{\theta x}-k_x)a}{\pi(k_{\theta x}-k_x)} \end{aligned} \tag{2.151}$$

The field everywhere in the space $(\hat{x},\hat{z})$ is

$$\phi(x,z) = \int_{-\infty}^{+\infty} \Phi(k_x)e^{i(k_x x + k_z z)}dk_x \tag{2.152}$$

where $k_z = (k - k_x)^{\frac{1}{2}}$. This equation is well known in the seismic exploration community as "forward phase shift modelling" when k_z and z are positive, or the "phase shift migration" when k_z and z are negative, see Clearbout (1985) for example.

The Gibbs phenomena that the inverse Fourier transform introduces via equation 2.152 causes difficulties in the forward modelling of a wave field. To reduce this problem the edges of the beam can be modulated by a slowly decreasing function such as a cosine ramp, for example. Let a monochromatic acoustic beam (monofrequency ω) be travelling at an angle θ with respect to the z axis. Let the wave field be of infinite extent in the $\hat{y}$ direction and known on a given $(\hat{x},\hat{y})$ plane. For convenience let this plane be at $z = 0$. Let the intensity modulation function $F(x)$ be of the following form

$$F(x) = \begin{cases} 0 & : \ x < -b \\ \frac{1}{2}(\cos(k_0(x+a)) + 1) & : \ -b \le x < -a \\ 1 & : \ -a \le x \le a \\ \frac{1}{2}(\cos(k_0(x-a)) + 1) & : \ b \ge x > a \\ 0 & : \ x > b \end{cases} \tag{2.153}$$

where $b > a > 0$ and $b = a + \frac{\pi}{k_0}$. In this case $F(x)$ describes the intensity distribution of the field on the plane $z = 0$. The beam is of intensity 1 between $-a$ and a with cosine ramps at the edges. For convenience the time dependence is left out. The potential field is completely described on the plane $z = 0$ by

$$\phi(x, 0) = F(x)e^{ik_{\theta x}x} \tag{2.154}$$

In the Fourier domain equation 2.154 is

$$\Phi(k_x) = \frac{k_0^2}{2\pi\left[k_0^2 - (k_{\theta x} - k_x)^2\right]} \frac{\sin\left[(k_{\theta x} - k_x)b\right] + \sin\left[(k_{\theta x} - k_x)a\right]}{(k_{\theta x} - k_x)} \tag{2.155}$$

The derivation of $\Phi(k_x)$ is given in detail in appendix A. Equation 2.155 is a sum of two sinc functions with frequencies a and b

$$\Phi(k_x) = b\frac{\sin\left[(k_{\theta x} - k_x)b\right]}{(k_{\theta x} - k_x)\,b} + a\frac{\sin\left[(k_{\theta x} - k_x)a\right]}{(k_{\theta x} - k_x)\,a} \tag{2.156}$$

modulated by the function

$$T(k_x) = \frac{k_0^2}{2\pi\left[k_0^2 - (k_{\theta x} - k_x)^2\right]} \tag{2.157}$$

The presence of the function $T(x)$ damps the ringing part of $\Phi(k_x)$. This damping depends on the wave number k_0 of the damping functions $\frac{1}{2}[\cos[k_0(x \pm a)] + 1]$. The smaller k_0 is the larger the damping of $\Phi(k_x)$ is and less Gibbs phenomena is observed. $\Phi(k_x)$ is plotted in figure 2.20 for a given angle $\theta = 15^o$, medium velocity of 1500 m/s (i.e. $k = 3267.3$ m^{-1} and $k_{\theta x} = 845.6$ m^{-1}), and a slit opening of $2a = 7$ cm. Two plots are shown without and with the damping function in figures 2.20-a and 2.20-b respectively. The ringing is greatly reduced with the damping function and this is useful for modelling purposes. We see that the amplitude decreases as k_x increases or decreases from $k_{\theta x}$. The maximum amplitude, equal to $\frac{a}{\pi}$ in case (a), is located at $k_{\theta x}$. Only a small range of angles around the main angle of incidence θ are significant in the decomposition. This decomposition may contain inhomogeneous plane waves if energy is present in the region $|k_x| > k$. All the Fourier components have the same wave number in their particular direction of propagation. We notice in figure 2.20 that the dominant wave number corresponds to that of the plane wave propagating in the direction perpendicular to the beam. We also notice the ringing character of $\Phi(k_x)$ (Fig. 2.20-a). This is due to the fact that in the description of the wave field on the plane $z = 0$ the function $F(x)$ is not a smoothly varying function of x

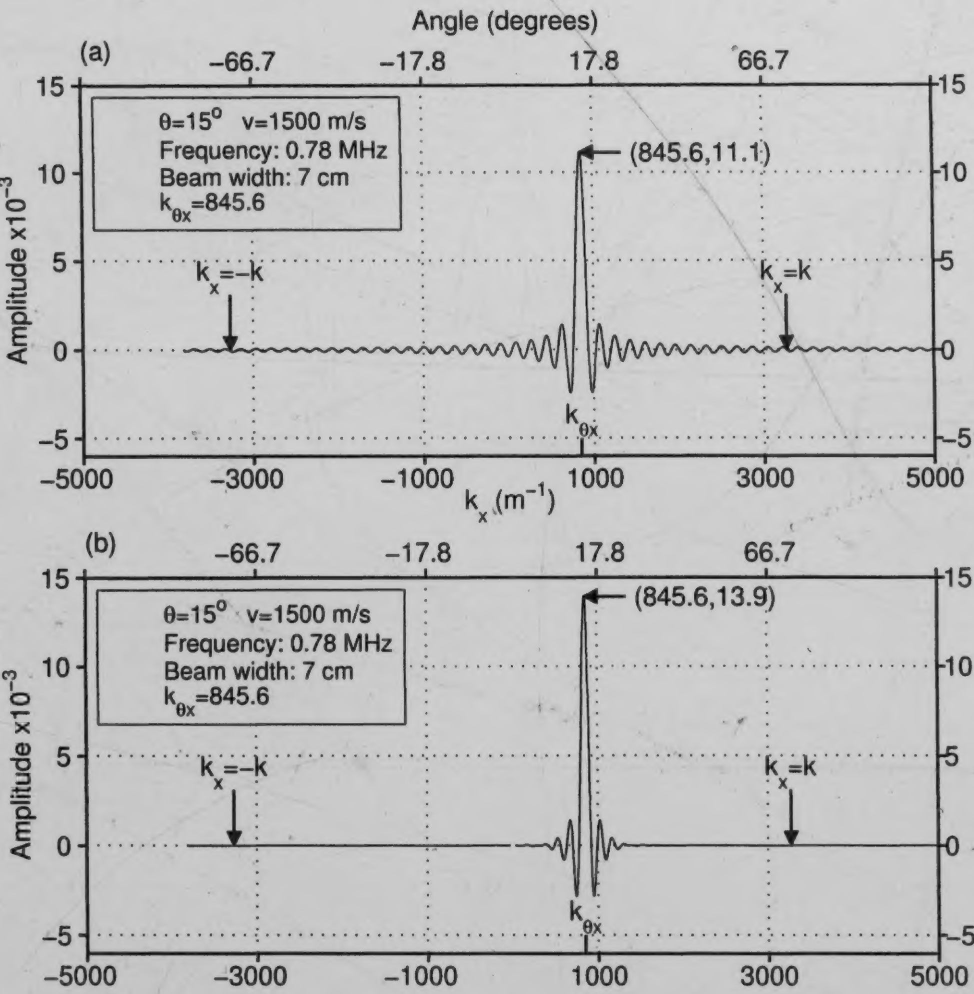

Figure 2.20: (a) : Plot of $\Phi(k_x)$ given by equation 2.151. (b) : Plot of $\Phi(k_x)$ given by equation 2.156 with the edges of the beam modulated by a cosine ramp. Note the maximum amplitude when the wave number equals $k_{\theta x}$.

but rather is discontinuous at the edges. This ringing effect is greatly reduced when $\Phi(k_x)$ is modulated by the function given by equation 2.157 (Fig. 2.20-b). The inverse Fourier transform of $\Phi(k_x)$ will lead to Gibbs phenomena as described in many text books (see e.g. Wylie (1961)); the original data is not properly recovered as such ringing effects will be significant. To obtain the field at all $z > 0$ each Fourier component is multiplied by the operator $e^{ik_z z}$ where $k_z = (k^2 - k_x^2)^{\frac{1}{2}}$. This phase shift operator will forward continue the data in space, in the direction of propagation if k_z is positive, or in the opposite direction if k_z is negative. The space domain wave field is then recovered by taking the real part of the inverse Fourier transform.

2.8 Bounded acoustic pulses

The meaning given here to bounded acoustic pulses are wave fields generated by exciting a transducer of a given shape and size by a time-limited pulse. This will generate a pulse that is bounded in time (frequency) and space (wave number). The use of bounded acoustic pulses in laboratory experiments is convenient. Let $\phi(x, 0, t)$ be the wave potential field generated by a line segment source located at $z = 0$, one example is given in figure 2.21. By analogy to the monochromatic bounded acoustic beam discussed above the wave potential field of a bounded acoustic pulse can be written in the Fourier domain as

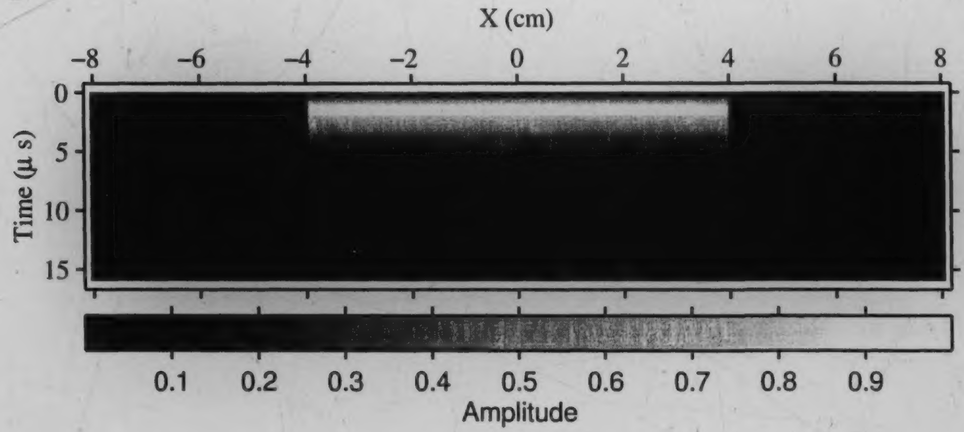

Figure 2.21: An example of a synthetic bounded acoustic pulse. The width is 0.08 m centred at $x = 0$. The frequency bandwidth is 0.2-1.2 MHz. The potential wave field shown here is at position $z = 0$ where the source is located.

$$\phi(x, 0, t) = \frac{1}{4\pi^2} \int_{-\infty}^{+\infty} \int_{-\infty}^{+\infty} \Phi(k_x, 0, \omega) e^{ik_x x} e^{i\omega t} dk_x d\omega \tag{2.158}$$

where the function $\Phi(k_x, 0, \omega)$ is given by the Fourier integral

$$\Phi(k_x, 0, \omega) = \int_{-\infty}^{+\infty} \int_{-\infty}^{+\infty} \phi(x, 0, t) e^{-ik_x x} e^{-i\omega t} dx dt \tag{2.159}$$

In the case of a pulse the integration limits are reduced to the spatial interval $[x_1,\ x_2]$ and to the time interval $[t_1,\ t_2]$.

$$\Phi(k_x, 0, \omega) = \int_{x_1}^{x_2} \int_{t_1}^{t_2} \phi(x, 0, t) e^{-ik_x x} e^{-i\omega t} dx dt \tag{2.160}$$

$\phi(x, 0, t)$ at the plane $z = 0$ is given by equation 2.158. The wave field described by equation 2.160 can now be extended to the whole space $z > 0$ by forward continuation (or to $z < 0$ by backward continuation) as in the previous sections. This continuation is achieved by the multiplication of each frequency component ω of $\Phi(k_x, 0, \omega)$ by the phase shift operator $e^{ik_z \Delta z}$ followed by the inverse Fourier transform in k_x and ω. k_z is simply the wave number in the $\hat{z}$ direction defined as

$$k_z = (k_\omega^2 - k_x^2)^{\frac{1}{2}} \tag{2.161}$$

where k_ω is the wave number in the medium for each frequency component present in the wave field $\Phi(k_x, 0, \omega)$ and k_x is the wave number in the $\hat{x}$ direction (spatial Fourier components). The wave field in the space $(\hat{x}, \hat{z}, t)$ is then given by

$$\phi(x, z, t) = \frac{1}{4\pi^2} \int_{-\infty}^{+\infty} \int_{-\infty}^{+\infty} \Phi(k_x, 0, \omega) e^{ik_x x} e^{i\omega t} e^{ik_z z} dk_x d\omega \tag{2.162}$$

Equation 2.162 is an exact solution that describes precisely the wave field everywhere in the space $(\hat{x}, \hat{z}, t)$ given the known wave field $\phi(x, 0, t)$ at $z = 0$. Now let a reflector be at depth $z = h$. The wave field at this interface is

$$\phi(x, h, t) = \frac{1}{4\pi^2} \int_{-\infty}^{+\infty} \int_{-\infty}^{+\infty} \Phi(k_x, 0, \omega) e^{ik_x x} e^{i\omega t} e^{ik_z h} dk_x d\omega \tag{2.163}$$

The reflected wave field ϕ^r at $z = h$ is

$$\phi^r(x, h, t) = \frac{1}{4\pi^2} \int_{-\infty}^{+\infty} \int_{-\infty}^{+\infty} R(k_x) \Phi(k_x, 0, \omega) e^{ik_x x} e^{i\omega t} e^{ik_z h} dk_x d\omega \tag{2.164}$$

where $R(k_x)$ is the reflection coefficient at the boundary. The reflected wave field everywhere is then produced by backward continuation as

$$\phi^r(x, z, t) = \frac{1}{4\pi^2} \int_{-\infty}^{+\infty} \int_{-\infty}^{+\infty} R(k_x) \Phi(k_x, 0, \omega) e^{ik_x x} e^{i\omega t} e^{ik_z h} e^{-ik_z \Delta z} dk_x d\omega \tag{2.165}$$

where $\Delta z = |h - z|$. Equation 2.165 describes precisely the reflected wave field everywhere in the space $(\hat{x},\ \hat{z},\ \mathrm{t})$.

2.9 Modelling of bounded acoustic beams

In order to better understand the behaviour of bounded acoustic beams and bounded acoustic pulses as they propagate through a medium at a given velocity the exact solution for the propagation will be used. This is described by equation 2.152 for bounded acoustic beams and by equation 2.162 for bounded acoustic pulses.

2.9.1 Monochromatic flat acoustic beams

Here a flat acoustic beam means one with a flat wave front of a given width around the centre of its axis of propagation. The amplitude in this uniform region of the beam is constant. Let such a beam travel in the $\hat{z}$ direction. This type of beam can be achieved, for example, by a piezo-electric plate continuously vibrating at a given frequency f_0. For purposes of illustration only let this frequency be 0.2 MHz and the medium be water with a velocity of 1500 m/s. Then the wavelength is $\lambda = 0.0075$ m. Let the width of the beam be 0.06 m and the potential field be known on the plane $z = 0$. Note that here the wave is supposed to be of infinite extent in the $\hat{y}$ direction. This bounded acoustic beam can then be extended to the whole space of constant velocity. The wave field that is continued forward along the $\hat{z}$ direction is shown on figure 2.22. This is a snapshot at a given time. As the wave travels away from the plane $z = 0$, which we could also consider as a source, it diffracts and spreads. The diffracted energy from the edges interferes with the central portion of the beam. The amplitude of the beam edges increase, a result of diffraction effects, as these migrate inwards and merge together at about $z = 7$ cm. The axial amplitude of the beam oscillates, due to perturbation from the diffracted energy from the edges. The peak amplitude along the axis of the beam is actually attained when the diffractions from the edges of the beam merge together. Thereafter the axial amplitude decreases with distance. This decrease is mainly governed by geometrical spreading. This is best illustrated in figure 2.23 and figure 2.24 by the peak amplitude of the cross section of the beam (perpendicular to the propagation axis). In figure 2.24 where the propagation extends to a longer distance than in figures 2.22 and 2.23 we distinguish three regions where the peak axial amplitude of the beam behaves quite differently:

- Region I: Near the source (0 to 5 cm) the amplitude oscillates around the initial value of 1. This is essentially due to diffraction effects from the edges.

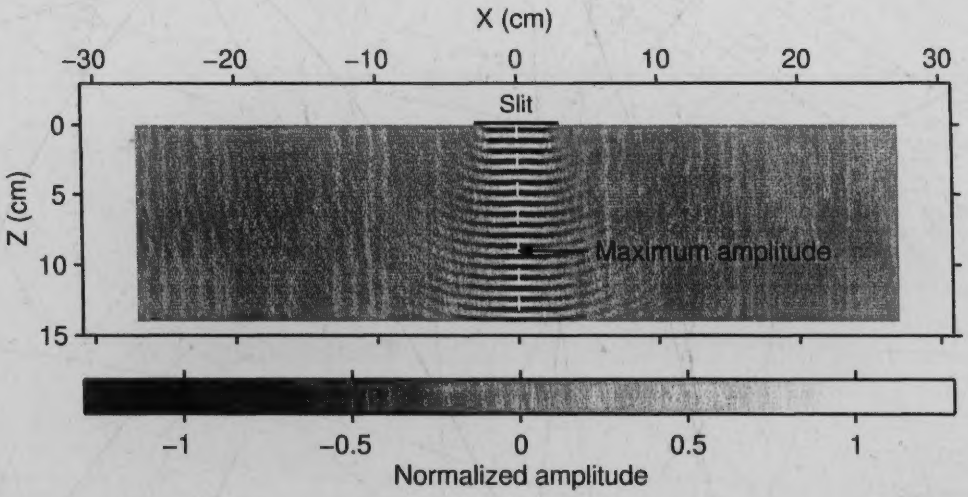

Figure 2.22: Downward continuation along $\hat{z}$ direction of a monochromatic bounded flat beam wave field normalized to the input. The width of the beam is 0.06 m and the frequency is 0.2 MHz. The dashed line shows the beam axis.

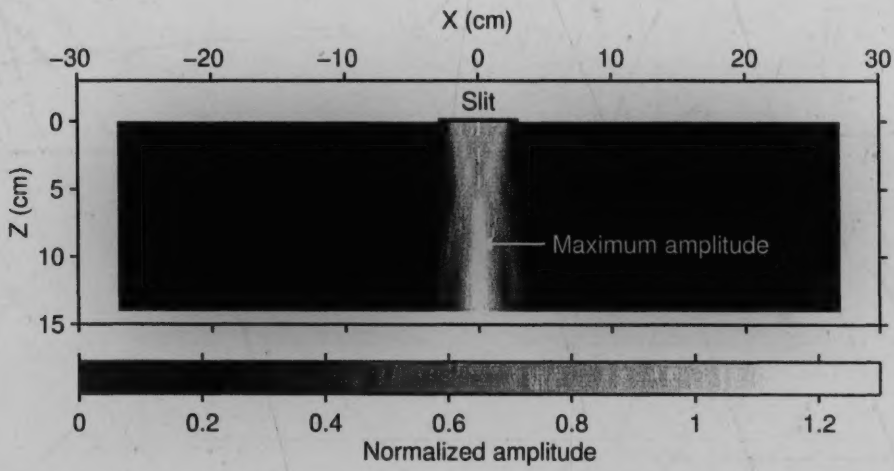

Figure 2.23: The amplitude, normalized to the input, along the cross section of the beam shown in figure 2.22. The dashed line is the beam axis. See also figure 2.24.

- Region II: Increase of amplitude (5 cm to 8 cm) to reach a peak at about 8 cm this is essentially due to the increase of the amplitudes of the edges as the latter migrate towards the centre (Fig. 2.23).

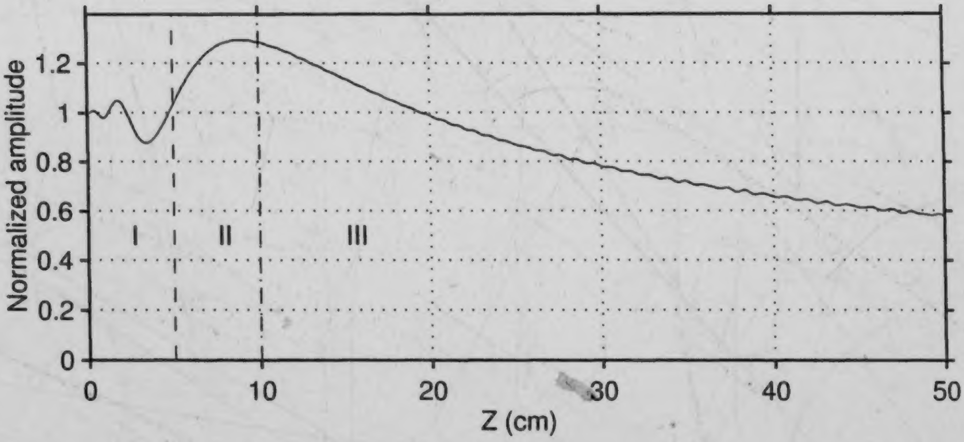

Figure 2.24: The amplitude envelope (Hilbert transform in the $\hat{x}$ direction) along the axis of the beam shown in figure 2.22. Note the change of amplitude along the axis. Three regions I, II, and III where the amplitude behaves quite differently are distinguishable (see text for more details). The wave field is normalized to the input.

- Region III: A decrease of amplitude thereafter (10 cm and up) this is due primarily to geometrical spreading. As figure 2.24 shows, the amplitude along the propagation axis of the beam oscillates as diffracted energy from the edges of the beam perturbs this region.

2.9.2 Monochromatic Gaussian beams

2.9.2.1 Propagation

A bounded Gaussian acoustic beam is a beam where the intensity distribution across the wave front may be described by a bell shaped Gaussian distribution. The behaviour of these beams differs somewhat from flat beams in the near field. In the far field, however, the behaviour is more similar. The amplitude along the axis of the beam decreases as the beam propagates away from the source. The amplitude decrease is primarily governed by geometrical spreading. This type of beam does not exhibit the inward propagating diffraction effects seen in figure 2.22. This is illustrated in the example given in figure 2.25 with the same characteristics as that of figure 2.22 except that the amplitude envelope is a Gaussian. Figures 2.26 and 2.27 illustrate the behaviour of the beam as a constant phase travels away from

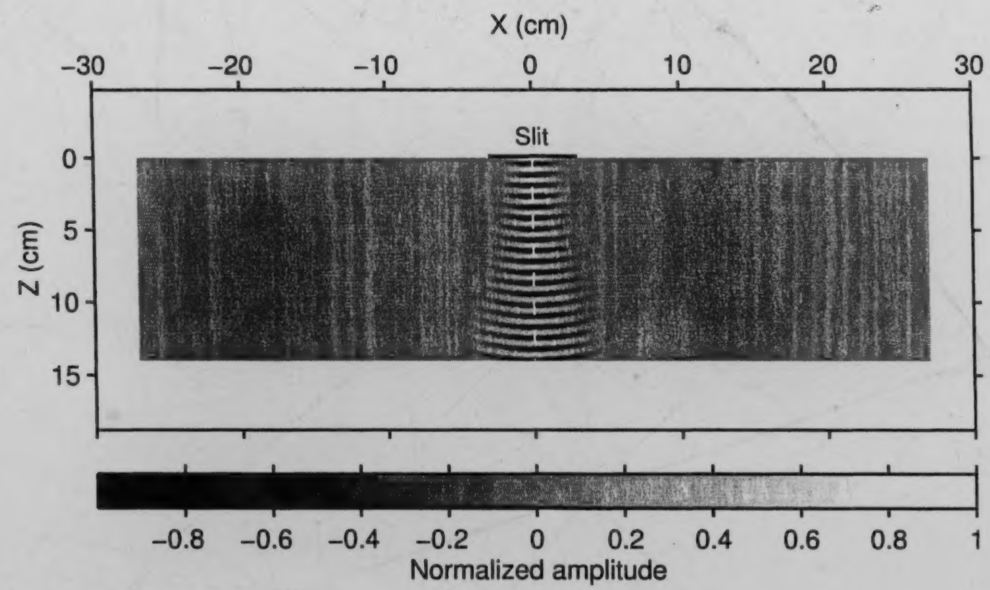

Figure 2.25: Downward continuation of a monochromatic bounded Gaussian beam normalized to the input. The dashed line shows the beam axis.

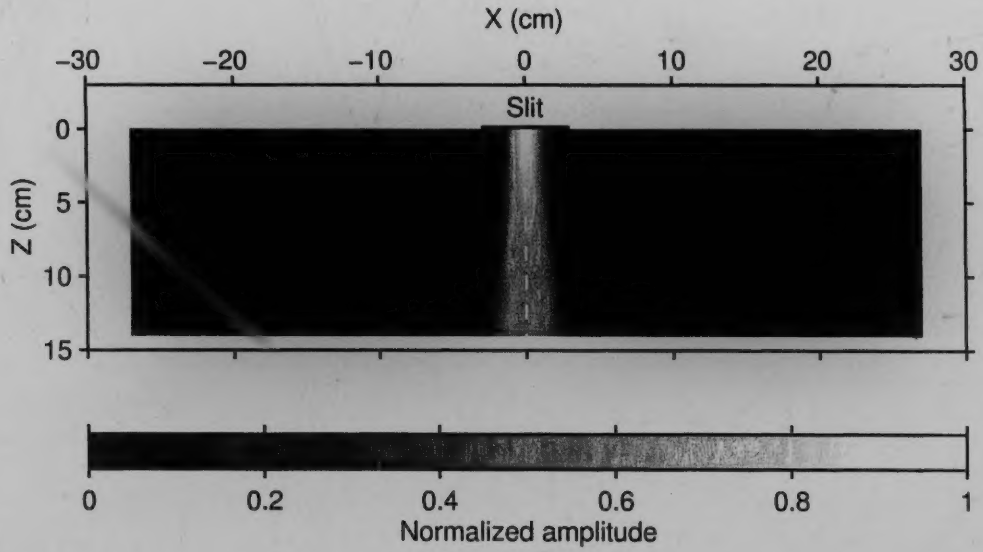

Figure 2.26: The amplitude envelope, normalized to the input, along the cross section of the beam shown in figure 2.25. The dashed line is the beam axis.

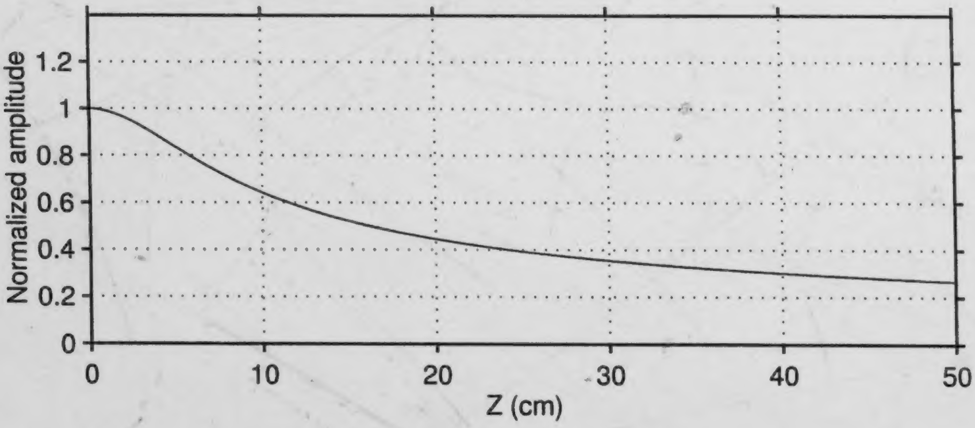

Figure 2.27: The amplitude envelope (Hilbert transform in x), normalized to the input, along the axis of the beam shown in figure 2.25.

the source.

2.9.2.2 Acoustic beam reflectivity

Here will be presented a reflectivity of a monochromatic Gaussian beam of width 8 cm. The source will be located above the z=0 plane and, for convenience, only the wave field below z=0 will be displayed. Let the beam width versus wavelength ratio be γ. A two medium space will be used where the first medium containing the incident and reflected energy is water and the second medium is a solid: soda-lime glass. The characteristics of the media are summarized in table 2.3 above. The frequency of the monochromatic acoustic Gaussian beam will be varied from 0.1 MHz to 2 MHz in a series of example calculations. The wavelength in the fluid

Material	P velocity m/s	S velocity m/s	Density kg/m^3
Glass	5787	3455	2492
Water	1498	-	995

Table 2.3: Laboratory measured properties of the fluid (water) and the glass sample used in the numerical example.

(velocity: 1498 m/s) varies from 15 mm to 0.75 mm. Therefore the wavelength is large compared to the beam width. Geometrical spreading will be more apparent in the figures for the lower frequency examples because of the scale at which these are produced. The reflected bounded beam exhibits no apparent lateral shift in the reflected beam. Similar behaviour of the reflected beam is noticeable at P and S pre-critical angles of incidence where a partial reflection occurs (Figs. 2.28 and 2.29). For the media used here the S-critical angle of incidence is 25.66° and the Rayleigh angle is 28.1°. The Rayleigh angle is the angle at which the phase of the reflection coefficient is exactly 180°.

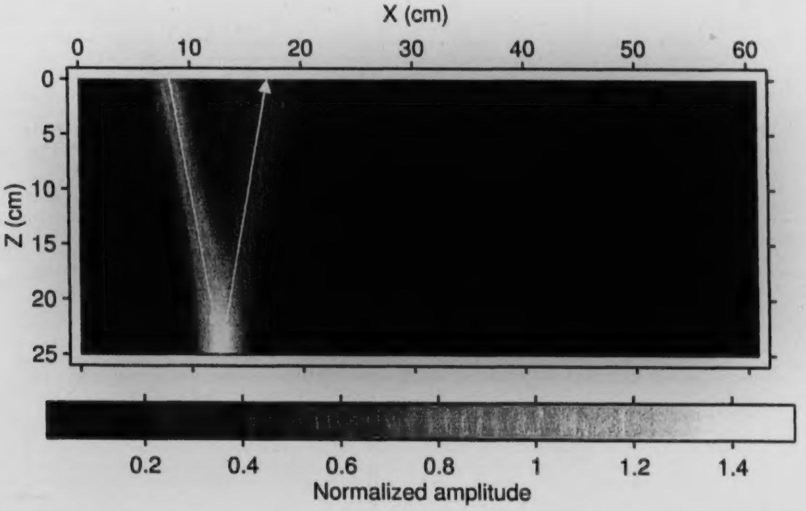

Figure 2.28: Amplitude envelope of a monochromatic Gaussian beam ($f = 0.5$ MHz, 8 cm wide, and $\gamma = 26.7$) reflected from a fluid-glass interface. The angle of incidence, $10^o < \theta_p^c = 15.00^o$, The axis of the incident and reflected beams are highlighted by the white arrows.

First a beam of 0.5 MHz (Wavelength $\lambda = 3$ mm) is incident at an angle of 10^o that is below the P-critical angle of incidence. We see a partial reflection occurring with no apparent shift of the beam (Fig. 2.28). A similar result is found when the angle of incidence is 20^o that is in between the P and S critical angles of incidence (Fig. 2.29). In figure 2.30 the beam is incident at an angle of 35^o, which is well above the S-critical angle of incidence $\theta_S^c = 25.66^o$. We see that total reflection occurs as explained in earlier sections in this chapter. Again this angle corresponds

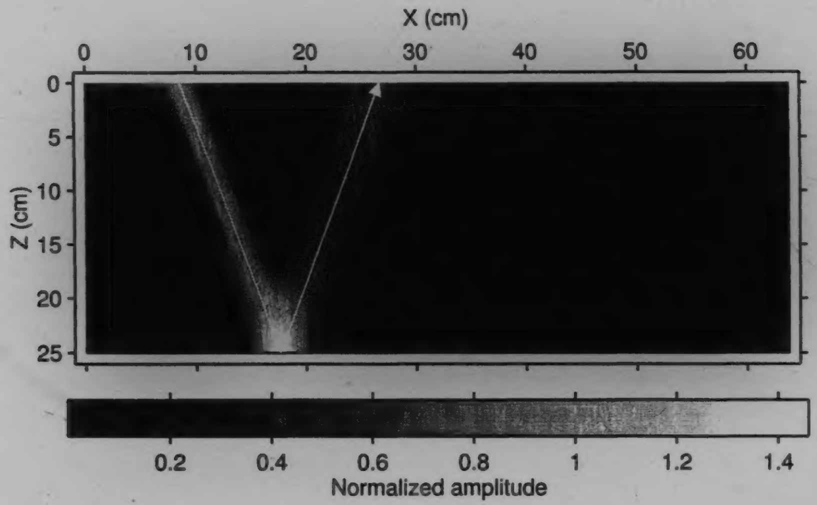

Figure 2.29: Same conditions as in figure 2.28 except for the angle of incidence of 20° that is greater than the P critical angle $\theta_p^c = 15.00^o$ and less than the shear critical angle $\theta_s^c = 25.66^o$.

to the angle of incidence where the reflected wave horizontal (parallel to the boundary) velocity is the Rayleigh wave velocity in the absence of the fluid. Solving for surface wave propagation along the interface between the solid and a vacuum leads to a velocity that equals the apparent velocity along the boundary of a reflected wave at the same interface when the vacuum is replaced by a fluid. In the following examples the beam will be incident at the Rayleigh angle where the maximum spatial dispersion is expected.

In the examples in figures 2.31 through 2.34 we see that no distortion is apparent in the reflected beam although it clearly shows the apparent lateral shift discussed in section 2.5. The frequency used is relatively high 3 MHz, 2 MHz, 1 MHz, and 0.5 MHz with wavelengths of 0.5 mm, 0.75 mm, 1.5 mm, and 3 mm, respectively. The calculated Schoch displacement (dashed line) is close to that expected for the first example, slightly off for the second one, and clearly off in the third example. This suggests that the Schoch displacement is only valid in the case of a very large beam width compared to the wavelength.

Distortion will appear at lower frequencies but keeping the beam width constant.

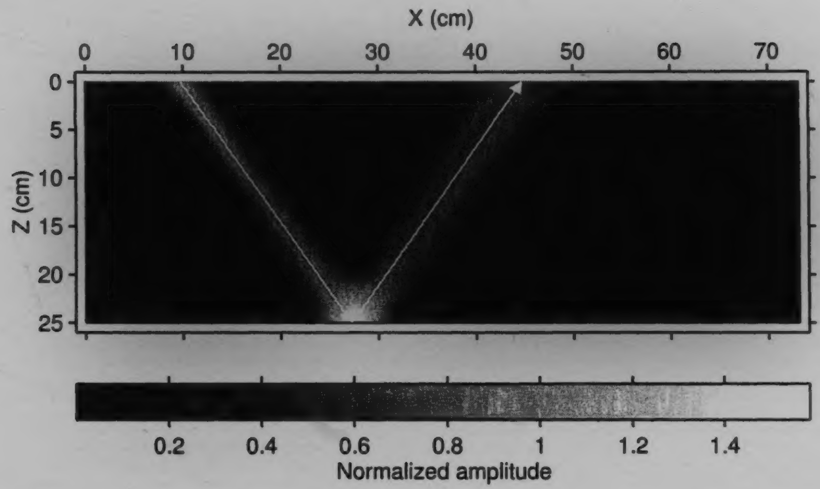

Figure 2.30: Amplitude envelope of a monochromatic Gaussian 0.5 MHz beam (8 cm wide) from a fluid-glass interface. The angle of incidence, 35°, is greater than the shear critical angle $\theta_s^c = 25.66^o$. Total reflection occurs with no shift of the beam. The axis of the beam at angles of incidence and reflection is highlighted by the white arrows. The ratio of the beam width versus the wavelength is 26.7.

The reflected beam exhibits various patterns of energy distribution. This is evident in the next two examples in figures 2.35 and 2.36 where distortion is apparent as the intensity distribution is no longer uniform across the beam. A null strip (very low intensity) in the reflected beam is evident in the example of figure 2.35 near the geometrical reflection axis. Moreover, in the example of figure 2.36, several null strips (or low intensity strips) are evident. These null strips are similar to those apparent in the schlieren photographs as shown earlier (Schoch, 1950; Diachok and Mayer, 1970; Neubauer and Dragonette, 1974; Breazeale et al., 1977; Ngoc and Mayer, 1980). In these last two examples the frequencies are relatively low, 0.2 MHz and 0.1 MHz respectively and the Schoch displacement is in total disagreement as expected. Here the Schoch displacement is much larger than the observation. This is in agreement that its validity is only for the cases where the beam width is very large compared to wavelength. In all the examples discussed sequentially in this section in figures 2.31 through 2.36, the ratio of the beam width versus the wavelength decreases as the wavelength increases. The ratio varies from 160.21 to 5.34. It is also apparent in these figures that the strips of higher intensity are not

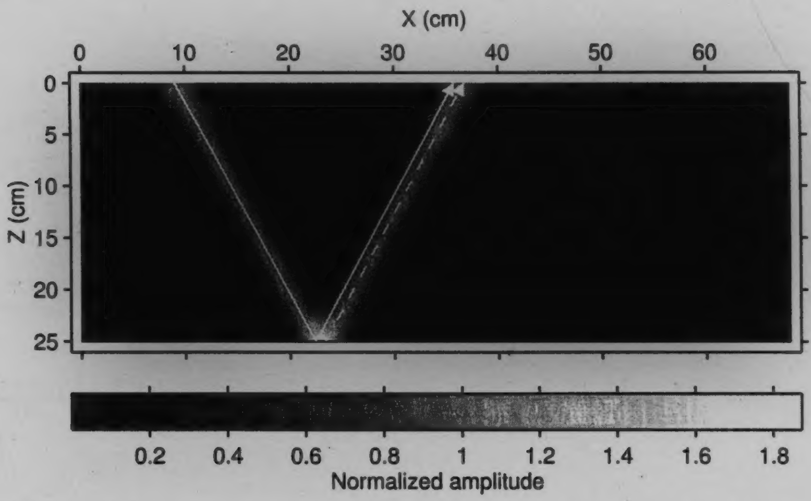

Figure 2.31: Amplitude envelope of a monochromatic Gaussian 3 MHz beam (width 8 cm) from a fluid-glass interface. The angle of incidence is the Rayleigh angle (28.1^o). The beam is apparently shifted upon reflection and the dashed arrow is at the calculated Schoch displacement. The ratio of the beam width versus the wavelength is 160.21.

perfectly parallel to the geometrical reflection ray. This is due to the short beam width. When the beam width increases under the same conditions the reflected energy, although displaced, remains parallel to the geometrical reflection ray. This can be seen in the examples of figure 2.37 and figure 2.38. These examples are similar to those of figure 2.35 and figure 2.36 except that the beam width is tripled. We see that the number of null strips is reduced and that the energy is reflected parallel to the geometrical reflection ray. It is difficult to describe beam displacement when the beam is distorted. Instead it is more meaningful to discuss the intensity distribution and define the point at which maximum intensity occurs in a cross-section. The first derivative of the phase of the reflection coefficient is not sufficient to describe the displacement of the maximum intensity as higher derivatives must be taken into account and Schoch displacement approximation fails to predict this point. Consequently, the analysis of reflectivity curves are complicated and require modelling on a case by case basis; simple analytical expressions such as Zoeppritz's equations are not sufficient to interpret experimental observations.

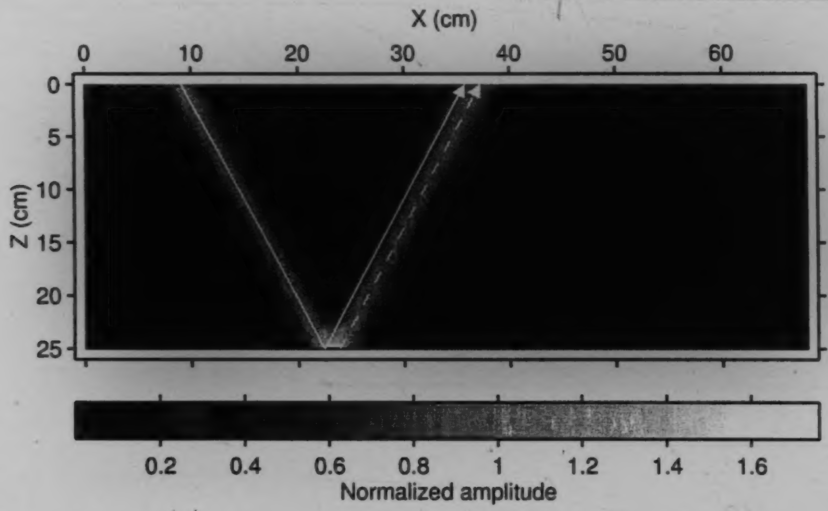

Figure 2.32: Amplitude envelope of a monochromatic 2 MHz Gaussian beam (width 8 cm) from a fluid-glass interface. The angle of incidence is the Rayleigh angle (28.1°). The beam is apparently shifted upon reflection and the dashed arrow is at the calculated Schoch displacement. The ratio of the beam width versus the wavelength is 106.81.

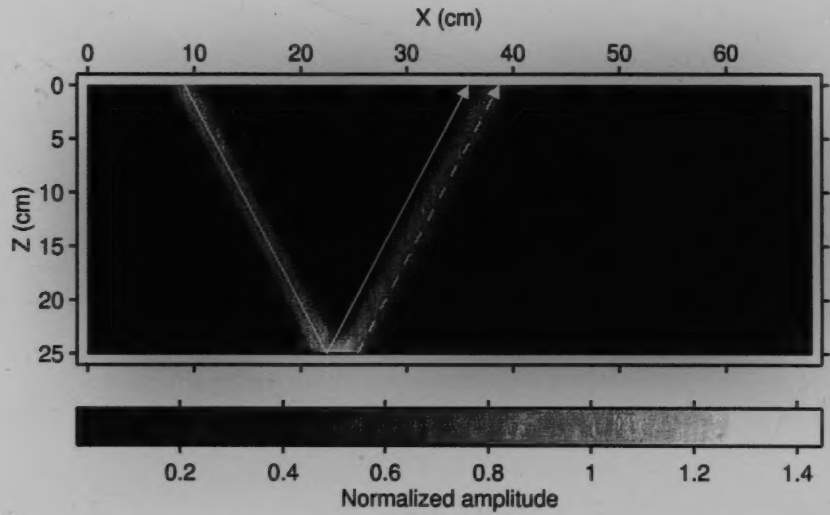

Figure 2.33: Similar to figure 2.32 with a frequency of 1 MHz. The ratio of the beam width versus the wavelength is 53.40. Incidence at Rayleigh angle of 28.1°.

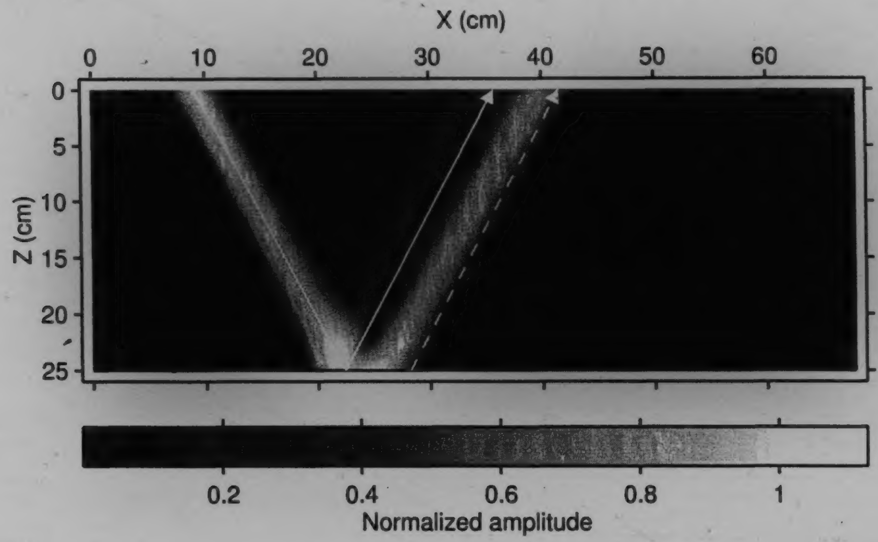

Figure 2.34: Similar to figure 2.32 with a frequency of 0.5 MHz. The ratio of the beam width versus the wavelength is 26.70. Angle of incidence at Rayleigh angle of 28.1°.

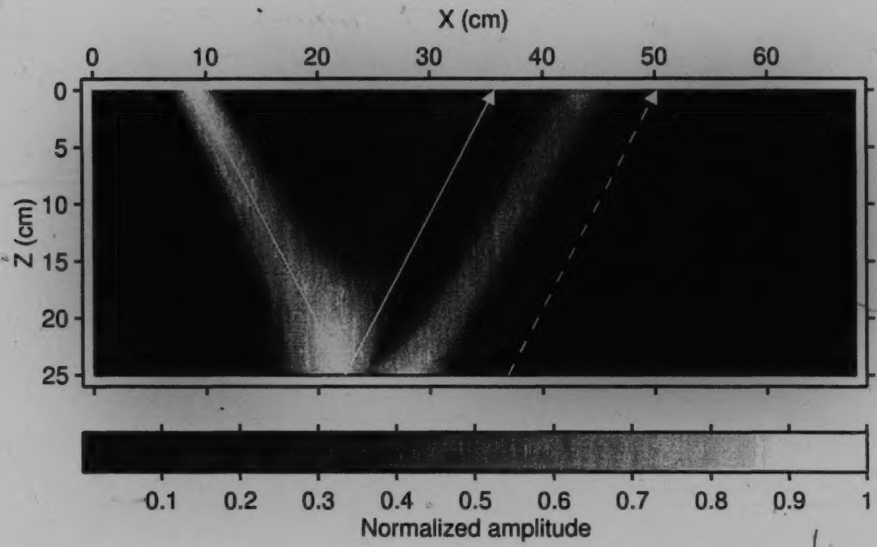

Figure 2.35: Similar to figure 2.32 with a frequency of 0.2 MHz. The ratio of the beam width versus the wavelength is 10.68. Incidence at angle of 28.1°.

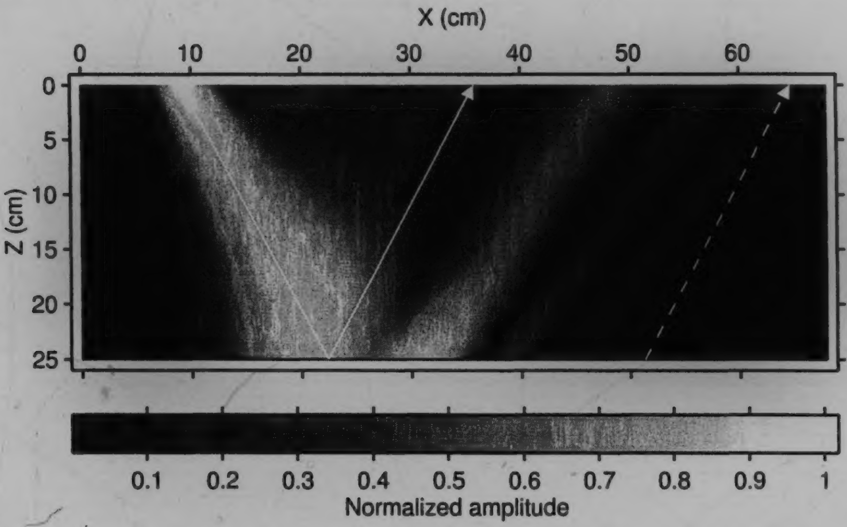

Figure 2.36: Similar to figure 2.32 with a frequency of 0.1 MHz. The ratio of the beam width versus the wavelength is 5.34. Incidence at angle of 28.1°.

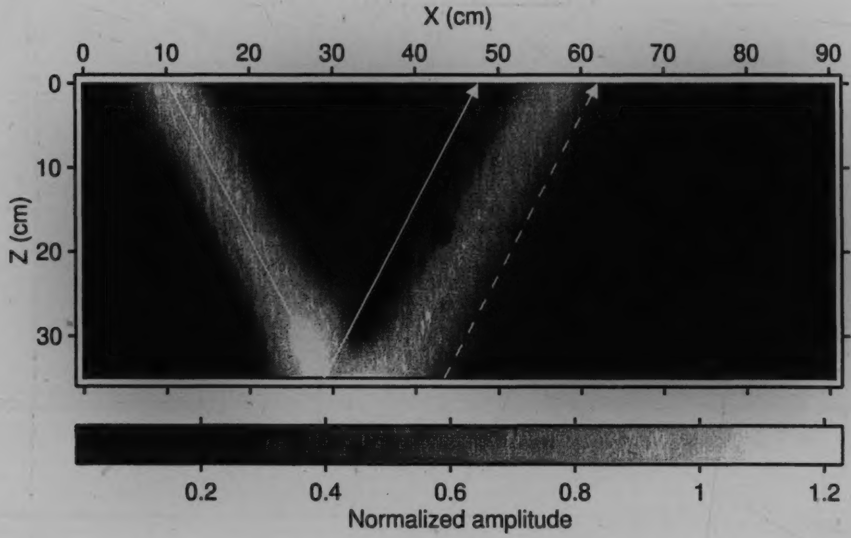

Figure 2.37: Amplitude envelope of a monochromatic 0.2 MHz Gaussian beam (24 cm wide) from a fluid-glass interface. The angle of incidence is the Rayleigh angle (28.1°). The beam is shifted and the dashed line is the calculated Schoch displacement. The ratio of the beam width versus the wavelength is 32.0.

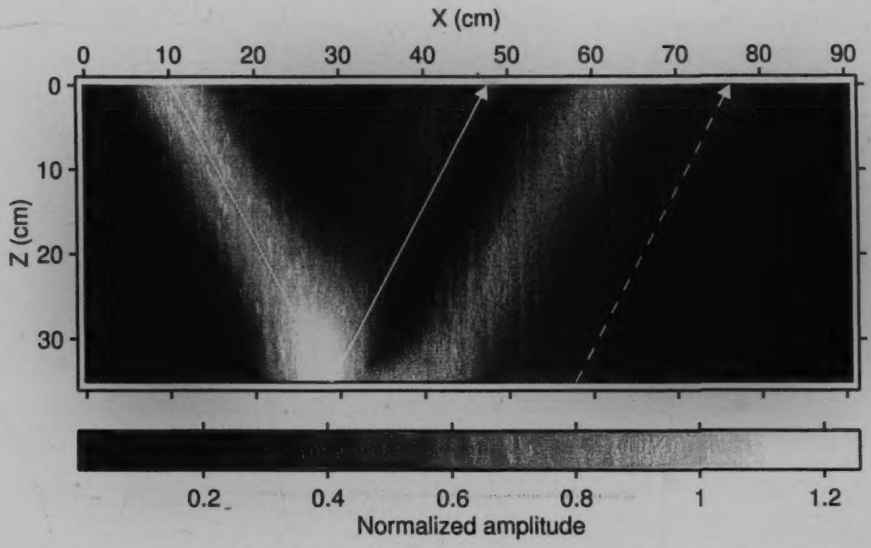

Figure 2.38: Amplitude envelope of a monochromatic 0.1 MHz Gaussian beam (24 cm wide) from a fluid-glass interface. The angle of incidence is the Rayleigh angle (28.1°). The beam is shifted and the dashed line is the calculated Schoch displacement. The ratio of the beam width versus the wavelength is 16.0.

2.10 Modelling of bounded acoustic pulses

In this section we model the propagation and reflectivity of bounded acoustic pulses. This will be the basis of all subsequent experiments. Equation 2.162 and 2.165 are exact descriptions of the propagation and reflection of a bounded acoustic pulse respectively. These equations will be used in all calculations. The solid medium is a copper alloy with its properties listed in table 2.4. A source of 8 cm width lies at

Material	P velocity m/s	S velocity m/s	Density kg/m^3
Copper	4789	2300	8901
Water	1493	-	995

Table 2.4: Laboratory measured properties of the fluid (water) and the copper alloy sample used in the numerical example.

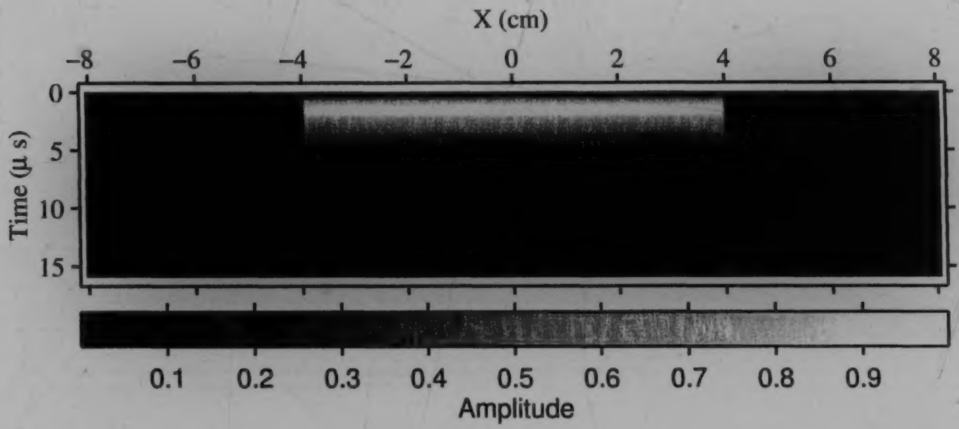

Figure 2.39: Amplitude envelope of the source generated bounded acoustic pulse at $z = 0$ used in the numerical calculations. The frequency bandwidth is 0.2-1.2 MHz.

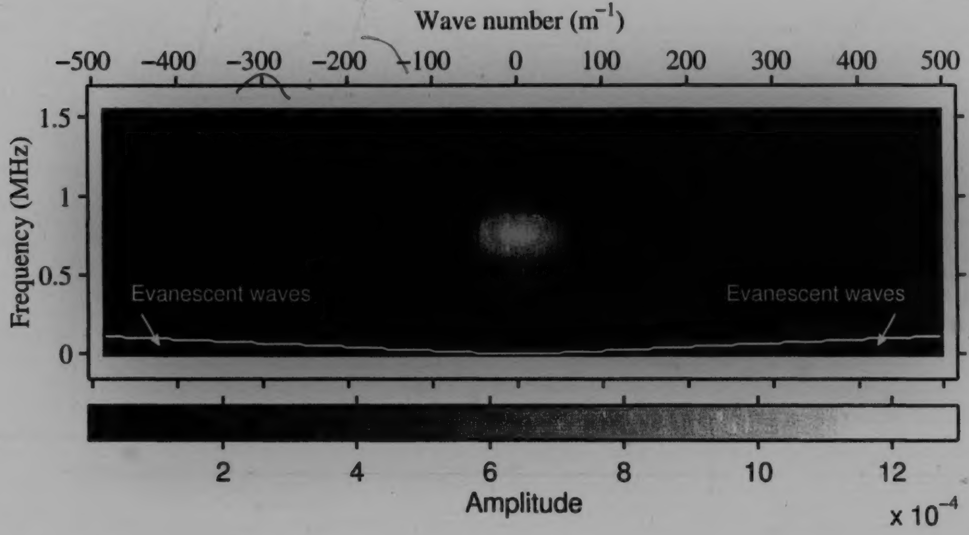

Figure 2.40: F-k spectrum of the acoustic bounded pulse of figure 2.39.

$z = 0$ in a water medium of velocity 1493 m/s. The generated bounded acoustic pulse potential wave field is assumed to be of the form given in figure 2.39. The central frequency of the pulse is at 0.78 MHz and the bandwidth is 0.2-1.2 MHz (Figs. 2.39 and 2.40). The wavelength then varies from $\lambda = 0.75$ mm to $\lambda = 1.5$ mm. Therefore the bounded acoustic pulse width is much larger than the wavelength. For this case the calculated Rayleigh angle, as defined in earlier sections, is 43.97°. In the figures presented in this section the amplitude envelope (Hilbert transform in time) of the wave fields are shown as important points appear better in these type of plots. The modelled bounded acoustic pulse shift will be compared to the calculated Schoch displacement. The S-wave velocity will also be inferred from the modelled Rayleigh angle and the P-wave velocity. It will be shown that the minimum reflectivity is observable at the Rayleigh angle.

2.10.1 Propagation

As the wave propagates forward in the water it also diffracts from the edges of the transducer. Figure 2.41 shows the amplitude envelope (via Hilbert transform) of the cross-section of the wave field. The propagation extends to the far field of 3 m. The energy at the edges migrates towards the centre of the bounded acoustic pulse. Figures 2.42 and 2.43 illustrate better this behaviour. The amplitude of the edges increase with propagation distance, mainly due to diffracted energy that moves inwards. The amplitude along the axis of the bounded acoustic pulse as it propagates

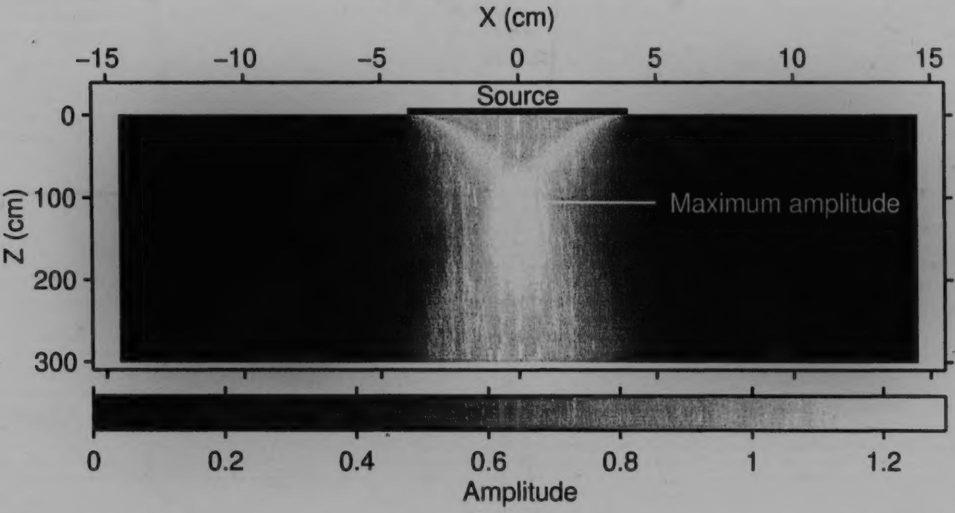

Figure 2.41: The maximum of the amplitude envelope of the cross-section of the bounded acoustic pulse as it propagates in the $\hat{z}$ direction. The wave field shown here extends to the far field. The vertical dashed line shows the axis of the pulse. Note that the vertical axis is compressed relative to the horizontal one.

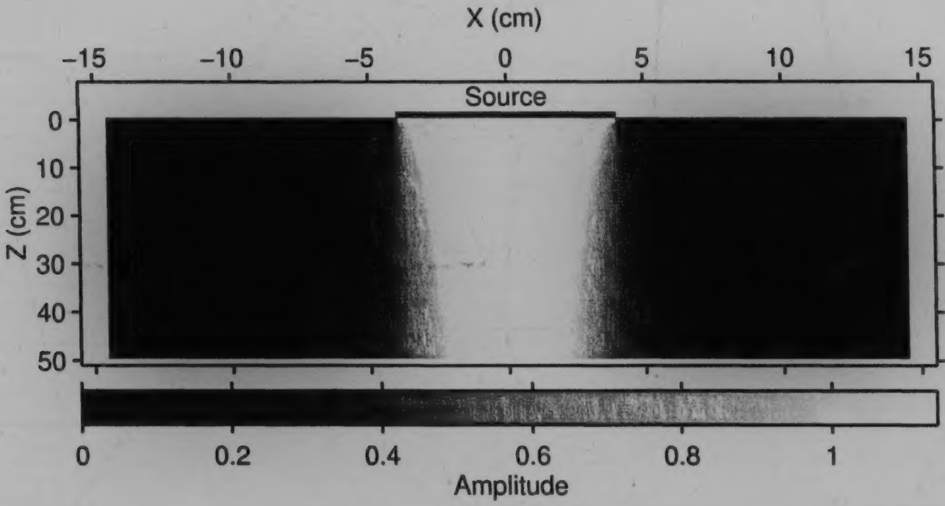

Figure 2.42: The maximum of the amplitude envelope of the cross-section of the bounded acoustic pulse as it propagates in the $\hat{z}$ direction. The near-field is shown here. The vertical dashed line shows the axis of the pulse.

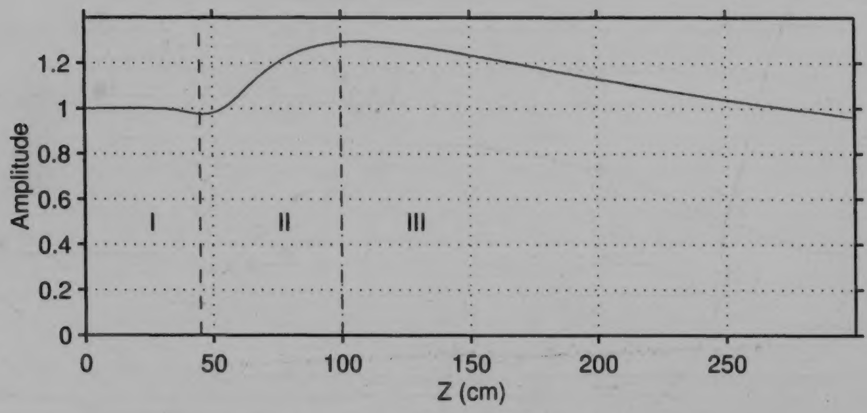

Figure 2.43: The maximum amplitude along the axis of a propagating bounded acoustic pulse. We distinguish three regions where the relative behaviour is quite different (see text for more details).

in the $\hat{z}$ direction remains constant until about $z = 45$ cm, a distance at which the edges start merging together making the amplitude at the centre higher than the initial value reaching a peak value at about one metre away from the source. The amplitude decreases thereafter with no diffraction effects. Spreading of the beam is

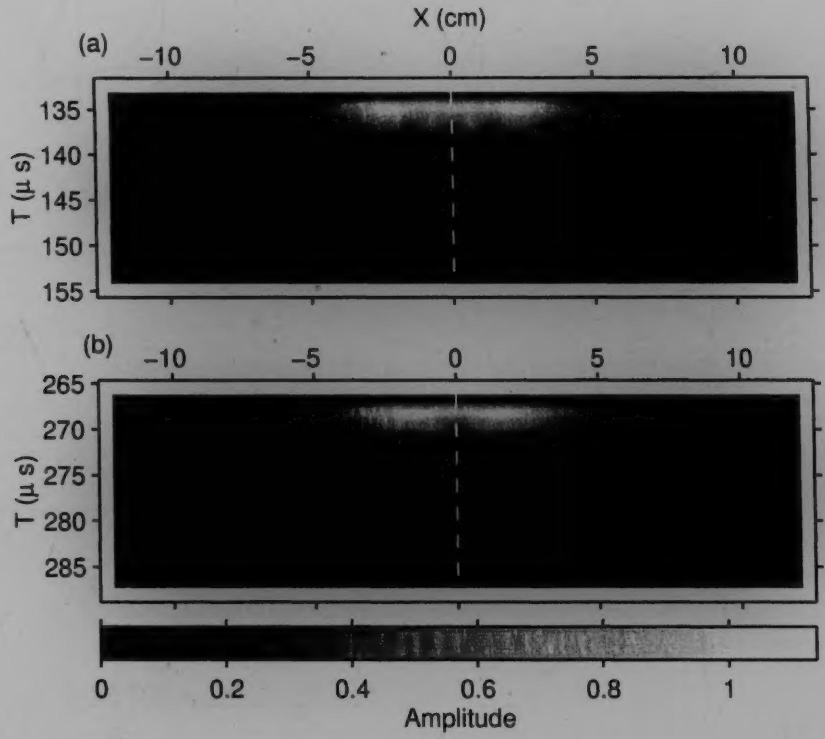

Figure 2.44: Forward continuation of the wave field of figure 2.39 to a distance of $z = 20$ cm (a) and to a distance of $z = 40$ cm (b). Note the motion of the diffracted energy inwards. The vertical line shows the axis of the pulse (see text for more details).

primarily responsible for further decay in the amplitude along the axis. Thus the bounded acoustic pulse exhibits a variable behaviour mainly in three regions:

- Region I: From $z = 0$ to about 45 cm where the amplitude is nearly constant.
- Region II: From $z = 45$ cm to about 1 m where the amplitude increases.
- Region III: From $z = 1$ m and thereafter where the amplitude decays.

It is apparent from figure 2.43 that the amplitude along the axis of propagation of the beam remains stable to a relatively large distance of about 30 cm, compared to bounded acoustic pulse width. The forward continuation of the original field at $z = 0$ of figure 2.39 is shown in figure 2.44, where the amplitude envelope of the wave field is presented at two distances, $z = 20$ cm and $z = 40$ cm away from the source. It is important here to note that according to the numerical results and the discussion given above, the bounded acoustic pulse behaviour is suitable to laboratory experimental studies such as reflectivity. Experiments conducted within this limit will require little or no corrections to the observed amplitudes. A source of the same size as described above will be used in the forthcoming reflectivity experiments from a various set of materials immersed in water. The experiments are conducted in a water tank with propagation distances within region I where the amplitude along the axis is nearly constant.

2.10.2 Bounded acoustic pulse reflectivity

There are many factors that will influence the behaviour of a reflected bounded acoustic pulse. These include the aperture of the transducer, the properties of the fluid and the solid, and the transducer bandwidth, among others. This is relatively complex and to highlight some interesting characteristics a series of examples is given.

The reflectivity of the bounded acoustic pulse 8 cm wide, discussed above, will be developed. A two medium space will be used where the first medium is water from which the bounded acoustic pulse is incident onto a copper alloy solid medium. The characteristics of the media are summarized in table 2.4 above. The spatial pulse width is quite large compared to the wavelength (1.9 mm at the dominant frequency of 0.78 MHz). The reflectivity of the bounded acoustic pulse from the interface is modelled via equation 2.165 as a function of incidence angle and is shown in figure 2.45. The calculated plane-wave Zoeppritz's solution using equation 2.88 for a monochromatic plane wave is shown for purposes of comparison. The measurement points are equidistant from the geometrical reflecting point that remains constant for all angles of incidence. We see that the reflectivity of the bounded acoustic pulse matches quite well the plane wave solution except in the vicinity of those incidence angles where there is a substantial change in the plane wave reflectivity. The most important difference is that at the Rayleigh angle where we see a large decrease in the reflected amplitude. This is expected as the bounded acoustic pulse experiences an important apparent displacement laterally along the interface at this angle. Thus the reflectivity around the Rayleigh angle is a measure of the wave field at the edge of the

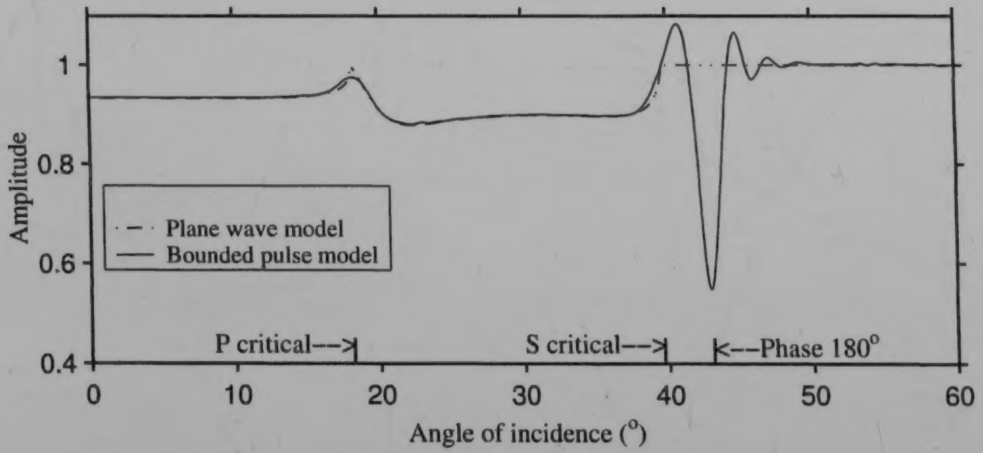

Figure 2.45: Reflection coefficient of a reflected bounded acoustic pulse from a copper plate immersed in water in contrast with a plane wave reflectivity response. Note the large drop in amplitude at the Rayleigh angle.

bounded acoustic pulse where the field is quite low in amplitude. Furthermore the reflected wave field is distorted. At the P and S wave critical angles the reflectivity is somewhat averaged. Indeed at any principle angle of incidence there are plane wave components with an angle of incidence that is lower and others with angle of incidence that is higher than the principle propagation angle. Thus all sharp edges will be smoothed out relative to the expected theoretical monochromatic plane wave reflectivity.

Figure 2.46 shows three frames as the bounded acoustic pulse impinges at S pre-critical angle of incidence onto the interface and reflected back to the liquid medium. In this case no apparent shift nor distortion in the reflected field is apparent.

Figure 2.47 shows three frames as the bounded acoustic pulse impinges at Rayleigh angle (43.97°) onto the interface and reflected back to the liquid medium. We see clearly that reflection does not occur at the expected geometrical point. We see rather a displaced wave field to the right by about 6.8 cm, a value that is close to the width of the incident bounded acoustic pulse. Thus the displacement is substantial and the calculated Schoch displacement of 6.4 cm is close to the observed one of 6.8 cm. The disagreement is within 6%. In this case the bounded acoustic

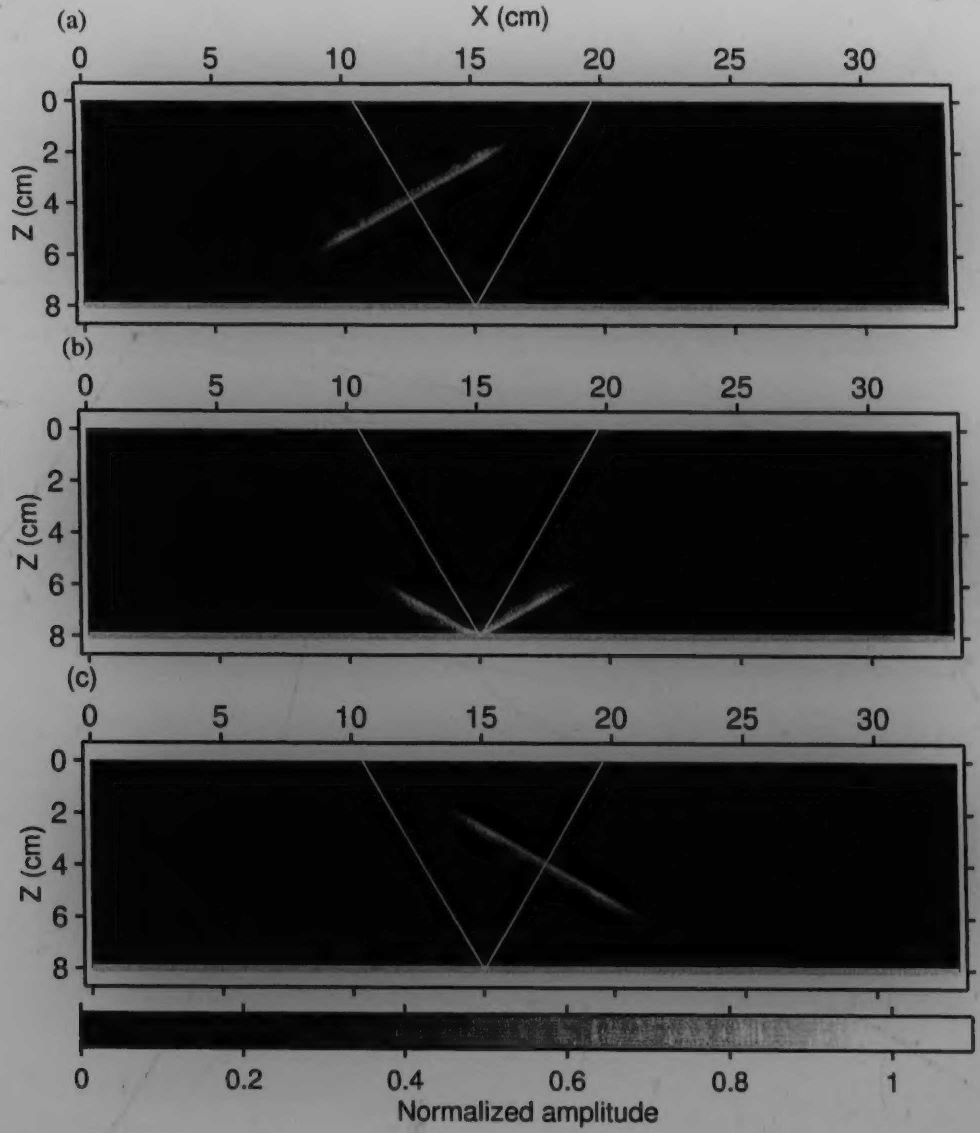

Figure 2.46: Three time snap shots of a bounded acoustic pulse impinging from a water medium onto a copper solid and reflected back to the water (see material properties in table 2.4). Bounded acoustic pulse width: 8 cm. Central frequency: 0.78 MHz. Frequency bandwidth: 0.2-1.2 MHz. Incidence at shear pre-critical angle of incidence (30^o). (*a*): Incident bounded acoustic pulse, (*b*): Wave field strikes the boundary. (*c*): Reflected bounded acoustic pulse.

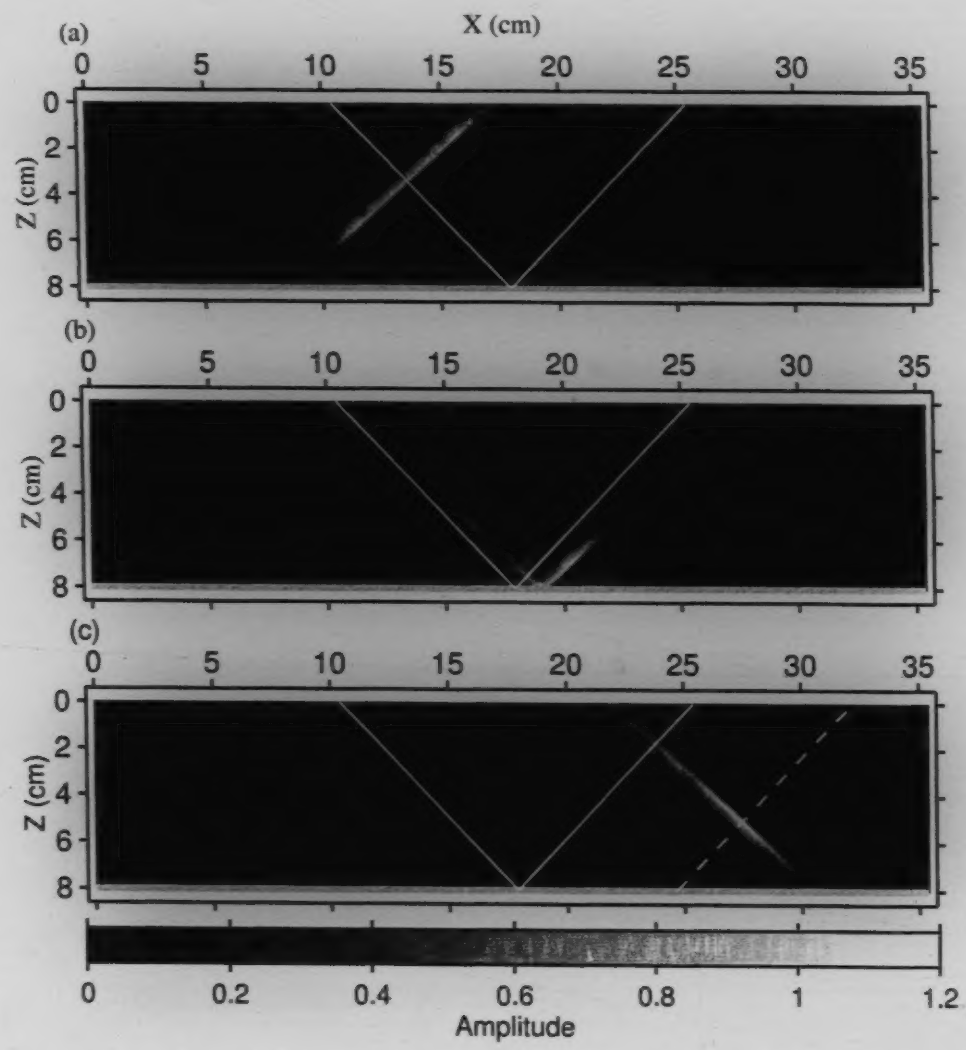

Figure 2.47: Three time snap shots of a bounded acoustic pulse impinging from a water medium onto a copper solid and reflected back to the water (see material properties in table 2.4). Bounded acoustic pulse width: 8 cm. Central frequency: 0.78 MHz. Frequency bandwidth: 0.2-1.2 MHz. Incidence at the Rayleigh angle (43.1^o). (*a*): Incident bounded acoustic pulse, (*b*): Wave field strikes the boundary. (*c*): Reflected bounded acoustic pulse. A substantial displacement of the reflected bounded acoustic pulse is noticeable from the expected geometrical reflection. The dashed line shows the maximum amplitude of the reflected wave field.

pulse is not displaced in its entirety but rather spatially dispersed. The meaning given here to the spatial dispersion is that each wave number component present in the incident wave field is shifted by a different amount according to its frequency and its angle of incidence. As a result energy is still present around the geometrical reflection direction.

It is possible to infer the S-wave velocity from the observed Rayleigh angle (Neubauer and Dragonette, 1974). Indeed, use of the Rayleigh angle information may be the only way to obtain this information given that the reflectivity curve has no readily apparent feature that may be picked at θ_s^c. Neubauer and Dragonette (1974) have attributed the null strip as giving the minimum observable reflectivity. In fact the search for the null strip is not necessary in order to observe a minimum amplitude in the reflectivity response. Keeping the source and the receiver at angles defined by geometrical reflection will allow one to observe a minimum amplitude in the reflectivity response. The Rayleigh angle is coincident with the minimum reflectivity response. In the case described here no null strip is evident in the reflected bounded acoustic pulse of the numerical results in figure 2.47. Now let this Rayleigh angle be θ_R. The horizontal velocity of the reflected wave field in the liquid is

$$V_R = \frac{V_f}{\sin\theta_R} \tag{2.166}$$

where V_f is the velocity in the fluid. The Rayleigh wave velocity (Ewing et al., 1957) is then given by the solution $0 < c < V_s$ of the equation

$$\frac{c^6}{V_s^6} - 8\frac{c^4}{V_s^4} + c^2\left(\frac{24}{V_s^2} - \frac{16}{V_p^2}\right) - 16\left(1 - \frac{V_s^2}{V_p^2}\right) = 0 \tag{2.167}$$

V_p and V_s are the P-wave and S-wave velocities of the solid respectively. This equation can be rewritten to solve for the S-wave velocity. To do so the knowledge of V_p and V_R is required. V_R can be measured from the observed Rayleigh angle whereas V_p can be measured from the P-critical angle θ_p^c when available. But in general the shape of the reflectivity at this critical angle is a smooth curve that does not allow a precise reading of this angle. It is preferable to measure directly the P-wave velocity via a pulse transmission experiment. Equation 2.167 can then be rewritten as

$$\frac{16}{V_p^2}V_s^8 - 16\left(1 - \frac{V_R^2}{V_p^2}\right)V_s^6 + 24V_R^2V_s^4 - 8V_R^4V_s^2 + V_R^6 = 0 \tag{2.168}$$

This equation admits, in general, more than one solution that satisfies the condition $0 < V_s < V_p$. But a unique solution can be achieved by using the fact that the Rayleigh angle θ_R is close to the shear critical angle θ_s^c. In the case of a low compressibility solid the S-wave velocity can be approximated from equation 2.167 by letting the compressional wave velocity of the solid be infinite. Then equation 2.167 admits one real solution $V_R = 0.9194V_s$ (Ewing et al., 1957). This solution can then be used to infer V_s and will be given by

$$V_s = 1.0467V_R \tag{2.169}$$

In the present numerical example given above the Rayleigh angle is 43.97° and the deduced horizontal velocity from equation 2.169 of the reflected wave front is $V_R = 2150$ m/s. This leads to an S-wave velocity of $V_s = 2251$ m/s which is close to the input S-wave velocity of $V_s = 2300$ m/s within 2.1%. However if we use equation 2.168 with the compressional wave velocity given in table 2.4 we get the S-wave velocity of $V_s = 2300$ m/s that is more precise (in this case exact) than that inferred from equation 2.169. The discrepancy will be larger when equation 2.169 is applied to low compressible solids but implementation of equation 2.168 leads to better results. Indeed, to find the material properties, the P-wave velocity V_p is needed. It is therefore better to make use of it to obtain a more accurate S-wave velocity.

2.11 Discussion

In light of what was discussed in the previous sections the Rayleigh angle phenomena is attributed purely to a spatial dispersive and interference effect. It is worth noting that Schoch (1950), as reiterated by Brekhovskikh (1960), associated this effect to a phase shift of the reflected wave field. Since then, however, there have been a number of alternative explanations. Here it is believed the experimental results in the next chapter, however, will confirm the above Schoch's and Brekhovskikh's analysis. The word spatial is used here in analogy to the velocity dispersion effect in dispersive media.

A bounded acoustic beam will have a distribution of horizontal wave numbers in the Fourier domain according to its width and wavelength. That is, each Fourier plane wave component present in the wave field is displaced by a different quantity according to its angle of incidence. A larger spatial beam width corresponds to a narrower band of wave numbers distribution (or equivalently a range of angles of incidence) in the Fourier domain. If the beam width is wide enough such that the vast majority of angles of incidence present in the decomposition are close to the principal angle of incidence in the direction of beam propagation then the whole beam would be uniformly displaced along the boundary. In such a case the Schoch displacement approximation gives a very good estimate of the displacement as indicated in figures 2.32 and 2.33.

On the other hand, if the beam width is narrow compared to wavelength then the distribution of its wave number components will be broader. In this case, significant proportions of the beam will have wave numbers that correspond to angles of incidence both less than and greater than the θ_R. As such, (see figures 2.35 and 2.36 for example), the various components of the beam will have a range of displacements. The beam will appear highly dispersed and the intensity distribution distorted as indicated in these figures.

Some workers (Tamir and Bertoni, 1973; Bertoni and Tamir, 1973; Breazeale et al., 1977) have attributed the beam displacement and distortion to the existence of a Rayleigh wave that is excited at the interface between the fluid and the solid. In this concept, the Rayleigh wave propagates along the interface as a surface wave in the solid. They presume this Rayleigh wave can leak energy into the liquid and thus is attenuated in the direction of propagation. Indeed an evanescent surface wave does exist after the S-critical angle of incidence but this wave should not contribute to the boundary energy balance as was demonstrated earlier in the solution of the boundary value problem in section 2.5. Consequently it cannot leak energy upwards into the liquid. Furthermore, if this wave were to loose energy as it propagated its horizontal wave number must be complex valued as proposed by Bertoni and Tamir (1973). This violates the foundation of the solution given to the boundary value problem; that is, the projection of all wave numbers of all wave modes generated at the boundary on the interface must be equal to that of the incident wave according to Snell's law (Equation 2.85). The wave number of the incident wave is real valued as considered in the solution to the boundary value problem in section 2.4.

In the plane wave decomposition of the bounded acoustic pulse inhomogeneous waves might be present but these do not carry enough energy to create a leaky wave strong enough to counter balance the reflected wave to create null strips as observed in experiments (Schoch, 1950; Brekhovskikh, 1960; Neubauer and Dragonette, 1974; Breazeale et al., 1977). It is also clear in figure 2.40 that inhomogeneous wave energy is almost absent in the Fourier decomposition of the incident bounded acoustic pulse. The spectrum shown in figure 2.40 is for normal incidence, however the same result is found for all angles of incidence. Instead of invoking the Rayleigh wave, here the phenomenon is interpreted as a purely effect of spatial dispersion. The dispersion, and hence the displacement, depends on the wavelength (frequency). Indeed, the larger the wavelength relative to the transducer dimensions the larger the distribution of the components in the Fourier domain with the result that more dispersion occurs. Conversely, the broader the relative frequency range the smaller and more uniform the displacement is.

From what has been described in the previous sections, we see that in order to investigate wave propagation and particularly reflectivity experiments one must well characterize the initially generated wave field. First, the characteristics of both bounded monochromatic acoustic beams and bounded acoustic pulses change with distance from the source due to diffraction. That is, there can be significant changes in amplitude along the axis of the transducer. However bounded acoustic pulses exhibit relatively long distances over which the amplitude along the axis of propagation is uniform (Figs. 2.42 and 2.43). This amplitude remains constant at much larger distances than in monochromatic bounded acoustic beams. This will allow the recorded events to become less sensitive to small diffracted arrivals from the apparatus. Precisely because they are limited in time, interference between the energy at the axis with that diffracted from the edges is lessened. These type of wave fields are preferred over the monochromatic bounded acoustic beams in laboratory experiments as the corrections, that might be difficult, needed to account for axial amplitude variations are reduced or eliminated. Further, the larger the source the greater the distance the wave field will maintain uniform amplitude along the propagation axis. For example a source 8 cm wide (0.78 MHz peak frequency) will produce a pulse that propagates with constant axial amplitude to a distance of approximately 30 cm (Fig. 2.43). This is important in a practical sense because it means that within this distance spreading corrections are not required if a sufficiently small receiving transducer is used.

It is worthwhile to note that in the preceding theory all wave fields were supposed to be of infinite extent in the third dimension $\hat{y}$. If this is not taken into account in the Fourier decomposition (by solving a 3D problem) errors might be substantial if the width of the bounded acoustic pulse is too small. To minimize these errors the length of the source in the $\hat{y}$ direction should be as large as possible in any experiment and must be greater than the width in the $\hat{x}$ direction.

2.12 Conclusions

This chapter began with a review of fundamental theory of plane wave propagation in fluids, of plane wave reflectivity, of Rayleigh angle effects, and of monochromatic spatially bounded acoustic beam. This review leads to the development of a technique of modelling a bounded acoustic pulse. The theoretical or numerical modelling presented in this chapter suggest that bounded acoustic pulses offer a good way to probe various materials using reflectivity. While the initial idea of using "large transducers" to do this were supported it is necessary to characterize well the wave field generated by each individual source used in experiments. It was shown that bounded acoustic pulses are well suited for laboratory experiments. However, because the pulse is spatially bounded its reflectivity from a fluid-solid interface exhibits an apparent lateral displacement along the interface when the phase change of the reflection coefficient is not negligible (i.e. at post S-critical angle of incidence). Substantial displacements occur at the maximum phase of the reflection coefficient at the so-called Rayleigh angle. When the beam width is much larger than the wavelength, at this particular angle of incidence the wave field is displaced or shifted laterally in its entirety. For wave fields with small widths severe distortion occurs in the intensity distribution of the reflected beam. This phenomenon is interpreted as a spatial dispersion due to interference of the various components of the pulse of differing wave number (angle of incidence) and hence displacement.

Further, it is unlikely that a Rayleigh wave generated at the interface is strong enough by itself to oppose the reflected wave field and create null strips as observed in experiments by other workers. Inhomogeneous waves that can be present in the decomposition of the incident wave field would not be strong enough to excite a strong leaky Rayleigh wave. Indeed in the numerical modelling calculations the same result is obtained whether inhomogeneous waves are included or not. The results agree with the dispersive effect.

This behaviour can occur at any boundary between two media if the phase of the reflection coefficient changes abruptly. The reflectivity of a bounded acoustic pulse from a fluid-solid interface exhibits a large drop of amplitude at the Rayleigh angle of incidence. In general a minimum reflectivity will be observable at the Rayleigh angle when maximum bounded acoustic pulse shift occurs. The observed Rayleigh angle can be used to infer the S-wave velocity and, indeed, may be necessary to employ as there is no clear indication of the S-wave critical angle of incidence in the reflectivity curve. Near the P and S critical angles an averaged reflectivity is observed in the bounded acoustic pulse response because sharp changes in the amplitude of the reflected wave, as calculated through Zoeppritz's equations, are smoothed out. Thus the reflectivity obtained from a bounded acoustic pulse is very close to that anticipated by Zoeppritz's equations except at the Rayleigh angle and at the P and S critical angles of incidence. In the next chapter a method of calibrating the reflectivity from well known solids we will presented. It will be also shown that the numerical modelling presented here agrees very well with the experiments providing evidence to support the theoretical ideas of Schoch (1950) presented here.

Chapter 3

Laboratory calibration of reflectivity using bounded acoustic pulses

Introduction

The main purpose is to fundamentally study the acoustic reflectivity from a fluid filled porous medium. The previous chapter showed, however, that such experiments are not necessarily easily interpreted due to the real effects of finite transducer geometry even on well understood elastic materials. The concept of a bounded acoustic pulse was introduced in the last chapter. Here will be given the results of a series of reflectivity experiments of such a pulse on a variety of solids. The results confirm the validity of the theory, and, also provide a calibration of the experimental configuration. Laboratory acoustic reflectivity experiments can be problematic when acoustic source and receiver transducers are not well characterized. To obtain reliable results from such experiments it is important to characterize the source and receiver used in experimental work. Furthermore, the shape and type of sources one can use in experiments can lead to large variations in the recorded signals that must be separated from the background noise. Small sources can lead to various diffracted events and undesired reflections from the experimental setup that could be as strong as the desired acoustic response one seeks to acquire. Large sources, on the other hand offer a good signal strength that could be recorded even without amplification.

The generated acoustic pulse from a large transducer can travel relatively long distances with the amplitude along the axis of propagation remaining constant. Events other than the desired reflectivity are much weaker and arrive later in the recorded trace making event separation easy. The propagation and reflectivity of bounded acoustic pulses from a fluid-solid interface was studied in great detail in chapter 2. The numerical models presented in chapter 2 showed that the reflectivity response from fluid-solid boundaries agrees quite well with Zoeppritz's equations except at angles of incidence where the phase (or the amplitude) of the reflection coefficient changes abruptly. There an apparent displacement of the bounded acoustic pulse along the interface upon reflection was observed. At incidence angles where the absolute value of the reflection coefficient exhibits sharp changes the reflectivity response is also smoothed.

Here, will be described a laboratory method for reflectivity tests. The method relies mainly on the use of a large transducer that generates a wide bounded acoustic pulse. The transmitted signal is recorded by a highly directional point-like receiver. The experiments are conducted in a water filled tank. A mechanical scanner is first used to characterize the source and the receiver behaviour. An acoustic goniometer is then used to acquire the reflectivity response from well known solid materials. Reflectivity experiments were conducted on three blocks composed of a soda-lime glass, an aluminium alloy, and a copper plate. The apparatus and the experimental setup used here will first be described including a discussion of source and receiver character. The observed reflectivities will be found to agree with those expected from theory developed in the last chapter. As such, these results both confirm the theory and serve as an important calibration of the experimental technique.

3.1 Experimental equipment and setup

A large variety of experimental equipment was developed specially for this experiment. This equipment included a large piezo-electric transmitter, a tiny piezo-electric receiver, a mechanical 3D scanning device, and an acoustic goniometer to carefully mount the transducers and sample. While the descriptions may be brief, it is worth noting that the transducer developments in particular required a great deal of repeated attempts with a number of failures before an acceptable signal was obtained.

3.1.1 Transmitter

A large acoustic source is constructed using a piezo-electric plate (PZT-840, American Piezo Ceramics Inc.) that is 10.2 cm×7.6 cm and 0.254 cm thick. It is mounted in a casing made out of an electrically non-conducting material (Fig. 3.1). The resonance frequency of the plate is in the order of 0.78 MHz. The transducer face directly in contact with water is coated with two thin layers (< 0.001 cm): a layer of electrically conductive epoxy covered with a layer of acrylic lacquer. This electrically isolates the electrode from the surrounding water while allowing maximum acoustic coupling. A thin layer of highly conductive copper is bonded to the back face of the transducer with conductive epoxy. In this way a high electrical coupling is obtained.

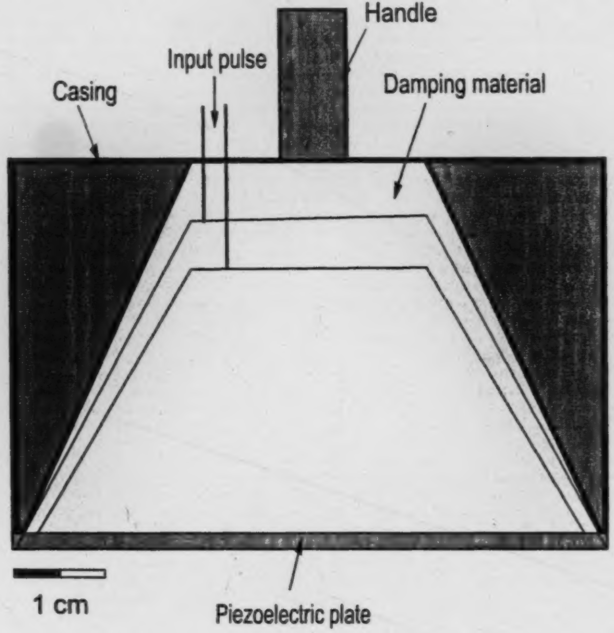

Figure 3.1: Cut-away schematic view drawn to scale of transmitting acoustic source used in all experiments. The source is 8.27 cm wide in the third dimension not shown.

The chamber to the back of the plate is filled with a urethane rubber (Flexane^{TM}) and tungsten mixture. The purpose of this mixture is to mechanically dampen the piezo-electric plate in order to shorten its pulse length, or equivalently, increase the transducer frequency bandwidth. The mixture is both highly attenuating and has an elastic impedance (ρV) close to that of the PZT-840 piezo-electric material permitting a narrower pulse to be transmitted into the surrounding liquid. This construction procedure has reduced drastically the ringing effect of the transducer produced when excited by a broad band pulse.

3.1.2 Receiver

The receiver is constructed with a very small and very thin piezo-electric plate cut from a PZT-850 (American Piezo Ceramics Inc.) The receiver is 1.9 mm x1.9 mm and 2.01 mm thick, mounted in a plastic casing (Fig. 3.2). As for the acoustic source described above, the face of the plate in contact with water is coated with two layers of a thin conductive epoxy and a thin acrylic lacquer. The plate has a surface area of 3.6 mm^2, only 0.046% that of the area of the source (7752 mm^2). The width of the receiver is on the order of the wavelength of the source pulse (about 1.9 mm) and, as will be seen the bounded source pulse is highly uniform over such dimensions. As such, the receiver is treated as a near-point receiver.

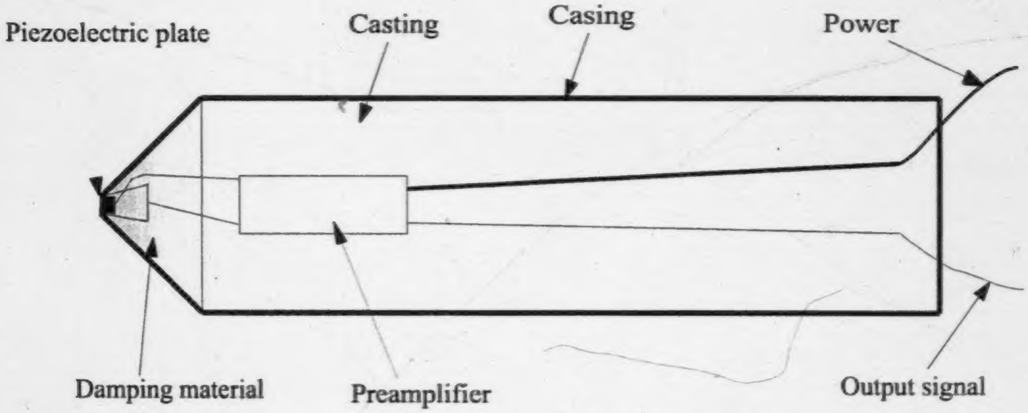

Figure 3.2: The near-point receiver with a preamplifier used in all experiments. The piezo-electric plate is 1.9 mm×1.9 mm and 2.01 mm thick.

The signal is boosted by a preamplifier mounted near the transducer to increase the signal to noise ratio. The gain of the preamplifier can be set to either 2 or 4 and its phase response is tested and found to be nearly zero over the frequency bandwidth of the pulse. The back of the transducer is also filled with a same damping material used for the source reducing the ringing effect. The resonance frequency of the receiver is of the order of 1 MHz.

Tests on the receiver have shown that it is highly directional and picks mainly wave arrivals with wave fronts parallel to the surface of the transducer, this minimizes the effect of non directed scattered energy.

3.1.3 Three dimensional acoustic scanner

In order to characterize the source and the receiver transducers a three dimensional in-house acoustic scanner (Fig. 3.3) was constructed. This apparatus allows the wave field in the fluid created by the source to be sampled at any interval to distances up to 40 cm. The acoustic source allowed motion is along the vertical axis, whereas the receiver is free to move in three dimensions. Thus the wave field produced by the source can be monitored in a large volume in front of the source. A

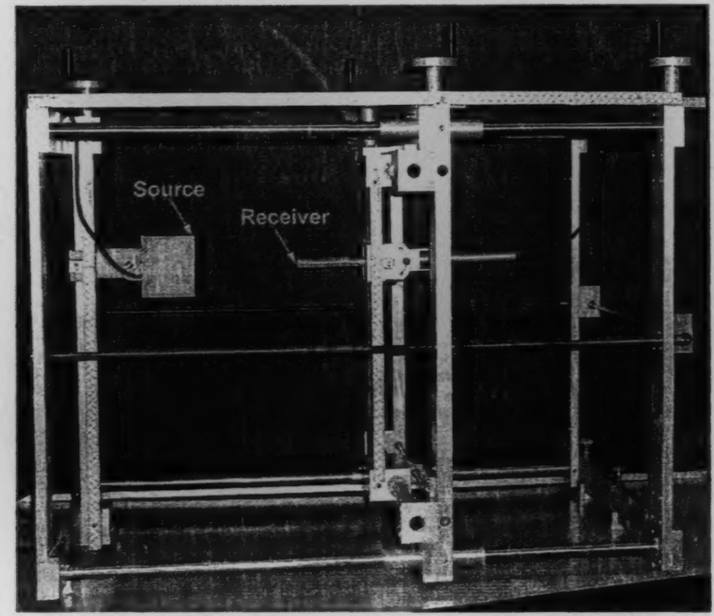

Figure 3.3: The acoustic scanner used to characterize the source and the receiver. The device is immersed in a water tank. Note the large transducer source compared to the near-point receiver.

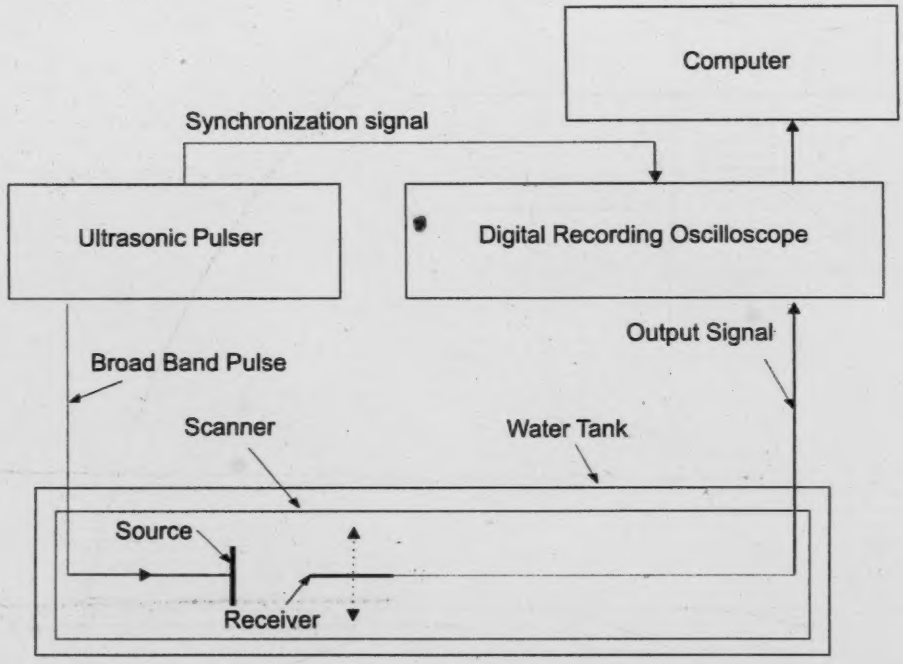

Figure 3.4: Setup for recording of a bounded acoustic pulse at a given distance away from the source. The diagram is not to scale. The dotted arrows show the scanning directions.

diagram of the experimental setup to record the wave field along an axis perpendicular to the axis of propagation of the bounded acoustic pulse is shown in figure 3.4. The ultrasonic pulser (Panametrics pulser Model 5800) sends a broad band pulse signal (12.5 to 100 μJ) that excites the transmitter to produce a narrow frequency bandwidth bounded acoustic pulse about its resonance frequency of 0.78 MHz. The receiver senses the signal as (i.e. variations in pressure in the water) it moves along a line parallel to the face of transmitter. The pre-amplified signal is then sent to the digital recording oscilloscope (Tektronix TDS 420A) for previewing and recording at the sampling rate of 0.040 μs.

The advantages of these characterization experiments are to well define the behaviour of the source-receiver pair. The use of large source is justified in the sense that it allows the generated bounded acoustic pulse to propagate large distances (30 cm) with a relatively stable amplitudes around the propagation axis as shown in chapter 2. This minimizes any corrections which could be needed if a smaller source were used. The point receiver in the other hand has to be as small as possible to minimize the averaging effect of large receiving transducers. The energy transmitted by the source is large at far field that even a tiny receiver could still pick a large arrival. The directionality of the source and receiver minimizes any obliquely arriving energy that might be scattered by the equipment. The acoustic scanner permits us to measure the near and the far wave field that would be compared to models to test the validity of the theory described in chapter 2.

3.2 Acoustic goniometer

An acoustic goniometer with two arms, one holding the source and the other the receiver, can be positioned at different angles of incidence and reflection (Fig. 3.5). A correct scale diagram of the experimental setup to record the wave field at a given angle of incidence is shown in figure 3.6. We notice the relative size of the source

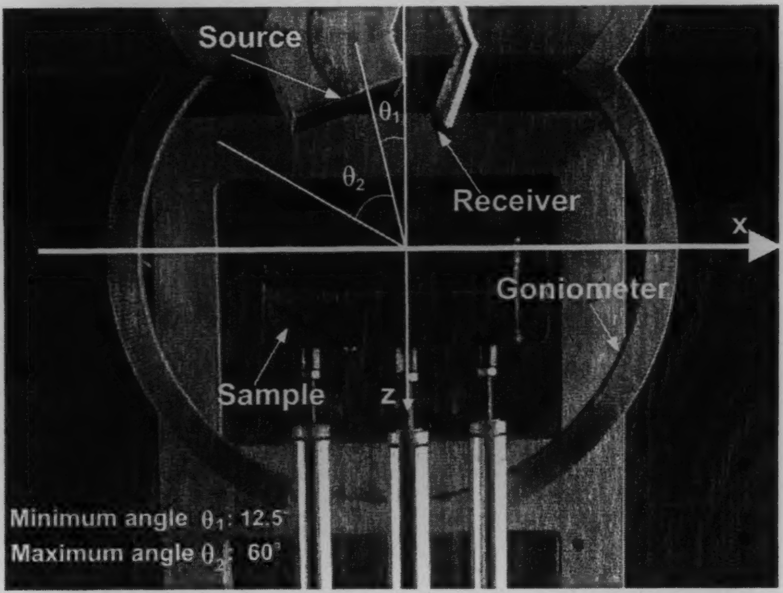
Source
θ_1
θ_2
Receiver
x
Goniometer
Sample
z
Minimum angle θ_1: 12.5°
Maximum angle θ_2: 60°

Figure 3.5: Photograph of the reflectivity experiment from a soda-lime glass sample in water using an acoustic goniometer. A transmitting source produces a bounded acoustic pulse and a near-point receiver captures the signal reflected from the water-glass interface. Note that top of goniometer is out of the water and is not seen.

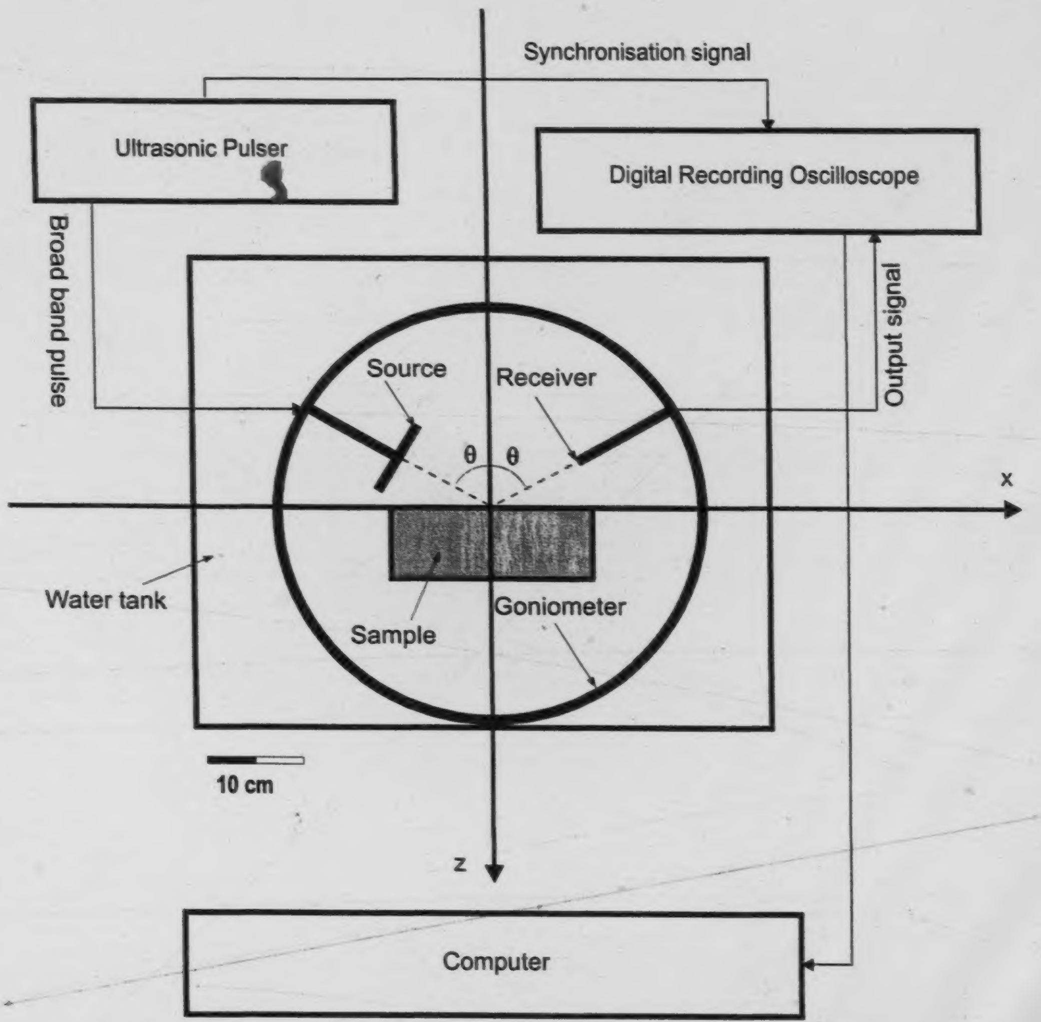

Figure 3.6: Diagram of the reflectivity experiment corresponding to the photograph of figure 3.5. The goniometer, the source, the receiver, and the sample are drawn to scale.

compared to receiver and the goniometer. By design this experimental setup records only the wave field at the centre of the reflected bounded acoustic pulse. Further, the centres of the transmitter and receiver remain at constant distance regardless of the angle of incidence; this reduces or eliminates any geometrical spreading corrections required. The bounded acoustic pulse path is shown in gray without taking into account the geometrical spreading.

With this setup, and primarily due to the physical size of the source, measurements cannot be taken at angles of incidence less than the minimum angle of incidence of 12.5^0. Large angles of incidence are also limited to 60^o, at this angle the source and the glass sample (or any other sample of the same size) are nearly in physical contact allowing no further movement of the source. Another problem beyond this angle of 60^o is that other arrivals, such as a direct wave from the transmitter to the receiver, interfere with the reflected signal. Consequently quantitative measurements are limited to angles of incidence between 12.5^o and 60^o.

This experimental setup has further advantages. Because the bounded acoustic pulse produced by the source is strong and the receiver highly directional, events arriving off the axis of the reflection path are much weaker and do not noticeably disturb the reflected signal.

The angles are directly measured on a scale with tick marks of 0.25^o with a reading error of about 0.05^o. The angles in the experiments were measured in steps of 0.5^o with a reading error of about 0.01^o. The source and receiver are aligned using a laser to ensure that the measured reflected energy by the receiver is indeed coming from the centre of the source. The alignment is done for both the source and the receiver by replacing each at a time by a laser source. The sample surface is always aligned with the diameter of the goniometer and its surface coincides with a plane perpendicular to the plane of the goniometer (Fig. 3.6).

3.3 Source and receiver characterization results

The experiments in this thesis rely on signal fidelity and quality. As such it is important that the specialized transducers developed be well characterized. In this section we discuss the signals produced by the source and the measurement of the bounded acoustic pulse. This information is critical to later modelling of expected reflected responses.

The signal produced by the source is recorded by the near-point receiver at a distance of 2 cm and a sampling rate of 0.04 μs. It has a narrow frequency bandwidth (0.2 MHz to 1.2 MHz). The wavelet and the amplitude spectra are shown in figure 3.7. The bounded acoustic pulse is recorded using the setup of figure 3.4. The

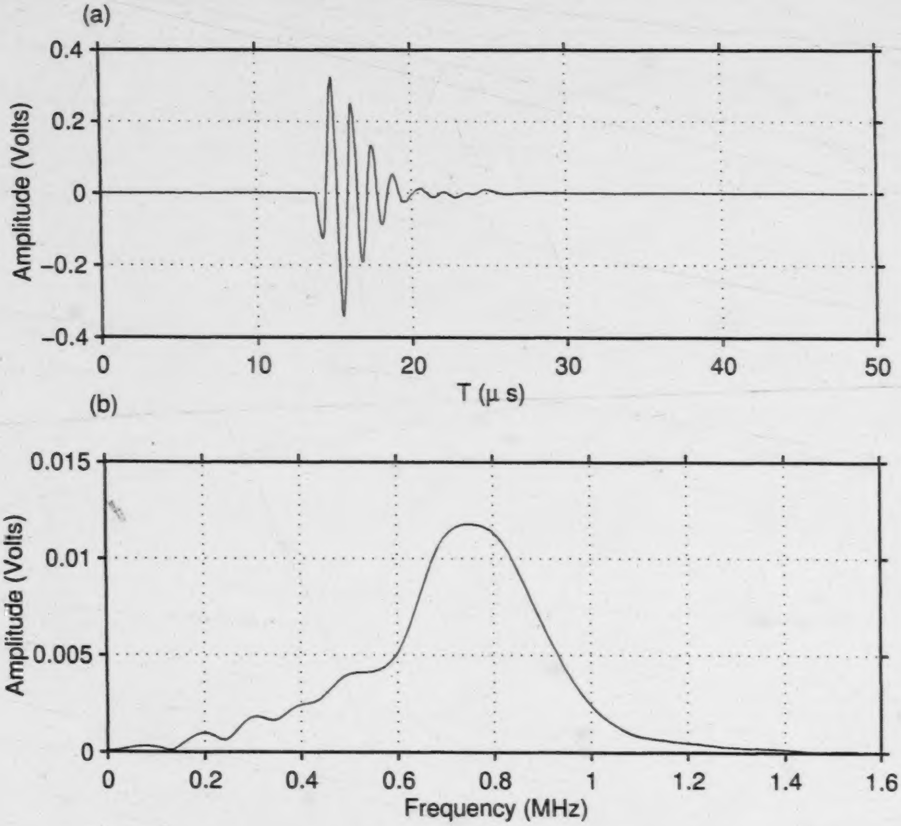

Figure 3.7: (a) Waveform observed along the axis of the transmitter at a distance of 2 cm. (b) Amplitude spectra of (a). The frequency bandwidth is about 0.2 to 1.2 MHz.

receiver is positioned 2 cm away from the source and the bounded acoustic pulse is sampled along a line parallel to the plane of the source transducer at 1 mm and 2 mm steps for the vertical and horizontal directions respectively. The normalized recorded waveforms are shown in figure 3.8 in both the vertical and the horizontal direction. The vertical and horizontal recorded wave fields are not acquired at the same conditions. The velocity in the water varied slightly during the vertical and horizontal data acquisition respectively. The generated bounded acoustic pulse has a flat arrival time and a nearly-constant amplitude in a large area around the axis of propagation. We also notice, as expected, that the bounded acoustic pulse is wider in the horizontal direction than in the vertical direction according to the

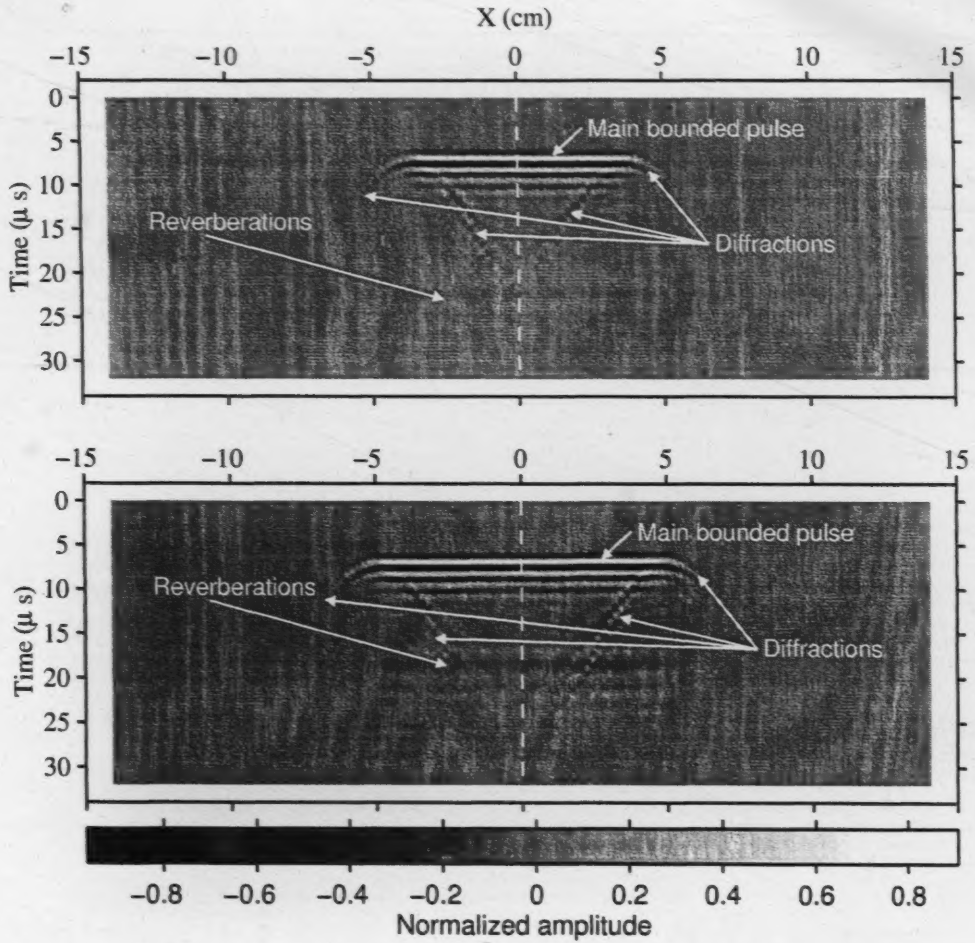

Figure 3.8: (a) Source wave field recorded 2 cm from the source along a line parallel to the plane of the source transducer in the vertical direction. (b) Wave field in the horizontal direction at the same distance. The vertical line represents the centre-axis of propagation.

lateral dimensions of the source. Some coherent noise is also noticeable after the main bounded acoustic pulse. These events might have been generated by ringing between the back of the piezo-electric plate and the plastic housing (Fig. 3.1) within the damping material, perhaps because of insufficient attenuation or because of the closeness of the receiver to the source. These events occur at slightly different times, probably due to the variation in the fluid velocity as mentioned above. Diffractions from the edges of the transducer are also clearly apparent. However, at the centre of the bounded acoustic pulse diffractions and reverberations do not interfere with the first arrivals of interest.

As noted earlier, it is important that we understand the bounded acoustic pulse. One aspect of this is knowing how the pulse will change with propagation distance. The wave field is modelled near the source given in figure 3.8 as it propagates in the fluid medium using the methods described in chapter 2. Specifically, we now calculate its shape and amplitude at a distance of 35 cm from the same plane and compare these calculations to the experimental wave field recorded at the same distance. To do so recall the equation 2.162 describing the wave field as an integral in the space ($\hat{x}$,$\hat{z}$,t), this equation is

$$\phi(x,z,t) = \frac{1}{4\pi^2}\int_{-\infty}^{+\infty}\int_{-\infty}^{+\infty}\Phi(k_x,0,\omega)e^{ik_x x}e^{i\omega t}e^{ik_z z}dk_x d\omega \tag{3.1}$$

where $\Phi(k_x, 0, \omega)$ is the wave field recorded on the plane $z = 0$ transformed into the Fourier domain (k_x, ω). k_x and k_z are the horizontal ($\hat{x}$) and the vertical ($\hat{z}$) wave numbers respectively. $\phi(x, z, t)$ is the wave field everywhere in the space ($\hat{x}, \hat{z}$) and at any time t. Using equation 3.1 the wave field recorded at 2 cm away from the source is calculated at a distance of 35 cm. This is accomplished by first taking the double Fourier transform of wave field recorded at $z = 0$ in time and x, phase shifting by multiplication by the operator $e^{ik_z z}$ where $z = 0.35$ m, and finally taking the double inverse Fourier transform. To speed up the process the Fast Fourier Transform algorithm can be used. Depending on memory availability the process can be done in steps in the $\hat{z}$ direction that sum up here to the desired distance of 35 cm.

The observed and calculated wave fields at a distance of 35 cm are shown in figure 3.9. We notice that these are in excellent agreement despite the reverberations present in the model. This distance of 35 cm is greater than the source-receiver distance of 20 cm used in the reflection experiments. We notice that the "reverberations events" are present in the model above 250 μs but not in the observed data. This further supports the contention that these events are probably a result from the proximity of the source and receiver (2 cm) when the input wave field data is acquired.

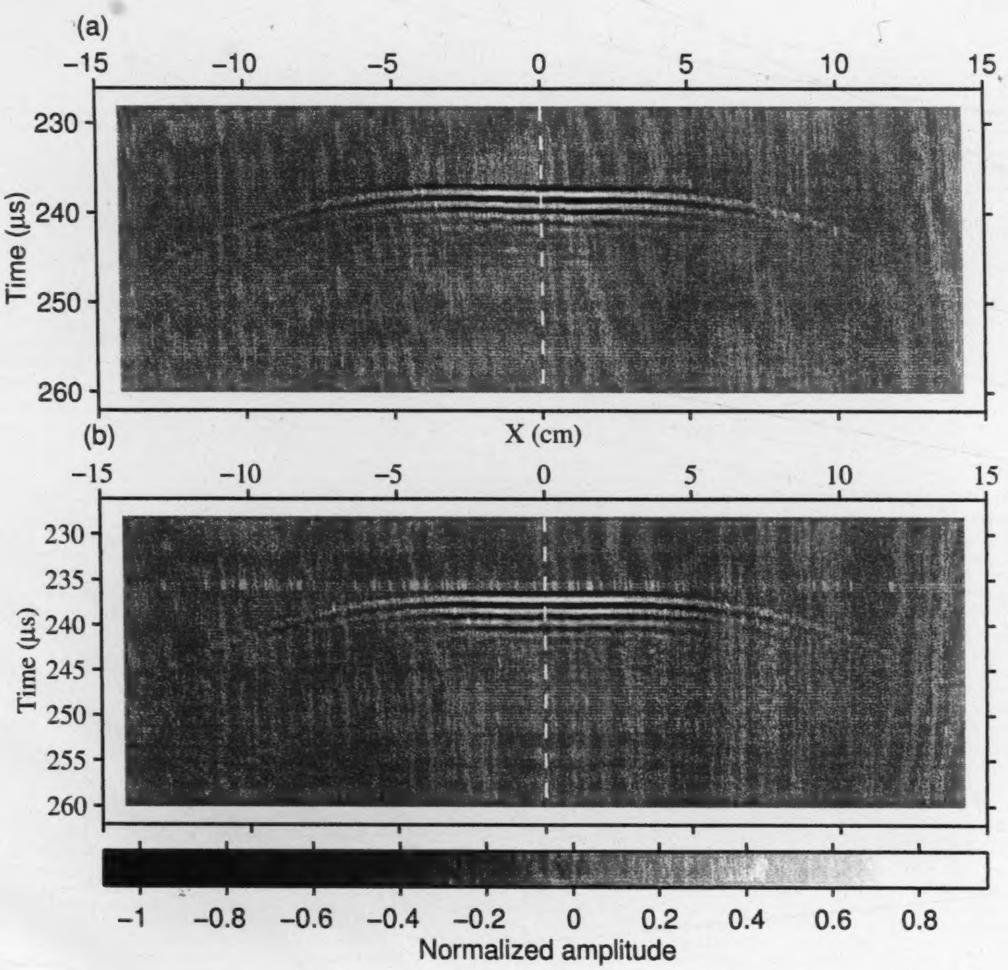

Figure 3.9: a) Observed wave field at a distance of 35 cm from the source. b) Modelled wave field at the same distance. The input to the model is the vertical scan shown in figure 3.8-a.

The maximum amplitude envelope, calculated through the Hilbert transform, of both observed and modelled wave fields at distances of 2 cm and 35 cm are compared in figure 3.10. At 2 cm both the vertical and horizontal wave fields show a large area around the axis of propagation where the amplitude is nearly-constant. However the horizontal bounded acoustic pulse is wider than the vertical one. At 35 cm the model and the observed amplitudes are in excellent agreement despite a misalignment of about 2 mm, this is likely due to the precision of the scanner positioning system at

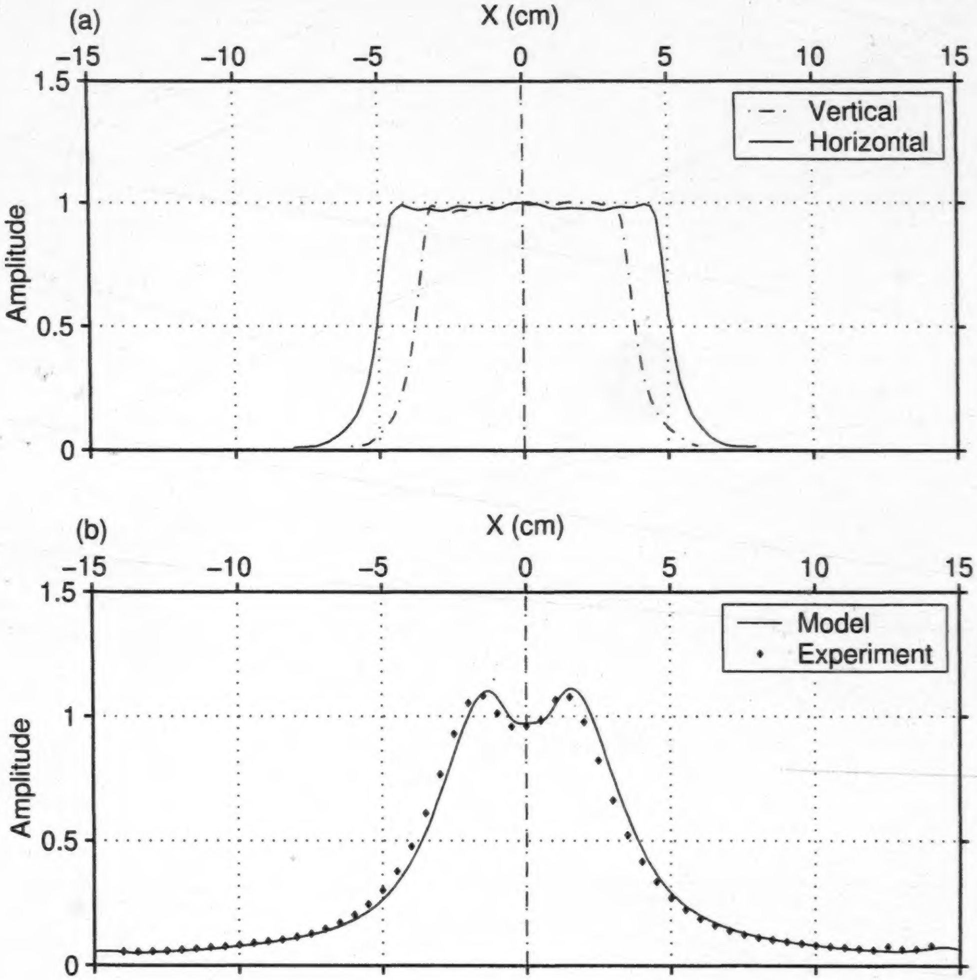

Figure 3.10: The normalized maximum of the amplitude envelope, calculated through the Hilbert transform. (a) Observed wave field at 2 cm away from the source in two directions, vertical and horizontal. (b) Modelled and observed wave field at 35 cm away from the source in the vertical direction.

the 35 cm distance. The edges of the bounded acoustic pulse increase in amplitude and migrate inwards towards the centre as predicted by the model given in chapter 2. This is evident in the amplitude envelope of the cross section of the acoustic bounded acoustic pulse as it propagates in the fluid as shown in the composite image of figure 3.11-a. The wave field as predicted by the model in chapter 2 spreads energy

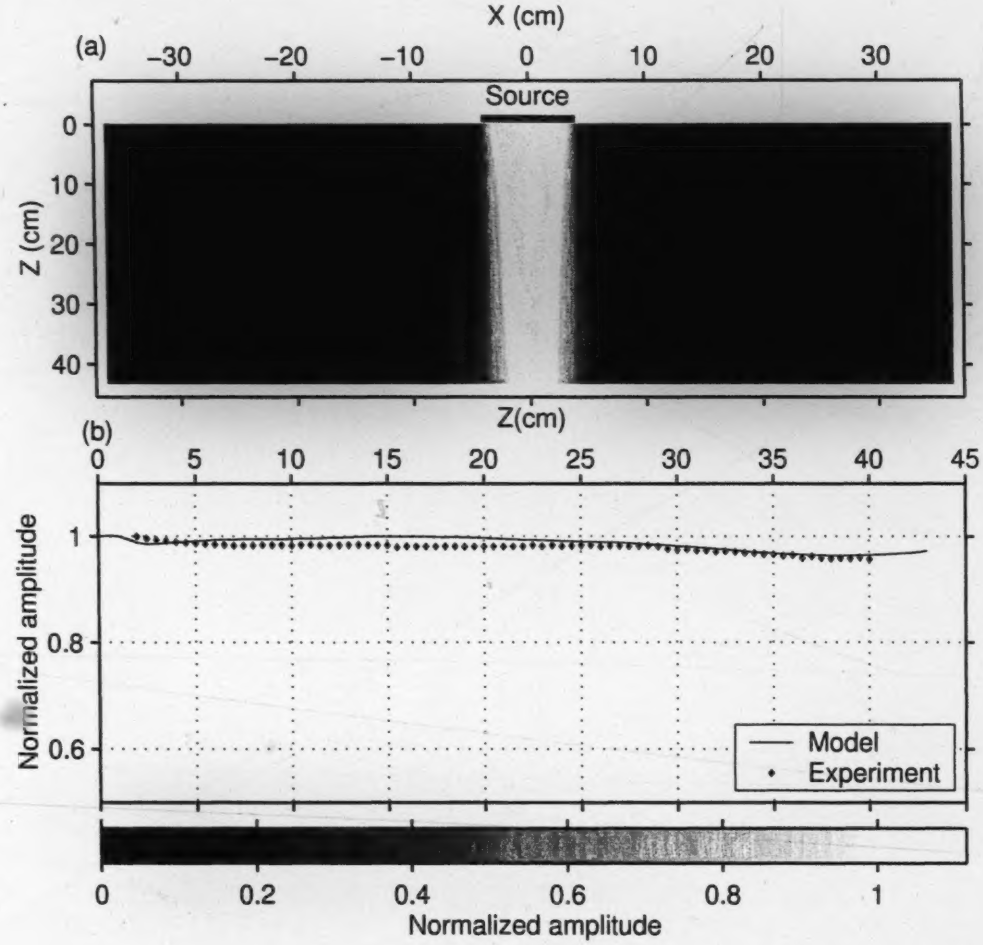

Figure 3.11: Forward model from 0 cm to 40 cm of the wave field shown in figure 3.8. a) Colours represent the peak of the amplitude envelope at each distance z. b) Peak of amplitude envelope along the axis of the same transducers as calculated and as observed. The amplitude along the axis of propagation in the $\hat{z}$ direction remains nearly constant to about 30 cm.

outwards and inwards by diffraction as it propagates. The amplitude at the centre of the acoustic bounded acoustic pulse as a function of propagation distance is given in figure 3.11-b with the model superimposed. We see that they are in very good agreement. This confirms that the forward modelling of the bounded acoustic pulse using equation 3.1 adequately and effectively describes the wave field at any point in front of the acoustic source and places further confidence in the reflectivity modelling in previous and later chapters.

3.4 Reflectivity results and discussion

In order to perform reflectivity experiments on complex, and not necessarily well understood, materials such as fluid-saturated porous media, it is imperative that the source and the receiver be calibrated on well known materials. Here reflectivity experiments are conducted on blocks of three solid, isotropic, and low attenuation materials (Fig. 3.12): a soda-lime glass, a copper alloy, and an aluminium alloy.

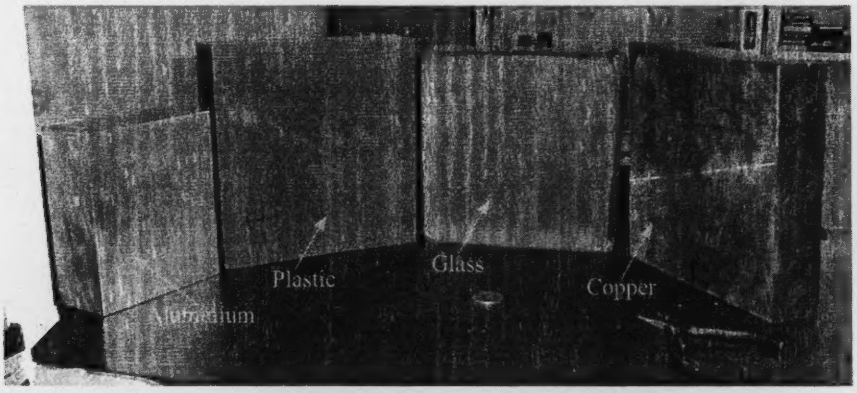

Figure 3.12: The three samples used in the experiments, an aluminium sample, a glass sample, and a copper sample. The plastic sample was not used. Coin is a 1988 Canadian dollar for scale

The surfaces used for the reflectivity experiments were flattened within 0.075 mm for the glass and 0.025 mm for the copper and aluminium. This was the maximum that could be achieved with the available equipment used. Waveforms were acquired with incidence angle from these blocks using the goniometer setup (Fig. 3.5 and 3.6). A wide range of angles of incidence was covered from 12.5^o to 60^o, i.e. those angles allowed by the physical setup of the experiment. The P and S wave velocities for the three samples were directly measured in independent ultrasonic pulse transmission tests. These materials are non-porous and the properties are assumed constant throughout the measurements. The density was determined by weight and volume measurements on the samples. The velocity of water was measured in each test

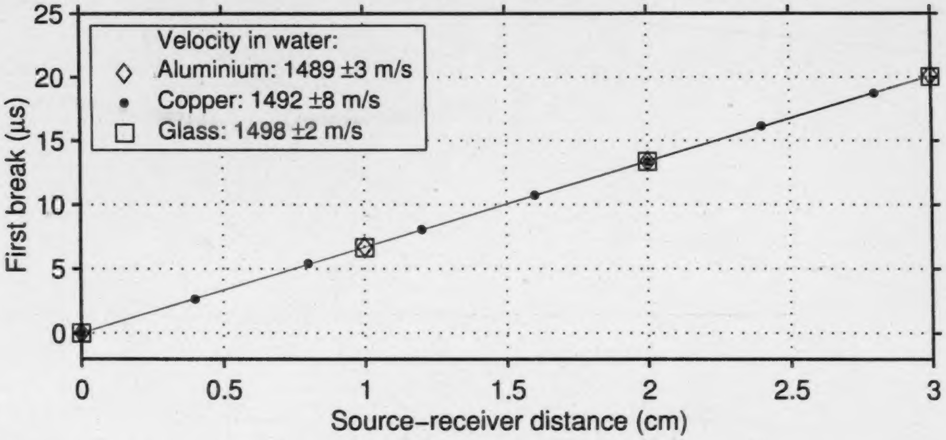

Figure 3.13: Water velocities during the experiments on the aluminium alloy, copper alloy, and glass blocks of figure 3.12. The source-receiver distance is normalized with respect to the first offset.

by ultrasonic transmission through the fluid at various distances. The results are summarized in figure 3.13 where the error in the velocity is calculated by taking twice the standard deviation of the time picks at various offsets. The density of water was directly measured with a densitometer during each and was found to vary very little and assumed to be 995±1 kg/m^3 for all the forthcoming experiments. It is also worthwhile to mention that the water used is distilled water but its purity may not have been kept high due to the filtration system used that could have added some gas. To keep this problem to the minimum the water was regularly replaced. The compressional V_p and shear V_s velocities are measured using the multiple reverberations by fitting a line through the maximum energy. This is only done when the wavelet does not show large distortions within the multiples else the first break is used. The errors are taken to be twice the standard deviation or one time sample and 0.25 mm in the thickness measurements of the samples. The measured properties of the fluid and the solids are listed in table 3.1 and are in agreement with published values (Gray, 1963).

From the measured properties of table 3.1 other useful parameters can be calculated. The elastic properties of the materials, the Rayleigh wave velocity, and the critical angles are calculated and are listed in table 3.2. The bulk modulus K and

Material	V_p m/s	V_s m/s	ρ kg/m^3	ρ_w kg/m^3	V_w m/s
Glass	5787 ± 10	3455 ± 2	2492 ± 15	995 ± 1	1498 ± 2
Copper	4789 ± 14	2300 ± 9	8901 ± 60	995 ± 1	1493 ± 7
Aluminium	6442 ± 30	3134 ± 2	2699 ± 20	995 ± 1	1489 ± 3

Table 3.1: Properties of the materials used in the reflectivity experiments where V_p is the P-wave velocity, V_s the S-wave velocity, ρ the density of the solid material. The density ρ_w and the velocity V_w of water are given in the last two columns as measured during each experiment with a densitometer and wave propagation in the water respectively. Because of the change in conditions for each experiment the velocity of water in the tank has slightly changed from one experiment to the other.

Material	θ_p^c ^{o}	θ_s^c ^{o}	θ_R ^{o}	V_R m/s
Glass	15.00 ± 0.05	25.69 ± 0.05	28.29 ± 0.06	3161 ± 2
Copper	18.17 ± 0.14	40.48 ± 0.42	43.96 ± 0.47	2151 ± 8
Aluminium	13.36 ± 0.09	28.37 ± 0.08	30.57 ± 0.10	2928 ± 3

Table 3.2: The P-wave critical angle θ_P^c, the S-critical angle θ_S^c, the Rayleigh angle, and the Rayleigh wave velocity calculated from the properties of the materials listed in table 3.1.

the shear modulus μ are given respectively by

$$K = \rho\left(V_p^2 - \frac{4}{3}V_s^2\right) \tag{3.2}$$

$$\mu = \rho V_s^2 \tag{3.3}$$

The Young's modulus is given by

$$E = \frac{9K\mu}{3K + \mu} \tag{3.4}$$

and the Poisson's ratio by

$$\nu = \frac{3K - 2\mu}{6K + 2\mu} \tag{3.5}$$

Material	K GPa	μ GPa	E GPa	ν -	K_w GPa
Glass	43.8 ± 1.4	29.7 ± 0.2	72.8 ± 0.8	0.22 ± 0.01	2.2 ± 0.1
Copper	141.4 ± 4.4	47.1 ± 0.7	127.1 ± 2.1	0.35 ± 0.01	2.2 ± 0.1
Aluminium	76.7 ± 2.5	26.5 ± 0.2	71.3 ± 0.8	0.34 ± 0.01	2.2 ± 0.1

Table 3.3: Parameters calculated using the properties of the materials listed in table 3.1. K, μ, E, and σ are the bulk modulus, the shear modulus, Young's modulus, and Poisson's ratio respectively. K_w is the bulk modulus of the water.

These material properties are calculated in the present experiments for the glass, copper, and aluminium. The results are listed in table 3.3. The P and S wave critical angles are given by

$$\theta_p^c = \sin^{-1}\left(\frac{V_w}{V_p}\right) \tag{3.6}$$

$$\theta_s^c = \sin^{-1}\left(\frac{V_w}{V_s}\right) \tag{3.7}$$

The Rayleigh wave velocity corresponds to a surface wave that can propagate at the surface of the solid in the absence of the fluid. If the P and S wave velocities are known the Rayleigh wave velocity can be calculated (Ewing et al., 1957)

$$\frac{c^6}{V_s^6} - 8\frac{c^4}{V_s^4} + c^2\left(\frac{24}{V_s^2} - \frac{16}{V_p^2}\right) - 16\left(1 - \frac{V_s^2}{V_p^2}\right) = 0 \tag{3.8}$$

This equation, where the unknown velocity is c, admits always a real positive solution less than V_s. This solution is the Rayleigh wave velocity V_R. Note that here the Rayleigh wave solution is completely independent of the fluid. Thus if a surface wave propagates along the interface with the Rayleigh wave velocity it must ignore the presence of the fluid. The Stoneley wave potentially could be present, but its velocity is nearly the same as water and is not detected in this experiment. Indeed in the fluid-solid boundary value problem discussed in chapter 2 surface waves exist only after the P-wave critical angle of incidence. There exists an angle at which the apparent horizontal wave velocity of the reflected wave into the fluid equals that of the Rayleigh wave velocity. This angle that is commonly called the Rayleigh angle is given simply by

$$\theta_R = \sin^{-1}\left(\frac{V_w}{V_R}\right) \tag{3.9}$$

Now compare the S-wave critical angle of incidence and the Rayleigh angle. We know that $\frac{V_w}{V_R} > \frac{V_w}{V_s}$ since $V_R < V_s$ and therefore $\sin\theta_s^c < \sin\theta_R$. This shows that the Rayleigh angle θ_R is always greater than the S-wave critical angle of incidence θ_s^c. In the present experimental work the calculated Rayleigh wave velocities and angles for the three cases studied here are given in table 3.2.

Recall the equation describing the reflected bounded acoustic pulse from a fluid solid boundary. This equation is:

$$\phi(x,z,t) = \frac{1}{4\pi^2}\int_{-\infty}^{+\infty}\int_{-\infty}^{+\infty} R(k_x)\Phi(k_x,0,\omega)e^{i[k_x x+k_z(2h+|z|)+\omega t]}dk_x d\omega \tag{3.10}$$

Here $\Phi(k_x,0,\omega)$ is the two dimensional Fourier transform in the $\hat{x}$ direction and time t of the wave field at $z=0$. $R(k_x)$ is the complex reflection coefficient at the boundary between the fluid and the solid. k_z is dependent on k_x and is given by $k_z = (k^2 - k_x^2)^{\frac{1}{2}}$. h is the distance between the plane $z = 0$ and the interface. Using the properties given in table 3.1 we can calculate the reflection coefficient at the boundary for any angle of incidence. Using equation 3.10 we can calculate the wave field at the plane of the receiver and thus model the reflectivity from the boundary. These calculated results are given in figures 3.14, 3.15, and 3.16 for glass, copper alloy, and aluminium alloy respectively. Three normalized curves are shown in each of these figures: the experimental measurements, the plane wave solution (i.e. Zoeppritz's equations), and the bounded acoustic pulse model. Note that the bounded acoustic pulse observed and modelled reflectivities are determined by normalizing the reflected amplitude by that for the pulse directly transmitted without reflection but with the same travel distance. The peak amplitude envelope value was employed.

The experimental results are in excellent agreement with the bounded acoustic pulse model even down to the fine details of various extremes at angles post θ_R. The standard deviation of the difference between the experimental measurements and the calculated model for each case are, 1.1 % for the glass, 3.4 % for the copper, and 1 % for the aluminium. The copper standard deviation is larger in part because of the deviation the experimental and model result at θ_s^c. These deviations are quite

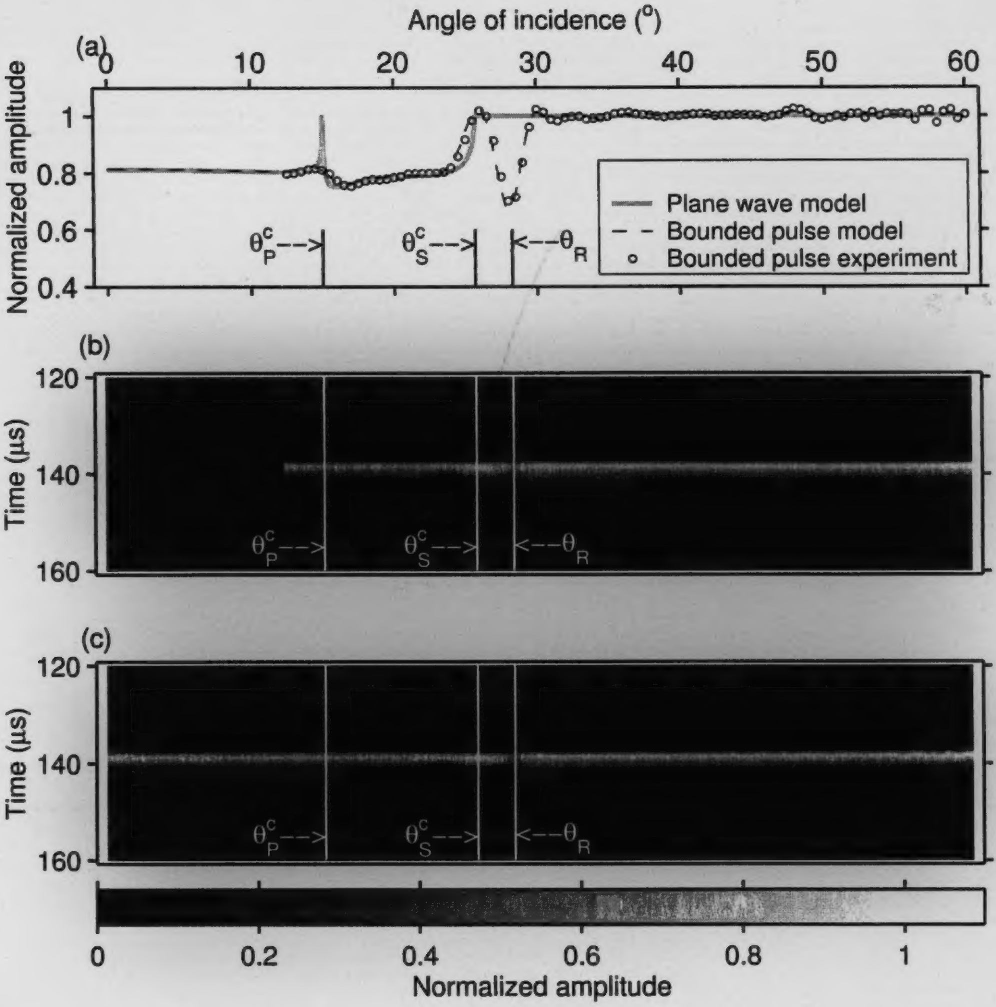

Figure 3.14: The reflectivity from a water-glass interface. Material properties are listed in table 3.1. a) Three normalized curves are shown, the experimental bounded acoustic pulse measurements, the plane wave solution, and the bounded acoustic pulse model. b) and c) are the amplitude envelope of: b) Bounded pulse experiment, c) Bounded pulse model.

small as most of the discrepancies occur beyond the S-critical angle of incidence. The plane wave solutions (Zoeppritz's equations) are in good agreement except near the critical angles θ_p^c, θ_s^c, and θ_R. Further, the plane wave theory cannot account for the oscillatory behaviour of the reflectivity at post θ_R angle of incidence. It

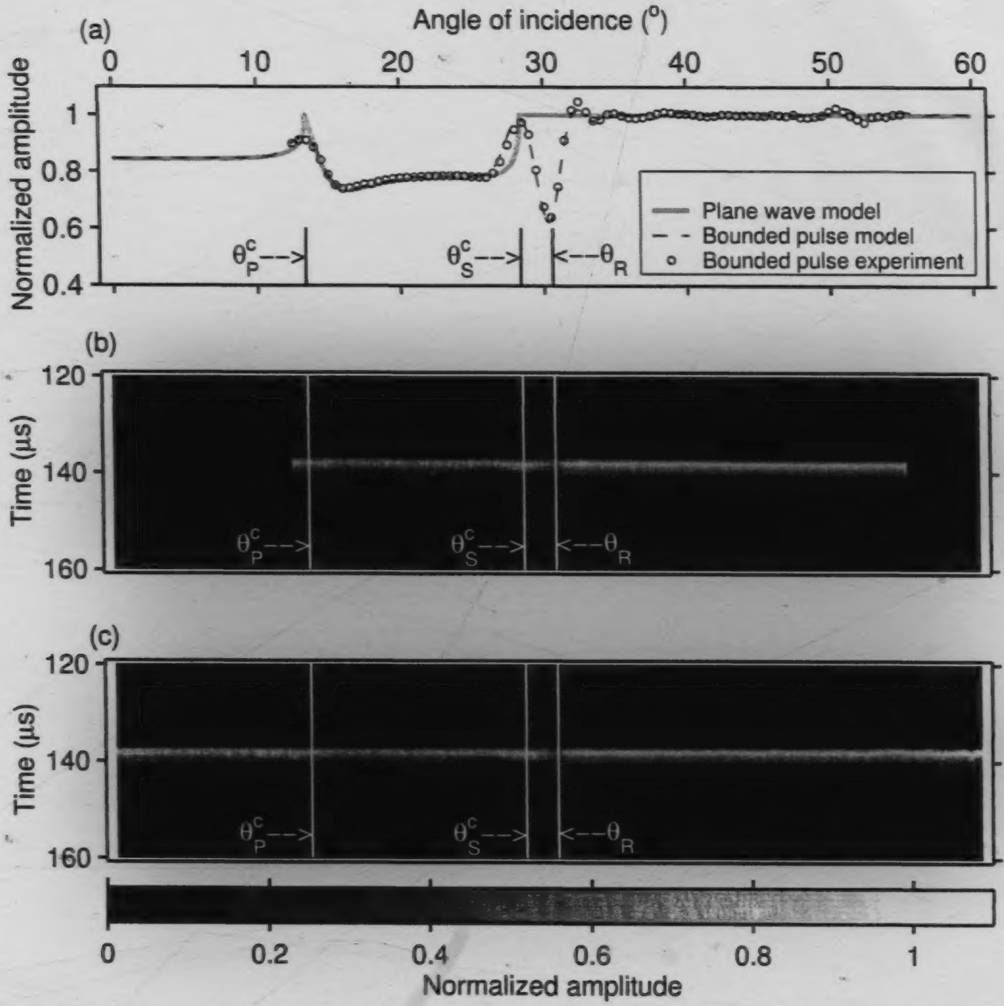

Figure 3.15: The reflectivity from a water-aluminium interface. Material properties are listed in table 3.1. a) Three normalized curves are shown, the experimental measurements, the plane wave solution, and the bounded acoustic pulse model. b) and c) are the amplitude envelope of: b) Bounded pulse experiment, c) Bounded pulse model.

is further worth noting that this oscillatory behaviour was thought to initially be representative of noise in the experiment. The later modelling, however, shows this "bumpy" character to be a real physical effect inherent to such type of measurement. At the Rayleigh angle the plane wave solution does not show any abrupt drop in

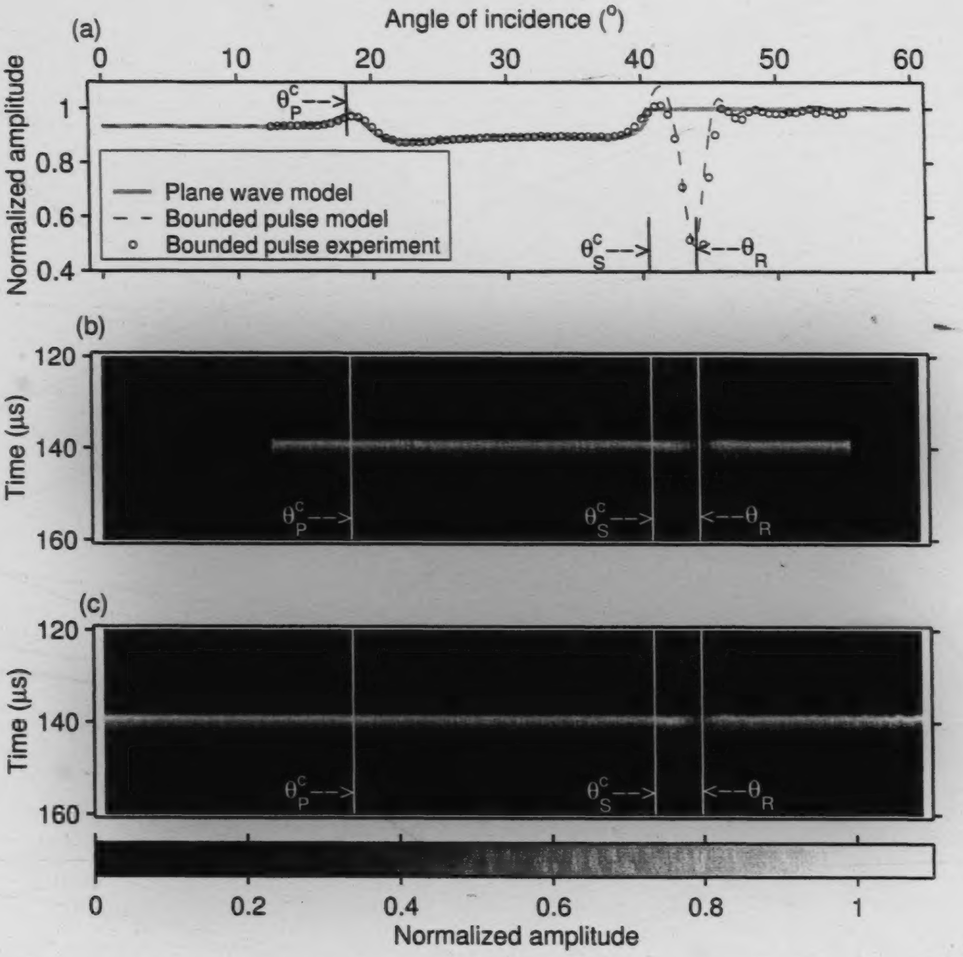

Figure 3.16: The reflectivity from a water-copper interface. Material properties are listed in table 3.1. a) Three normalized curves are shown, the experimental bounded acoustic pulse measurements, the plane wave solution, and the bounded acoustic pulse model. b) and c) are the amplitude envelope of: b) Bounded pulse experiment, c) Bounded pulse model.

amplitude.

Near θ_P^c and θ_S^c angles the measured and calculated reflection coefficients are smoothed because the bounded acoustic pulse contains a variety of wave numbers as explained in chapter 2. Thus there is a good agreement between the experiment and the calculated reflectivity via modelling with a bounded acoustic pulse and via Zoeppritz's equations except at the P critical angle, the S critical angle, and the Rayleigh angle. In figures 3.14, 3.15, and 3.16 are also shown another view of these amplitude results. The panels b) and c) of these figures display the maximum amplitude envelope calculated via the Hilbert transform. The models and the experiments are in excellent agreement. The direct arrivals at large angles of incidence in the experiments (Fig. 3.17) interfere with the reflected signal of interest and increase the standard deviation calculated above and limit, as mentioned earlier, the maximum angle to about 60^o.

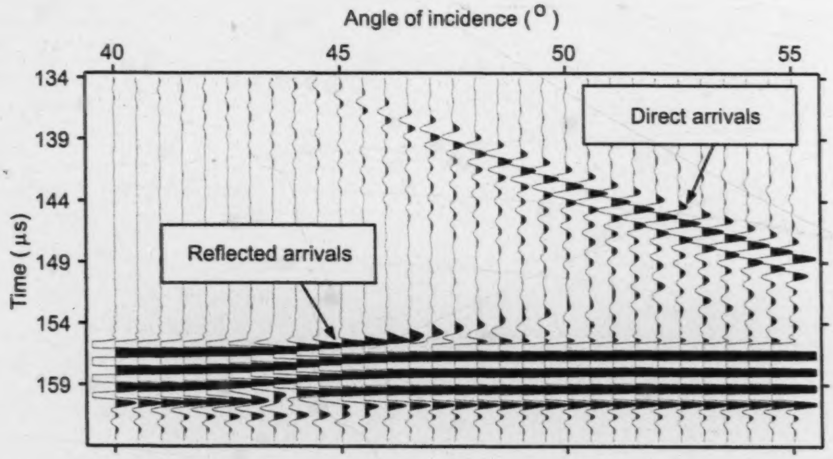

Figure 3.17: The direct arrivals in the water-copper reflectivity experiment at large angles of incidence. Their intensity increases with angle of incidence. The data is amplified and the reflected arrivals are clipped to better show the direct arrivals.

The analysis to present has focussed on amplitudes but the phase shifts upon reflection also contain information as noted in chapter 2. Consequently, we take a close look at the wave form at the Rayleigh angle. The experimental and modelled traces are compared in the first two panels in figures 3.18, 3.19, and 3.20. As the angle of incidence approaches the Rayleigh angle the recorded and modelled signal experiences an evident phase shift. The character of the wavelet changes as it is flipped and distorted. The signal seems to be arriving a little earlier as the trailing lobes suggest. The phase distortion is confirmed in the plotted phase shifts as a function of angle of incidence shown in the third panel of these figures for each

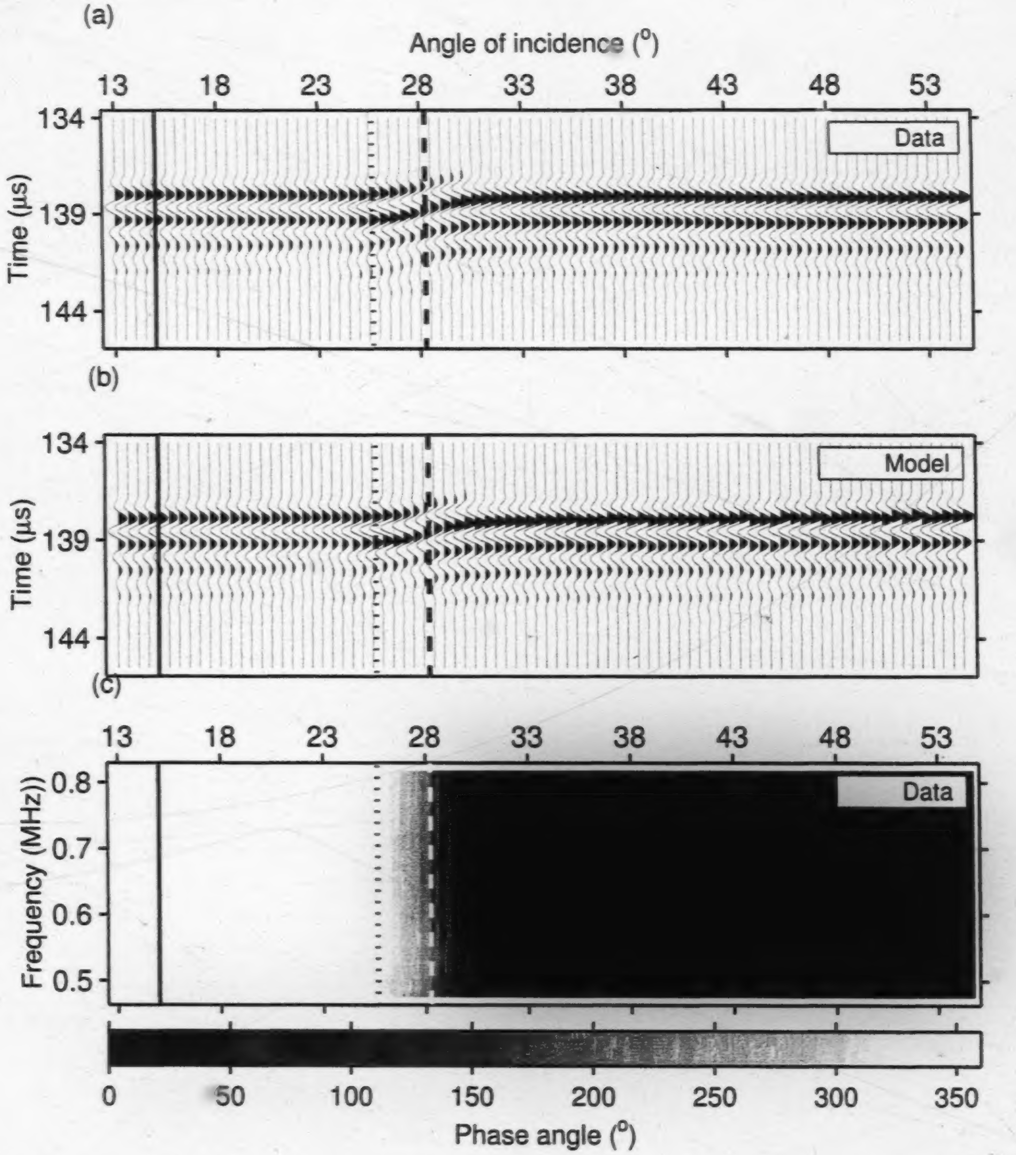

Figure 3.18: Water-glass reflectivity experiment. (a) The recorded and (b) the modelled traces around the Rayleigh angle of incidence. c) The unwrapped phase difference between the direct arrival and each recorded reflected trace. The solid, the dotted, and the dashed vertical lines show the P-critical, S-critical, and Rayleigh angles of incidence respectively.

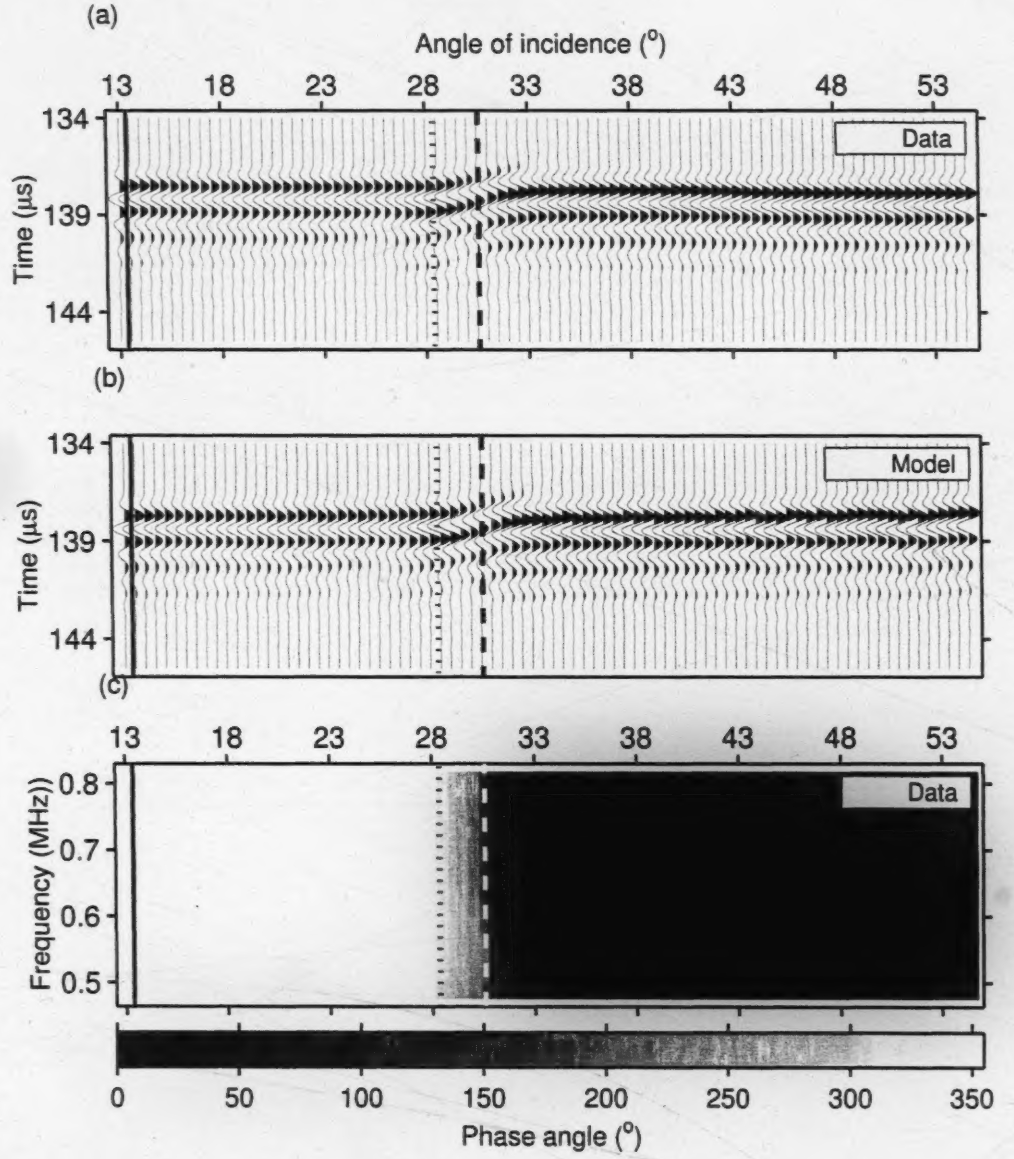

Figure 3.19: Water-aluminium reflectivity experiment. (a) The recorded and (b) the modelled traces around the Rayleigh angle of incidence. c) The unwrapped phase difference between the direct arrival and each recorded reflected trace. The solid, the dotted, and the dashed vertical lines show the P-critical, S-critical, and Rayleigh angles of incidence respectively.

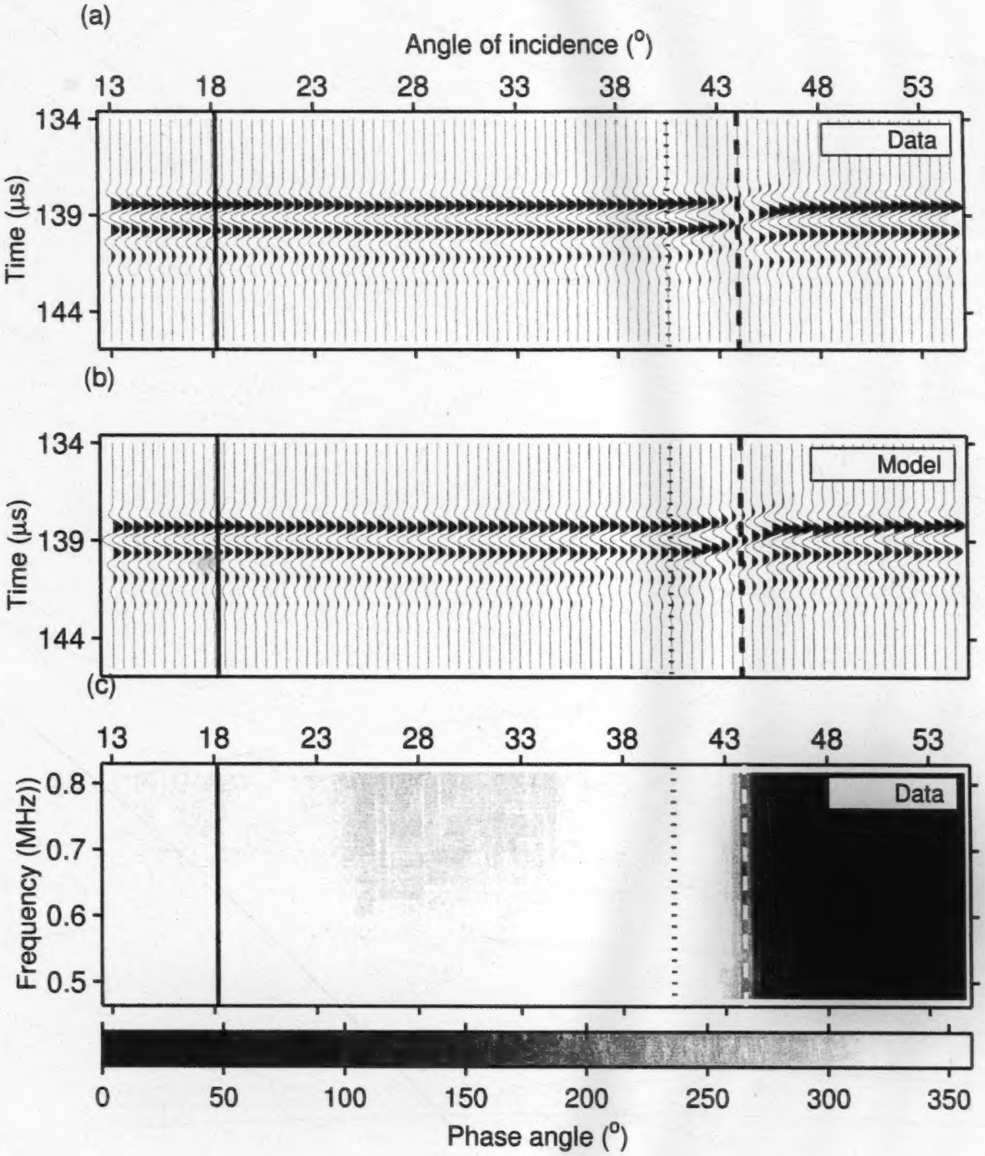

Figure 3.20: Water-copper reflectivity experiment. (a) The recorded and (b) the modelled traces around the Rayleigh angle of incidence. c) The unwrapped phase difference between the direct arrival and each recorded reflected trace. The solid, the dotted, and the dashed vertical lines show the P-critical, S-critical, and Rayleigh angles of incidence respectively.

experiment. There is a great similarity between the model and the experiment. The signal experiences a large phase distortion upon reflection near the Rayleigh angle of incidence θ_R. Near this angle the phase of the reflection coefficient changes by nearly 2π.

3.4.1 Material property measurements

The purpose of reflectivity measurements is to obtain some information on the elastic properties of the medium under study. Here a variety of elastic properties are inferred from the observed reflectivity curves and compared to more direct observations obtained in pulse transmission experiments. In the previous chapter, and as reported by earlier workers (Schoch, 1950; Brekhovskikh, 1960), the angle at which the greatest shift occurs, and as indicated by the minimum in the reflected amplitude, at an angle of incidence with the horizontal slowness equal to that of the Rayleigh wave. It wasalso experimentally observed by later workers (Diachok and Mayer, 1970; Neubauer and Dragonette, 1974; Breazeale et al., 1977). It is worthwhile noting that this effect was first observed in optics (Goos and Hänchen, 1947). While we may not yet fully comprehend why this should be, it is useful to test the idea.

First we calculate the Rayleigh wave velocity from the measurement of θ_R. It is worthwhile noting that both the compressional and shear wave velocities are required to calculate the Rayleigh wave velocity through equation 3.8. Then the angle can be calculated via equation 3.9. The Rayleigh angles θ_R measured from the observations and the Rayleigh wave velocity V_R inferred via equation 3.9 are summarized in table 3.4. These results are compared to those calculated via equation 3.8 and equation 3.9 for the three experiments, glass, copper, and aluminium. These are in excellent agreement with each other as the discrepancies are very low.

It is possible to infer the S-wave velocity from the observed θ_R and the compressional wave velocity V_P. The P-wave velocity can be either measured in an independent experiment or if available using the P-critical angle of incidence from the reflectivity response (Table 3.5). Recall equation 2.168

$$\frac{16}{V_p^2}V_s^8 - 16\left(1 - \frac{V_R^2}{V_p^2}\right)V_s^6 + 24V_R^2V_s^4 - 8V_R^4V_s^2 + V_R^6 = 0 \qquad (3.11)$$

Material	Measured θ_R (^{o})	Inferred V_R (m/s)	Calculated V_R (m/s)
Glass	28.20 ± 0.1	3170 ± 15	3161 ± 2
Copper	44.03 ± 0.1	2148 ± 14	2151 ± 8
Aluminium	30.38 ± 0.1	2944 ± 15	2928 ± 3

Table 3.4: The Rayleigh angle θ_R measured from the reflectivity measurements and the inferred Rayleigh wave velocity V_R.

Material	Measured θ_p^c ^{o}	Inferred V_p m/s	Measered V_p m/s
Glass	14.4 ± 0.5	6024 ± 213	5787 ± 10
Copper	18.6 ± 0.25	4687 ± 83	4789 ± 14
Aluminium	13.2 ± 0.25	6502 ± 134	6442 ± 30

Table 3.5: The observed critical angle θ_p^c, and the inferred P-wave velocity V_P for the glass, aluminium, and copper.

where the unknown is the S-wave velocity V_s. An approximation can also be made to this equation and be used without the knowledge of the compressional wave velocity (Neubauer and Dragonette, 1974). It is more precise to use the full Rayleigh wave equation 3.8 and therefore it is adopted here. For a given V_P and a given V_R the solution V_s to this equation is non unique in the range $V_R < c < V_P$. But it is always possible to use the constraint that the S-critical angle of incidence is close to the Rayleigh angle and therefore choose the S-critical θ_s^c angle of incidence that is the closest to the Rayleigh angle θ_R. Using this fact we take the solution that gives the closest θ_s^c to θ_R. Using the observed θ_R, the velocity of water V_w, and an independent measurement of the compressional velocity V_P, the corresponding S-wave velocities V_s are inferred for the glass, copper, and aluminium. The results are summarized in table 3.6 and compared to the S-wave velocities measured via independent ultrasonic transmission experiments. The results are in excellent agreement with each other.

It is also possible to estimate the density of the solid material by using the re-

Material	Measured V_s m/s	Inferred V_s m/s
Glass	3455 ± 2	3467 ± 20
Copper	2300 ± 9	2297 ± 16
Aluminium	3134 ± 2	3153 ± 18

Table 3.6: The inferred S-wave velocities from the observed Rayleigh angles given in table 3.1. The measured V_s given here is measured independently via ultrasonic transmission.

flection coefficient and the results already established for the P-wave velocity and the S-wave velocity. Between the P and S critical angles of incidence the observed reflectivity using the bounded acoustic pulse is very close to that obtained from Zoeppritz's equation. Therefore the magnitude (or alternatively the phase) of the reflectivity in this zone can be used to invert for the density of the solid material. Between P and S critical angles of incidence the reflection coefficient given by equation 2.88 can be rewritten as

$$A = \frac{4[k_x^2 - k_p^2]^{\frac{1}{2}}[k_s^2 - k_x^2]^{\frac{1}{2}}k_x^2 - \rho k_s^4[k_x^2 - k_p^2]^{\frac{1}{2}}[k^2 - k_x^2]^{-\frac{1}{2}} - i(2k_x^2 - k_s^2)^2}{4[k_x^2 - k_p^2]^{\frac{1}{2}}[k_s^2 - k_x^2]^{\frac{1}{2}}k_x^2 + \rho k_s^4[k_x^2 - k_p^2]^{\frac{1}{2}}[k^2 - k_x^2]^{-\frac{1}{2}} - i(2k_x^2 - k_s^2)^2} \tag{3.12}$$

The absolute value of the reflection coefficient given above can be used to solve for the density ρ that is the ratio between the density of the water and that of the solid. This equation then can be rearranged and a fourth degree polynomial in ρ can be derived which can be solved numerically. The solution is non unique. A unique solution can be found by restricting the density to be greater than that of water. The results are summarized in table 3.7. The errors in the measured densities are calculated based upon the reading error on the scale used for weighing and measuring the volume of the samples. The error is taken to be 1 g for the weight reading and 0.25 mm in the length measurements. For the inferred densities the errors are based on one standard deviation from the mean density calculated from the value of the reflection coefficient in the range of angles between the P and S critical angles. The range is 6^o centred between the P and S critical angles of incidence. The inferred densities are close to those measured directly through weighing. The errors are in the same range for both the measured and the inferred densities. The precision on the inferred densities depends on the noise present in the observed data. The glass sample shows larger errors in the inferred density as the reflection coefficient curve for this sample is noisier than the copper and aluminium samples.

Material	Measured ρ_s	$\Delta\rho_s$	Inferred ρ_s	$\Delta\rho_s$
	kg/m^3	%	kg/m^3	%
Glass	2492 ± 15	0.6	2495 ± 80	3.2
Copper	8901 ± 60	0.7	8870 ± 90	1.0
Aluminium	2699 ± 20	0.7	2715 ± 45	1.7

Table 3.7: Inferred and measured densities ρ_s of the glass, copper, and aluminium from the reflectivity of the bounded acoustic pulse in the range of angles were the reflectivity response is very close to that of the plane wave solution derived from Zoeppritz's equations. $\Delta\rho_s$ gives the % error.

The inferred S-wave velocities calculated from the observed Rayleigh angle, water velocity, and compressional velocities are in excellent agreement with the independently measured S-wave velocities via ultrasonic pulse transmission. It is worthwhile noting that the measurement of the Rayleigh angle can be achieved without searching for an absolute minimum reflectivity. Neubauer et al. (1974) have used a different technique to search for the minimum reflectivity such as a null strip that would appear in a reflected beam. In general the reflected bounded acoustic pulse can have more than one very local minimum as shown in chapter 2. The search for the absolute minimum can be experimentally complicated and is not required to find the Rayleigh angle. Indeed in the present experiments the position of the source and the receiver are kept at equal angles of incidence and emergence respectively. No search for the minimum reflectivity was performed. The results given here for the material properties are in excellent agreement with those measured directly by ultrasonic pulse transmission.

3.4.2 Summary of the results

The reflectivity of a bounded acoustic pulse from a water-solid boundary can be used to derive the physical and acoustic properties of solid materials. The reflectivity response of a bounded acoustic pulse from a water-solid boundary exhibits a large amplitude drop at the Rayleigh angle near the S-critical angle of incidence. The sharp changes in the reflectivity curves calculated from the plane wave solution derived from Zoeppritz's equations are smoothed out. The Rayleigh angle, the P-critical angle of incidence (or an independent measurement of the compressional wave velocity), and the absolute value of the reflection coefficient from a water-solid boundary are used to infer the physical and acoustic properties of the three solids. Direct measurement of the density and velocity of sound of the water are required. The results are summarized in table 3.8. These inferred properties are in excellent agreement with the direct measurement of these properties via ultrasonic pulse transmission through the solids.

Material	θ_R ^{o}	V_p m/s	V_s m/s	ρ_s kg/m^3
Glass	28.2 ± 0.1	5787 ± 10	3467 ± 20	2495 ± 80
Copper	44.0 ± 0.1	4789 ± 14	2297 ± 16	8870 ± 90
Aluminium	30.4 ± 0.1	6442 30	3153 ± 18	2715 ± 45

Table 3.8: Summary of the inferred materials properties from the reflectivity response of a bounded acoustic pulse from a water-solid boundary. The experiments were conducted on a glass, copper, and aluminium blocks immersed in water. The observed critical angle θ_p^c, Rayleigh angle θ_R, and reflectivity response were used to infer the compressional wave velocity V_P, the S-wave velocity V_s, and the density ρ_s of the solid materials.

3.5 Conclusions

Reflectivity experiments were successfully carried out on three solid materials with a range of elastic physical properties. The laboratory method uses an acoustic source constructed from a large piezo-electric plate and a near-point piezo-electric receiver. The wave field generated by the source is a bounded acoustic pulse limited in time and space. It exhibits a narrow range of propagation angles around the principle angle of propagation. As confirmed in the laboratory, the amplitude near the axis of propagation remains nearly constant as far as 30 cm away from the source. Therefore, the signal of interest near the centre of the bounded acoustic pulse is much stronger than any other event that could be scattered by the apparatus. The use of a point receiver minimizes the wave field smoothing a larger receiver induces. The use of this source-receiver configuration permits investigation of materials in a small confined volume, this is important in many laboratory based experiments.

The characterization of the source and receiver was performed using a scanner in a water filled tank. Measurements confirmed the expected predictions by the theory using an exact solution for the forward modelling of a bounded acoustic pulse based on the Fourier integral pair. It was possible to invert for the material properties using the measured fluid velocity and the observed reflectivity.

The observed reflectivity from three solids was compared to that calculated for a bounded acoustic pulse and to that anticipated by Zoeppritz's equations (plane wave solution). The reflectivity measurements were in excellent agreement with the more realistic bounded acoustic pulse models. Consequently, the measurements here both confirm the theoretical developments and act in calibration of the experimental methodology, a result with important consequences for the later tests on fluid-saturated porous media.

Chapter 4

Plane waves and bounded acoustic pulses in fluid-saturated porous media

4.1 Introduction

The ultimate goal of this study is to make the first experimental reflectivity measurement from fluid-saturated porous materials. Plane waves, bounded acoustic beams, and bounded acoustic pulses were already studied both theoretically and experimentally in great detail in chapters 2 and 3 for elastic and isotropic materials. Here a similar procedure will be followed for fluid-saturated porous materials. Bounded acoustic beams will not be studied in detail as it is found in chapter 2 that bounded acoustic pulses are more suitable for experimental laboratory work. In order to properly model bounded acoustic pulses in fluid-saturated porous materials a theoretical study of plane waves in such materials will first be reviewed. This will be followed by analysis of bounded acoustic pulses and modelling examples. Both wave propagation in fluid-saturated porous materials and in the next chapter reflectivity from a boundary between a fluid and fluid-saturated porous material will be considered.

One main objective of the present study is the analysis of experimental reflectivity from a boundary of water and a water-saturated porous synthetic rock. It is essential to compare a model that would explain the laboratory observations. Since the early work of Biot (1956a; 1956b) many workers have developed similar theories adapted to particular situations for materials with various pore-geometries (Dvorkin and Nur, 2000a; Dvorkin and Nur, 2000b; Dvorkin et al., 2000). de la Cruz/Spanos (1985; 1989b) have developed an alternative theory based on a different physical background. For the present work these two theories were both found to be sufficient to explain the forthcoming experimental observations.

Fluid-saturated porous materials are two phase-materials composed of a porous solid skeleton and a fluid saturant. The fluid saturant can move within the pores of the solid skeleton as a wave propagates through. To avoid confusion, here the solid skeleton is referred to as the "frame" and to the mineral grains as the solid material. First a review of wave propagation in porous materials will be given following the early work of Biot (1956a; 1956b) and a relatively recent work of de la Cruz/Spanos (1985; 1989b). These theories will be treated using complex scalar and vector potentials and make use of the complex constant that relates the potentials in the solid skeleton and in the fluid for a given wave type. This differs from earlier treatments and allows the mathematics involved to be significantly simplified in the description of the theories, particularly the reflection-transmission at a boundary between water and a water-saturated porous medium. Both propagation and reflection-transmission will be illustrated by examples. Further, a more direct way to provide a set of easily measurable properties allows us to avoid determination of some of the more poorly physically constrained parameters necessary in the original presentation of Biot. These theories will be compared within the framework of this particular experimental study.

4.2 Biot theory

The original derivations of Biot are summarized in appendix B. Scalar and vector potentials are instead employed here as these will simplify the equations of motion. It is convenient to use Helmhotz decomposition and express the displacement vector $\vec{u}$ in terms of the scalar potential ϕ and the vector potential $\vec{\psi}$. For the solid and the fluid components the displacements can be written as

$$\vec{u}^{(s)} = \vec{\nabla}\phi^{(s)} + \vec{\nabla} \times \vec{\psi}^{(s)} \tag{4.1}$$

$$\vec{u}^{(f)} = \vec{\nabla}\phi^{(f)} + \vec{\nabla} \times \vec{\psi}^{(f)} \tag{4.2}$$

where the superscripts ${}^{(s)}$ and ${}^{(f)}$ denote the solid and the fluid respectively. Recall the coupled equations of motion B.32 and B.33 derived in appendix B

$$\begin{aligned}(1-\beta)\rho^{(s)}\frac{\partial^2}{\partial t^2}\vec{u}^{(s)} - \rho_{12}\frac{\partial^2}{\partial t^2}\left(\vec{u}^{(s)}-\vec{u}^{(f)}\right) + F(\omega)\frac{\eta\beta^2}{K}\frac{\partial}{\partial t}\left(\vec{u}^{(s)}-\vec{u}^{(f)}\right) = \\ \mu_M\nabla^2\vec{u}^{(s)} + (A+\mu_M)\vec{\nabla}\left(\vec{\nabla}\cdot\vec{u}^{(s)}\right) + Q\vec{\nabla}\left(\vec{\nabla}\cdot\vec{u}^{(f)}\right)\end{aligned} \tag{4.3}$$

$$\begin{aligned}\beta\rho^{(f)}\frac{\partial^2}{\partial t^2}\vec{u}^{(f)} + \rho_{12}\frac{\partial^2}{\partial t^2}\left(\vec{u}^{(s)}-\vec{u}^{(f)}\right) - F(\omega)\frac{\eta\beta^2}{K}\frac{\partial}{\partial t}\left(\vec{u}^{(s)}-\vec{u}^{(f)}\right) = \\ Q\vec{\nabla}\left(\vec{\nabla}\cdot\vec{u}^{(s)}\right) + R\vec{\nabla}\left(\vec{\nabla}\cdot\vec{u}^{(f)}\right)\end{aligned} \tag{4.4}$$

where β is the porosity, η the shear viscosity, K the permeability, $\rho^{(s)}$ the density of the solid (mineral grains), $\rho^{(f)}$ the density of the fluid, ρ_{12} is the coupling mass density due to relative motion of the fluid with respect to the solid, μ_M the shear modulus of the solid skeleton (frame), and finally A, Q, and R are the so called Biot parameters. These parameters will be studied in detail later.

4.2.1 Propagation of dilatational waves

To allow only dilatational waves to propagate apply the divergence operator to equations 4.3 and 4.4 and use equation 4.1 and 4.2

$$\begin{aligned}(1-\beta)\rho^{(s)}\frac{\partial^2}{\partial t^2}\phi^{(s)} - \rho_{12}\frac{\partial^2}{\partial t^2}\left(\phi^{(s)}-\phi^{(f)}\right) + F(\omega)\frac{\eta\beta^2}{K}\frac{\partial}{\partial t}\left(\phi^{(s)}-\phi^{(f)}\right) &= \\ \nabla^2\left[(A+2\mu_M)\,\phi^{(s)} + Q\phi^{(f)}\right]\end{aligned} \tag{4.5}$$

and

$$\begin{aligned}\beta\rho^{(f)}\frac{\partial^2}{\partial t^2}\phi^{(f)} + \rho_{12}\frac{\partial^2}{\partial t^2}\left(\phi^{(s)}-\phi^{(f)}\right) - F(\omega)\frac{\eta\beta^2}{K}\frac{\partial}{\partial t}\left(\phi^{(s)}-\phi^{(f)}\right) &= \\ \nabla^2\left[Q\phi^{(s)} + R\phi^{(f)}\right]\end{aligned} \tag{4.6}$$

which are the coupled equations for the propagation of dilatational waves. Now consider plane wave solutions of the form

$$\phi^{(s)} = D^{(s)}e^{i\left(\omega t-\vec{k}\cdot\vec{x}\right)} \tag{4.7}$$

$$\phi^{(f)} = D^{(f)}e^{i\left(\omega t-\vec{k}\cdot\vec{x}\right)} \tag{4.8}$$

where $D^{(s)}$ and $D^{(f)}$ are the complex amplitudes of the wave potential in the solid and the fluid respectively. These complex amplitudes contain both the amplitude and relative phase information of the solid component with respect to the fluid component. This information will be used in this study to clarify many aspects related to the behaviour of all wave modes that can propagation in fluid-saturated porous materials. $\vec{k}$ is the complex wave number, $\vec{x}$ is the position vector, ω is the radial frequency, and i is the square root of -1. The complex form of the potential is used for mathematical convenience only and the physical displacements are given by the real parts of equations 4.1 and 4.2. With these solutions equations 4.5 and 4.6 lead to

$$\begin{aligned}\left[k^2\left(A+2\mu_M\right)-\omega^2\left(1-\beta\right)\rho^{(s)}+\omega^2\rho_{12}+i\omega F(\omega)\frac{\eta\beta^2}{K}\right]\phi^{(s)}+&\\ \left[k^2Q-\omega^2\rho_{12}-i\omega F(\omega)\frac{\eta\beta^2}{K}\right]\phi^{(f)}&=0\end{aligned}\tag{4.9}$$

$$\begin{aligned}\left[k^2Q-\omega^2\rho_{12}-i\omega F(\omega)\frac{\eta\beta^2}{K}\right]\phi^{(s)}+&\\ \left[k^2R+\omega^2\rho_{12}-\omega^2\beta\rho^{(f)}+i\omega F(\omega)\frac{\eta\beta^2}{K}\right]\phi^{(f)}&=0\end{aligned}\tag{4.10}$$

For a given propagating wave the potential fields ϕ in the solid and in the fluid are related to each other by a complex number. This can be readily established by taking the ratio of the complex scalar potentials given in equations 4.7 and 4.8. This complex number is $\zeta=\frac{D^{(s)}}{D^{(f)}}$ then we can write

$$\phi^{(s)}=\zeta\phi^{(f)}\tag{4.11}$$

Equations 4.9 and 4.10 then lead to the second order equation

$$a\zeta^2+b\zeta+c=0\tag{4.12}$$

where a, b, and c are

$$\begin{aligned}a&=-\left(A+2\mu_M\right)\left(\omega\rho_{12}+iF(\omega)\frac{\eta\beta^2}{K}\right)+\\&\quad Q\left(\omega(1-\beta)\rho^{(s)}-\omega\rho_{12}-iF(\omega)\frac{\eta\beta^2}{K}\right)\end{aligned}\tag{4.13}$$

$$\begin{aligned}b&=\left(A+2\mu_M\right)\left(\omega\rho_{12}-\omega\beta\rho^{(f)}+iF(\omega)\frac{\eta\beta^2}{K}\right)+\\&\quad R\left(\omega(1-\beta)\rho^{(s)}-\omega\rho_{12}-iF(\omega)\frac{\eta\beta^2}{K}\right)\end{aligned}\tag{4.14}$$

$$c=Q\left(\omega\rho_{12}-\omega\beta\rho^{(f)}+iF(\omega)\frac{\eta\beta^2}{K}\right)+R\left(\omega\rho_{12}+iF(\omega)\frac{\eta\beta^2}{K}\right)\tag{4.15}$$

Equation 4.12 admits two solutions ζ_1 and ζ_2. Therefore two compressional waves can propagate in a fluid-saturated porous medium. The average displacement $\vec{u}$ can be written as (Deresiewicz and Skalak, 1963)

$$\vec{u} = \beta\vec{u}^{(f)} + (1-\beta)\vec{u}^{(s)} \tag{4.16}$$

which is also valid for the scalar potential ϕ ($\vec{u} = \vec{\nabla}\phi$ for a P-wave). The average potential of the aggregate is then given by

$$\phi = (1-\beta)\phi^{(s)} + \beta\phi^{(f)} = \left[\zeta_l(1-\beta) + \beta\right]\phi^{(f)} \tag{4.17}$$

For each of the solutions ζ_1 and ζ_2 equations 4.9 and 4.10 can be combined to lead

$$\left[\zeta_l(1-\beta)\rho^{(s)} + \beta\rho^{(f)}\right]\frac{\partial^2\phi^{(f)}}{\partial t^2} = \left[\zeta_l(A + 2\mu_M + Q) + R + Q\right]\nabla^2\phi^{(f)} \tag{4.18}$$

where $l = 1, 2$ for the two solutions. Note that $\phi^{(s)}$ and ϕ satisfy also equation 4.18. Using a plane wave solution for the potential field ϕ in equation 4.18 the dispersion relation leads to

$$k_l = \omega\left[\frac{\zeta_l(1-\beta)\rho^{(s)} + \beta\rho^{(f)}}{\zeta_l(A + 2\mu_M + Q) + R + Q}\right]^{\frac{1}{2}} \tag{4.19}$$

Letting $k_l = k_{rl} - ik_{il}$ then the real and imaginary parts of k_l provide the phase velocity and attenuation of each wave type respectively. These two solutions are those of two dilatational waves, commonly known as the fast dilatational wave and the slow dilatational wave. Equation 4.18 can then be written for plane P-waves as

$$\nabla^2\phi^{(f)} + k_l^2\frac{\partial^2\phi^{(f)}}{\partial t^2} = 0 \tag{4.20}$$

which is the wave equation for compressional waves, the fast ($l = 1$) and the slow P-wave ($l = 2$), in a fluid-saturated porous material.

4.2.2 Rotational waves

To allow only rotational waves to propagate apply the curl operator to equations 4.3 and 4.4 and use equation 4.1 and 4.2

$$(1-\beta)\rho^{(s)}\frac{\partial^2}{\partial t^2}\vec{\psi}^{(s)} - \rho_{12}\frac{\partial^2}{\partial t^2}\left(\vec{\psi}^{(s)} - \vec{\psi}^{(f)}\right) + F(\omega)\frac{\eta\beta^2}{K}\frac{\partial}{\partial t}\left(\vec{\psi}^{(s)} - \vec{\psi}^{(f)}\right) = \mu_M\nabla^2\vec{\psi}^{(s)} \tag{4.21}$$

$$\beta\rho^{(f)}\frac{\partial^2}{\partial t^2}\vec{\psi}^{(f)} + \rho_{12}\frac{\partial^2}{\partial t^2}\left(\vec{\psi}^{(s)} - \vec{\psi}^{(f)}\right) - F(\omega)\frac{\eta\beta^2}{K}\frac{\partial}{\partial t}\left(\vec{\psi}^{(s)} - \vec{\psi}^{(f)}\right) = 0 \tag{4.22}$$

Now consider solutions of the form

$$\vec{\psi}^{(s)} = \hat{x}_2 D^{(s)} e^{i\left(\omega t - \vec{k}\cdot\vec{x}\right)} \tag{4.23}$$

$$\vec{\psi}^{(f)} = \hat{x}_2 D^{(f)} e^{i\left(\omega t - \vec{k}\cdot\vec{x}\right)} \tag{4.24}$$

where $\vec{D}^{(s)} \cdot \vec{k} = 0$ and $\vec{D}^{(f)} \cdot \vec{k} = 0$. Using these solutions equations 4.21 and 4.22 lead to

$$\left[k^2\mu_M - (1-\beta)\,\rho^{(s)}\omega^2 + \rho_{12}\omega^2 + iF(\omega)\omega\frac{\eta\beta^2}{K}\right]\vec{\psi}^{(s)} - \left[\rho_{12}\omega^2 + iF(\omega)\omega\frac{\eta\beta^2}{K}\right]\vec{\psi}^{(f)} = 0 \tag{4.25}$$

$$\left[\rho_{12}\omega + iF(\omega)\frac{\eta\beta^2}{K}\right]\vec{\psi}^{(s)} + \left[\beta\rho^{(f)}\omega - \rho_{12}\omega - iF(\omega)\frac{\eta\beta^2}{K}\right]\vec{\psi}^{(f)} = 0 \tag{4.26}$$

For a given propagating wave the vector potential field $\vec{\psi}$ in the solid and fluid components are related to each other again here by a complex number. This complex number is $\zeta_3 = \frac{D^{(s)}}{D^{(f)}}$

$$\vec{\psi}^{(s)} = \zeta_3\vec{\psi}^{(f)} \tag{4.27}$$

Using equation 4.27 in equation 4.26 we get

$$\zeta_3 = -\frac{\beta\rho^{(f)}\omega - \rho_{12}\omega - iF(\omega)\frac{\eta\beta^2}{K}}{\rho_{12}\omega + iF(\omega)\frac{\eta\beta^2}{K}} \tag{4.28}$$

Therefore we have one solution, only one S-wave can propagate in a fluid-saturated porous material. Equations 4.21 and 4.22 can be combined to

$$\left[(1-\beta)\rho^{(s)}\zeta_3 + \beta\rho^{(f)}\right]\frac{\partial^2}{\partial t^2}\vec{\psi}^{(f)} = \mu_M\zeta_3\nabla^2\vec{\psi}^{(f)} \tag{4.29}$$

Using a plane wave solution for the vector potential field $\vec{\psi}$ the dispersion relation leads to the complex wave number given by

$$k_3 = \omega\left[\frac{(1-\beta)\rho^{(s)}\zeta_3 + \beta\rho^{(f)}}{\mu_M\zeta_3}\right]^{\frac{1}{2}} \tag{4.30}$$

Letting $k_3 = k_{r3} - ik_{i3}$ then the real and imaginary parts of k_3 provide the phase velocity and the attenuation of the S-wave. Equation 4.29 can be simply rewritten as

$$\nabla^2\vec{\psi}^{(f)} + k_3^2\frac{\partial^2}{\partial t^2}\vec{\psi}^{(f)} = 0 \tag{4.31}$$

which is the wave equation for the propagation of S-waves in a fluid-saturated porous material.

4.3 de la Cruz/Spanos theory

The original work of de la Cruz/Spanos is summarized in appendix C. Here this theory will be treated using scalar and vector potentials as for the Biot theory. Recall the coupled equations of motion derived in appendix C

$$\begin{aligned}(1-\beta)\rho^{(s)}\frac{\partial^2}{\partial t^2}\vec{u}^{(s)} - \rho_{12}\frac{\partial^2}{\partial t^2}\left(\vec{u}^{(s)}-\vec{u}^{(f)}\right) + \frac{\eta\beta^2}{K}\frac{\partial}{\partial t}\left(\vec{u}^{(s)}-\vec{u}^{(f)}\right) &= \\ \mu_M\nabla^2\vec{u}^{(s)} + \left[(1-\beta)\left[K^{(s)}+\frac{1}{3(1-\beta)}\mu_M\right]-\delta_s K^{(s)}\right]\vec\nabla\left(\vec\nabla\cdot\vec{u}^{(s)}\right) & \\ +\delta_f K^{(s)}\vec\nabla\left(\vec\nabla\cdot\vec{u}^{(f)}\right) & \qquad (4.32)\end{aligned}$$

$$\begin{aligned}\beta\rho^{(f)}\frac{\partial^2}{\partial t^2}\vec{u}^{(f)} + \rho_{12}\frac{\partial^2}{\partial t^2}\left(\vec{u}^{(s)}-\vec{u}^{(f)}\right) - \frac{\eta\beta^2}{K}\frac{\partial}{\partial t}\left(\vec{u}^{(s)}-\vec{u}^{(f)}\right) &= \\ K^{(f)}\delta_s\vec\nabla\left(\vec\nabla\cdot\vec{u}^{(s)}\right) + K^{(f)}\left(\beta-\delta_f\right)\vec\nabla\left(\vec\nabla\cdot\vec{u}^{(f)}\right) + & \\ \left\{(1-\beta)\eta\left[\frac{\mu_M}{(1-\beta)\mu^{(s)}}-1\right]\frac{\partial}{\partial t}\left[\nabla^2\vec{u}^{(s)}+\frac{1}{3}\vec\nabla\left(\vec\nabla\cdot\vec{u}^{(s)}\right)\right]\right\} + & \\ \left\{\beta\eta\frac{\partial}{\partial t}\left[\nabla^2\vec{u}^{(f)}+\frac{1}{3}\vec\nabla\left(\vec\nabla\cdot\vec{u}^{(f)}\right)\right]\right\} + & \\ \left\{\xi_f\frac{\partial}{\partial t}\left[\delta_s\vec\nabla\left(\vec\nabla\cdot\vec{u}^{(s)}\right)+\left(\beta-\delta_f\right)\vec\nabla\left(\vec\nabla\cdot\vec{u}^{(f)}\right)\right]\right\} & \qquad (4.33)\end{aligned}$$

where β is the porosity, η the shear viscosity, ξ_f the bulk viscosity, K the permeability, $K^{(f)}$ the bulk modulus of the fluid, $K^{(s)}$ the bulk modulus of the solid (mineral grains), $\mu^{(s)}$ the shear modulus of the solid (mineral grains), $\rho^{(s)}$ the density of the solid (mineral grains), $\rho^{(f)}$ the density of the fluid, ρ_{12} is the coupling mass density due to relative motion of the fluid with respect to the solid, μ_M the shear modulus of the solid skeleton (frame), and finally δ_s and δ_f are two parameters called by the authors the solid and the fluid dilation parameters. These parameters will be studied in detail later.

4.3.1 Propagation of dilatational waves

To allow only dilatational waves apply the divergence operator to equations 4.32 and 4.33 and use equation 4.1 and 4.2.

$$\begin{aligned}(1-\beta)\rho^{(s)}\frac{\partial^2}{\partial t^2}\phi^{(s)} - \rho_{12}\frac{\partial^2}{\partial t^2}\left(\phi^{(s)}-\phi^{(f)}\right) + F(\omega)\frac{\eta\beta^2}{K}\frac{\partial}{\partial t}\left(\phi^{(s)}-\phi^{(f)}\right) &= \\ \left[(1-\beta)K^{(s)}+\frac{4}{3}\mu_M-\delta_s K^{(s)}\right]\nabla^2\phi^{(s)}+\delta_f K^{(s)}\nabla^2\phi^{(f)} & \qquad (4.34)\end{aligned}$$

$$\begin{aligned}\beta\rho^{(f)}\frac{\partial^2}{\partial t^2}\phi^{(f)} + \rho_{12}\frac{\partial^2}{\partial t^2}\left(\phi^{(s)} - \phi^{(f)}\right) - F(\omega)\frac{\eta\beta^2}{K}\frac{\partial}{\partial t}\left(\phi^{(s)} - \phi^{(f)}\right) &= \\ K^{(f)}\delta_s\nabla^2\phi^{(s)} + K^{(f)}\left(\beta - \delta_f\right)\nabla^2\phi^{(f)} + \\ \frac{4}{3}\eta\left[\left(\frac{\mu_M}{\mu^{(s)}} + \beta - 1\right)\nabla^2\frac{\partial}{\partial t}\phi^{(s)} + \nabla^2\frac{\partial\phi^{(f)}}{\partial t}\right] + \\ \xi_f\left[\delta_s\nabla^2\frac{\partial\phi^{(s)}}{\partial t} + \left(\beta - \delta_f\right)\nabla^2\frac{\partial\phi^{(f)}}{\partial t}\right] \end{aligned} \tag{4.35}$$

which are the coupled equations for the propagation of dilatational waves in a fluid-saturated porous material. To treat this theory in the same frequency range as the Biot theory a viscosity correction factor $F(\omega)$ (see appendix B) is applied to the Darcy term (third term in both equations 4.34 and 4.35). Consider plane wave solutions of the form given in equations 4.7 and 4.8. Using these solutions in equations 4.34 and 4.35 we get

$$\begin{aligned}\left[k^2\left[(1-\beta-\delta_s)K^{(s)} + \tfrac{4}{3}\mu_M\right] - \omega^2\left(1-\beta\right)\rho^{(s)} + \omega^2\rho_{12} + i\omega F(\omega)\tfrac{\eta\beta^2}{K}\right]\phi^{(s)} + \\ \left[k^2\delta_f K^{(s)} - \omega^2\rho_{12} - i\omega F(\omega)\tfrac{\eta\beta^2}{K}\right]\phi^{(f)} = 0\end{aligned} \tag{4.36}$$

$$\begin{aligned}\left[k^2K^{(f)}\delta_s - \omega^2\rho_{12} - i\omega F(\omega)\tfrac{\eta\beta^2}{K}\right]\phi^{(s)} + \\ \left[k^2K^{(f)}\left(\beta-\delta_f\right) + \omega^2\rho_{12} - \omega^2\beta\rho^{(f)} + i\omega F(\omega)\tfrac{\eta\beta^2}{K}\right]\phi^{(f)} + \\ i\omega\left[k^2\tfrac{4}{3}\eta\left(\tfrac{\mu_M}{\mu^{(s)}} + \beta - 1\right) + \xi_f\delta_s k^2\right]\phi^{(s)} + i\omega\left[\tfrac{4}{3}\eta k^2 + k^2\xi_f\left(\beta-\delta_f\right)\right]\phi^{(f)} = 0\end{aligned} \tag{4.37}$$

Now using equation 4.11 in equations 4.36 and 4.37 to a second order equation is obtained

$$a\zeta^2 + b\zeta + c = 0 \tag{4.38}$$

where a, b, and c are

$$\begin{aligned} a \;=\; & \left[\omega\left(1-\beta\right)\rho^{(s)} - \omega\rho_{12} - iF(\omega)\frac{\eta\beta^2}{K}\right] \times \\ & \left[K^{(f)}\delta_s + i\omega\left[\frac{4}{3}\eta\left(\frac{\mu_M}{\mu^{(s)}} + \beta - 1\right) + \xi_f\delta_s\right]\right] - \\ & \left[\omega\rho_{12} + iF(\omega)\frac{\eta\beta^2}{K}\right]\left[(1-\beta-\delta_s)K^{(s)} + \frac{4}{3}\mu_M\right]\end{aligned} \tag{4.39}$$

$$\begin{aligned} b \;=\; & \left[\omega\rho_{12} + iF(\omega)\frac{\eta\beta^2}{K}\right]\left[K^{(f)}\delta_s + i\omega\frac{4}{3}\eta\left(\frac{\mu_M}{\mu^{(s)}} + \beta - 1\right) + i\omega\xi_f\delta_s\right] + \\ & \left[\omega\left(1-\beta\right)\rho^{(s)} - \omega\rho_{12} - iF(\omega)\frac{\eta\beta^2}{K}\right] \times \\ & \left[K^{(f)}\left(\beta-\delta_f\right) + i\omega\frac{4}{3}\eta + i\omega\xi_f\left(\beta-\delta_f\right)\right] - \left[\omega\rho_{12} + iF(\omega)\frac{\eta\beta^2}{K}\right]\delta_f K^{(s)} + \\ & \left[\omega\rho_{12} - \omega\beta\rho^{(f)} + iF(\omega)\frac{\eta\beta^2}{K}\right]\left[(1-\beta-\delta_s)K^{(s)} + \frac{4}{3}\mu_M\right] \end{aligned} \tag{4.40}$$

$$\begin{aligned} c \;=\; & \left[\omega\rho_{12} + iF(\omega)\frac{\eta\beta^2}{K}\right]\left[K^{(f)}\left(\beta-\delta_f\right) + i\omega\frac{4}{3}\eta + i\omega\xi_f\left(\beta-\delta_f\right)\right] + \\ & \left[\omega\rho_{12} - \omega\beta\rho^{(f)} + iF(\omega)\frac{\eta\beta^2}{K}\right]\delta_f K^{(s)} \end{aligned} \tag{4.41}$$

Equation 4.38 admits two solutions and therefore two dilatational waves can propagate in a fluid-saturated porous medium according to the present theory.

4.3.2 Rotational waves

To allow only rotational waves to propagate apply the curl operator to equations 4.32 and 4.33 and use equation 4.1 and 4.2

$$\begin{aligned} (1-\beta)\rho^{(s)}\frac{\partial^2}{\partial t^2}\vec{\psi}^{(s)} - \rho_{12}\frac{\partial^2}{\partial t^2}\left(\vec{\psi}^{(s)} - \vec{\psi}^{(f)}\right) + \frac{\eta\beta^2}{K}\frac{\partial}{\partial t}\left(\vec{\psi}^{(s)} - \vec{\psi}^{(f)}\right) &= \\ \mu_M\nabla^2\vec{\psi}^{(s)} & \qquad (4.42) \\ \beta\rho^{(f)}\frac{\partial^2}{\partial t^2}\vec{\psi}^{(f)} + \rho_{12}\frac{\partial^2}{\partial t^2}\left(\vec{\psi}^{(s)} - \vec{\psi}^{(f)}\right) - \frac{\eta\beta^2}{K}\frac{\partial}{\partial t}\left(\vec{\psi}^{(s)} - \vec{\psi}^{(f)}\right) &= \\ (1-\beta)\eta\left[\frac{\mu_M}{(1-\beta)\mu^{(s)}} - 1\right]\frac{\partial}{\partial t}\nabla^2\vec{\psi}^{(s)} + \beta\eta\frac{\partial}{\partial t}\nabla^2\vec{\psi}^{(f)} & \qquad (4.43) \end{aligned}$$

Now consider solutions of the form

$$\vec{\psi}^{(s)} = \hat{y}D^{(s)}e^{i\left(\omega t - \vec{k}\cdot\vec{x}\right)} \tag{4.44}$$

$$\vec{\psi}^{(f)} = \hat{y}D^{(f)}e^{i\left(\omega t - \vec{k}\cdot\vec{x}\right)} \tag{4.45}$$

where $\vec{D}^{(s)} \cdot \vec{k} = 0$ and $\vec{D}^{(f)} \cdot \vec{k} = 0$. Using these solutions equations 4.42 and 4.43 lead to

$$\begin{aligned}
\left[k^2\mu_M - (1-\beta)\,\rho^{(s)}\omega^2 + \rho_{12}\omega^2 + iF(\omega)\omega\frac{\eta\beta^2}{K}\right]\vec{\psi}^{(s)} - & \\
\left[\rho_{12}\omega^2 + iF(\omega)\omega\frac{\eta\beta^2}{K}\right]\vec{\psi}^{(f)} &= 0 \qquad (4.46)\\
\left[\rho_{12}\omega + iF(\omega)\frac{\eta\beta^2}{K} - ik^2(1-\beta)\eta\left[\frac{\mu_M}{(1-\beta)\mu^{(s)}} - 1\right]\right]\vec{\psi}^{(s)} + & \\
\left[\beta\rho^{(f)}\omega - \rho_{12}\omega - iF(\omega)\frac{\eta\beta^2}{K} - i\beta\eta k^2\right]\vec{\psi}^{(f)} &= 0 \qquad (4.47)
\end{aligned}$$

For a given propagating wave the vector potential field $\vec{\psi}$ in the solid and fluid components are related to each other again here by a complex number. Let this complex number be $\zeta_3 = \frac{D^{(s)}}{D^{(f)}}$

$$\vec{\psi}^{(s)} = \zeta_3\vec{\psi}^{(f)} \qquad (4.48)$$

Equations 4.46 and 4.47 lead to the second order equation

$$a\zeta^2 + b\zeta + c = 0 \qquad (4.49)$$

$$\begin{aligned}
a &= (1-\beta)\eta\left[(1-\beta)\,\rho^{(s)}\omega^2 - \rho_{12}\omega^2 - iF(\omega)\omega\frac{\eta\beta^2}{K}\right]\left[\frac{\mu_M}{(1-\beta)\mu^{(s)}} - 1\right] \qquad (4.50)\\
b &= (1-\beta)\eta\left[\rho_{12}\omega^2 + iF(\omega)\omega\frac{\eta\beta^2}{K}\right]\left[\frac{\mu_M}{(1-\beta)\mu^{(s)}} - 1\right] + \\
&\quad \beta\eta\left[(1-\beta)\,\rho^{(s)}\omega^2 - \rho_{12}\omega^2 - iF(\omega)\omega\frac{\eta\beta^2}{K}\right] + i\mu_M\left[\rho_{12}\omega + iF(\omega)\frac{\eta\beta^2}{K}\right] \qquad (4.51)\\
c &= \beta\eta\left[\rho_{12}\omega^2 + iF(\omega)\omega\frac{\eta\beta^2}{K}\right] + i\mu_M\left[\beta\rho^{(f)}\omega - \rho_{12}\omega - iF(\omega)\frac{\eta\beta^2}{K}\right] \qquad (4.52)
\end{aligned}$$

Equation 4.49 admits two solutions, therefore two S-waves can propagate in a fluid-saturated porous rock according to the present theory. The S-wave with the larger velocity is called the shear fast wave and the lower velocity one is called the slow S-wave. These will be looked at in more details when the two theories are compared.

4.4 Porosity-pressure wave propagation

It is important to reiterate that the de la Cruz/Spanos theory, in contrast with the Biot theory, allows for a dynamic porosity. The porosity change couples with the fluid pressure change resulting in additional dilatational processes. The processes stemming from this coupling will not be studied in detail here but a summary will given in this section.

If one allows the porosity to change as a compressional wave propagates in a fluid-saturated porous material, a coupling occurs between the porosity and the pressure of the fluid saturant. A wave, called second sound in mechanics, is caused by dynamic coupling between the porosity and fluid pressure changes. This problem is addressed by Spanos (2001) where all dilatational processes are allowed in the formulation of the problem. The equations of motion, the pressure equation, and the porosity equation lead to 4 dilatational solutions that are:

- A sound wave where both the solid skeleton and the fluid experience compressions nearly in phase and consequently this wave experiences low attenuation. The velocity of this wave is greater than the sound wave in the fluid and less than that in the solid skeleton.
- A sound wave where both the solid skeleton and the fluid experience compressions almost out of phase and consequently this wave experiences high attenuation. The velocity of this wave is less than the sound wave in the fluid.
- A fluid flow coupled to the solid skeleton deformations (close to the incompressible limit of the fluid) where a change in porosity and pressure propagates through the solid skeleton. At the high frequencies used in the present experiments this process propagates faster than the first S-wave and about 400-500 m/s slower than the fast P-wave.
- A porosity diffusion process.

The first two processes described above are the fast and slow P waves described earlier. At low frequencies the last two processes are strongly coupled with each other and are a result of pressure-porosity changes. The waves linked to the porosity-pressure coupling are observed to damp out with distance of propagation leaving behind an increase in pressure that equilibrates though a diffusion process. A complete description of the theory can be found in Spanos (2001) chapter VIII.

The porosity-pressure coupling has already been applied in industrial technologies such as groundwater, waste disposal, and oil recovery (Spanos, 2001).

4.5 Porous media parameters

In order to properly model wave propagation and reflectivity experiments in a fluid-saturated porous material several parameters need to be determined through laboratory measurements. For the Biot theory the parameters are:

- The density of the porous solid (mineral grains) $\rho^{(s)}$.
- The density of the fluid saturant $\rho^{(f)}$.
- The porosity β.
- The permeability K.
- The shear viscosity of the fluid η.
- The shear modulus of the solid skeleton μ_M.
- The coupling mass density between the fluid and the solid ρ_{12}.
- The bulk moduli due to the interaction of the fluid and the solid R, Q, and A which have been defined in terms of the static measurements of K_{un}, K_M, $K^{(f)}$, and μ_M.

For the de la Cruz/Spanos theory the parameters are:

- The density of the porous solid (mineral grains) $\rho^{(s)}$.
- The density of the fluid saturant $\rho^{(f)}$.
- The porosity β.
- The permeability K.
- The shear viscosity of the fluid η.
- The shear modulus of the solid skeleton μ_M.
- The coupling mass density between the fluid and the solid ρ_{12}.
- The shear modulus of the solid mineral grains $\mu^{(s)}$.
- The bulk modulus of the solid mineral grains $K^{(s)}$.

- The bulk modulus of the fluid saturant $K^{(f)}$.

- The bulk viscosity of the fluid ξ_f.

- The dilation parameter for the solid δ_s.

- The dilation parameter for the fluid δ_f.

The parameters $\rho^{(s)}$, $\rho^{(f)}$, β, K, μ_M, $\mu^{(s)}$, $K^{(s)}$, η, and $K^{(f)}$ can, in principle, be determined through standard laboratory measurements. The fluid bulk viscosity ξ_f, discussed in chapter 2, can be inferred from ultrasonic attenuation measurements (Bhatia and Singh, 1986). The other parameters involve more complex laboratory experiments and will be discussed below.

4.5.1 Parameters for the Biot theory

The Biot parameters A, Q, and R are given by (Appendix B)

$$R = M\beta K_{un} \tag{4.53}$$

$$Q = M\left(K_{un} - K_{un}\beta - K_M\right) \tag{4.54}$$

$$A = \frac{Q^2}{R} + K_M - \frac{2}{3}\mu_M \tag{4.55}$$

where M is given by

$$M = \frac{\beta K_{un}}{\left(K_{un} + \gamma K_{un}^2 - K_M\right)} \tag{4.56}$$

In the above equations the measurable quantities are:

- The bulk modulus K_{un} measured in an unjacketed test experiment as described in appendix B section B.2.2.

- The bulk modulus K_M measured in an jacketed test experiment as described in appendix B section B.2.1.

- The shear modulus μ_M.

- The coefficient of fluid content γ measured in test experiment as described in appendix B section B.2.3.

The coefficient of fluid content is given by

$$\gamma = \Delta V - \frac{1}{K_{un}} + \frac{1}{K^{(f)}} \tag{4.57}$$

and if the solid material is isotropic and homogeneous then equation 4.57 becomes

$$\gamma = \beta \left(\frac{1}{K^{(f)}} - \frac{1}{K^{(s)}} \right) \tag{4.58}$$

and equations 4.53-4.56 hold with $K_{un} = K^{(s)}$. See appendix B for more details and the significance of the various parameters involved in equations 4.57 and 4.58.

The relation 4.58 is used by many workers to model the acoustic wave propagation through porous media. However this relation might be too restrictive (Hickey and Sabatier, 1997). Hickey et al. (1995) have shown that the coefficient of fluid content can be calculated by

$$\gamma = \beta \left(\frac{1}{K^{(f)}} - \frac{1}{K_{un}} \right) + (1 - \beta) \left(\frac{1}{K^{(s)}} - \frac{1}{K_{un}} \right) \tag{4.59}$$

The second term on the right hand side represents the deformation associated with a change in porosity during an unjacketed test experiment. This term vanishes when $K_{un} = K^{(s)}$ and equation 4.59 becomes equation 4.58.

It is also possible to allow the bulk modulus K_M and the shear modulus μ_M of the solid skeleton to be complex to account for losses associated to various processes within the aggregate (Biot, 1962a; Biot, 1962b). Stoll et al. (1981) have incorporated complex shear and bulk moduli for the solid skeleton in an acoustic reflectivity modelling study from boundaries between water and water-saturated lose porous sediments, such as the ocean floor. The complex form of the shear and bulk moduli allows for viscoelastic losses within the solid skeleton (solid frame). However it is important to note that it is allowed only if K_M and μ_M are frequency independent as equations 4.53 through 4.56 were derived based upon static laboratory experiments.

To complete the set of parameters given above that are needed for modelling wave propagation in fluid-saturated porous media the dynamic mass transfer ρ_{12} and the viscosity correction factor $F(\omega)$ must be determined. It is possible to infer ρ_{12} from the measurement of the S-wave velocity. However ρ_{12} is very sensitive to small variations of the S-wave velocity as it will be shown later. According to Johnson et al. (1987) this coefficient is independent of the mechanical properties of the solid and the fluid but it is always proportional to the fluid density and porosity. This coefficient is defined by the following equations

$$\tilde{\rho_{12}} = -(\tilde{\varsigma} - 1)\beta\rho^{(f)} \qquad (4.60)$$

$$\tilde{\varsigma} = \varsigma + i\frac{\eta\beta}{\omega K\rho^{(f)}}F(\omega) \qquad (4.61)$$

where $\tilde{\rho_{12}}$ is defined as the dynamic drag factor. ς is the dimensionless quantity known as the tortuosity, that is the ratio of the length of a direct path between two points in the porous material over the length of the shortest path joining the same points through the voids within the porous material and $\tilde{\varsigma}$ is defined as the complex viscosity. $F(\omega)$ is the viscosity correction factor defined as

$$F(\omega) = \left[1 - i\frac{4\varsigma^2 K^2\rho^{(f)}\omega}{\eta\Delta^2\beta^2}\right]^{\frac{1}{2}} \qquad (4.62)$$

where Δ has dimensions of length and is given within:

$$\frac{2}{\Delta} = \frac{\int|\vec{u}_p(\vec{r}_w)|^2 dA}{\int|\vec{u}_p(\vec{r})|^2 dV} \qquad (4.63)$$

where the integration in the numerator is over the walls of the pore-grain interface and that of the denominator is over the pore volume. This is just the surface to pore volume of the interface where each area is weighted to the local value of the field. The derivation of these results can be found in Johnson et al. (1987). The complex tortuosity given by equation 4.61 suggests that the dynamic mass transfer $\tilde{\rho_{12}}$ is dominated by viscous effects at low frequencies and by inertial effects at high frequencies. A cross over frequency can be defined as

$$\omega_c = \frac{\eta\beta}{K\rho^{(f)}} \qquad (4.64)$$

At low frequencies ($\frac{\omega_c}{\omega} \ll 1$) viscous effects dominate and at high frequencies ($\frac{\omega_c}{\omega} \gg 1$) inertial effects dominate. At frequencies close to ω_c the viscous effects and inertial effects are of comparable magnitude.

It is important here to note that the complex drag coefficient $\tilde{\rho_{12}}$ is defined by simply combining the mass transfer ρ_{12} and the Darcy term appearing in the original Biot theory, a combination valid only for plane waves. $\tilde{\rho_{12}}$ is given by

$$\tilde{\rho_{12}} = \rho_{12} + iF(\omega)\frac{\eta\beta^2}{\omega K} \qquad (4.65)$$

This term appears in all the 4 equations describing P and S plane wave propagation in porous media. Assuming that $\rho_{12} = -(\varsigma - 1)\beta\rho^{(f)}$ equations 4.61 and 4.65 lead to equation 4.60. These results will be detailed later for practical purposes.

The relative movement of the fluid with respect to the solid skeleton depends on the viscous penetration depth (Warner and Beamish, 1994) that is given by

$$\delta_{visc} = \left[\frac{2\eta}{\rho^{(f)}\omega}\right]^{\frac{1}{2}} \tag{4.66}$$

for an oscillation of angular frequency ω. This defines a second critical frequency $\omega_c' = \frac{2\eta}{\rho^{(f)}R^2}$ at which $\delta_{visc} = R$ where R is the pore radius. At frequencies $\omega \ll \omega_c'$ the penetration depth is larger than the pore size and the fluid essentially moves with the solid skeleton, on the other hand when $\omega \gg \omega_c'$ the viscous penetration depth is smaller than the pore size and this portion of the fluid essentially decouples from the solid skeleton. This change in behaviour will accordingly affect the sound velocity and attenuation. Thus there is a pore size that determines the crossover from low-frequency to high-frequency behaviour. This approximation for the viscosity correction factor was used by Warner and Beamish (1994) in the study of sound propagation in superfluid-filled porous media. For modelling wave propagation in porous media both the tortuosity ς and the parameter Δ must be determined.

4.5.2 Parameters for the de la Cruz/Spanos theory

For this theory most of the parameters can be determined in standard laboratory experiments as mentioned earlier. ρ_{12} can be determined in the same way as for the Biot theory. The last two parameters, the dilation parameters δ_s and δ_f for the solid and the fluid respectively must be determined. This is done in laboratory measurement test as given in Hickey et al. (1995). The details of the measurements can be found in the appendix C. The solid and fluid dilation parameters are given respectively by

$$\delta_s = \beta\frac{K_{bp}\left((1-\beta)K^{(s)} - K_{bc}\right)}{\beta K_{bp}\left(K^{(s)} - K_f\right) + K_f K_{bc}} \tag{4.67}$$

$$\delta_f = \beta\frac{K^{(f)}\left(K_{bc} - \beta K_{bp}\right)}{\beta K_{bp}\left(K^{(s)} - K_f\right) + K_f K_{bc}} \tag{4.68}$$

where K_{bp} and K_{bc} are measurable bulk moduli in experimental laboratory tests and the others parameters are as described within the present section. K_{bp} and K_{bc} are the bulk moduli measured in drained compressibility tests and are defined as

$$\frac{1}{K_{bc}} = -\frac{1}{V_0}\left(\frac{\Delta V}{\Delta p}\right)_{p^{(f)}=p_0} \tag{4.69}$$

$$\frac{1}{K_{bp}} = -\frac{1}{V_0}\left(\frac{\Delta V}{\Delta p^{(f)}}\right)_{p=p_0} \tag{4.70}$$

where V_0 is the initial volume of the sample, p is the confining pressure, and $p^{(f)}$ is the fluid pore pressure. These experiments are given in more detail in appendix C.

4.6 Comparison between Biot's theory and de la Cruz/Spanos theory

It is shown in sections 4.2 and 4.3 that two dilatational waves can propagate in a fluid-saturated porous material for both Biot and de la Cruz/Spanos theories. It is also shown, however, that two S-waves can propagate in a fluid-saturated porous material in de la Cruz/Spanos theory whereas only one S-wave can propagate according to Biot theory. It is important to recall here that the two theories are based on different physical backgrounds. Biot has treated the fluid-porous material at a macroscopic point of view whereas de la Cruz/Spanos theory has treated the fluid-porous material first at a microscopic point of view before averaging to obtain their final result as macroscopic equations of motion. Looking closely at the wave equations 4.32 and 4.33 we notice extra terms that are not present in the Biot theory. These terms are enclosed between braces and are present only in equation 4.33. All other terms in both equations have their counterparts in the wave equations of Biot theory given by equations 4.3 and 4.4 despite the differences in the formulation of the various parameters. These extra terms between braces are terms that originated from the formulation of the stress in the fluid component. In de la Cruz/Spanos theory the stress due to both the shear and bulk viscous effects are included. These terms are responsible for the second S-wave not present in the Biot theory. A second S-wave can propagate with the bulk viscosity taken into account or not. These terms can be very important particularly when high viscosity fluids are considered.

In the forthcoming reflectivity experiments on synthetic porous samples only water will be used. Water is a low viscosity fluid and the extra terms in de la Cruz/Spanos theory will turn out to have very little effect on the results in this case. Furthermore in the framework of the present study the various bulk moduli that could be measured in laboratory experimental tests are not readily available. The size of the mineral grains in the porous synthetic samples that are used in the experiments vary in a small range. Therefore it is assumed that the samples are isotropic and the unjacketed bulk modulus K_{un} is taken to be close to the bulk modulus $K^{(s)}$ of the solid mineral grains.

Hickey et al. (1995) has given a comparison between Biot and de la Cruz/Spanos theories and will be reviewed below. For clarity the coefficients Q, R, A, and γ as defined in the Biot theory in appendix B will be written with a subscript $_c$ and $_b$ for the de la Cruz/Spanos and Biot theories respectively. Recall the fluid pressure equation C.18 and the porosity equation C.19 of de la Cruz/Spanos theory

$$\frac{1}{K^{(f)}}\frac{\partial p^{(f)}}{\partial t} = -\vec{\nabla}\cdot\frac{\partial \vec{u}^{(f)}}{\partial t} - \frac{1}{\beta}\frac{\partial \beta'}{\partial t} \tag{4.71}$$

$$\frac{\partial \beta}{\partial t} = \delta_s\vec{\nabla}\cdot\frac{\partial \vec{u}^{(s)}}{\partial t} - \delta_f\vec{\nabla}\cdot\frac{\partial \vec{u}^{(f)}}{\partial t} \tag{4.72}$$

where β is the unperturbed porosity and β' is the perturbed porosity. Note that whenever not explicitly mentioned β is the perturbed porosity. The above equations lead to

$$-\beta(p^{(f)} - p_0) = K^{(f)}\delta_s\vec{\nabla}\cdot\vec{u}^{(s)} + K^{(f)}\left(\beta - \delta_f\right)\vec{u}^{(f)} \tag{4.73}$$

where $p^{(f)}$ is the fluid pressure, and p_0 is the initial fluid pressure. All other parameters have the same significance as those used in previous sections. In the Biot theory the equation of the fluid pressure is written as

$$-\beta\left(p^{(f)} - p_0\right) = Q\vec{\nabla}\cdot\vec{u}^{(s)} + R\vec{u}^{(f)} \tag{4.74}$$

comparing the two equations one has

$$\begin{aligned} Q &= K^{(f)}\delta_s & (4.75)\\ R &= K^{(f)}\left(\beta - \delta_f\right) & (4.76) \end{aligned}$$

Finally comparing equations 4.32 in the de la Cruz/Spanos theory and equation 4.3 of the Biot theory the coefficient Q must also be

$$Q = K^{(s)}\delta_f \tag{4.77}$$

Combining equation C.37 with equation 4.75 and equation C.44 for $\theta = 1$, using the notation $K_{(\theta)}(1) = K_{un}$ and $K_{bc} = K_M$ we obtain

$$Q_c = \frac{\beta K_{un} K^{(f)} \left[(1-\beta) K^{(s)} - K_M\right]}{K_{un}\left[(1-\beta)\, K^{(f)} + \beta K^{(s)}\right] - K_M K^{(f)}} \tag{4.78}$$

The expression for Q as given in the Biot theory by equation B.20 after using equation C.50 for the coefficient of fluid content is

$$Q_b = \frac{\beta K_{un}^2 K^{(f)} \left[(1-\beta) K^{(s)} - K_M\right]}{K_{un}^2\left[(1-\beta)\, K^{(f)} + \beta K^{(s)}\right] - K^{(s)} K_M K^{(f)}} \tag{4.79}$$

It is obvious that equations 4.78 and 4.79 are equal only if $K_{un} = K^{(s)}$.

Combining equation C.37 with equation 4.76 and equation C.44 for $\theta = 1$ we obtain

$$R_c = \frac{\beta^2 K_{un} K^{(f)} K^{(s)}}{K_{un}\left[(1-\beta)\, K^{(f)} + \beta K^{(s)}\right] - K_M K^{(f)}} \tag{4.80}$$

The expression for R as given in the Biot theory by equation B.19 after using equation C.50 for the coefficient of fluid content is

$$R_b = \frac{\beta^2 K_{un}^2 K^{(f)} K^{(s)}}{K_{un}^2\left[(1-\beta)\, K^{(f)} + \beta K^{(s)}\right] - K^{(s)} K_M K^{(f)}} \tag{4.81}$$

Again here it is obvious that equations 4.80 and 4.81 are equal only if $K_{un} = K^{(s)}$.

Comparing equations 4.32 in the de la Cruz/Spanos theory and equation 4.3 of the Biot theory the coefficient A is for de la Cruz/Spanos theory

$$A_c = \left[(1-\beta) - \delta_s\right] K^{(s)} - \frac{2}{3}\mu_M \tag{4.82}$$

Using equations 4.75, 4.76, 4.77, and 4.82 we get

$$A_c = \frac{Q_c^2}{R_c} + K_M - \frac{2}{3}\mu_M + \frac{(1-\beta) K^{(f)} (K_{un} - K^{(s)}) K_M}{\beta K_{un} K^{(s)}} \tag{4.83}$$

and for the Biot theory the coefficient A is found to be

$$A_b = \frac{Q_b^2}{R_b} + K_M - \frac{2}{3}\mu_M \tag{4.84}$$

Again A_b and A_c are equal if we have $K_{un} = K^{(s)}$.

The last coefficient to compare is the coefficient of fluid content γ. For de la Cruz/Spanos theory we have

$$\gamma = \beta \left[\frac{1}{K^{(f)}} - \frac{1}{K_{un}} \right] + (1-\beta) \left[\frac{1}{K^{(s)}} - \frac{1}{K_{un}} \right] \tag{4.85}$$

and for the Biot theory we have

$$\gamma = \beta \left[\frac{1}{K^{(f)}} - \frac{1}{K_{un}} \right] \tag{4.86}$$

and it is obvious that equations 4.85 and 4.86 will be equal only if $K_{un} = K^{(s)}$.

Equations 4.75 and 4.77 lead to

$$\frac{K^{(s)}}{K^{(f)}} = \frac{\delta_s}{\delta_f} \tag{4.87}$$

which is the compatibility condition between the two theories. Using this condition in equation C.40 we get

$$\frac{1}{K_{bp}} = \frac{1}{K_M} - \frac{1}{K^{(s)}} \tag{4.88}$$

Equation C.44 for $\theta = 1$, the hydrostatic limit as assumed above for Q, R, A, and γ, becomes

$$\frac{1}{K_{un}} = \frac{1}{K_M} - \frac{1}{K_{bp}} \tag{4.89}$$

and using equation 4.88 in equation 4.89 we get

$$\frac{1}{K_{un}} = \frac{1}{K^{(s)}} \tag{4.90}$$

which again is the same condition for the parameters Q, R, A, and γ to be equivalent for both theories. Therefore if $K_{un} = K^{(s)}$ then the two theories are equivalent but de la Cruz/Spanos theory contains extra terms mostly related to viscosity as discussed in section 4.3. The importance of these terms will be discussed later.

Now recall the equation of fluid content 4.57 for the Biot theory

$$\gamma = \Delta V - \frac{1}{K_{un}} + \frac{1}{K^{(f)}} \tag{4.91}$$

If the unjacketed bulk modulus K_{un} is large compared to the bulk modulus of the fluid the coefficient of fluid content is dominated by ΔV, the volume of fluid that enters the pores under an unjacketed test. The expression of the coefficient of fluid content in de la Cruz/Spanos theory does not require the measurement of the volume of fluid that enters the pores during an unjacketed test even when the unjacketed bulk modulus K_{un} differs from that of the mineral grains $K^{(s)}$. The coefficient of fluid content for both theories are plotted against K_{un} in figure 4.1. If $K_{un} = K^{(s)}$ the two theories provide the same coefficient of fluid content provided that the bulk modulus of the mineral grains $K^{(s)}$ and that of the fluid $K^{(f)}$ are known. In the case where the unjacketed bulk modulus K_{un} differs from that of the mineral grains $K^{(s)}$ the de la Cruz/Spanos theory provides the coefficient of fluid content if the unjacketed bulk modulus K_{un} is known and the Biot theory requires both the unjacketed bulk modulus K_{un} and the volume ΔV of fluid that enters the pores during the unjacketed test. It is always possible to find a value of ΔV for the two equations 4.85 and 4.91 to be equivalent. It still remains to do laboratory experiments to compare the two equations in nature. Therefore equation 4.85 is preferred for modelling fluid-saturated materials when the unjacketed bulk modulus is not equal to the bulk modulus of the mineral grains.

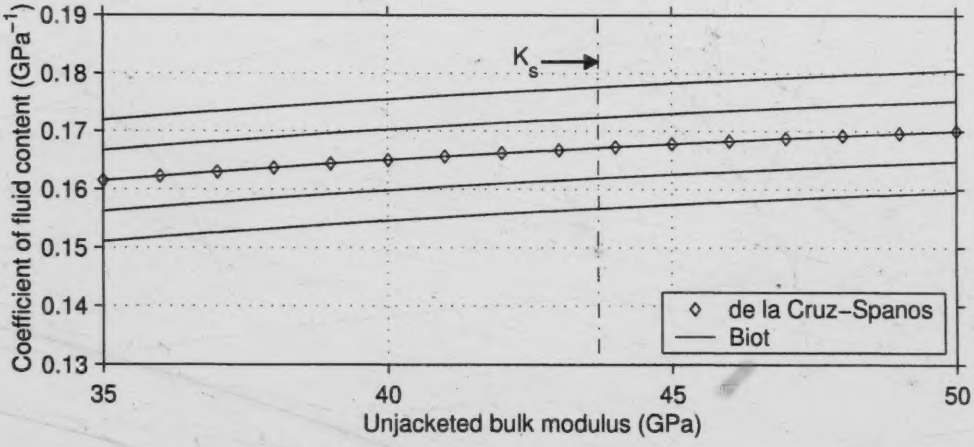

Figure 4.1: The coefficient of fluid content γ against the unjacketed bulk modulus K_{un}. Equation 4.85 is used to calculate γ for de la Cruz/Spanos theory and equation 4.91 is used for Biot theory. The volume that enters the pores in the unjacketed test is varied from -0.251×10^{-9} to -0.272×10^{-9} $\mathrm{m}^3/\mathrm{m}^3$. The two equations lead to the same result for $\Delta V = -0.261 \times 10^{-9}$ $\mathrm{m}^3/\mathrm{m}^3$.

The two theories would give the same models within the mentioned extra terms.

The equation of motion of de la Cruz/Spanos theory would become

$$\begin{aligned}(1-\beta)\rho^{(s)}\frac{\partial^2}{\partial t^2}\vec{u}^{(s)} - \rho_{12}\frac{\partial^2}{\partial t^2}\left(\vec{u}^{(s)}-\vec{u}^{(f)}\right) + F(\omega)\frac{\eta\beta^2}{K}\frac{\partial}{\partial t}\left(\vec{u}^{(s)}-\vec{u}^{(f)}\right) &= \\ \mu_M\nabla^2\vec{u}^{(s)} + [A+\mu_M]\vec{\nabla}\left(\vec{\nabla}\cdot\vec{u}^{(s)}\right) + Q\vec{\nabla}\left(\vec{\nabla}\cdot\vec{u}^{(f)}\right) & \end{aligned} \tag{4.92}$$

$$\begin{aligned}\beta\rho^{(f)}\frac{\partial^2}{\partial t^2}\vec{u}^{(f)} + \rho_{12}\frac{\partial^2}{\partial t^2}\left(\vec{u}^{(s)}-\vec{u}^{(f)}\right) - F(\omega)\frac{\eta\beta^2}{K}\frac{\partial}{\partial t}\left(\vec{u}^{(s)}-\vec{u}^{(f)}\right) &= \\ Q\vec{\nabla}\left(\vec{\nabla}\cdot\vec{u}^{(s)}\right) + R\vec{\nabla}\left(\vec{\nabla}\cdot\vec{u}^{(f)}\right) + & \\ \left\{(1-\beta)\eta\left[\frac{\mu_M}{(1-\beta)\mu_s}-1\right]\frac{\partial}{\partial t}\left[\nabla^2\vec{u}^{(s)}+\frac{1}{3}\vec{\nabla}\left(\vec{\nabla}\cdot\vec{u}^{(s)}\right)\right]\right\} + & \\ \left\{\beta\eta\frac{\partial}{\partial t}\left[\nabla^2\vec{u}^{(f)}+\frac{1}{3}\vec{\nabla}\left(\vec{\nabla}\cdot\vec{u}^{(f)}\right)\right]\right\} + & \\ \left\{\frac{\xi_f}{K^{(f)}}\frac{\partial}{\partial t}\left[Q\vec{\nabla}\left(\vec{\nabla}\cdot\vec{u}^{(s)}\right)+R\vec{\nabla}\left(\vec{\nabla}\cdot\vec{u}^{(f)}\right)\right]\right\} & \end{aligned} \tag{4.93}$$

Equations 4.92 and 4.93 are equivalent to equations 4.3 and 4.4 developed in the Biot theory with extra terms involving particle velocities shown between braces. The importance of these extra terms will be examined in the next section on numerical modelling.

de la Cruz and Spanos stated that if the strains of the Biot theory are reinterpreted including the dynamic porosity then the Biot theory becomes a static limit of their theory.

4.7 Modelling wave propagation in porous media

Modelling wave propagation in fluid-saturated porous media is of interest in many domains of research, such as understanding the interaction between the solid and the fluid constituents, and characterization of porous rocks to find their mechanical and physical properties. We first model an example of a fluid-saturated porous medium that is close to those used in experimental tests described later. Here the material is assumed to be isotropic and homogeneous and therefore the unjacketed bulk modulus K_{un} is taken to be equal to the bulk modulus of the mineral grains $K^{(s)}$.

As a high viscosity example take glycerol with the properties described in table 4.1. and as a low viscosity fluid take a water-saturated porous sample with the

$\rho^{(f)}$	$k^{(f)}$	η	ξ_f
kg/m^3	GPa	Pa.s	Pa.s
1261.3	4.664	1.499	1.649

Table 4.1: Properties of glycerol used in the present example. The data is from Bathia (1986) and Hickey (1994).

Parameter	Description	Value	Units
$\rho^{(s)}$	Density of the mineral grains	2450	kg/m^3
$\rho^{(f)}$	Density of the fluid saturant (water)	995	kg/m^3
η	Shear viscosity of the fluid saturant (water)	0.001	Pa.s
ξ_f	Bulk viscosity of the fluid saturant (water)	0.0025	Pa.s
$K^{(f)}$	Bulk modulus of the fluid saturant (water)	2.215	GPa
$K^{(s)}$	Bulk modulus of the mineral grains	43.7	GPa
$\mu^{(s)}$	Shear modulus of the mineral grains	25.8	GPa
β	Porosity of the solid material	0.39	--
K	Permeability	20×10^{-12}	m^2
ς	Tortuosity	1.5	--

Table 4.2: Properties of the illustrative water-saturated porous material used for the modelling of wave propagation using both the Biot theory and de la Cruz/Spanos theory. All parameters are close to measured ones in the laboratory except for the shear and bulk viscosities that are after Litovitz (1960).

solid skeleton and the fluid saturant described by the parameters of table 4.2. These values taken for this example are for illustration purposes only. These are similar to what was anticipated the physical properties of the test samples to be in the forthcoming experiments. Here the "dry" solid skeleton (filled with air) is assumed to behave for small deformations as a homogeneous, isotropic, linear viscoelastic (HILV) material (Borcherdt, 1977; Borcherdt, 1982). The complex bulk and shear moduli can be derived from the compressional and shear wave velocities and the associated attenuations of the solid skeleton. Here the values of the phase velocities and attenuations are given in table 4.3. The derived complex bulk and shear moduli

P phase velocity $V_p^{(s)}$ (m/s)	S phase velocity) $V_S^{(s)}$ (m/s)	P attenuation $\alpha_{0P}^{(s)}$ (m^{-1})	S attenuation $\alpha_{0S}^{(s)}$ (m^{-1})
2500	1550	10.2	25.

Table 4.3: The compressional and shear wave phase velocities and the associated attenuations of the "dry" solid material at 0.78 MHz.

are given in table 4.4. The results are assumed and the derivation of the procedure to obtain these parameters will be described in the next chapter. The acoustic source signal that will be employed for the forthcoming experiments in porous media is the same as the one described in chapter 2 and chapter 3. The frequency range of the input signal is 0.2-1.2 MHz with a peak amplitude at 0.78 MHz. The average radius of the solid grains of the sample considered here is about 180 μm with an approximate average pore radius of about 35 μm. This leads to an approximate viscous penetration depth of $\delta_{visc} = 1.6$ μm and a critical frequency $\omega_c = 1.6$ kHz. As the frequency of the input signal is above ω_c and is very approximate a viscosity correction factor will be applied in the present case. In the present illustrative modelling two results will be displayed, one for a low frequency range 0 Hz-20 kHz, and a second for a relatively high frequency range of 0 MHz to 2 MHz. The second frequency range includes the frequency bandwidth of the signal that will be employed in the experiments on porous media. The first frequency range will highlight the frequencies where changes in the wave propagation behaviour are expected to differ from the high frequency behaviour. The calculated viscosity correction factor using equation 4.62 and the parameters taken from table 4.2 is shown in figure 4.2. The real

Fluid	K_M GPa	μ_M GPa	ρ_{12} kg/m^3	Δ μm
Water	$4.553 + i0.021$	$3.509 + i0.057$	-194	10
Glycerol	$4.631 + i0.021$	$3.651 + i0.058$	-246	10

Table 4.4: The complex bulk and shear moduli of the solid skeleton, the mass transfer ρ_{12}, and the assumed characteristic length Δ of the pore size of the porous material. The real and imaginary parts of the moduli are in GPa.

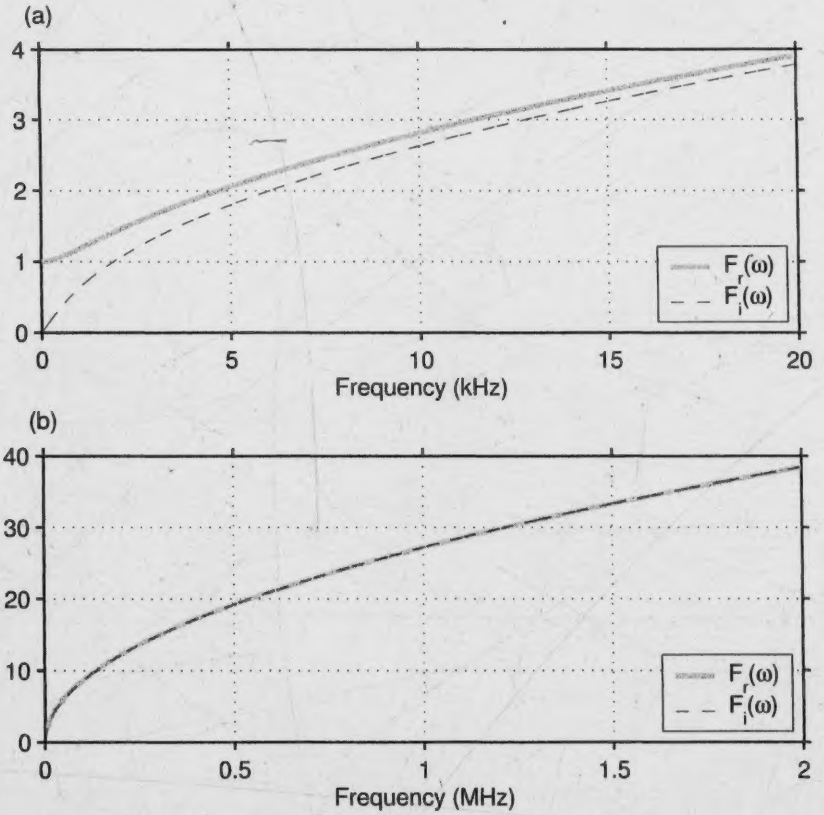

Figure 4.2: The real and imaginary parts of the viscosity correction factor $F(\omega)$ calculated using equation 4.62. The parameters are taken from table 4.2. (a) Low frequencies. (b) High frequencies. Here a value of $\Delta = 10^{-6}$m is assumed to calculate the correction factor $F(\omega)$.

and imaginary parts of the viscosity correction factor differ at low frequencies (Fig. 4.2-a) but are indistinguishable at high frequencies (Fig. 4.2-b). The dynamic mass transfer ρ_{12} (Tab. 4.4) is dominated by inertial effects for the case of water and by the viscous effects for the case of glycerol according to the results calculated for the frequency 0.78 MHz. The parameters of table 4.2 and table 4.3 and the calculated viscosity correction factor are used to calculate the Biot and de la Cruz/Spanos parameters and the results are presented in table 4.5.

The phase velocity of the S, the fast P, and the slow P waves are shown in

Fluid	A	Q	R	δ_f	δ_s
	GPa	GPa	GPa	-	-
Water	$3.524 - i0.019$	$1.051 - i0.001$	0.811	0.0241	$0.4746 - i0.0004$
Glycerol	$4.867 - i0.022$	$2.066 - i0.002$	1.598	0.0473	$0.4429 - i0.0004$

Table 4.5: The derived parameters A, Q, R, δ_f, and δ_s of the water-saturated porous material and a glycerol-saturated porous material. The units of the real and imaginary parts of A, Q, and R are in GPa. δ_f and δ_s are dimensionless.

figure 4.3 at a low frequency range and in figure 4.4 at a high frequency range. The corresponding attenuations are shown in figures 4.5 and 4.6. The phase velocities of the fast P-wave and the S-wave exhibit very little dispersion at low frequencies and almost no dispersion at high frequencies. On the other hand the slow P-wave exhibits large dispersion at low frequencies and very little at high frequencies.

In these examples the solutions for both theories discussed in this chapter are presented. The second S-wave is left at the end of the section and will be discussed alone as it is not present in the Biot theory formulation. It is noticeable that for this case the results are indistinguishable for both theories despite the extra terms that are included in the calculation using de la Cruz/Spanos theory. It is important here to note that the S-wave velocity of the fluid-saturated porous sample decreases from the S velocity of the "dry" skeleton whereas the fast P-wave velocity increases from the P-wave velocity of the "dry" skeleton. This suggests the following observations, many of which are already well known:

- The S-wave velocity of the water-saturated porous sample is dominated by the increase of the density of the sample.
- The shear modulus is not influenced by the presence of the fluid within the pores under the implicit assumptions employed.
- The bulk modulus of the fluid-saturated porous sample is higher than that of the "dry" sample.
- The presence of the fluid increases the stiffness of the porous skeleton. This effect is greater than the increase in the density of the sample.

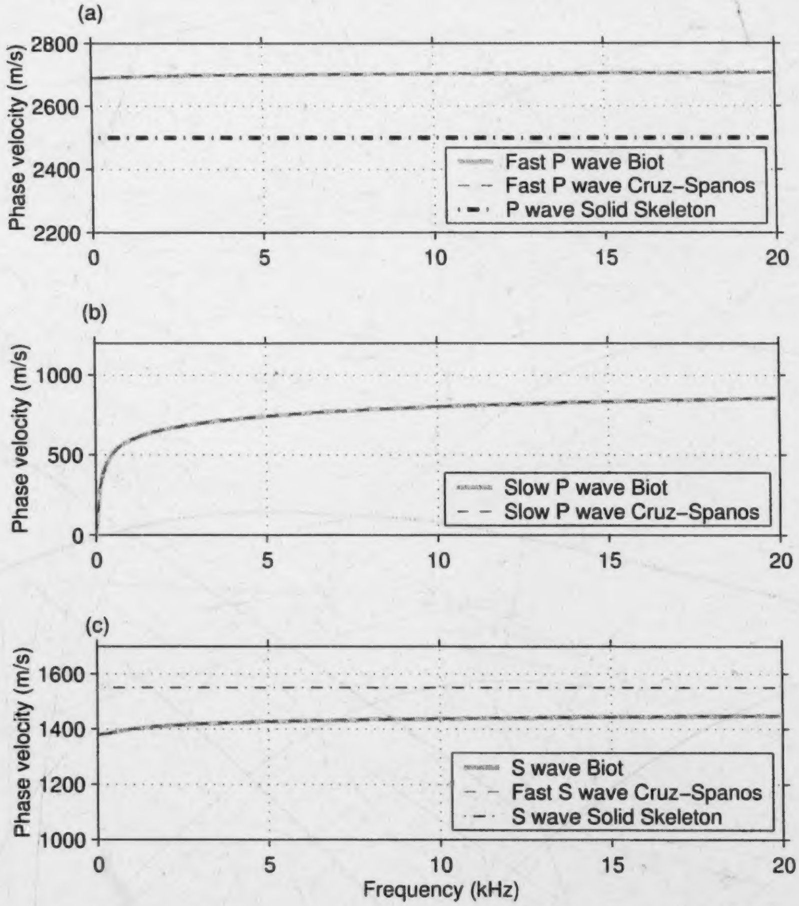

Figure 4.3: Calculated phase velocities of the fast P-wave, the slow P-wave, and the S-wave at a frequency range 0-20 kHz in a water-saturated porous material.

- The attenuation of the fast P-wave is relatively small whereas those of the S and slow P waves are large.

- The fast P and S wave attenuations of the empty solid skeleton contribute in part to the overall attenuation of the fluid-saturated porous sample (Figs. 4.5 and 4.6).

- At high frequencies (0.2-1.2 MHz) the attenuations of all the wave modes are nearly linear functions of frequency. In ranges where the attenuation is nearly linear with frequency, the quality factor will be approximately constant,

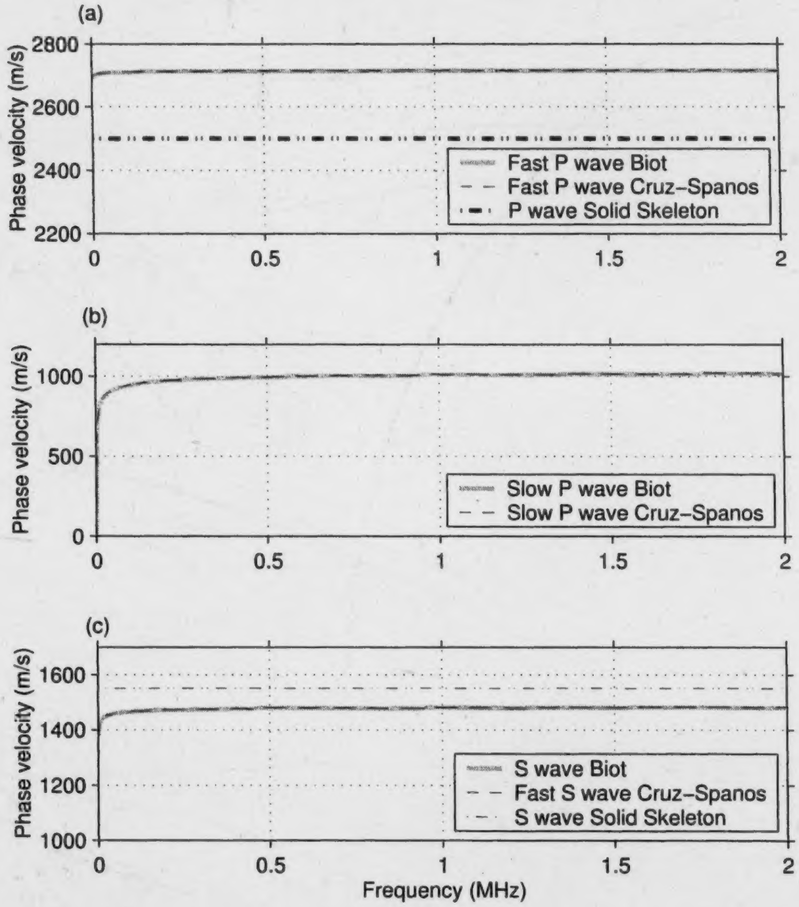

Figure 4.4: The phase velocities of the fast P, the slow P, and the S waves at a frequency range 0-2 MHz in a water-saturated porous material. Note, for this particular case the differences in the velocities predicted by each of the theories cannot be seen.

however an absolute measure of the attenuation cannot be obtained in this manner. An absolute measure would require measurements over an adequate range of low frequencies where a noticeable curvature is in the attenuation curves are expected.

- The attenuation functions change more rapidly at low frequencies, particularly for the slow P-wave.

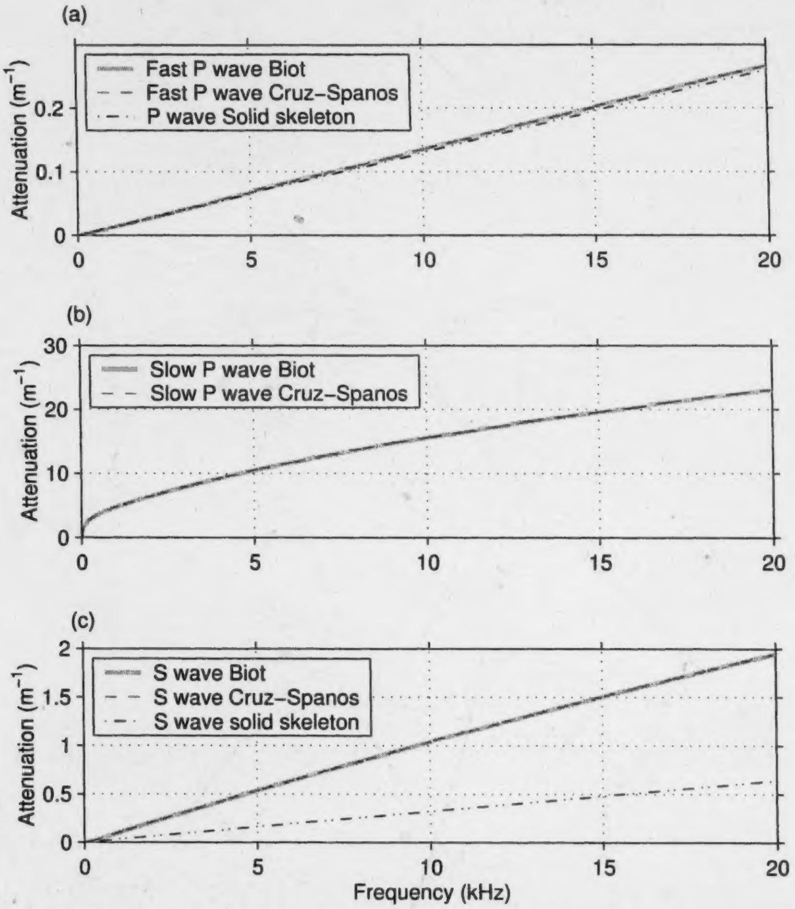

Figure 4.5: The attenuations of the fast P-wave, the slow P-wave, and the converted S wave at a frequency range 0-20 kHz in a water-saturated porous material.

- The shape of these curves is essential in the determination of the true attenuations from the actual laboratory measurements of the attenuations.

Note also that in this case both Biot and de la Cruz/Spanos theories attenuation predictions are indistinguishable.

To further study the behaviour of all the wave modes present it is essential to look at the relative amplitudes and phase angles of the motions between the solid and fluid field components. The relative amplitudes and relative phase angles are given by the complex coefficient ratios ζ_1, ζ_2, and ζ_3 given by the frequency dispersion relations for the fast P, the slow P, and the S waves. The absolute value is the relative

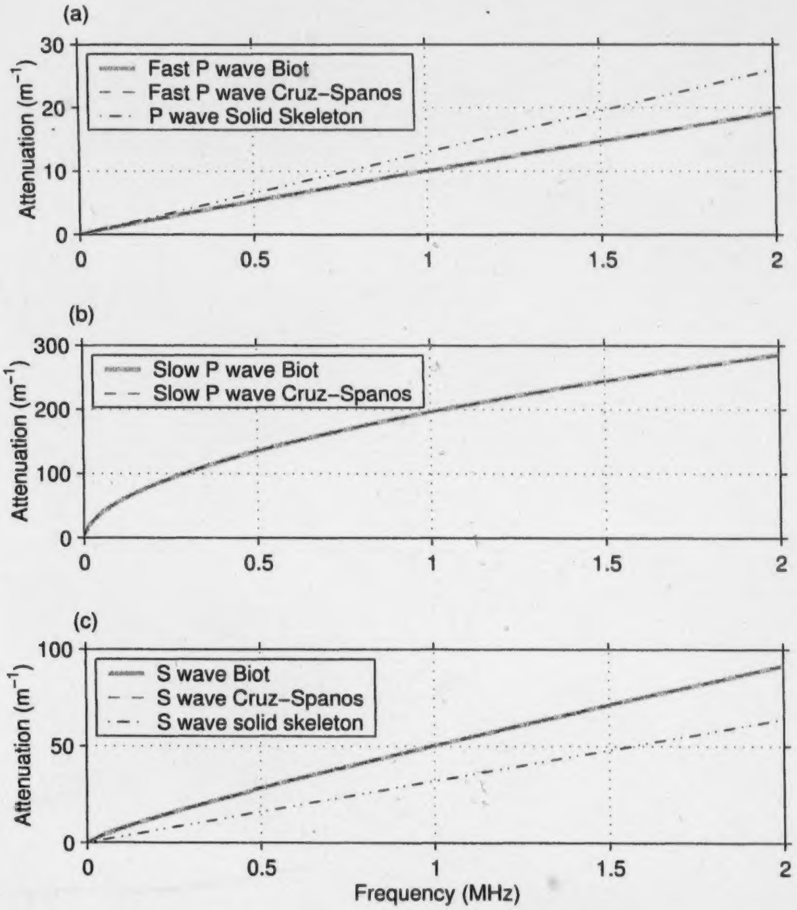

Figure 4.6: The attenuations of the fast P, the slow P, and the converted S waves at a frequency range 0-2 MHz in a water-saturated porous material.

amplitude and the angle is the relative phase. Note that in the formulation used in this chapter these coefficients are given for the solid over the fluid components. Therefore a high relative amplitude indicates a solid component dominance whereas a low value indicates a fluid component dominance.

The relative amplitudes and relative phase angles are given in figures 4.7 through 4.10 for the frequency range of 0-20 kHz and for the frequency range of 0-2 MHz. The relative amplitude of the fast P and the S waves exhibit a solid component dominance and the slow P-wave exhibits a fluid component dominance. This behaviour is more

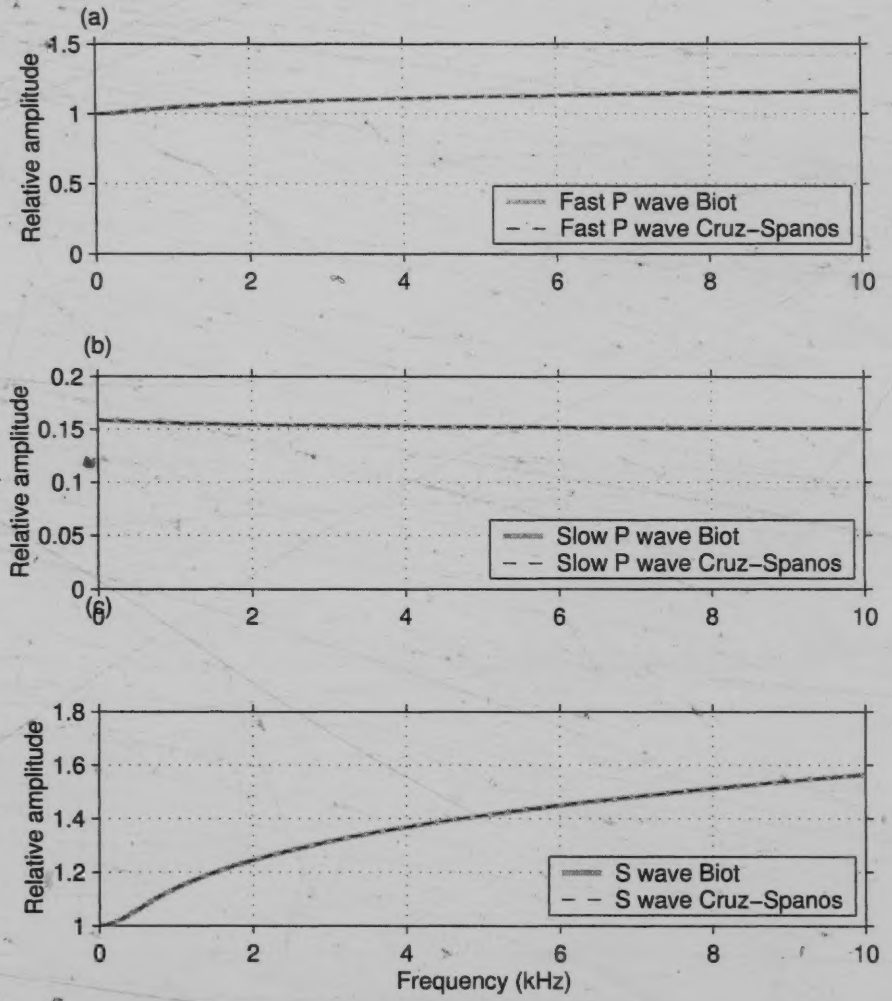

Figure 4.7: The relative amplitudes (solid over fluid) of the fast P, the slow P, and the S waves at a frequency range 0-20 kHz in a water-saturated porous material.

pronounced at high frequencies. The relative phase shows better this behaviour as a low phase angle indicates that the relative movement of the solid and the fluid is low. The larger the phase angle the greater the relative movement between the fluid and the solid is. In figure 4.9 and figure 4.10 the relative phases of the fast P, the slow P, and the S waves are shown for the frequencies in the range of 0-20 kHz and 0-2 MHz respectively.

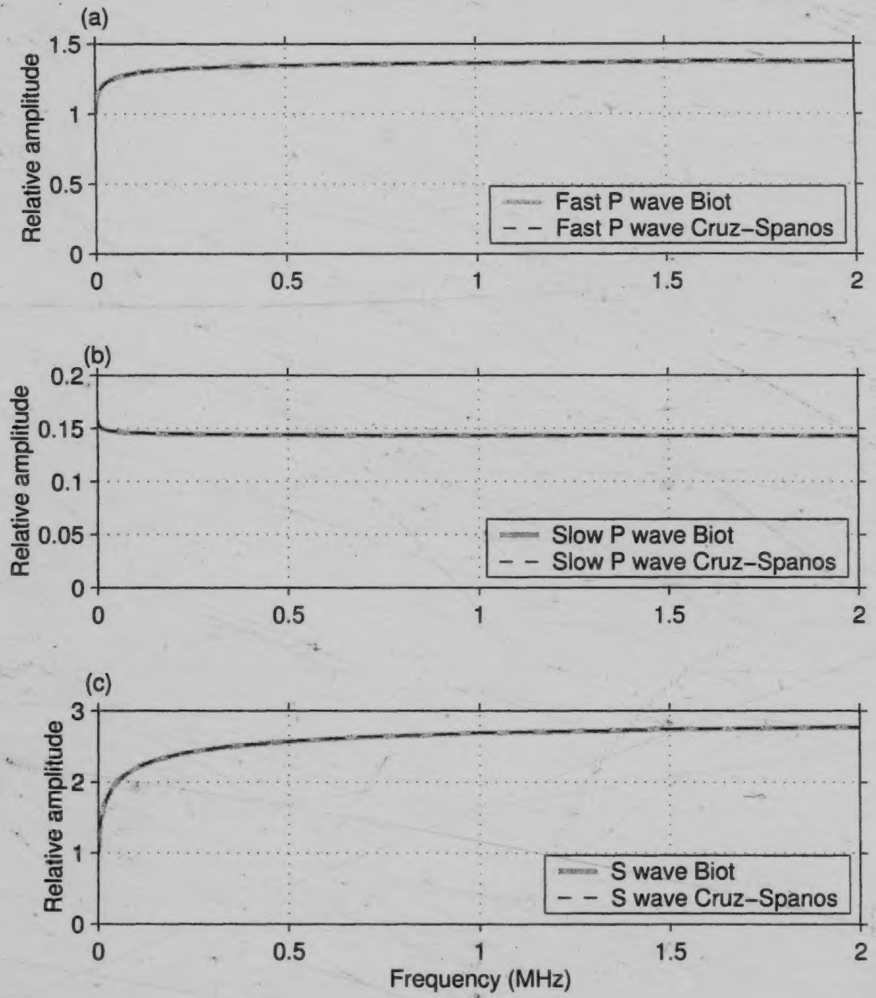

Figure 4.8: The relative amplitudes (solid over fluid) of the fast P, the slow P, and the converted S waves in a high frequency range 0-2 MHz in a water-saturated porous material.

The relative phase angle for the fast P and S waves is low with a value of nearly 5^o and 10^o respectively but still contributes to the attenuation. The slow P-wave on the other hand exhibit a relative phase angle of nearly 180^o and consequently a large relative solid-fluid movement. Therefore, the slow P-wave is mainly a wave that is dominated by fluid flow, and consequently a high dependance on the fluid properties and the pore geometry of the solid skeleton is expected for this wave.

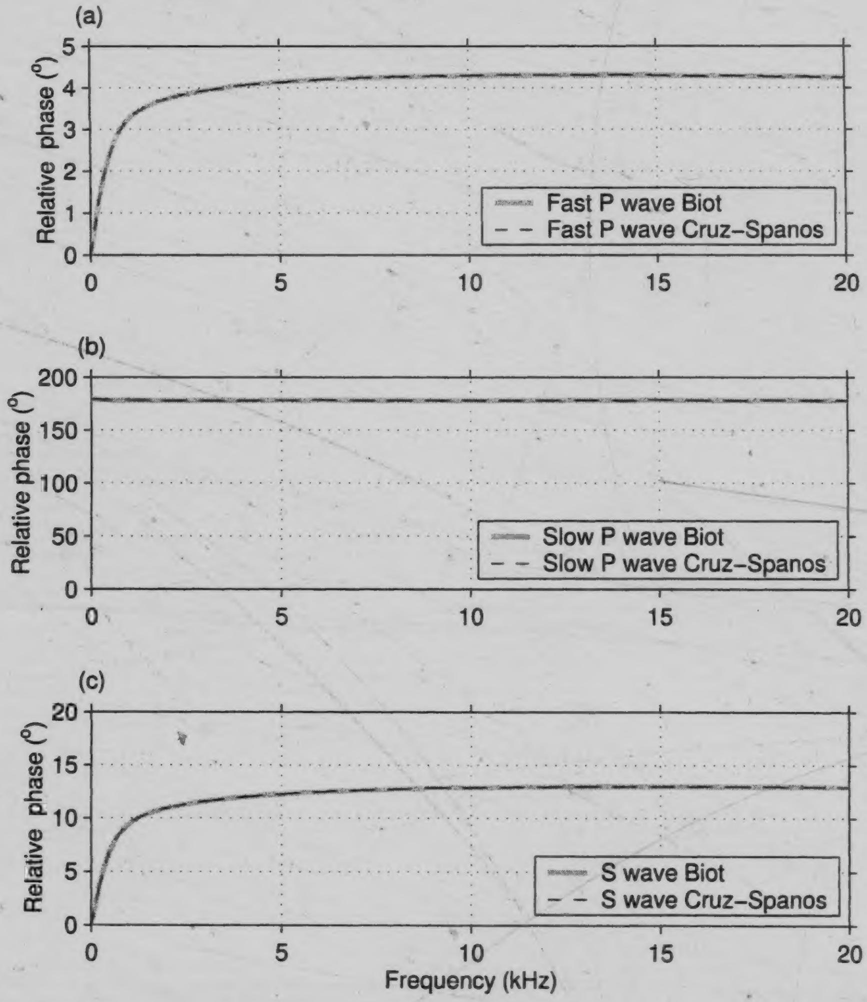

Figure 4.9: The relative phase (solid over fluid) of the fast P, the slow P, and the converted S wave in a low frequency range 0-20 kHz in a water-saturated porous material.

For an illustrative example results at 0.78 MHz, a frequency at the peak of the input signal that will be used in the forthcoming experiments on porous media, will be given. The amplitude of the fast P-wave is 35% higher in the solid skeleton than in the fluid with a relative phase angle between the two motions of 1.8°. The amplitude of the S-wave is 165% higher in the solid skeleton than in the fluid with a phase angle of 5.71°. The amplitude of the slow P-wave is 86% higher in the fluid

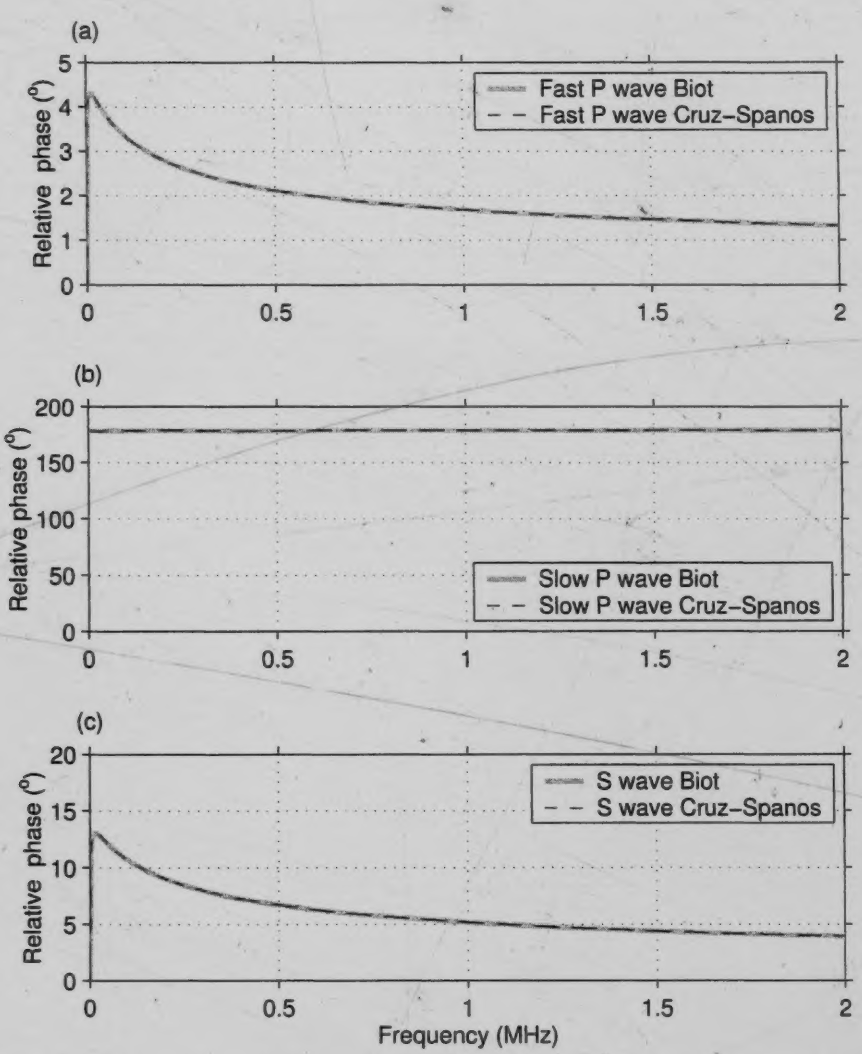

Figure 4.10: The relative phase angles (solid over fluid) of the fast P, the slow P, and the converted S waves at a frequency range 0-2 MHz in a water-saturated porous material.

than in the solid skeleton with a relative phase angle of 179°. The fluid and the solid movements for the slow P-wave at this frequency are nearly opposite of each other and therefore it has more viscous losses and higher attenuation that the fast P and S waves.

The de la Cruz/Spanos theory shows that a second S-wave also can propagate in a

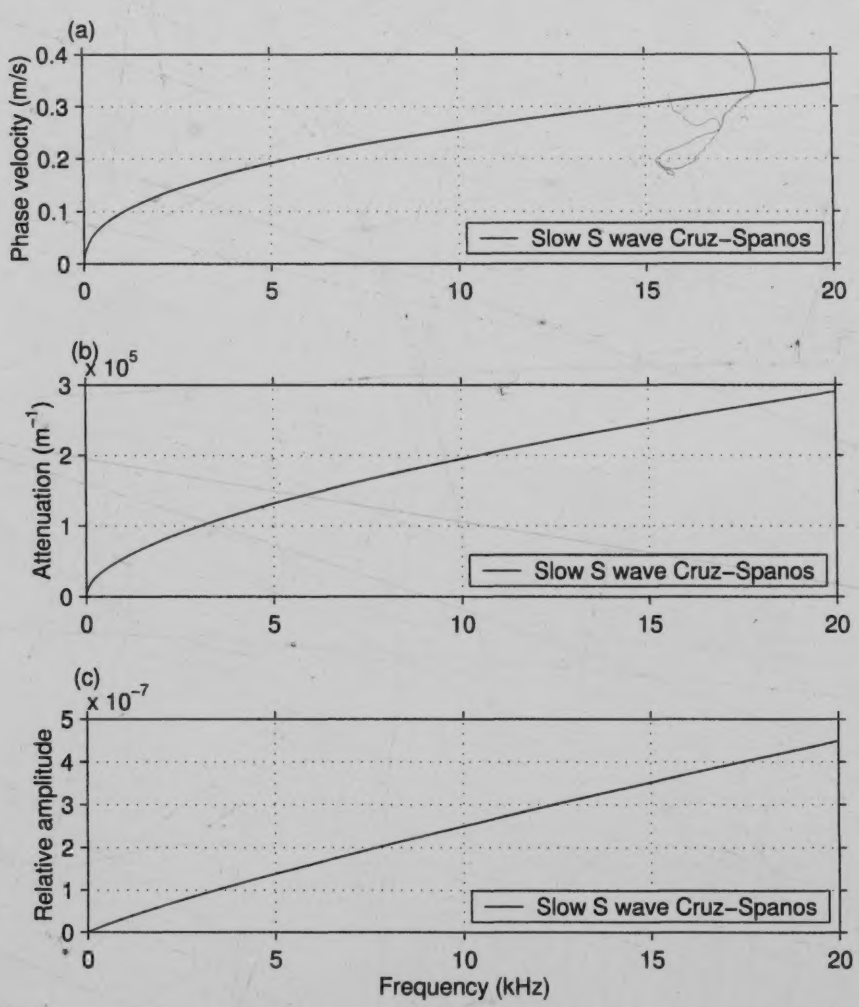

Figure 4.11: The phase velocity, the attenuation, and relative amplitudes (solid over fluid components) of the slow S-wave in de la Cruz/Spanos theory at a frequency range 0-20 kHz. Water and water-saturated porous material boundary.

fluid-saturated porous material. As explained earlier the second S-wave is essentially due to the presence of the extra terms in the formulation of the theory derived from the inclusion of the viscous stresses in the fluid stress tensor. Therefore one can expect that this wave will be essentially dominated by the fluid viscosity. Indeed the relative amplitude for this wave is highly dominated by the fluid component as illustrated by figures 4.11 and 4.12 for the frequencies in the range of 0-20 kHz and 0-

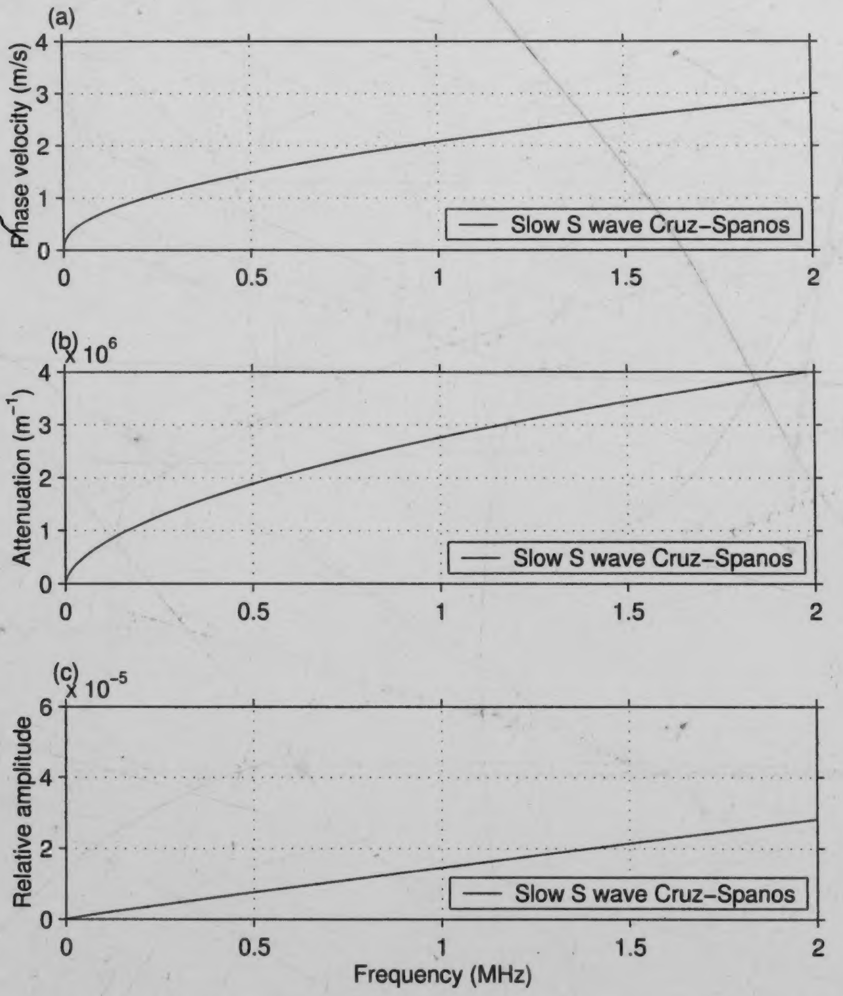

Figure 4.12: The phase velocity, the attenuation, and relative amplitudes (solid over fluid components) of the slow S-wave in de la Cruz/Spanos theory at a frequency range 0-2 MHz. Water and water-saturated porous material boundary.

2 MHz respectively. It also exhibits an extremely high attenuation and a vanishing low phase velocity. Therefore the slow S-wave can be neglected for low viscosity fluids. Consequently, the two theories are nearly equivalent for the low viscosity fluid-saturated porous material studied here.

Differences between the theories are, however, significant for high viscosity fluids. As an illustration the water is replaced by glycerol with properties given in table 4.1.

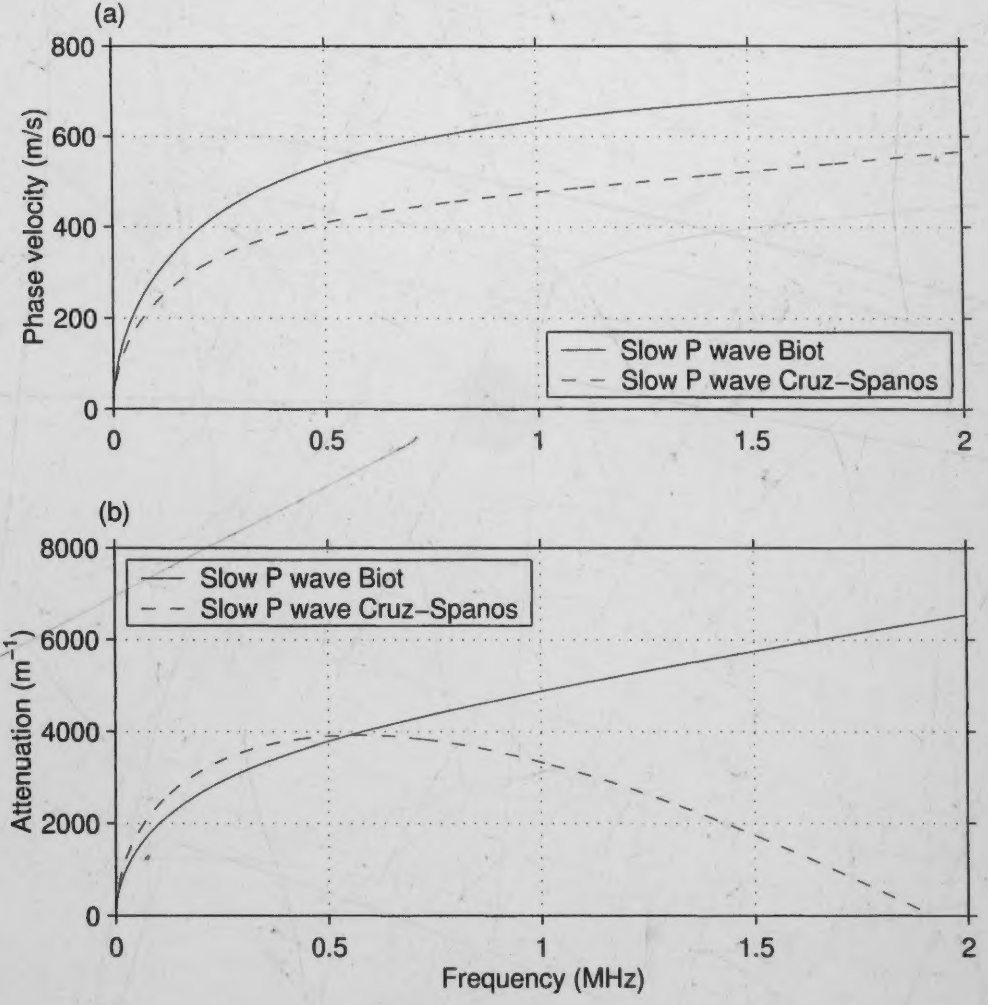

Figure 4.13: The phase velocity and the attenuation, of the slow P-wave in a glycerol-saturated porous material at a frequency range 0-2 MHz.

The calculated parameters are given in tables 4.4 and 4.5. As before, the fast P and S waves velocities and attenuations are the same. The results for the two theories show a difference only for the slow P-wave as shown in figure 4.13. The second S-wave result is shown in figure 4.14. Obviously there is a difference both in the phase velocity and attenuation of the slow P-wave as expected. The second S-wave present in de la Cruz/Spanos theory is more significant in this example than in the water saturated porous material example. This wave behaves as an S-wave in the fluid

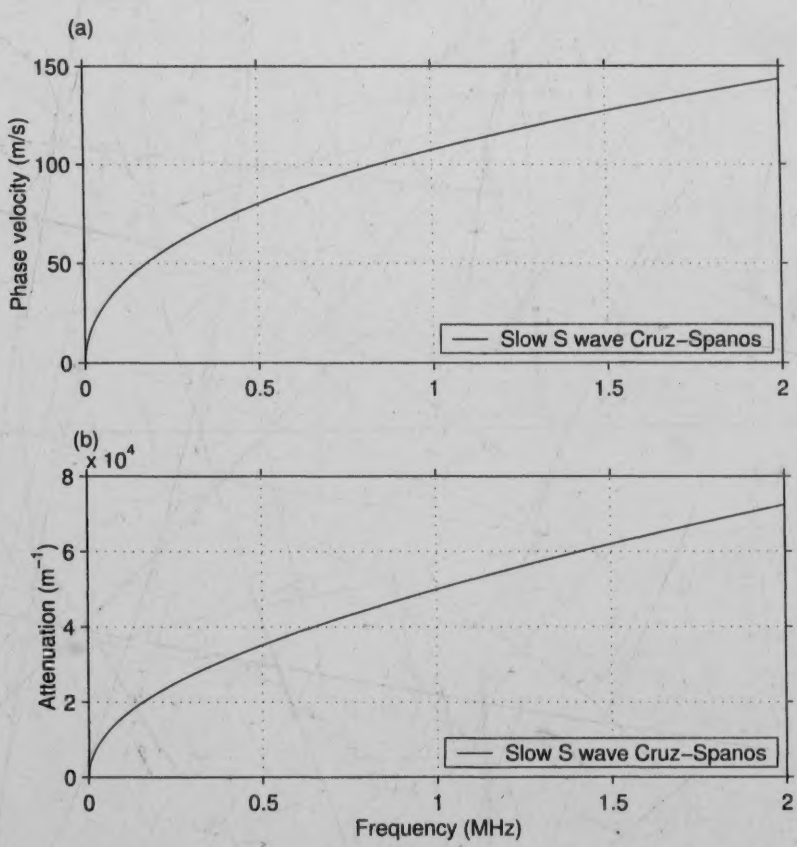

Figure 4.14: The phase velocity and the attenuation, of the slow S-wave (de la Cruz/Spanos theory) at a frequency range of 0-2 MHz.

as the results here are almost identical to those presented for wave propagation in glycerol using the Navier-Stokes equation in chapter 2 (Figs. 2.5, 2.6). Regardless, the attenuation of both waves remains large and they are likely to be difficult to detect in nature.

4.8 Influence of the solid skeleton properties on wave propagation

In this section a study of the influence of the solid skeleton properties on the wave propagation will be examined numerically. It would be expected that the permeability and viscosity will influence greatly the propagation of the slow P-wave as it highly depends on fluid flow. The goal here is to determine the parameters that influence the different wave modes.

The propagation of pure elastic, i.e. non-dissipative, waves in fluid-saturated materials is discussed in Biot (1956a). Pure elastic waves propagate in the absence of energy losses in the solid component and in the absence of viscous losses. Energy losses will be negligible only when the solid is purely elastic and the fluid is non-viscous or the permeability is significantly very high. In most rocks these conditions are very rarely met. As waves propagate through a fluid-saturated porous medium, the fluid movement relative to the solid contributes to the overall attenuation. The influence of the solid skeleton properties and fluid flow will be considered here. It is important to note the attenuation might also be influenced by other processes (Biot, 1962a; Biot, 1962b) such as chemical interactions that are not considered here. As well we have ignored potential of heterogeneous fluid pressure in the pore space that leads to what is called "squirt flow" mechanisms (O'Connell and Budiansky, 1977; Dvorkin and Nur, 2000a; Dvorkin and Nur, 2000b).

The influence of the relative motion between the fluid and the solid components depends also on fluid viscosity and permeability since these two parameters influence greatly the relative motion and thus energy losses. Two examples are shown in figures 4.15 and 4.16 where the permeability is varied while other parameters are kept constant as for the water-saturated porous material described in tables 4.2 and 4.4. For low permeability materials the increase of permeability results in an increase of the attenuation of the S and fast P waves while the attenuation of the slow P-wave decreases (Fig. 4.15). In the example given in figure 4.15 the permeability varied from 0.004×10^{-12} m^2 to 0.01×10^{-12} m^2. The drop of the attenuation of the slow P-wave with increasing permeability is directly related to the fact that the fluid motion has less resistance to flow, the slow P-wave being mainly driven by fluid flow. On the other hand the relative flow for the fast P and S waves are less important as for these two waves the relative phase angle between the fluid and solid components is small. An increase of permeability (for low permeability materials) will allow more flow causing more viscous losses. However for high permeability materials (Fig. 4.15) where the permeability varied from 0.04×10^{-12} m^2 to 0.1×10^{-12} m^2 we notice a different behaviour for the fast P and S waves with the attenuation instead

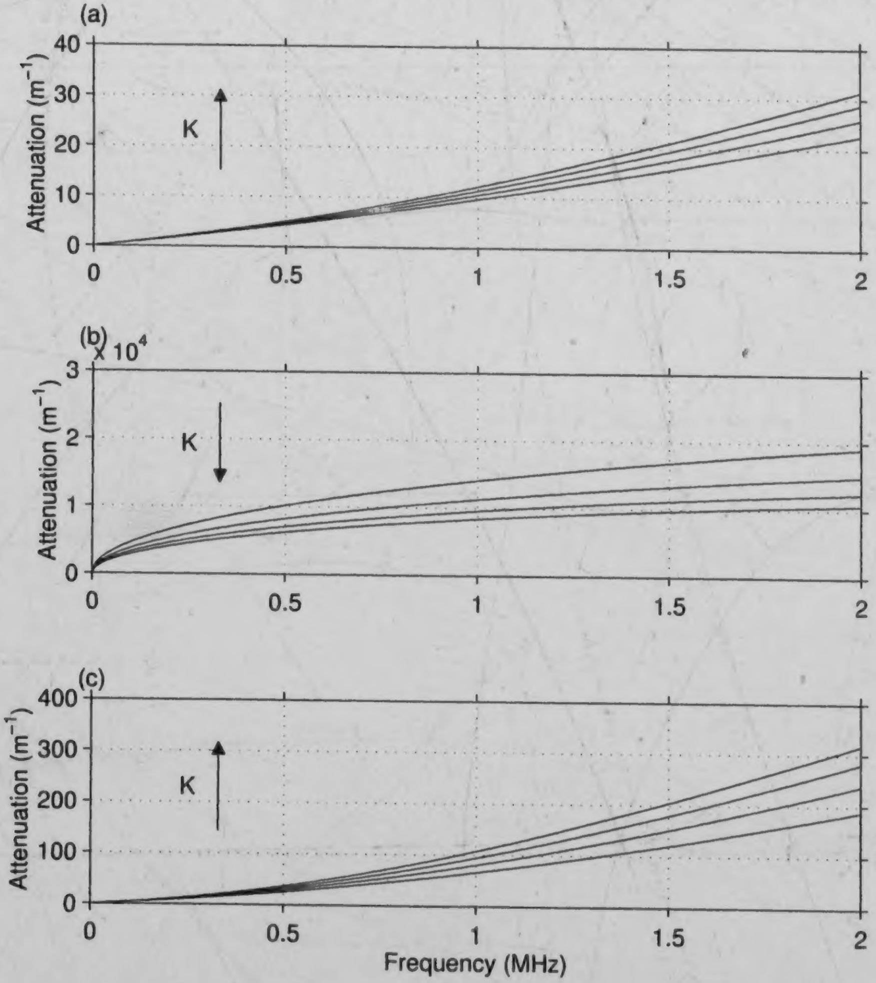

Figure 4.15: Influence of permeability on the attenuation of the fast P-wave (a), the slow P-wave (b), and the S-wave (c) in a water-saturated porous material. Permeability K varies from 0.004×10^{-12} m^2 to 0.01×10^{-12} m^2 (0.00412 D to 0.01031 D) increasing as indicated by the arrows.

decreasing with increasing permeability. For high permeability materials an increase of permeability would make the viscous losses less pronounced and therefore the attenuation would decrease with a permeability increase. However the attenuation of the slow P-wave would still decrease as this type of wave is mainly flow driven.

It is important to note here that the attenuation part linked directly to fluid

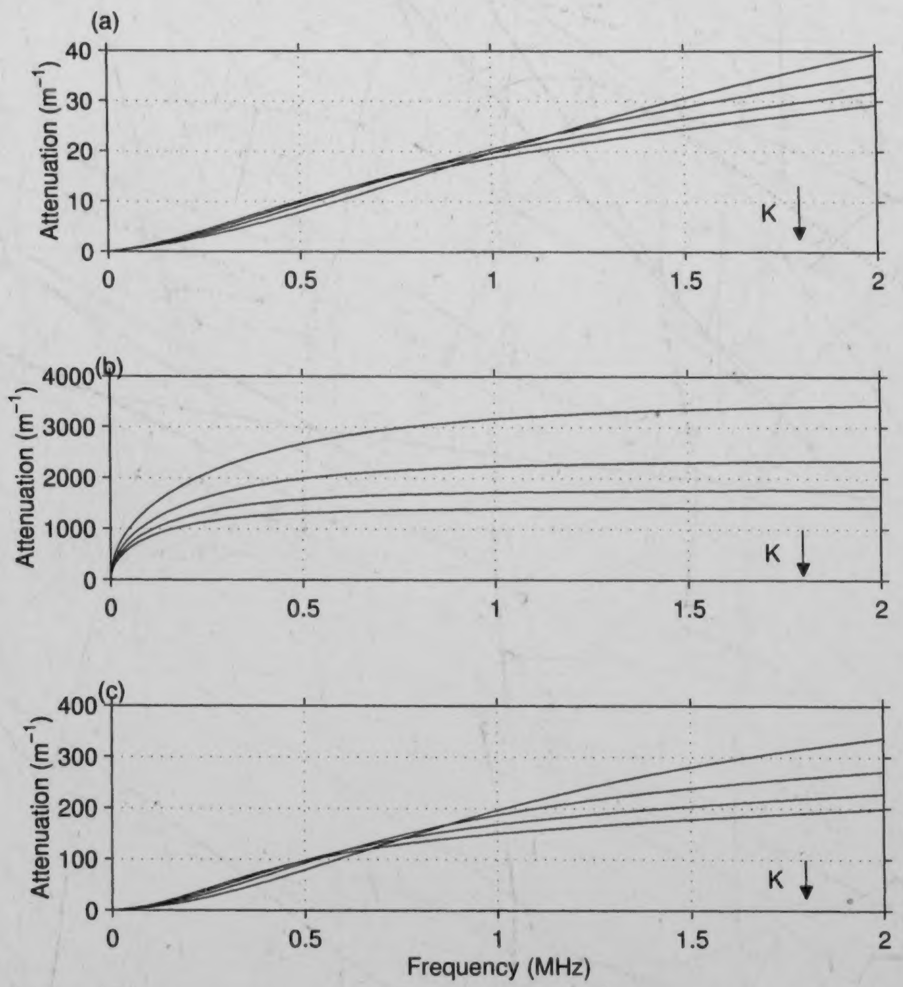

Figure 4.16: Influence of permeability on the attenuation of the fast P-wave (*a*), the slow P-wave (*b*), and the S-wave (*c*) in a water-saturated porous material. Permeability K varies from 0.04×10^{-12} m^2 to 0.1×10^{-12} m^2 (0.0412 D to 0.1031 D) increasing as indicated by the arrows.

flow is represented in the equations of motion by $\frac{F(\omega)\eta\beta^2}{K}$ which is the viscous drag coefficient. η is the shear viscosity, $F(\omega)$ is the viscosity correction factor, β is the porosity, and K is the permeability. Therefore an increase of viscosity would have the same effect as a decrease of permeability or vice-versa.

Now it is important to examine the effect of the solid skeleton on the different

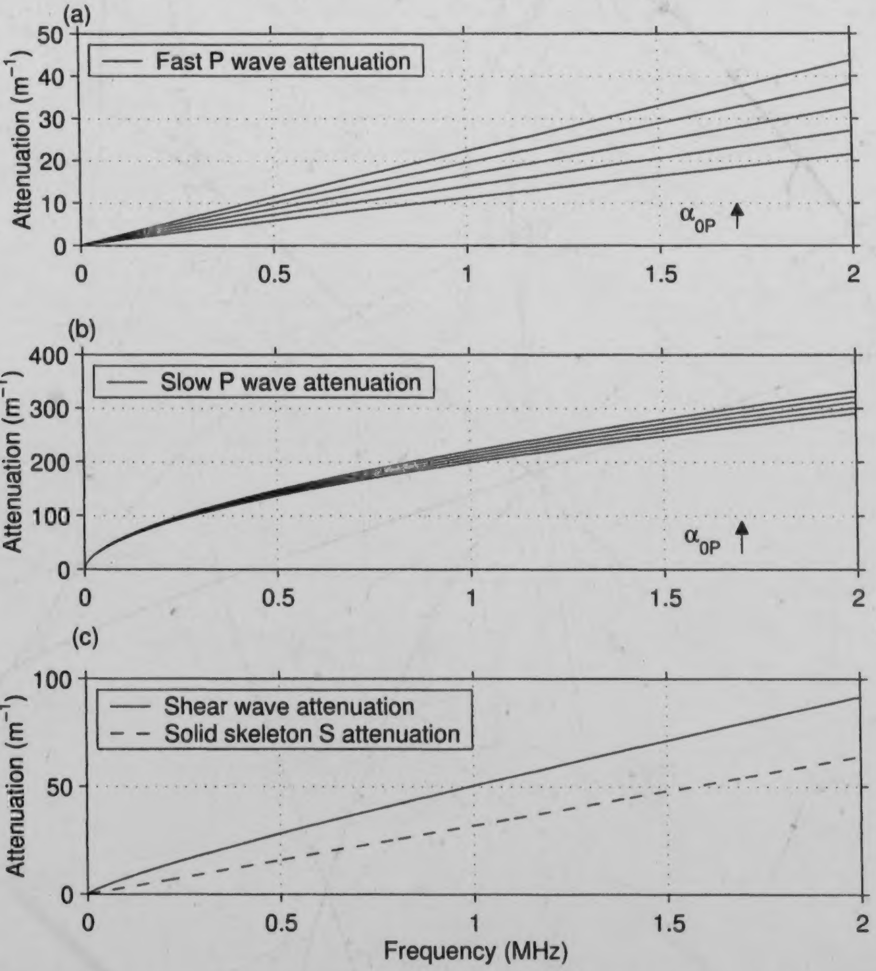

Figure 4.17: Influence of the P-wave attenuation of the solid skeleton on the overall attenuation in a water-saturated porous material. (a) fast P-wave, (b) slow P-wave, and (c) S-wave. The arrow shows the direction of increase of α_{0P} for the curves shown. The S-wave attenuation of the solid skeleton is kept at $\alpha_{0S} = 10^{-6}$ s/m. α_{0P} varied from 2×10^{-6} s/m to 5×10^{-6} s/m.

waves modes propagating in fluid-saturated porous materials. Let a porous material be described again by the parameters given in tables 4.2 and 4.4 except now the attenuation of the P and S waves in the solid skeleton are varied. In figure 4.17 the S-wave attenuation of the solid skeleton is kept at 10^{-6} s/m while the P-wave attenuation is varied from 2×10^{-6} s/m to 5×10^{-6} s/m. The increase of the P-wave

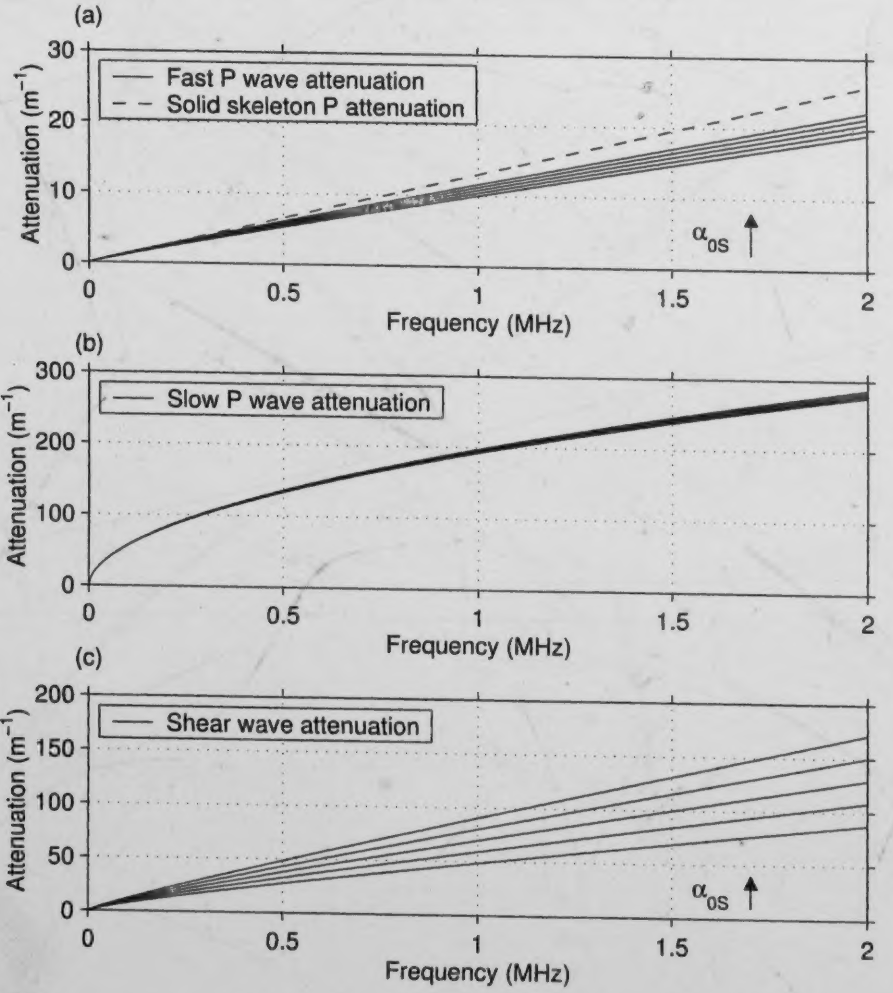

Figure 4.18: Influence of the S-wave attenuation of the solid skeleton on the overall attenuation in a water-saturated porous material. (*a*) fast P-wave, (*b*) slow P-wave, and (*c*) S-wave. The arrow shows the direction of increase of α_{0S} for the curves shown. The P-wave attenuation of the solid skeleton is kept at $\alpha_{0P} = 1 \times 10^{-6}$ s/m. α_{0S} varied from 20×10^{-6} s/m to 50×10^{-6} s/m.

attenuation of the solid skeleton has no effect on the S-wave attenuation and very little effect on the slow P-wave. Therefore the attenuation of the P-wave of the solid skeleton affects mainly the fast P-wave attenuation. In figure 4.18 the P-wave attenuation of the solid skeleton is kept at 1×10^{-6} s/m while the S-wave attenuation of the solid skeleton is varied from 20×10^{-6} s/m to 50×10^{-6} s/m. The increase of the S-wave attenuation of the solid skeleton also has very little effect on the overall attenuation of the slow P-wave. The change of the S-wave attenuation of the solid skeleton affects mainly both the S-wave and fast P-wave attenuations. Therefore the solid skeleton attenuation has very little effect on the slow P-wave which is in agreement with the fact that this wave is mainly flow driven and affected mainly by parameters that contribute to resistance to flow such as permeability K, viscosity η, porosity β, and pore structure of the solid skeleton.

4.9 Choice of parameters to model fluid-saturated porous materials

In contrast with homogeneous, isotropic, and elastic media, fluid-saturated porous materials involve more parameters that are required in order to properly model wave propagation in such media. In this section we focus on how to properly choose the various parameters involved in the description of wave propagation in fluid-saturated porous materials.

As described in section 4.5 most of the parameters can be measured in laboratory experiments. However some of these parameters are not readily measurable such as the mass transfer ρ_{12} and the viscosity correction factor $F(\omega)$. These are dynamic parameters and therefore need to be determined or inferred in dynamic experiments. ρ_{12} is given by equation 4.60 and the viscosity correction factor $F(\omega)$ by

$$F(\omega) = \left[1 + i\frac{4\varsigma^2 K^2 \rho^{(f)}\omega}{\eta\Delta^2\beta^2}\right]^{\frac{1}{2}} \tag{4.94}$$

where Δ has dimensions of length and is given within:

$$\frac{2}{\Delta} = \frac{\int |\vec{u}_p(\vec{r}_w)|^2 dA}{\int |\vec{u}_p(\vec{r})|^2 dV} \tag{4.95}$$

Most of the parameters present in equation 4.94 are otherwise readily measurable. These are the permeability K, the shear viscosity η, the porosity β, and the fluid density $\rho^{(f)}$. The dynamic parameter Δ is not readily measurable as relative fluid-solid movement must be found. One way to determine these parameters is to fit the observed data, for example in a reflectivity experiment, to the modelled one by a choice of a proper set of these parameters. $F(\omega)$ given by equation 4.94 is the complex conjugate of that given by equation 4.62 as found in Johnson et al. (1987). The reason the conjugate is used here is important to mention as one must always keep in mind the way the problems are solved. In this study the wave number $\vec{k}$ is defined as $k_r - ik_i$ as the solutions for wave propagation were defined as $e^{i(\omega t - \vec{k}\cdot\vec{x})}$ where $\vec{x}$ is the position vector. An alternate, perhaps more direct, approach to determine these very difficult to measure dynamic parameters will be described here.

Recall the equations of propagation of S-waves in fluid-saturated porous media. These are given by the coupled equations

$$(1-\beta)\rho^{(s)}\frac{\partial^2}{\partial t^2}\vec{\psi}^{(s)} - \rho_{12}\frac{\partial^2}{\partial t^2}\left(\vec{\psi}^{(s)} - \vec{\psi}^{(f)}\right) + F(\omega)\frac{\eta\beta^2}{K}\frac{\partial}{\partial t}\left(\vec{\psi}^{(s)} - \vec{\psi}^{(f)}\right) = \mu_M\nabla^2\vec{\psi}^{(s)} \quad (4.96)$$

$$\beta\rho^{(f)}\frac{\partial^2}{\partial t^2}\vec{\psi}^{(f)} + \rho_{12}\frac{\partial^2}{\partial t^2}\left(\vec{\psi}^{(s)} - \vec{\psi}^{(f)}\right) - F(\omega)\frac{\eta\beta^2}{K}\frac{\partial}{\partial t}\left(\vec{\psi}^{(s)} - \vec{\psi}^{(f)}\right) = 0 \quad (4.97)$$

In these coupled equations there are seven unknown parameters, which are the porosity β, the mass transfer ρ_{12}, the viscosity correction factor $F(\omega)$, the fluid shear viscosity η, the permeability K, the shear modulus of the solid skeleton μ_M, and the fluid density $\rho^{(f)}$. It is important to note that μ_M can be determined by evacuating the fluid and measuring the S-wave velocity of the "dry" solid skeleton. In that case, equations 4.96 and 4.97 lead to

$$(1-\beta)\rho^{(s)}\frac{\partial^2}{\partial t^2}\vec{\psi}^{(s)} = \mu_M\nabla^2\vec{\psi}^{(s)} \quad (4.98)$$

A measurement of the shear plane wave velocity and attenuation of the "dry" solid skeleton will give a good approximation for the complex valued μ_M. Replacing the process by saturating the sample by a fluid with density $\rho^{(f)}$ equations 4.96 and 4.97 lead to

$$(1-\beta)\rho^{(s)}\frac{\partial^2}{\partial t^2}\vec{\psi}^{(s)} + \beta\rho^{(f)}\frac{\partial^2}{\partial t^2}\vec{\psi}^{(f)} = \mu_M\nabla^2\vec{\psi}^{(s)} \quad (4.99)$$

Recall that the solid and fluid components for the shear plane wave are related by a complex number ζ_3. A measurement of the S-wave velocity and attenuation leads to the determination of the complex number ζ_3 (equation 4.28) and would be given by

$$\zeta_3 = \frac{\omega^2\beta\rho^{(f)}}{k_3^2\mu_M - \omega^2(1-\beta)\rho^{(s)}} \quad (4.100)$$

For plane waves equations 4.97 and 4.98 lead to

$$\omega^2(1-\beta)\rho^{(s)} - \omega^2(\zeta_3 - 1)\left[\rho_{12} + iF(\omega)\frac{\eta\beta^2}{\omega K}\right] = k_3^2\mu_M\zeta_3 \tag{4.101}$$

$$\beta\rho^{(f)} + (\zeta_3 - 1)\left[\rho_{12} + iF(\omega)\frac{\eta\beta^2}{\omega K}\right] = 0 \tag{4.102}$$

Now let the drag coefficient $\tilde{\rho_{12}}$ be replaced by G for clarity as it is different from ρ_{12}. G is given by

$$G = \rho_{12} + iF(\omega)\frac{\eta\beta^2}{\omega K} \tag{4.103}$$

Equation 4.102 is readily solved for G and leads to

$$G = \frac{\beta\rho^{(f)}}{1-\zeta_3} \tag{4.104}$$

G also appears in the coupled equations 4.5 and 4.6 for propagation of P plane waves. Therefore the measurement of the shear modulus of the "dry" solid skeleton μ_M, the density of the mineral grains $\rho^{(s)}$, the density of the fluid $\rho^{(f)}$, the porosity β, and the fluid-saturated shear velocity and attenuation that will define k_3 is sufficient. This is an important point as measuring these parameters allows one to avoid the measurement of the shear viscosity η, the permeability K, and particularly the mass transfer ρ_{12}, and the viscosity correction factor $F(\omega)$. This approach simplifies tremendously the problem and reduces drastically the number of measurements and more importantly the mass transfer ρ_{12} and the viscosity correction factor $F(\omega)$ need not to be inferred and therefore no model is required for these parameters. However to extrapolate the data to other frequencies a model for both ρ_{12} and $F(\omega)$ is required. Assuming the model for ρ_{12} is that given by equation 4.60 and the model for $F(\omega)$ that given by equation 4.94 it is possible to infer the parameter Δ and it is given by

$$\Delta = \frac{2\varsigma K}{\beta\delta_{visc}}\left(\frac{1}{F_r F_i}\right)^{\frac{1}{2}} \tag{4.105}$$

where δ_{visc} is given by equation 4.66, F_r the real part of $F(\omega)$, and F_i the imaginary part of $F(\omega)$. This result assumes the knowledge of β, ς, η, $\rho^{(f)}$, and K.

If the frequency is high enough so that the real and imaginary parts of $F(\omega)$ are approximately equal then equation 4.104 can be used to infer ρ_{12} and $F(\omega)$ without assuming a model for ρ_{12}. In this case equation 4.104 can be rewritten as

$$\rho_{12} + F_r(\omega)\frac{\eta\beta^2}{\omega K}(i-1) = G_r + iG_i \tag{4.106}$$

where $F_r(\omega)$ is the real part of $F(\omega)$. Equation 4.106 then provides F_r and ρ_{12}. These are given by

$$\rho_{12} = G_r + G_i \tag{4.107}$$

$$F(\omega) = \frac{G_i K \omega}{\eta \beta^2}(1+i) \tag{4.108}$$

The mass transfer ρ_{12} and the viscosity correction factor $F(\omega)$ are given in readily measurable quantities that are the permeability K, the porosity β, the fluid shear viscosity η, and G. Taking the approximation for $F(\omega)$ given by Johnson et al. (1987) for high frequencies we have

$$\Delta = \frac{\varsigma\beta}{G_i}\left(\frac{2\rho^{(f)}\eta}{\omega}\right)^{\frac{1}{2}} \tag{4.109}$$

Now return to the illustration example treated in the previous sections. Let us assume that the S-wave velocity and attenuation of the fluid-saturated porous sample are measured properly. Following the procedure described above using the wave number for the S-wave as a result from the modelling in section 4.8 we get ρ_{12}, $F(\omega)$, and consequently Δ. The results using the exact and the approximate methods are identical and are given in table 4.6. *This shows that it is very useful to use the shear velocity and attenuation measurements of the fluid-saturated porous sample hence avoiding any assumption with regards to ρ_{12} and $F(\omega)$. It is also important to note these parameters are very sensitive to small variations of the fluid-saturated S-wave velocity and attenuation.*

Shear wave velocity m/s	Shear wave attenuation m^{-1}	ρ_{12} $\mathrm{kg/m^3}$	Δ $\mu\mathrm{m}$
1480.6	40.62	−194	10

Table 4.6: The inferred ρ_{12}, and Δ from the S-wave velocity and attenuation of the fluid-saturated porous sample.

4.10 Conclusions

In the light of what has been developed in this chapter wave propagation in fluid-saturated porous materials involve more complex wave equations with several parameters that affect both the phase velocity and the overall attenuation. This is in contrast with the non-porous elastic and isotropic materials studied in chapters 2 and 3. In general theory suggests that three wave modes (or four if the slow S-wave is included) can propagate in fluid-saturated porous materials. It is found that both Biot and de la Cruz/Spanos theories lead to similar results when the unjacketed bulk modulus is equal to the bulk modulus of the solid mineral grains for a low viscosity fluid such as water. However, if the unjacketed bulk modulus is not equal to the bulk modulus of the mineral grains the volume of fluid that enters the pore during an unjacketed test need not to be measured in Hickey et. al (1995) parameter determination and must be measured in the Biot and Willis (1957) parameter determination. In the case of water as the fluid saturant the second S-wave present in the de la Cruz/Spanos theory can for practical purposes be neglected. It is also found that the slow P-wave is mainly driven by fluid flow and is affected very little by the attenuation of the solid skeleton. It is mainly affected by fluid properties and by the pore structure of the solid skeleton. The attenuations of the fast P-wave and the S-wave are highly dependent on the solid skeleton properties. For modelling wave propagation in fluid porous materials several parameters need to be measured to properly describe the behaviour of the observations one might seek in laboratory experiments such as reflectivity experiments. It is important to include as much as one can of all the parameters and reduce the assumptions in order to simplify the formulation of the model that would be used in comparison with observations.

Chapter 5

Reflection-transmission of plane waves and bounded acoustic pulses in fluid-saturated porous media

5.1 Introduction

In this chapter the boundary value problem at an interface between a fluid and a fluid-saturated porous material will be approached using both plane waves and bounded acoustic pulses in a similar manner as that employed in the fluid-elastic isotropic solid boundary value problem solved in chapter 2. Fluid-saturated porous materials are more complex and require many parameters in contrast with elastic-isotropic materials as discussed in chapter 4. To understand the reflectivity and transmission of bounded acoustic pulses in fluid-saturated porous materials the boundary value problem is first solved for plane waves and the result extended to bounded acoustic pulses. Bounded acoustic pulses as described in chapter 2 and chapter 3 can be decomposed onto plane wave components in the Fourier domain in both time and space.

In fluid-saturated porous materials two compressional waves, a fast P-wave and a slow P-wave can propagate. When low viscosity fluid saturates porous materials only one S-wave can propagate. A second S-wave, however, exists for high viscosity fluids as found in the de la Cruz/Spanos theory. In the present study all forthcoming reflectivity experiments will be conducted on synthetic sandstones with water as the fluid saturant. In the case where the unjacketed bulk modulus K_{un} is equal to the bulk modulus of the mineral grains $K^{(s)}$ and that the fluid saturant has low viscosity the Biot theory and de la Cruz/Spanos theory are nearly equivalent. Therefore it is assumed that the second S-wave is negligible.

In order to solve the boundary value problem a set of boundary conditions must be used. There are two sets of boundary conditions that were developed under different physical bases. One set of boundary conditions is developed by Deresiewicz and Skalak (1963) based on Biot theory. The other set of boundary conditions was developed by de la Cruz/Spanos (1989a). Here both sets of boundary conditions will be re-examined for the boundary between a fluid and a fluid-saturated porous material. The boundary value problem of a fluid and a fluid-saturated porous material will be treated in two dimensions and the reference frame will be that used in chapter 2 (Fig. 2.1).

5.2 Wave equations

Here the second S-wave is neglected and the unjacketed bulk modulus K_{un} is assumed equal to the bulk modulus of the mineral grains $K^{(s)}$. In a boundary value problem for reflectivity and transmission in fluid-saturated porous materials it is essential to first determine the wave numbers of all wave modes that would be generated at the boundary between the fluid and the fluid-saturated porous material assuming that all parameters were known. Each wave number will provide both the phase velocity and the attenuation for the corresponding wave mode. Depending on the boundary value problem two or three waves will be generated at the interface and would propagate into the fluid-saturated porous material. Only one P-wave can be reflected back into the fluid medium. Recall the wave equations for both compressional and shear waves in a porous medium from equations 4.5, 4.6, 4.21, and 4.22. These are

$$\begin{aligned}(1-\beta)\rho^{(s)}\frac{\partial^2}{\partial t^2}\phi^{(s)} - \rho_{12}\frac{\partial^2}{\partial t^2}\left(\phi^{(s)}-\phi^{(f)}\right) + F(\omega)\frac{\eta\beta^2}{K}\frac{\partial}{\partial t}\left(\phi^{(s)}-\phi^{(f)}\right) &= \\ \nabla^2\left[\left(A+2\mu_M\right)\phi^{(s)} + Q\phi^{(f)}\right] & \qquad (5.1)\end{aligned}$$

and

$$\beta\rho^{(f)}\frac{\partial^2}{\partial t^2}\phi^{(f)} + \rho_{12}\frac{\partial^2}{\partial t^2}\left(\phi^{(s)} - \phi^{(f)}\right) - F(\omega)\frac{\eta\beta^2}{K}\frac{\partial}{\partial t}\left(\phi^{(s)} - \phi^{(f)}\right) = \nabla^2\left[Q\phi^{(s)} + R\phi^{(f)}\right] \quad (5.2)$$

for dilatational waves and

$$(1-\beta)\rho^{(s)}\frac{\partial^2}{\partial t^2}\vec{\psi}^{(s)} - \rho_{12}\frac{\partial^2}{\partial t^2}\left(\vec{\psi}^{(s)} - \vec{\psi}^{(f)}\right) + F(\omega)\frac{\eta\beta^2}{K}\frac{\partial}{\partial t}\left(\vec{\psi}^{(s)} - \vec{\psi}^{(f)}\right) = \mu_M\nabla^2\vec{\psi}^{(s)} \quad (5.3)$$

$$\beta\rho^{(f)}\frac{\partial^2}{\partial t^2}\vec{\psi}^{(f)} + \rho_{12}\frac{\partial^2}{\partial t^2}\left(\vec{\psi}^{(s)} - \vec{\psi}^{(f)}\right) - F(\omega)\frac{\eta\beta^2}{K}\frac{\partial}{\partial t}\left(\vec{\psi}^{(s)} - \vec{\psi}^{(f)}\right) = 0 \quad (5.4)$$

for shear waves. Equations 5.1 through 5.4 were solved for planes waves in the previous chapter with wave numbers for the fast and slow P waves given by

$$k_l = \omega\left[\frac{\zeta_l(1-\beta)\rho^{(s)} + \beta\rho^{(f)}}{\zeta_l(A + 2\mu_M + Q) + R + Q}\right]^{\frac{1}{2}} \quad (5.5)$$

where the various parameters were defined in chapter 4. ζ_l is a complex number that relates the component of the corresponding P-wave in the solid and the component of the corresponding P-wave in the fluid. It is found from the frequency equation 4.12 where $l = 1, 2$ for the fast P and slow P waves respectively. The S-wave number is given by

$$k_3 = \omega\left[\frac{(1-\beta)\rho^{(s)}\zeta_3 + \beta\rho^{(f)}}{\mu_M\zeta_3}\right]^{\frac{1}{2}} \quad (5.6)$$

where ζ_3 is again a complex number that relates the component of the S-wave in the solid and the component of the S-wave in the fluid. It is given by equation 4.28.

Therefore if all parameters involved in equations 5.1 and 5.4 are known the wave numbers are determined by equations 5.5 through 5.6 where the complex constants ζ_l, for $l = 1$ and $l = 2$, are given via equation 4.12 and the complex constant ζ_3 via equation 4.28. These wave numbers provide the attenuation and phase velocity for each wave mode.

5.3 Stress components

Recall the stresses in the solid and in the fluid components respectively from equations B.1 and B.2

$$\sigma_{ij} = 2\mu_M e_{ij} + (Ae_{ll} + Q\epsilon_{kk})\,\delta_{ij} \tag{5.7}$$

$$s = Qe_{ll} + R\epsilon_{kk} \tag{5.8}$$

where again here the various parameters are defined in chapter 4. A repeated index implies summation over the index. e and ϵ are given by

$$e_{ij} = \frac{1}{2}\left(u_{i,j}^{(s)} + u_{j,i}^{(s)}\right) \tag{5.9}$$

$$\epsilon_{ij} = \frac{1}{2}\left(u_{i,j}^{(f)} + u_{j,i}^{(f)}\right) \tag{5.10}$$

where i, j means the derivative of the i^{th} component with respect to the j^{th} direction.

For a two dimensional problem use the reference frame defined in chapter 2 (Fig. 2.1) and let all displacements lie on the plane $(\hat{x}, \hat{z})$ and using Helmhotz decomposition, the displacement $\vec{u} = \vec{\nabla}\phi$ for dilatational waves and $\vec{u} = \vec{\nabla} \times \vec{\psi}$ for transverse waves, ϕ and $\vec{\psi}$ are the scalar and vector potential respectively. We consider only transverse waves with displacement components in the $\hat{x}$ and $\hat{z}$ directions only. In this case we consider only the vector potential with one component in the $\hat{y}$ direction. For dilatational waves, equation 5.9 leads to the components

$$e_{xx} = \frac{\partial^2 \phi^{(s)}}{\partial x^2} \tag{5.11}$$

$$e_{zz} = \frac{\partial^2 \phi^{(s)}}{\partial z^2} \tag{5.12}$$

$$e_{xz} = \frac{\partial^2 \phi^{(s)}}{\partial x \partial z} \tag{5.13}$$

where $e_{xz} = e_{zx}$. Equation 5.10 leads to a similar results by replacing the subscript

$^{(s)}$ by $^{(f)}$. Then equations 5.7 and 5.8 lead to the following stress components

$$\begin{aligned}
\sigma_{xx} &= 2\mu_M \frac{\partial^2 \phi^{(s)}}{\partial x^2} + A\left(\frac{\partial^2 \phi^{(s)}}{\partial x^2} + \frac{\partial^2 \phi^{(s)}}{\partial z^2}\right) + Q\left(\frac{\partial^2 \phi^{(f)}}{\partial x^2} + \frac{\partial^2 \phi^{(f)}}{\partial z^2}\right) && (5.14)\\
\sigma_{zz} &= 2\mu_M \frac{\partial^2 \phi^{(s)}}{\partial z^2} + A\left(\frac{\partial^2 \phi^{(s)}}{\partial x^2} + \frac{\partial^2 \phi^{(s)}}{\partial z^2}\right) + Q\left(\frac{\partial^2 \phi^{(f)}}{\partial x^2} + \frac{\partial^2 \phi^{(f)}}{\partial z^2}\right) && (5.15)\\
\sigma_{xz} &= 2\mu_M \frac{\partial^2 \phi^{(s)}}{\partial x \partial z} && (5.16)\\
s &= Q\left(\frac{\partial^2 \phi^{(s)}}{\partial x^2} + \frac{\partial^2 \phi^{(s)}}{\partial z^2}\right) + R\left(\frac{\partial^2 \phi^{(f)}}{\partial x^2} + \frac{\partial^2 \phi^{(f)}}{\partial z^2}\right) && (5.17)
\end{aligned}$$

The fluid pressure is given by $p^{(f)} = -\frac{s}{\beta}$ and in terms of Q and R as

$$p^{(f)} = -\frac{Q}{\beta}\left(\frac{\partial^2 \phi^{(s)}}{\partial x^2} + \frac{\partial^2 \phi^{(s)}}{\partial z^2}\right) - \frac{R}{\beta}\left(\frac{\partial^2 \phi^{(f)}}{\partial x^2} + \frac{\partial^2 \phi^{(f)}}{\partial z^2}\right) \tag{5.18}$$

For transverse waves the vector potential can be written as

$$\vec{\psi} = \hat{y}\psi_y \tag{5.19}$$

In this case equation 5.9 leads to the strain components

$$\begin{aligned}
e_{xx} &= -\frac{\partial^2 \psi_y^{(s)}}{\partial x \partial z} && (5.20)\\
e_{zz} &= \frac{\partial^2 \psi_y^{(s)}}{\partial x \partial z} && (5.21)\\
e_{xz} &= \frac{1}{2}\left(\frac{\partial^2 \psi_y^{(s)}}{\partial x^2} - \frac{\partial^2 \psi_y^{(s)}}{\partial z^2}\right) && (5.22)
\end{aligned}$$

where $e_{xz} = e_{zx}$ and equation 5.10 vanishes. Then equations 5.7 and 5.8 lead to the following stress components

$$\begin{aligned}
\sigma_{xx} &= -2\mu_M \frac{\partial^2 \psi_y^{(s)}}{\partial x \partial z} && (5.23)\\
\sigma_{zz} &= 2\mu_M \frac{\partial^2 \psi_y^{(s)}}{\partial x \partial z} && (5.24)\\
\sigma_{xz} &= \mu_M \left(\frac{\partial^2 \psi_y^{(s)}}{\partial x^2} - \frac{\partial^2 \psi_y^{(s)}}{\partial z^2}\right) && (5.25)\\
s &= 0 && (5.26)
\end{aligned}$$

In a real fluid the stress components are given by equation

$$\sigma_{ij} = -p^{(f)}\delta_{ij} + \left(\xi_f - \frac{2}{3}\eta\right)\vec{\nabla}\cdot\vec{v}\delta_{ij} + 2\eta v_{ij} \tag{5.27}$$

where $p^{(f)}$ is the fluid pressure, ξ_f is the bulk viscosity, η is the shear viscosity, $\vec{v}$ is the particle velocity, and δ_{ij} is the Kronecker delta. For a low viscosity fluid only the principle stress components of the stress tensor are non-zero

$$\sigma_{xx} = -p^{(f)} \tag{5.28}$$

$$\sigma_{zz} = -p^{(f)} \tag{5.29}$$

The fluid pressure can be expressed as

$$\vec{\nabla} p = -\rho^{(f)} \frac{\partial \vec{v}}{\partial t} \tag{5.30}$$

or

$$p = -\rho^{(f)} \frac{\partial^2 \phi}{\partial t^2} \tag{5.31}$$

The stress components derived in this section will be useful for solving the boundary value problem of a fluid and a fluid-saturated porous material.

5.4 Boundary conditions for a fluid-porous material interface

The two sets of boundary conditions at a boundary between a fluid and a fluid-saturated porous material that are considered here are that derived by Deresiewicz and Skalak (1963) and that derived by de la Cruz/Spanos (1989a). When a P-wave strikes a boundary between a fluid and a fluid-saturated porous material from the fluid medium only one wave is reflected as a P-wave. Three waves are transmitted into the fluid-saturated porous material, a fast P-wave, a slow P-wave, and an S-wave.

Let a medium (a) be a fluid and a medium (b) be a fluid-saturated porous material. Here the reference frame given in chapter 2 (Fig. 2.1) will be used.

5.4.1 Deresiewicz and Skalak boundary conditions in porous media

The complete derivation of the boundary conditions can be found in Deresiewicz and Skalak (1963). The boundary conditions at an open boundary between a fluid and a fluid-saturated porous material are

- The normal total stress on the bulk material of the porous medium and the stress in the fluid medium must be continuous at the boundary.
- The tangential stress in the porous medium must vanish at the boundary.
- The fluid pressure must be continuous across the boundary.
- The normal component of the averaged particle velocity over the bulk material in medium (*b*) and the normal fluid particle velocity in medium (*a*) must be continuous at the boundary.

In terms of equations these boundary conditions are

$$\{\sigma_{zz} + s\}_b = \left\{-p^{(f)}\right\}_a \tag{5.32}$$

$$\{\sigma_{xz}\}_b = 0 \tag{5.33}$$

$$\left\{p^{(f)}\right\}_b = \left\{p^{(f)}\right\}_a \tag{5.34}$$

$$\left\{(1-\beta)v_z^{(s)} + \beta v_z^{(f)}\right\}_b = \left\{v^{(f)}\right\}_a \tag{5.35}$$

where all parameters have the meaning as described in appendix B.1.

5.4.2 de la Cruz/Spanos boundary conditions in porous media

The complete derivation of the boundary conditions can be found in de la Cruz and Spanos (1989a). If the stress due to viscosity is neglected the boundary conditions at an open boundary between a fluid and a fluid-saturated porous material are then given by

- The normal stress in the solid skeleton of the porous medium and the normal stress in the fluid medium must be continuous at the boundary.
- The normal stress in the fluid of the porous medium (*b*) and the normal stress in the fluid medium (*a*) must be continuous at the boundary.
- The tangential stress in the solid skeleton of the porous medium (*b*) must vanish at the boundary because the fluid is assumed not to support shear stress.
- The normal component of the averaged particle velocity over the bulk material in medium (*b*) and the normal component of the fluid particle velocity in medium (*a*) must be continuous at the boundary.

It is important to note that here the stress in the bulk porous material (solid and fluid) is given by equation 18 in de la Cruz and Spanos (1989a)

$$\sigma_{ij} = \beta\sigma_{ik}^{(f)} + (1-\beta)\sigma_{ik}^{(s)} \tag{5.36}$$

whereas in Deresiewicz and Skalak (1963) it is given by

$$\sigma_{ij} = \sigma_{ik}^{(s)} + s \tag{5.37}$$

Therefore in order to make a reasonable comparison the boundary conditions stated here will be written according to equation 5.37. In light of this the present boundary conditions can be written as

$$\{\sigma_{zz}\}_b = \left\{-(1-\beta)p^{(f)}\right\}_a \tag{5.38}$$

$$\{s\}_b = \left\{-\beta p^{(f)}\right\}_a \tag{5.39}$$

$$\left\{\sigma_{xz}^{(s)}\right\}_b = 0 \tag{5.40}$$

$$\{v_z\}_b = \left\{v^{(f)}\right\}_a \tag{5.41}$$

In these conditions the authors defined the velocity in the fluid-saturated porous material from the equation of continuity (continuity of momentum per unit area). It is defined as

$$v_z = \frac{\rho^{(s)}(1-\beta)v_z^{(s)} + \beta\rho^{(f)}v_z^{(f)}}{\rho^{(s)}(1-\beta) + \beta\rho^{(f)}} \tag{5.42}$$

which is the density weighted and averaged velocity field in the bulk material per unit mass.

5.4.3 Comparison of the two boundary condition sets

Now compare equations 5.32 through 5.35 in Deresiewicz and Skalak (1963) with equations 5.38 through 5.41 of de la Cruz and Spanos (1989a). The first boundary condition given by equation 5.32 is simply the sum of the two boundary conditions given by equations 5.38 and 5.39. The boundary condition given by equation 5.34 and that given by equation 5.39 are equivalent. The boundary condition given by equation 5.33 is exactly equation 5.40. However the boundary condition given by equation 5.35 and that given by equation 5.41 are fundamentally different. In the Deresiewicz and Skalak (1963) boundary conditions the particle velocity of the solid skeleton and that in the fluid are averaged over the bulk material and equated to the particle velocity of the fluid medium. In the de la Cruz/Spanos boundary conditions however the velocity in the fluid-saturated medium is mass averaged over the bulk material per unit mass. Therefore the only difference between the two sets of boundary conditions is in the continuity of the particle velocity field.

5.5 Plane wave solutions

Consider plane wave solutions to the present boundary value problem. Let the fast P-wave, the slow P-wave, and the S-wave be respectively denoted by subscripts $_1$, $_2$, and $_3$ in the fluid-saturated medium (b). Let the waves in the fluid medium (a) have no subscripts. Denoting the position vector by $\vec{r}$ and the wave number by $\vec{k}$ the scalar potentials and vector potential are then

$$\begin{aligned}
\phi_1 &= B^{(s)} e^{i(\omega t - \vec{k}_1 \cdot \vec{r})} + B^{(f)} e^{i(\omega t - \vec{k}_1 \cdot \vec{r})} && (5.43)\\
\phi_2 &= C^{(s)} e^{i(\omega t - \vec{k}_2 \cdot \vec{r})} + C^{(f)} e^{i(\omega t - \vec{k}_2 \cdot \vec{r})} && (5.44)\\
\vec{\psi}_3 &= D^{(s)} \hat{y} e^{i(\omega t - \vec{k}_3 \cdot \vec{x})} + D^{(f)} \hat{y} e^{i(\omega t - \vec{k}_3 \cdot \vec{x})} && (5.45)
\end{aligned}$$

in the fluid-saturated porous medium (b) and

$$\begin{aligned}
\phi_{inc} &= e^{i(\omega t - \vec{k} \cdot \vec{r})} && (5.46)\\
\phi_{ref} &= E e^{i(\omega t - \vec{k} \cdot \vec{r})} && (5.47)
\end{aligned}$$

in the fluid medium (a). Using the fluid-solid complex amplitudes ratios $\zeta_l, l = 1, 2, 3$ and $\vec{k} = \hat{x} k_x + \hat{z} k_z$ equations 5.43 through 5.47 can be rewritten as

$$\begin{aligned}
\phi_1^{(f)} &= B^{(f)} e^{i(\omega t - k_{1x} x - k_{1z} z)} && (5.48)\\
\phi_1^{(s)} &= \zeta_1 B^{(f)} e^{i(\omega t - k_{1x} x - k_{1z} z)} && (5.49)\\
\phi_2^{(f)} &= C^{(f)} e^{i(\omega t - k_{2x} x - k_{2z} z)} && (5.50)\\
\phi_2^{(s)} &= \zeta_2 C^{(f)} e^{i(\omega t - k_{2x} x - k_{2z} z)} && (5.51)\\
\vec{\psi}_3^{(f)} &= D^{(f)} \hat{y} e^{i(\omega t - k_{3x} x - k_{3z} z)} && (5.52)\\
\vec{\psi}_3^{(s)} &= \zeta_3 D^{(f)} \hat{y} e^{i(\omega t - k_{3x} x - k_{3z} z)} && (5.53)\\
\phi_{inc} &= e^{i(\omega t - k_x x - k_z z)} && (5.54)\\
\phi_{ref} &= E e^{i(-\omega t - k_x x + k_z z)} && (5.55)
\end{aligned}$$

Using equations 5.15, 5.24, 5.16, and 5.25 the normal and tangential stress components in the fluid-saturated medium (b) are

$$\begin{aligned}\sigma_{zz} &= -\left[2\mu_M\zeta_1 k_{1z}^2 + (A\zeta_1 + Q)\,k_1^2\right]\phi_1^{(f)} - \left[2\mu_M\zeta_2 k_{2z}^2 + (A\zeta_2 + Q)\,k_2^2\right]\phi_2^{(f)} - \\ &\quad \left[2\mu_M k_{3x}k_{3z}\zeta_3\right]\psi_y^{(f)} \qquad (5.56)\\ \sigma_{xz} &= -\left[2\mu_M\zeta_1 k_{1x}k_{1z}\right]\phi_1^{(f)} - \left[2\mu_M\zeta_2 k_{2x}k_{2z}\right]\phi_2^{(f)} - \left[\mu_M\zeta_3\left(k_{3x}^2 - k_{3z}^2\right)\right]\psi_y^{(f)} \qquad (5.57)\end{aligned}$$

In the fluid-saturated porous material, the stress and pressure are given by

$$s = -\left[k_1^2\,(Q\zeta_1 + R)\right]\phi_1^{(f)} - \left[k_2^2\,(Q\zeta_2 + R)\right]\phi_2^{(f)} \qquad (5.58)$$

and

$$p^{(f)} = \left[\frac{k_1^2\,(Q\zeta_1 + R)}{\beta}\right]\phi_1^{(f)} + \left[\frac{k_2^2\,(Q\zeta_2 + R)}{\beta}\right]\phi_2^{(f)} \qquad (5.59)$$

respectively. The normal stress component in the fluid medium (a) is the fluid pressure that is

$$p = \rho^{(f)}\omega^2\left(\phi_{inc} + \phi_{ref}\right) \qquad (5.60)$$

The boundary conditions 5.32 through 5.35 lead to

$$\begin{aligned}&\left[2\mu_M\zeta_1 k_{1z}^2 + (A\zeta_1 + Q)\,k_1^2 + k_1^2\,(Q\zeta_1 + R)\right]\phi_1^{(f)} + \\ &\left[2\mu_M\zeta_2 k_{2z}^2 + (A\zeta_2 + Q)\,k_2^2 + k_2^2\,(Q\zeta_2 + R)\right]\phi_2^{(f)} + \left[2\mu_M k_{3x}k_{3z}\zeta_3\right]\psi_y^{(f)} = \\ &\rho^{(f)}\omega^2\left(\phi_{inc} + \phi_{ref}\right) \qquad (5.61)\\ &\left[2\zeta_1 k_{1x}k_{1z}\right]\phi_1^{(f)} + \left[2\zeta_2 k_{2x}k_{2z}\right]\phi_2^{(f)} + \left[\zeta_3\left(k_{3x}^2 - k_{3z}^2\right)\right]\psi_y^{(f)} = 0 \qquad (5.62)\\ &\left[\frac{k_1^2\,(Q\zeta_1 + R)}{\beta}\right]\phi_1^{(f)} + \left[\frac{k_2^2\,(Q\zeta_2 + R)}{\beta}\right]\phi_2^{(f)} = \rho^{(f)}\omega^2\left(\phi_{inc} + \phi_{ref}\right) \qquad (5.63)\\ &\left[(1-\beta)\zeta_1 + \beta\right]k_{1z}\phi_1^{(f)} + \left[(1-\beta)\zeta_2 + \beta\right]k_{2z}\phi_2^{(f)} + \\ &\left[(1-\beta)\zeta_3 + \beta\right]k_{3z}\psi_y^{(f)} = k_z\phi_{inc} - k_z\phi_{ref} \qquad (5.64)\end{aligned}$$

In order for these boundary conditions to hold for all x at $z = 0$ and at all times the exponential factor in all potentials must be equal. Therefore the following condition must be satisfied

$$k_x = k_{1x} = k_{2x} = k_{3x} \qquad (5.65)$$

which is simply a generalized Snell's law. This condition states that all horizontal ($\hat{x}$ direction) wave numbers for all generated wave modes at the boundary must be equal to that of the incident wave. As the incident wave is assumed to be a P-wave with no attenuation k_x must be real and therefore all horizontal waves numbers must be real. The above boundary conditions can then be rewritten as

$$\begin{aligned}
&\left[2\mu_M\zeta_1 k_{1z}^2 + (A\zeta_1 + Q)\,k_1^2 + k_1^2\,(Q\zeta_1 + R)\right] B^{(f)} + \\
&\left[2\mu_M\zeta_2 k_{2z}^2 + (A\zeta_2 + Q)\,k_2^2 + k_2^2\,(Q\zeta_2 + R)\right] C^{(f)} + \left[2\mu_M k_{3x}k_{3z}\zeta_3\right] D^{(f)} = \\
&-\rho^{(f)}\omega^2 - \rho^{(f)}\omega^2 E
\end{aligned} \tag{5.66}$$

$$\left[2\zeta_1 k_{1x}k_{1z}\right] B^{(f)} + \left[2\zeta_2 k_{2x}k_{2z}\right] C^{(f)} + \left[\zeta_3\left(k_{3x}^2 - k_{3z}^2\right)\right] D^{(f)} = 0 \tag{5.67}$$

$$\left[\frac{k_1^2\,(Q\zeta_1 + R)}{\beta}\right] B^{(f)} + \left[\frac{k_2^2\,(Q\zeta_2 + R)}{\beta}\right] C^{(f)} = \rho^{(f)}\omega^2 + \rho^{(f)}\omega^2 E \tag{5.68}$$

$$\begin{aligned}
&\left[(1-\beta)\zeta_1 + \beta\right] k_{1z}B^{(f)} + \left[(1-\beta)\zeta_2 + \beta\right] k_{2z}C^{(f)} + \\
&\left[(1-\beta)\zeta_3 + \beta\right] k_{3z}D^{(f)} = k_z - k_z E
\end{aligned} \tag{5.69}$$

This is a linear system of 4 equations with 4 unknowns. Rearranging the terms in these equations we have

$$TU = H \tag{5.70}$$

where T is a 4×4 known matrix, U is the unknown vector, and H is a known vector. The elements of H are

$$H_1 = \rho^{(f)}\omega^2 \tag{5.71}$$

$$H_2 = 0 \tag{5.72}$$

$$H_3 = \rho^{(f)}\omega^2 \tag{5.73}$$

$$H_4 = k_z \tag{5.74}$$

The elements of the unknown vector U are

$$U_1 = B^{(f)} \tag{5.75}$$

$$U_2 = C^{(f)} \tag{5.76}$$

$$U_3 = D^{(f)} \tag{5.77}$$

$$U_4 = E \tag{5.78}$$

The elements of the known square matrix T are

$$T_{11} = 2\mu_M \zeta_1 k_{1z}^2 + (A\zeta_1 + Q)\, k_1^2 + k_1^2\,(Q\zeta_1 + R) \tag{5.79}$$

$$T_{12} = 2\mu_M \zeta_2 k_{2z}^2 + (A\zeta_2 + Q)\, k_2^2 + k_2^2\,(Q\zeta_2 + R) \tag{5.80}$$

$$T_{13} = 2\mu_M k_{3x} k_{3z} \zeta_3 \tag{5.81}$$

$$T_{14} = -\rho^{(f)}\omega^2 \tag{5.82}$$

$$T_{21} = 2\zeta_1 k_{1x} k_{1z} \tag{5.83}$$

$$T_{22} = 2\zeta_2 k_{2x} k_{2z} \tag{5.84}$$

$$T_{23} = \zeta_3\left(k_{3x}^2 - k_{3z}^2\right) \tag{5.85}$$

$$T_{24} = 0 \tag{5.86}$$

$$T_{31} = \frac{k_1^2\,(Q\zeta_1 + R)}{\beta} \tag{5.87}$$

$$T_{32} = \frac{k_2^2\,(Q\zeta_2 + R)}{\beta} \tag{5.88}$$

$$T_{33} = 0 \tag{5.89}$$

$$T_{34} = -\rho^{(f)}\omega^2 \tag{5.90}$$

$$T_{41} = \left[(1-\beta)\zeta_1 + \beta\right] k_{1z} \tag{5.91}$$

$$T_{42} = \left[(1-\beta)\zeta_2 + \beta\right] k_{2z} \tag{5.92}$$

$$T_{43} = \left[(1-\beta)\zeta_3 + \beta\right] k_{3x} \tag{5.93}$$

$$T_{44} = k_z \tag{5.94}$$

As the solutions are not in a simple form they will not be given explicitly. The solutions will be studied in details in the next section.

The scalar and vector potentials for the reflected P-wave, transmitted P-waves, and transmitted S-wave can now be expressed using equations 5.48 through 5.55 for both the wave components in the solid skeleton and in the fluid. However the complex displacements (or velocities) for the P-waves are given by the gradient of the scalar potentials ϕ and for the S-wave by the curl of the vector potential $\vec{\psi}$. The physical displacements (or particle velocities), however, are the real parts of the complex displacements (or velocities).

The de la Cruz/Spanos boundary conditions lead to the same result except that the fourth boundary condition given by equation 5.64 is replaced by equation 5.41

with the velocity in the fluid-saturated porous material is defined by equation 5.42. This leads to the same linear equation 5.70 where the last row of the matrix T is replaced by

$$T_{41} = \frac{\left[\rho^{(s)}(1-\beta)\zeta_1 + \rho^{(f)}\beta\right]}{\rho^{(s)}(1-\beta) + \rho^{(f)}\beta} k_{1z} \tag{5.95}$$

$$T_{42} = \frac{\left[\rho^{(s)}(1-\beta)\zeta_2 + \rho^{(f)}\beta\right]}{\rho^{(s)}(1-\beta) + \rho^{(f)}\beta} k_{2z} \tag{5.96}$$

$$T_{43} = \frac{\left[\rho^{(s)}(1-\beta)\zeta_3 + \rho^{(f)}\beta\right]}{\rho^{(s)}(1-\beta) + \rho^{(f)}\beta} k_{3x} \tag{5.97}$$

$$T_{44} = k_z \tag{5.98}$$

5.6 Modelling with plane waves in porous media

Now an illustrative example of a boundary value problem will be treated in this section. Let a medium (a) be a fluid and a medium (b) be a fluid-saturated porous medium. The two media will have the material properties as given in tables 4.2, 4.3, and 4.4. Using equation 5.70 the reflected and transmitted potential fields were calculated. It is always important to verify the energy balance of the boundary. This will be done in the classical way of calculating the normal energy fluxes that strike the boundary and those that leave the boundary. The total energy flux must be balanced, therefore if normalized to the incident energy flux must equal 1. The normal energy flux given by equation 2.93 is valid for any type of wave. Here the energy flux for each wave mode present at the boundary is calculated. The result is shown in figure 5.1 where the total energy flux is 1. It is worthwhile noting that the contribution to the energy balance fast post P-wave critical angle of incidence is highly dominated by the slow P-wave. However it is also important to note that the total energy flux for any given wave mode must include the interaction energy between the velocity fields and the stresses for all the other waves present in the same medium. For example the transmitted fast P-wave energy flux is

$$J_{1z} = -\frac{1}{2}\left[v_{1z}^{*(s)}\sigma_{1zz}^{(s)} + v_{1x}^{*(s)}\sigma_{1xz}^{(s)}\right] - \frac{1}{2}\left[v_{1z}^{*(f)} s_1\right] \tag{5.99}$$

However the velocity field of this wave will interact with the stresses of the other waves present in the medium. Therefore this interaction energy must be included to properly account for all energy contributions of the fast P-wave to the energy

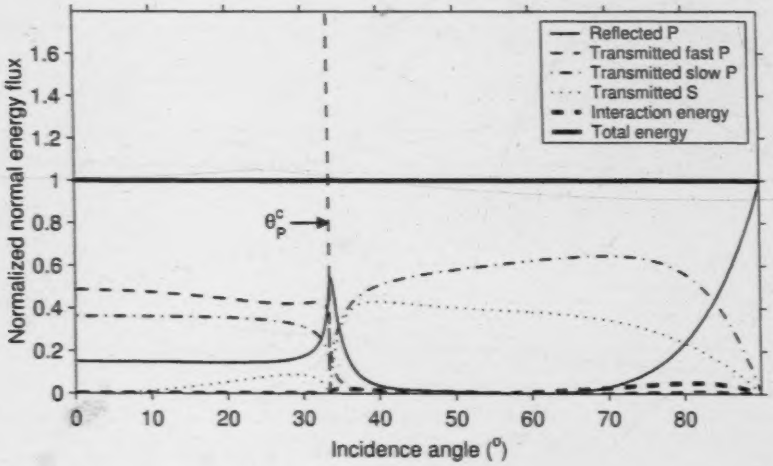

Figure 5.1: Absolute values of normalized energy fluxes normal to the boundary of all generated wave modes. Absolute values are shown. Note the dominance of the slow P-wave at past post P-wave critical angle of incidence.

balance of the boundary. The interaction energy is given by

$$JI_{1z} = -\frac{1}{2}\left[v_{1z}^{*(s)}\sigma_{2zz}^{(s)} + v_{1x}^{*(s)}\sigma_{2xz}^{(s)}\right] - \frac{1}{2}\left[v_{1z}^{*(f)}s_2\right] - \frac{1}{2}\left[v_{1z}^{*(s)}\sigma_{3zz}^{(s)} + v_{1x}^{*(s)}\sigma_{3xz}^{(s)}\right] \quad (5.100)$$

The energy flux of the transmitted fast P-wave is given by the real part of $J_{1z} + JI_{1z}$. In order to better understand how the interaction energy affects the energy balance of the boundary, the energy fluxes (including interaction energy) are plotted keeping the sign that shows whether the normal energy flux is directed away from the boundary or towards the boundary. In the present illustration the incident wave has a positive energy flux. Figure 5.2 shows energy fluxes of all wave modes with the correct sign and include the corresponding interaction energy. We notice that some waves exhibit a change of sign with angle of incidence. The transmitted fast P-wave and the transmitted S-wave show better this behaviour. The most obvious is the S-wave whose energy flux becomes negative above 60^o of angle of incidence. Above this angle the energy flux is directed towards the boundary as it is negative. Note also that the slow P-wave contributes much more than the S-wave to the energy balance of the boundary. The interaction energy varies with angle of incidence, it can either be positive or negative. However the interaction energy vanishes for non-attenuating media as shown in chapter 2. In contrast with pure elastic waves, surface waves in attenuating media do contribute to the energy balance of the boundary in

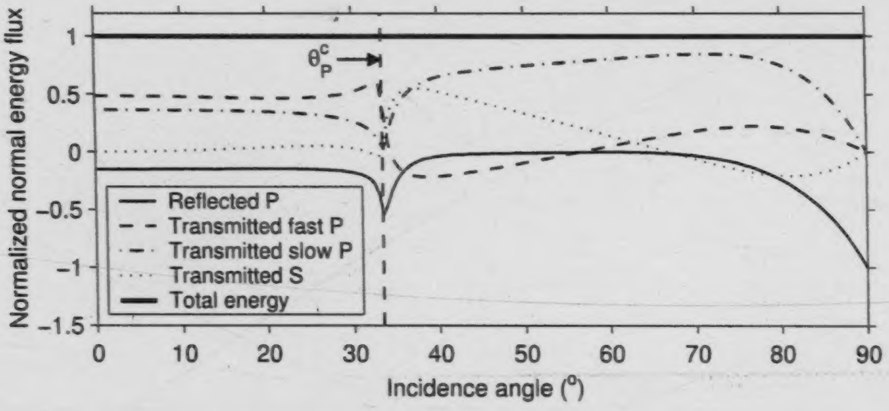

Figure 5.2: Normalized energy fluxes normal to the boundary of all generated wave modes. All energy fluxes are shown with the corresponding sign and include the corresponding interaction energy.

a reflection-transmission boundary value problem.

5.6.1 Amplitudes versus angle of incidence

Now we examine the amplitudes of the reflected P-wave, the transmitted fast P-wave, the transmitted slow P-wave, and the transmitted S-wave. In figure 5.3

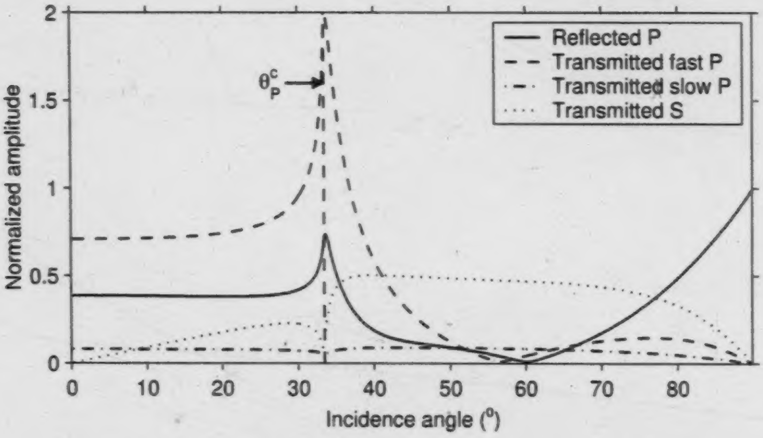

Figure 5.3: Normalized amplitudes in the solid skeleton of all generated wave modes at a boundary between water and a water-saturated porous material.

and figure 5.4 the amplitudes of the scalar potentials of the transmitted fast P-wave and the slow P-wave and the vector potential of the S-wave are presented for the fluid component and the solid component of the fluid-saturated porous material respectively. As it is noticeable the reflected wave does not show total reflection until the angle of of incidence of 90° is reached. The transmitted fast P-wave does appear after the P-wave critical angle of incidence and shows approximately an amplitude in the solid skeleton slightly higher than that in the fluid. The S-wave appears at all angles of incidence (except at normal incidence) with an amplitude higher in the solid skeleton than in the fluid. The slow P-wave however appears at all angles of incidence and the amplitude in the fluid is much higher than that in the solid skeleton. This reiterates the dominance by fluid flow of this wave.

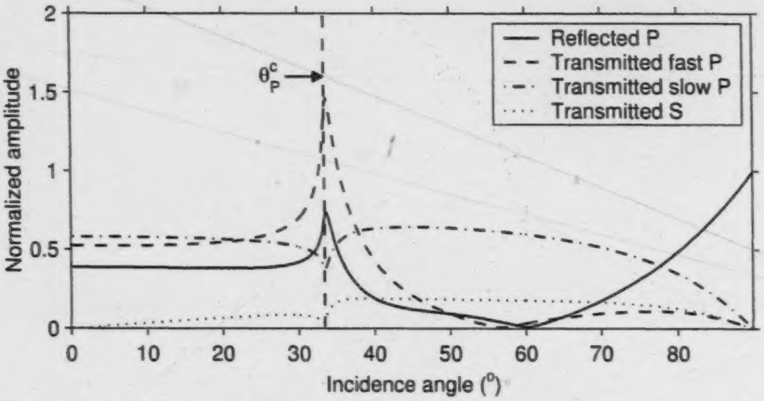

Figure 5.4: Normalized amplitudes in the fluid component of all generated wave modes at a boundary between water and a water-saturated porous material.

5.6.2 Phase angle versus angle of incidence

The phase angle against the angle of incidence is illustrated in figures 5.5 and 5.6 for the fluid and the solid skeleton respectively. The phase of the waves are nearly identical for the fast P-wave and the S-wave. However the phase of the slow P-wave in the solid is 180° out of phase with that in the fluid (Figs. 5.5 and 5.6).

Now we take a close look at the phase of the reflected wave as this will play a role in the reflectivity experiments forthcoming using a bounded acoustic pulse. The phase angle versus the angle of incidence of the reflected wave exhibit large changes

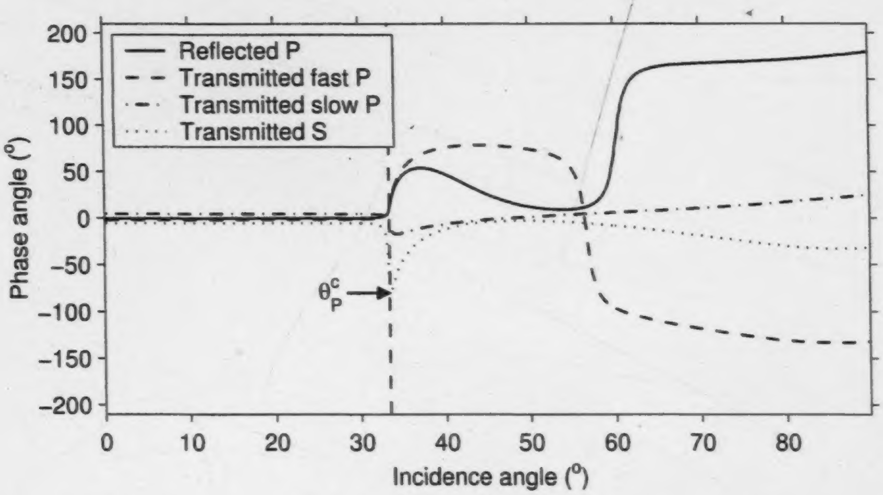

Figure 5.5: The phase of the fluid component for all generated wave modes at a boundary between water and the water-saturated porous material considered in section 4.7.

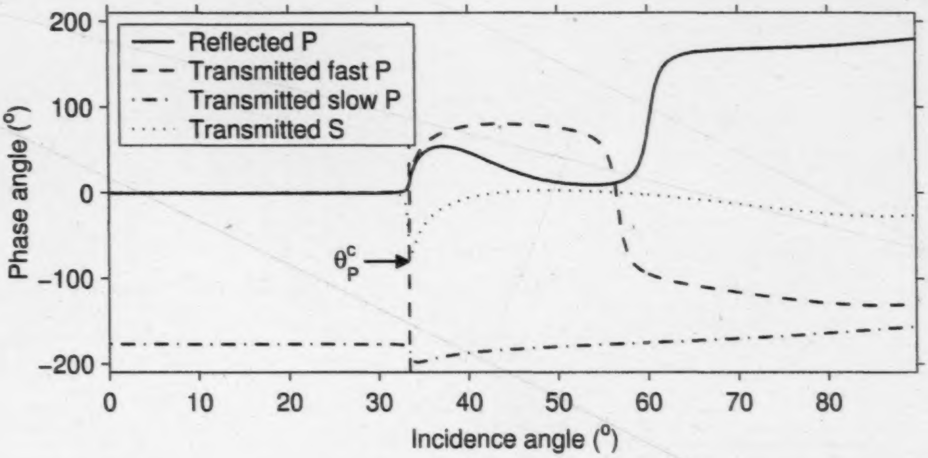

Figure 5.6: The phase of the solid component for all generated wave modes at a boundary between water and a water-saturated porous material considered in section 4.7.

beyond the P-wave critical angle of incidence (Fig. 5.7). First the phase angle of the reflected wave increases smoothly to a peak of 52.5^o at an incidence angle of about 37^o and then decreases to 8^o at an angle of incidence of 54^o. An abrupt jump of the

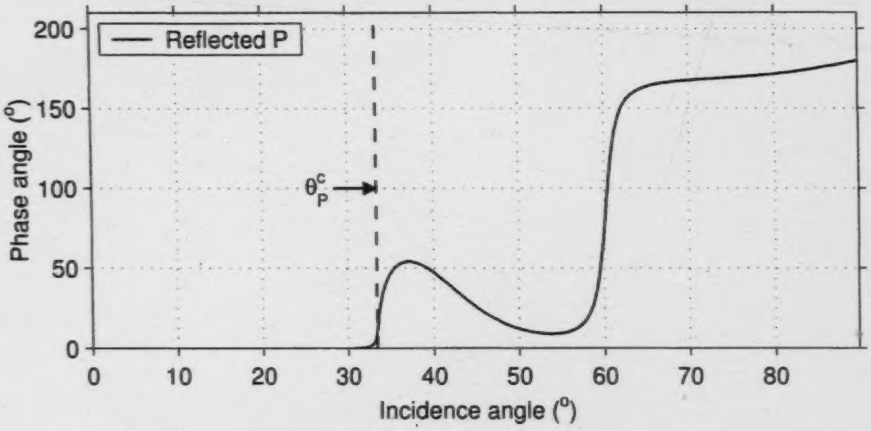

Figure 5.7: The phase of the reflected wave at a boundary between a fluid and a fluid-saturated porous material considered in section 4.7.

phase angle at an angle of incidence of 60° is noticeable. The phase angle changes by about 150°. We expect that this abrupt change will play a role similar to that observed in the elastic reflectivity studied in chapter 2 and chapter 3 when acoustic bounded pulses are reflected from a fluid and an elastic solid interface.

Industrial practice in petroleum geophysics uses reflectivity as a diagnostic for fluids; however, simpler elastic conditions are assumed. As such it is interesting to contrast elastic and poroelastic reflectivities. Now the same model will be assumed to be an elastic medium (i.e. Zoeppritz's equations where only one P-wave and one S-wave exist) with the P and S wave velocities assumed to be those calculated from the porous medium model in which the slow P-wave is present. The density of the medium is calculated using the densities of the water and of the solid grains according to the porosity. The results are shown in figure 5.8. For the sake of comparison the corresponding porous medium solutions are shown in figure 5.9. However, to better compare the two figures the waves in the porous medium are averaged over a unit volume of the solid and fluid components. The results obviously are different for the energy balance, the amplitudes, and the phase angles. The elastic medium theory does not describe properly the reflectivity-transmission at the boundary between the water and the water-saturated porous material in the frequency range of the signal used here.

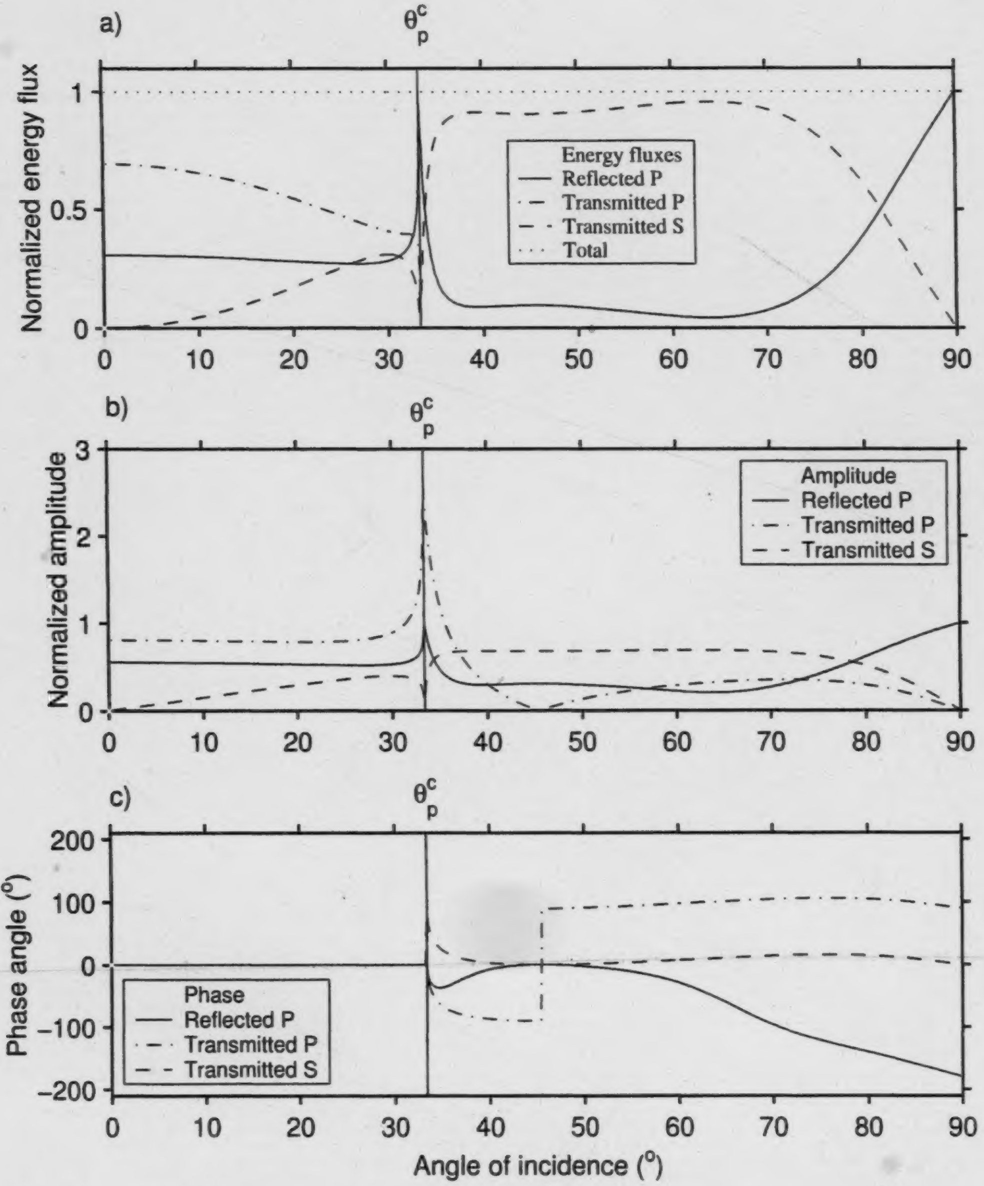

Figure 5.8: The reflectivity-transmission at the boundary between water and an elastic medium replacing the water-saturated porous material using Zoeppritz's equations. The P and S wave velocities are 2710 m/s and 1480 m/s respectively. a) Energy balance. b) Amplitudes. c) Phase angles.

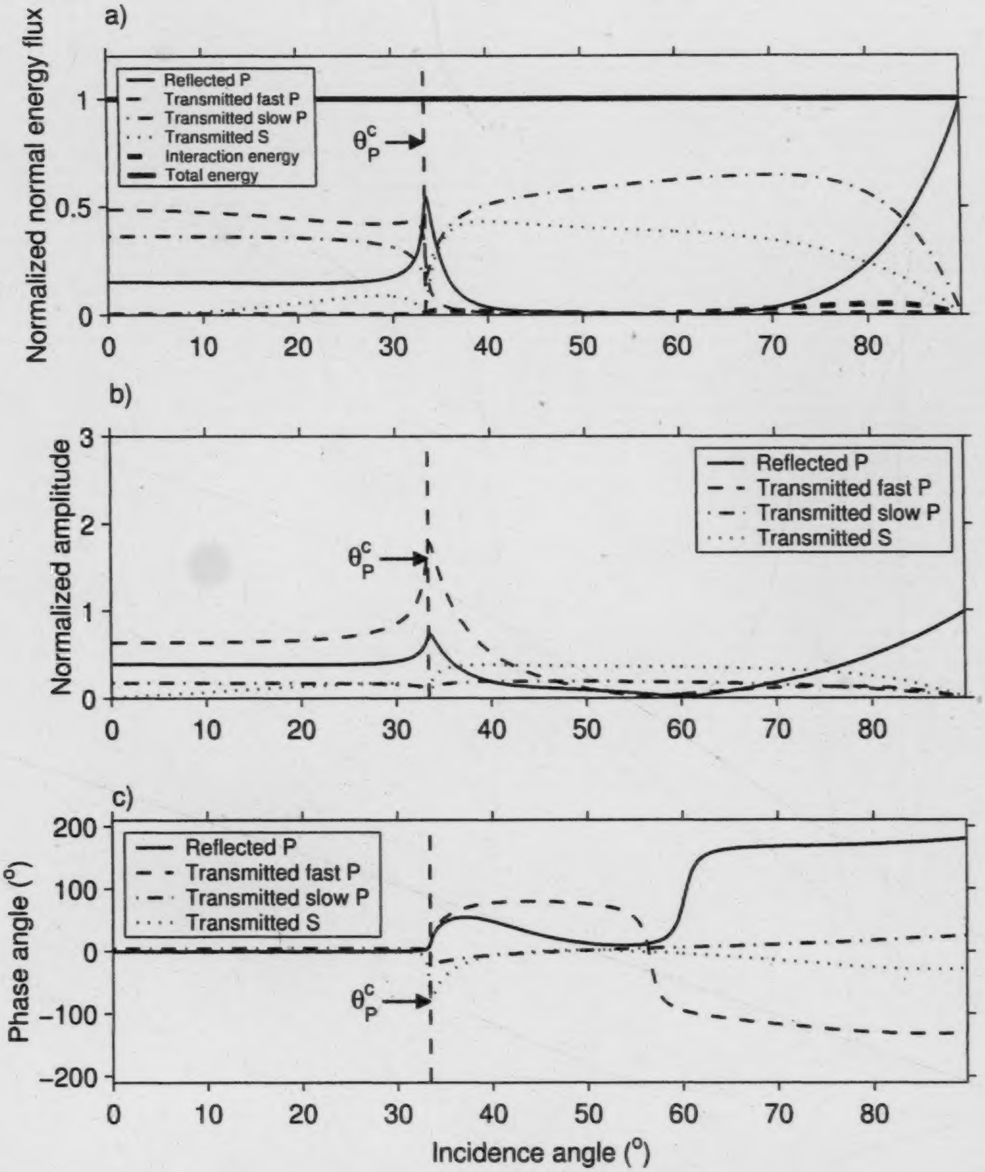

Figure 5.9: The reflectivity-transmission at the boundary between water and a water-saturated porous material. The wave fields are averaged over a unit volume of the bulk material. a) Energy balance. b) Amplitudes. c) Phase angles.

5.7 Bounded acoustic pulses in porous media

As for the reflectivity of acoustic bounded pulses from fluid-elastic solid interfaces the phase angle of the reflectivity response from a fluid and a fluid-saturated porous material will play a major role when abrupt changes occur in the phase of the reflection coefficient. Recall the representation of an acoustic bounded pulse by the Fourier integral pair from equations 2.158 and 2.159

$$\phi(x,0,t) = \frac{1}{4\pi^2}\int_{-\infty}^{+\infty}\int_{-\infty}^{+\infty}\Phi(k_x,0,\omega)e^{ik_x x}e^{i\omega t}dk_x d\omega \tag{5.101}$$

where the function $\Phi(k_x,0,\omega)$ is given by the Fourier integral

$$\Phi(k_x,0,\omega) = \int_{-\infty}^{+\infty}\int_{-\infty}^{+\infty}\phi(x,0,t)e^{-ik_x x}e^{-i\omega t}dxdt \tag{5.102}$$

and the reflected wave field ϕ^r at an interface located at $z = h$ (equation 2.164)

$$\phi^r(x,h,t) = \frac{1}{4\pi^2}\int_{-\infty}^{+\infty}\int_{-\infty}^{+\infty}R(k_x)\Phi(k_x,0,\omega)e^{ik_x x}e^{i\omega t}e^{ik_z h}dk_x d\omega \tag{5.103}$$

where $R(k_x)$ is the reflection coefficient at the interface. As for the elastic case equation 5.103 still holds for an interface between a fluid and a fluid-saturated porous material provided the reflection coefficient is properly replaced by the one calculated using the porous media wave propagation and boundary value problem. In this case the reflection coefficient is dependent on frequency and equation 5.103 will be properly rewritten as

$$\phi^r(x,z,t) = \frac{1}{4\pi^2}\int_{-\infty}^{+\infty}\int_{-\infty}^{+\infty}R(k_x,\omega)\Phi(k_x,0,\omega)e^{ik_x x}e^{i\omega t}e^{ik_z h}e^{ik_z \Delta z}dk_x d\omega \tag{5.104}$$

where $\Delta z = |h - z|$. Equation 5.104 is an exact expression of the reflected P-wave from the fluid and the fluid-saturated porous material.

5.8 Bounded acoustic pulse modelling in porous media

Using equation 5.104 an exact reflectivity response is obtainable when a wave field that is finite both in time and space is used. If the reflection coefficient exhibits large and abrupt jumps the reflected acoustic pulse will experiences a phase shift along the boundary of the fluid and the fluid-saturated porous material. Sharp changes in the amplitude of the reflection coefficient will also play a role in the reflectivity response of bounded acoustic pulses from fluid and fluid-saturated porous materials. Sharp changes seen in the single wave number plane wave will be smoothed (averaged over a small range of incidence angles) as has been already observed and discussed in the elastic reflectivity response studied in chapter 2 and 3. Furthermore the reflectivity response from interfaces between a fluid and a fluid-saturated porous material depends on frequency and consequently the pulse shape will be also affected.

Here the illustration example studied in previous sections will be used to model the reflectivity response using two acoustic bounded pulses of different widths and a frequency bandwidth of 0.2 MHz to 1.2 MHz. The result is presented in figure 5.10 where the responses of 2 cm wide and 8 cm wide bounded pulses are compared. The results of the two wave fields are shown along with the plane wave solution (Fig. 5.10-a). Clearly the phase change as shown in section 5.6 beyond the P-wave critical angle of incidence has a severe effect on the narrow 2 cm bounded pulse. The wide bounded 8 cm pulse has a closer reflectivity response to the plane wave solution in the vicinity and past the critical angle θ_p^c. Therefore it is a convenience to use large bounded acoustic pulse as sources to study reflectivity and transmission in porous materials.

5.9 Conclusions

As has been shown in the previous chapter and verified by modelling in the present chapter, the reflectivity response from a fluid and a fluid-saturated porous material is more complex than that from a fluid and an elastic solid material. The boundary conditions are different as more equations are needed to solve the boundary value problem due to the presence of a second P-wave in the fluid-saturated porous material for the case illustrated here. The slow P-wave contributes more to the energy balance of the boundary than the reflected P-wave or the transmitted S-wave at all angles of incidence. The phase of the slow P-wave in the solid skeleton is 180^o out of phase with that in the fluid and consequently the large attenuation. Therefore it is important to include this wave in modelling reflectivity response from

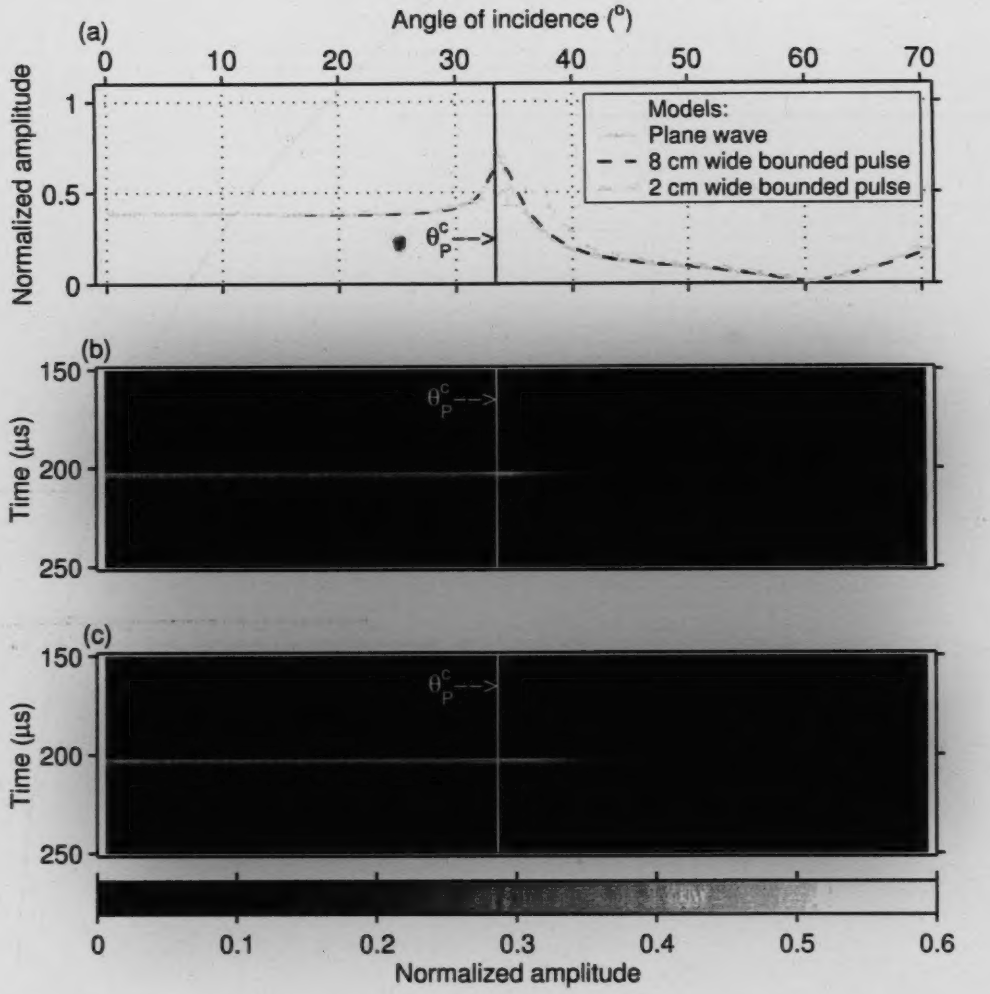

Figure 5.10: Theoretical reflectivity response at a water and a water-saturated porous material interface. The material is the same as that used in the illustration example in section 5.6. a) Three types of incident wave fields, a plane wave, an 8 cm wide source, and a 2 cm wide source are used. Amplitude envelope displays of the reflectivity for b) the 8 cm wide and the c) 2 cm wide bounded pulses calculated using equation 5.104. The frequency bandwidth is 0.2 MHz to 1.2 MHz.

fluid-saturated porous materials. All generated waves at the interface between a fluid and a fluid-saturated porous material are frequency dependant and exhibit attenuation that must be taken into account. The attenuation of the solid material, if not negligible, plays a major role in the overall attenuation. It is also shown numerically that Zoeppritz's equations do not properly describe the boundary value problem and show large discrepancy with the porous media theory. Laboratory measurements of reflectivity and transmission must take into account the size of the source used. Large acoustic wave fields lead to much closer measurements to the plane wave theory predictions.

Chapter 6

Experimental measurement of porous media parameters

6.1 Introduction

In current industrial practice, the change in the strength of seismic reflection with angle of incidence is increasingly employed in the search for hydrocarbons. Such measurements of Amplitude Variation with Offset (AVO) (or with Angle AVA) assume the reflectivity can be described as if occurring at the contact between two perfectly elastic materials. Usually, a variety of approximations to the full Zoeppritz's equations that describe the variation in reflectivity with angle of incidence from the interface between two elastic media are employed in AVO impedance inversions (e.g. Shuey (1985)). However the propagation of waves in porous media and the associated boundary conditions differ from that of elastic solids. Additional propagation modes are generated at the porous media boundaries and the reflectivity response is different from that anticipated by Zoeppritz's equations as shown in chapter 5. In most cases, however, AVO is most usually applied to detect fluids in porous rocks, but the elastic theory may not necessarily describe properly the reflectivity in this case. Attenuation and the existence of a second P-wave influence the reflectivity and transmission in fluid-saturated porous materials.

In this chapter six porous samples constructed from sintered soda-lime glass beads of various grain diameters are characterized.

To properly model the measured reflectivity several parameters must be first determined as pointed out in chapter 4 section 4.5. First a description of the synthetic porous samples is given followed by the methodology used for the determination of all parameters and then the corresponding measured parameters for the six synthetic porous samples used in the reflectivity experiments. The reflectivity results from the interface between water and water-saturated synthetic samples will be presented in chapters 8 and 9 with the corresponding calculated models for each synthetic sample. To the best of the author's knowledge, these are the first careful and complete experimental tests of reflectivity and transmission of acoustic waves from porous media.

The properties that will be measured are tortuosity ς, permeability K, P and S phase velocity of the solid skeleton, and the attenuation of the solid skeleton.

6.2 Tortuosity measurement

Tortuosity is a dimensionless quantity that is defined as the length of the shortest path joining two points through the voids within a porous material normalized to the length of the straight path joining the same points. This quantity is always positive and greater than unity. The more tortuous a porous medium is the more it resists flow and consequently is less permeable. The experimental measurements of tortuosity of porous materials using electrical conductivity leads to acceptable results provided that the solid portion of the porous sample is non-conductive (Johnson et al., 1982). If the solid skeleton is non-conductive a porous medium filled with a conductive fluid solution will exhibit a potential between two points as a function of the length through the voids joining these points and the current applied. Therefore electrical conductivity measurements in a saturated porous material with a conductive fluid solution can be used to infer tortuosity. In this section a description of such experiments will be given.

6.2.1 Experimental setup

The experimental setup for the tortuosity measurements in the present study is shown in figure 6.1. Figure 6.2 shows a photograph of the electrical conductivity experiment conducted on the saline solution. This setup is designed according to the size of the samples that are used in this study. A porous sintered glass bead sample

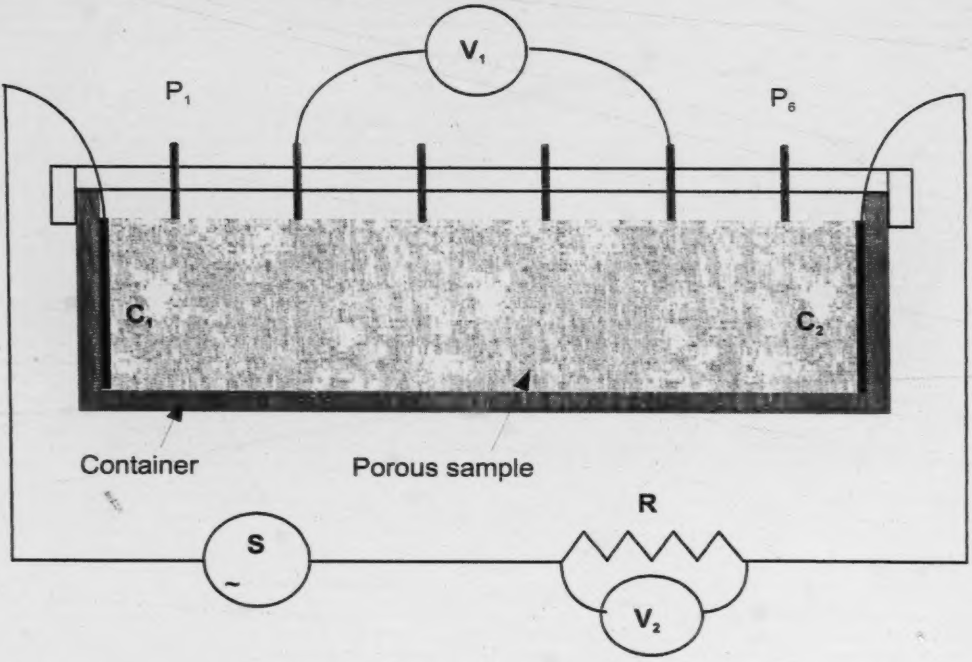

Figure 6.1: Setup for electrical conductivity measurement through porous media.

fits into a non-conductive container. The sample is impregnated to saturation under vacuum with an electrically conductive saline water solution. A low frequency (60 Hz) alternating current is input through two large end electrodes C_1 and C_2 that cover exactly two opposing sides of the sample. The current is deduced from the voltage V_2 across a known resistance R. This setup produces equipotential surfaces parallel to the current electrodes C_1 and C_2 provided that the structure of the sample is homogeneous. A voltage V_1 at the surface is obtained across electrodes $(P_1, ..., P_6)$ of known spacing. The experiment is repeated by replacing the sample with only the conductive saline water solution. For each sample the pair of voltages V_1 and V_2 are measured across different electrodes at the surface of the sample. Uniform results were obtained for all the samples that showed very little change in the readings between any two equidistant electrodes. This indicates the porosity is homogeneously distributed in the samples and therefore the tortuosity can be accurately deduced. The results on porous synthetic materials using this methodology will be given in the next chapter.

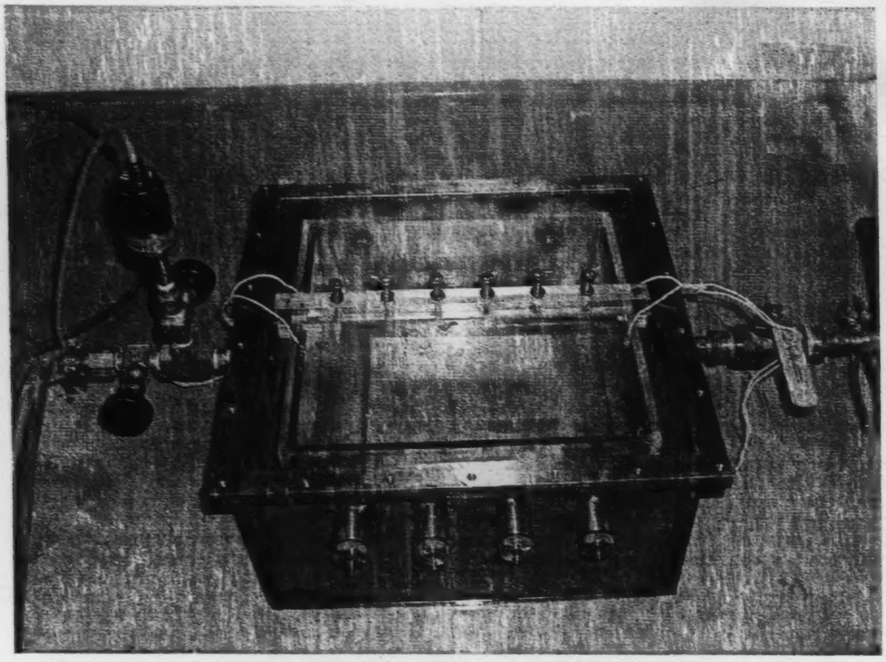

Figure 6.2: Photograph of the electrical conductivity experiment apparatus.

6.2.2 Tortuosity derivation

Here are given the relationships between electrical conductivity and sample tortuosity. Let $_p$ and $_s$ subscripts represent the porous sample and the saline solution, respectively. Let $_1$ and $_2$ subscripts for the potential V refer to the measured potentials V_1 and V_2, respectively, as shown in figure 6.1. Let Z and i be the impedance and the current, respectively. We can write

$$V_{2p} = Z_p i_p \tag{6.1}$$

$$V_{2s} = Z_s i_s \tag{6.2}$$

$$V_{1p} = R i_p \tag{6.3}$$

$$V_{1s} = R i_s \tag{6.4}$$

where the electrical impedances Z_p and Z_s are

$$Z_p = \frac{\rho L_p}{\beta S_p} \tag{6.5}$$

$$Z_s = \frac{\rho L_s}{S_s} \tag{6.6}$$

L_p is the distance between the electrodes P_1 and P_6 that follows the shortest tortuous path through the pore space. L_s is the direct straight line distance between the same electrodes. S_s is the area of the current electrodes C_1 (or C_2) in contact with the solution through the voids at the surface of the sample, hence given by $S_s = \beta A$ where A is the surface of the electrode and β the porosity. In the other hand S_p is the area of the current electrodes C_1 (or C_2) in contact with the solid skeleton at the surface of the sample, hence given by $S_p = (1 - \beta)A$. Using equations 6.1 through 6.4 we can write

$$\frac{V_{2p}}{V_{1p}} = \frac{Z_p}{Z_s}\frac{V_{2s}}{V_{1s}} \tag{6.7}$$

This equation can be rewritten as

$$V_{ps} = \varsigma V_{sp} \tag{6.8}$$

where $V_{ps} = V_{2p}V_{1s}$, $V_{sp} = \frac{S_s}{\beta S_p}V_{2s}V_{1p}$, and $\varsigma = \frac{L_p}{L_s}$ is the tortuosity of the sample. Thus the tortuosity is deduced directly from the slope of equation 6.8. If the porosity of the porous sample is uniform then the ratio $\frac{S_s}{S_p} = 1$ otherwise these surfaces must be measured.

6.3 Permeability measurements

Another parameter that characterizes porous media and plays a major role in the behaviour of the slow P-wave is the permeability K. Here a simple experiment is designed to measure the permeability of the synthetic porous samples used in this study. However this apparatus is only adequate for samples that have sufficiently large permeability.

6.3.1 Experimental setup

A modified falling head device was designed and constructed for permeability measurements. The experimental setup is given in figure 6.3 and a photograph in figure 6.4. It is based on fluid flow through a porous sample. The experiment is monitored by a digital camera that takes images at known given time intervals. The changing fluid levels in cylinders 1 and 2 are read from linear scales. During the falling head experiment automatic photographs are taken at short time intervals that vary with the speed of the falling of the water column. Snap shots are given in figure 6.5 taken at two different times that show the change in the water columns.

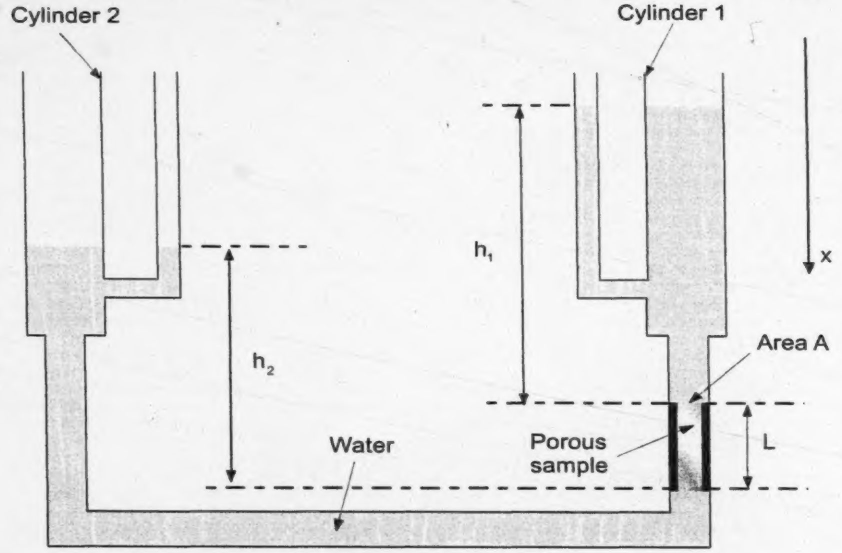

Figure 6.3: Schematic of the apparatus used to measure permeability. h_1 is the head between the top of the sample and the fluid level on cylinder 1. h_2 is the head between the bottom of the sample and the fluid level on cylinder 2.

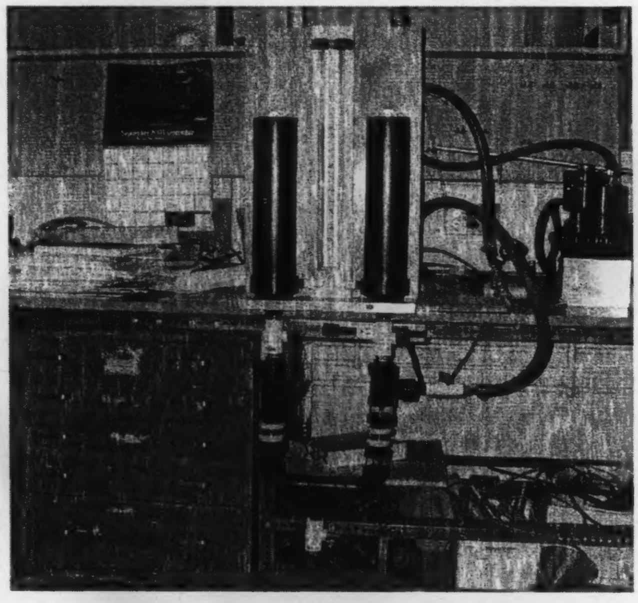

Figure 6.4: Photograph of the apparatus used to measure permeability.

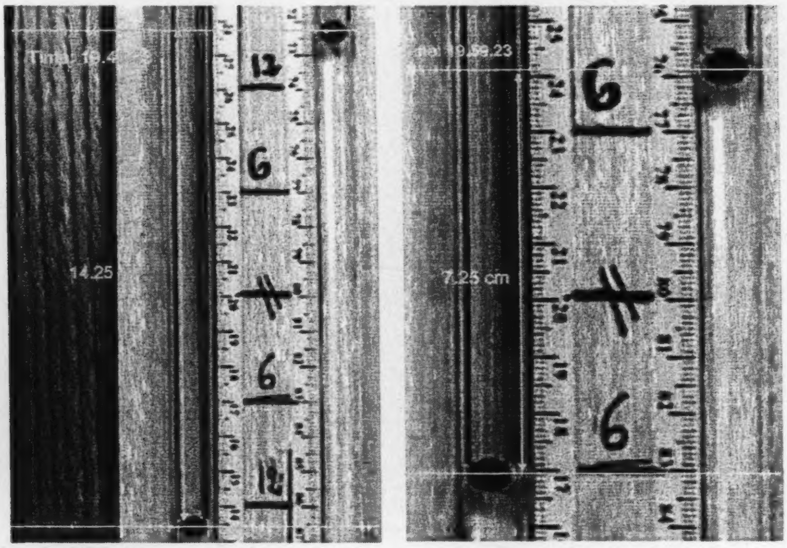

Figure 6.5: Two snap shots showing a difference in the water columns of 7 cm within 11 minutes time difference.

6.3.2 Permeability derivation

In this experiment the fluid flow is assumed governed by Darcy's law

$$q = -\frac{K}{\eta}\frac{dp}{dx} \tag{6.9}$$

where K is the permeability, η the fluid viscosity, q is the Darcy fluid velocity defined as the volume that flows through a unit surface area per unit time, and $\frac{dp}{dx}$ is the pressure gradient in the direction of flow from cylinder 1 to 2. The positive direction (Fig. 6.3) is taken in the direction of flow. At any given time the pressure gradient between the top and bottom of the sample is given by

$$\frac{dp}{dx} = -\frac{\rho g(h_1 - h_2)}{L} \tag{6.10}$$

where ρ is the density of the fluid, g is the gravitational acceleration, L the length of the sample, and h_1 and h_2 are the hydraulic heads as given in figure 6.3. Let $h' = h_1 - h_2$. This quantity is always positive since $h_1 > h_2$ at all times. The velocity q can be written as

$$q = -\frac{v_0}{2A}\frac{dh'}{dt} \tag{6.11}$$

where v_0 is the volume of fluid that flows through the porous sample per unit length per unit time, $\frac{dh'}{dt}$ is the change of h' per unit time, and A is the surface area of the base of the sample that is in contact with the sample. Using equations 6.10 and 6.11 in equation 6.9 we get

$$-\frac{dh'}{h'} = \frac{2K\rho gA}{v_0\eta L}dt \tag{6.12}$$

Integrating both sides we get

$$-\int_{h'_1}^{h'_2} \frac{1}{h'}dh' = \frac{2K\rho gA}{v_0\eta L}\int_{t_1}^{t_2} dt \tag{6.13}$$

which leads to

$$ln\left(\frac{h'_1}{h'_2}\right) = \frac{2K\rho gA}{v_0\eta L}\Delta t \tag{6.14}$$

where $\Delta t = t_2 - t_1$. Let $H = ln\left(\frac{h'_1}{h'_2}\right)$ and $P = \frac{2K\rho gA}{v_0\eta L}$ then we rewrite equation 6.14 as

$$H = P\Delta t \tag{6.15}$$

which is the equation of a straight line; the permeability can be deduced from its slope P. The permeability is then given by

$$K = \frac{Pv_0\eta L}{2\rho gA} \tag{6.16}$$

6.4 Phase velocity measurement

6.4.1 Methodology

To determine the solid skeleton properties the P and S wave phase velocities of the solid skeleton of a porous medium are needed. To illustrate the procedure used in the determination of the phase velocity, let $x_1(t)$ and $x_2(t)$ be two transmitted waveforms recorded at two different locations r_1 and r_2 as the wave travels through a given sample. The recorded waveforms $x_1(t)$ and $x_2(t)$ can be written as

$$x_1(t) = s(t) * g_1(t) * h_1(t) \tag{6.17}$$

$$x_2(t) = s(t) * g_2(t) * h_2(t). \tag{6.18}$$

where $s(t)$ is the input signal, $g(t)$ represents other energy losses than attenuation, and $h(t)$ is the attenuation response of the medium. $g(t)$ includes various effects such as the source and receiver coupling and instrument response. In the frequency domain equations 6.17 and 6.18 are

$$X_1(\omega) = S(\omega)G_1(\omega)H_1(\omega) \tag{6.19}$$

$$X_2(\omega) = S(\omega)G_2(\omega)H_2(\omega) \tag{6.20}$$

The deconvolution of the signal $x_2(t)$ with respect to the signal $x_1(t)$ is given by (Dziewonski and Hales, 1972)

$$X_{21}(\omega) = \frac{X_2(\omega)}{X_1(\omega)} = \frac{X_2(\omega)X_1^*(\omega)}{|X_1(\omega)|^2} \tag{6.21}$$

where $X_1^*(\omega)$ is the complex conjugate of $X_1(\omega)$. The numerator in equation 6.21 is the same as the cross-correlation of $x_2(t)$ with respect to $x_1(t)$. The wrapped phase of $x_{21}(t)$ is totally contained in the cross-correlation and is given by

$$\Delta\phi(\omega) = \phi_2(\omega) - \phi_1(\omega) + 2\pi n(\omega) \tag{6.22}$$

where $n(\omega)$ is an integer. The presence of this integer in the phase difference illustrates the non-uniqueness of the phase difference. To find the correct phase velocity from equation 6.22 a knowledge of the range of expected velocities or a third station is necessary (Dziewonski and Hales, 1972). Equation 6.22 leads to the time delay

$$t_d(\omega) = \frac{\Delta\phi(\omega)}{\omega} \tag{6.23}$$

and the phase velocity is then given by

$$c(\omega) = \frac{(r_2 - r_1)}{t_d(\omega)} \tag{6.24}$$

where r_1 and r_2 are the distances from the source to the stations 1 and 2 respectively. One major difficulty that makes use of the expression 6.24 problematic, however, is that the unwrapped phase of a waveform depends greatly on the low frequency noise component. Higher noise levels result in larger errors in the evaluation of the phase difference in the unwrapping process.

6.5 Attenuation measurements

6.5.1 Methodology

To include the attenuation of the P and S waves of the solid skeleton these must be measured. Attenuation of rocks can be measured in the laboratory by various methods. To do so the following procedure will be followed in the measurement of attenuation in a laboratory. The most common method when the level of noise is acceptable is the direct method. Assuming the source signal $s_1(t)$ and $s_2(t)$ are identical equations 6.27 and 6.28 lead to

$$\frac{X_1(\omega)}{X_2(\omega)} = \frac{G_1(\omega)}{G_2(\omega)} \frac{H_1(\omega)}{H_2(\omega)} \tag{6.25}$$

Taking the natural logarithm of 6.25 we get

$$ln\left(\frac{X_1(\omega)}{X_2(\omega)}\right) = ln\left(\frac{G_1(\omega)}{G_2(\omega)}\right) + ln\left(\frac{H_1(\omega)}{H_2(\omega)}\right) \tag{6.26}$$

Let the left hand side of equation 6.26 be $Y(\omega)$. Assume that G_1 and G_2 do not depend on frequency. G includes all energy loss effects except attenuation. These effects include source and receiver coupling, reflectivity, and instrumental response. In this case we can replace the first term on the right hand side by a constant B. The attenuation filter H_1 and H_2 can be written in the frequency domain as

$$H_1(\omega) = e^{-\alpha_0 f^N r_1} \tag{6.27}$$

$$H_2(\omega) = e^{-\alpha_0 f^N r_2} \tag{6.28}$$

$$\tag{6.29}$$

where $\alpha_0 f^N$ is in units m^{-1}. α_0 is the attenuation coefficient constant independent of frequency. f is the frequency and N is an exponent that varies in general from 2 to 0.5 as the frequency increases from the seismic frequency to ultrasonic frequency bands (Courtney and Mayer, 1993), and r the distance between the source and the receiver for each recorded signal. Using this model, equation 6.26 then becomes

$$Y(\omega) = \alpha_0 f^N (r_2 - r_1) + B \tag{6.30}$$

where r_2 must be larger than r_1. For a linear model (i.e. $N = 1$) equation 6.30 is that of a straight line where the slope determines the coefficient α_0. B is the intercept that contains information about all other losses such as source and receiver coupling, reflectivity, and instrumental response. This model is also used in the determination of the attenuation in vertical or cross-well seismic profiles using the frequency shift method (Quan and Harris, 1997).

6.6 Solid skeleton characterization

The solid component of the fluid-saturated porous material, is characterized by the measured P and S wave phase velocities of the "dry" solid skeleton. It is also important to estimate the P and S wave attenuations as these may play a large role in the behaviour of wave propagation in a fluid-saturated porous material as suggested by the modelling illustrated in figures 4.5 and 4.6. However the measured "dry" shear modulus and bulk modulus of the solid skeleton would be only valid to be used in the equations 4.53 through 4.56 if the phase velocities and attenuations of the "dry" solid skeleton is frequency independent as these equations were derived through static laboratory measurement tests. Due to the low degree of sintering and because the experiments are conducted at zero effective confining pressure the "dry" samples used in this study exhibit both nontrivial S and P wave attenuations.

6.6.1 Methodology

Assume that the "dry" solid skeleton (filled with air) behaves for small deformations as a *homogeneous, isotropic, and linear viscoelastic* (HILV) material (Borcherdt, 1977; Borcherdt, 1982). In doing so we neglect any other mode (for example Biot slow P-wave) generated during the measurements of the P and S wave arrivals. It is important to note that the amount of humidity that is present in the "dry" samples plays a major role in the velocity of the P-wave particularly (see e.g. King et al. (2002)). It is important not to completely "dry" the samples. In this study the samples were washed and then let "dry" at room temperature for about 24 hours. It is found that not all samples gave satisfactory results.

The equation of motion that govern the HILV is given by

$$\left[K_M + \frac{\mu_M}{3}\right] \vec{\nabla}\left(\vec{\nabla} \cdot \vec{u}\right) + \mu_M \nabla^2 \vec{u} = \rho \frac{\partial^2 \vec{u}}{\partial t^2} \tag{6.31}$$

where K_M and μ_M are the complex bulk and shear moduli of the HILV, and $\vec{u}$ is the particle displacement. Let ϕ and $\vec{\psi}$ be the scalar and vector potentials ($\nabla \times \vec{\psi} = 0$, and $\vec{\nabla} \times \phi = 0$). Using Helmhotz decomposition $\vec{u} = \vec{\nabla} \cdot \phi + \vec{\nabla} \times \vec{\psi}$ equation 6.31 can be written as

$$\left[K_M + \frac{4}{3}\mu_M\right] \nabla^2 \phi = \rho \frac{\partial^2 \phi}{\partial t^2} \tag{6.32}$$

for P-waves and

$$\mu_M \nabla^2 \vec{\psi} = \rho \frac{\partial^2 \vec{\psi}}{\partial t^2} \tag{6.33}$$

for S waves. Using plane wave solution of the form

$$\begin{aligned} \phi &= Ae^{i(\omega t - \vec{k_p}\cdot\vec{r})} && (6.34) \\ \vec{\psi} &= B\hat{y}e^{i(\omega t - \vec{k_s}\cdot\vec{r})} && (6.35) \end{aligned}$$

in equations 6.32 and 6.33 respectively we obtain

$$\begin{aligned} k_p^2 &= \frac{\rho}{\left(K_M + \frac{4}{3}\mu_M\right)}\omega^2 && (6.36) \\ k_s^2 &= \frac{\rho}{\mu_M}\omega^2 && (6.37) \end{aligned}$$

where $\vec{r}$ is the position vector. $\vec{k_s}$ and $\vec{k_p}$ are the wave numbers for the S and P waves respectively. For homogeneous plane waves with a wave number $k_p = \frac{\omega}{V_p} - i\alpha_p$ and $k_s = \frac{\omega}{V_s} - i\alpha_s$ for P and S waves respectively, equations 6.36 and 6.37 lead to the complex bulk and shear moduli

$$\begin{aligned} \mu_M &= \frac{\rho V_s^2 \omega^2}{(\omega^2 - \alpha_s^2 V_s^2 - 2i\alpha_s \omega V_s)} && (6.38) \\ K_M &= \frac{\rho \omega^2 V_p^2}{\left(\omega^2 - \alpha_p^2 V_p^2 - 2i\alpha_p \omega V_p\right)} - \frac{4}{3}\mu_M && (6.39) \end{aligned}$$

If a linear model $\alpha = \alpha_0 f$ is used for the attenuation then both moduli are independent of frequency. In this case equations 6.38 and 6.39 become

$$\begin{aligned} \mu_M &= \frac{4\pi^2 \rho V_s^2}{(4\pi^2 - \alpha_{0s}^2 V_s^2 - 4\pi i \alpha_{0s} V_s)} && (6.40) \\ K_M &= \frac{4\pi^2 \rho V_p^2}{\left(4\pi^2 - \alpha_{0p}^2 V_p^2 - 4\pi i \alpha_{0p} V_p\right)} - \frac{4}{3}\mu_M && (6.41) \end{aligned}$$

where $\alpha_0 f$ is a real constant and is in m^{-1} and consequently α_0 is in s.m^{-1}. In this model both the shear modulus μ_M and the bulk modulus K_M are complex but are independent of frequency.

To infer μ_M and K_M we need to measure both the P and S wave phase velocities and attenuations.

6.7 Conclusions

Important parameters that are needed to properly model wave propagation, transmission, and reflection in porous materials were discussed. The porosity and density can be directly measured through weights of "dry" and water-saturated samples. Simple experiments were constructed for the measurement of the tortuosity and permeability. The bulk and shear moduli of the fluid free solid skeleton were assumed to be frequency independent and consequently can be deduced from the measurements of the P and S wave velocities and attenuations.

Chapter 7

Transmission experiments through a water-saturated thin porous plate immersed in water

7.1 Introduction

Biot has derived a theory for propagation of acoustic waves in fluid-saturated porous media that predicted the existence of a second compressional wave in such media (Biot, 1956a) and (Biot, 1956b). Since then, several other approaches have been proposed such as that of de la Cruz and Spanos (1985). Numerous attempts have been made in the laboratory to detect the highly attenuated slow P-wave. Plona (1980) has first observed the slow dilatational wave in a porous synthetic rock. Then other workers have claimed to have observed this wave both in synthetic rocks (Johnson and Kojima, 1994), (Geerits and Kelder, 1997); and in a natural Nivelsteiner sandstone (Kedler and Smeulders, 1997). Here a modified experiment is presented that employs a large transducer to create a near plane wave for transmission through porous plates. This method has been successfully employed in the calibration of reflectivity on elastic materials in chapter 3 and in Bouzidi and Schmitt (2000). Here, the method allows a definitive detection of the slow dilatational wave that plays an important role in the characterization of the porous material. The attenuation of the recorded wave modes were measured. This is the first quantitative measurement, to the author's knowledge, of the attenuation of the slow compressional wave. The intrinsic attenuation due to fluid flow is dissociated from the observed attenuation that also includes the attenuation associated to the solid skeleton of the porous material.

In this chapter a transmission of a bounded acoustic pulse through a water-saturated porous material immersed in water was conducted on a thin synthetic porous plate constructed from sintered soda-lime glass beads. The sample labelled S082 that is originally designed for transmission measurements will also be used in reflectivity measurements as it was the only sample constructed that allowed for a complete characterization. It was constructed thin (2.46 cm) to allow the observation of the second P-wave. This elusive wave has been clearly observed in the present experiment. The same large acoustic bounded pulse source and near-point receiver were used in the experiments as for elastic media in chapter 3.

First a description of the synthetic porous sample will be given. It will be followed by the determination of all relevant parameters by the test devised in chapter 6. Then the transmission experiment will be described and results will be presented with the corresponding calculated models. Measurements of velocities and attenuations will be deduced from observations and compared later to calculated values.

7.2 Synthetic sample description

A porous synthetic plate was made from sintered glass beads using a graphite mold with an interior designed to be 2.50 cm thick and 22 cm for each of the other dimensions. The mold is packed with soda-lime glass beads with diameter ranging from 150 μm to 212 μm. The sample is then brought slowly to 700°C. The duration of the process has lasted about 4 hours. Then the oven was shut down and the sample was kept inside for about 20 hours. This process allowed the sample to cool down slowly and release stress that may build up during the cooling phase. This resulted in a very uniform sample 2.46 cm thick with nearly perfect flat surface. A picture of the sample is shown in figure 7.1 and another S.E.M. photograph of the surface of the sample is shown in figure 7.2. Note that the diameter of the glass beads supplied by the manufacturer are not very precise as they are designed for sand blasting purposes. Therefore the sample contains beads that are smaller or larger in diameter than the diameter range given above. The porosity of the sample and density of the glass beads are measured through weights of the "dry" and water-saturated porous sample under vacuum conditions. The tortuosity, the permeability,

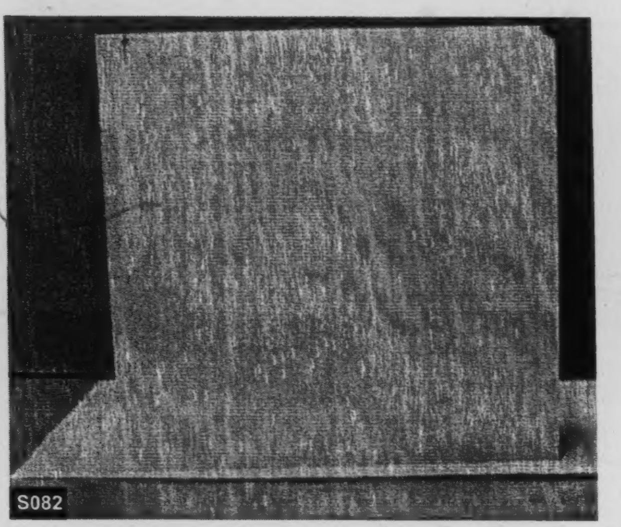

Figure 7.1: Photograph of the porous synthetic sandstone S082 used in the transmission experiment.

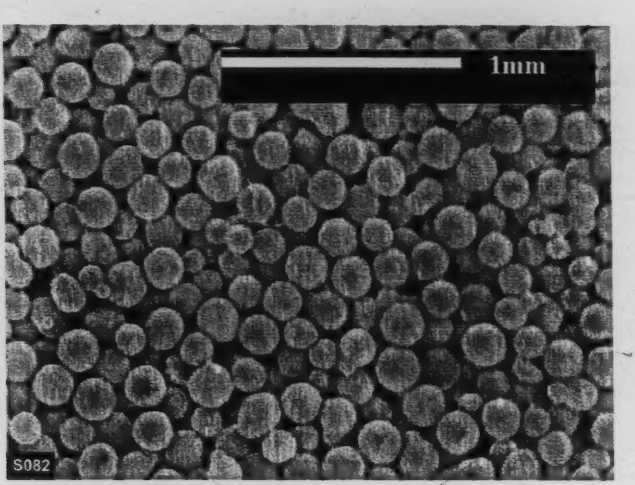

Figure 7.2: S.E.M photograph of the surface of the porous synthetic sandstone S082 used in the transmission experiment.

the "dry" velocities, and the attenuations of the porous sample are determined by the methods described in chapter 6 sections 6.3, 6.4, 6.5, and 6.6 respectively. The results are summarized in tables 7.1 and 7.2. The overall sample is uniform and it surface large enough (22 cm×22 cm) to receive a large incident acoustic bounded

Property	$\rho^{(s)}$	$\rho^{(f)}$	η	$K^{(s)}$	$K^{(f)}$	β	ς	K
Units	$kg.m^{-3}$	$kg.m^{-3}$	$Pa.s$	GPa	GPa	–	–	$m^{-2} \times 10^{-12}$
Value	2455	995	0.001	43.7	2.209	0.382	1.439	19.9
Error %	1.4	0.5	–	5	1	2.1	0.1	3.5

Table 7.1: Measured porous sample S082 characteristics and properties. $\rho^{(s)}$ mineral grain density, $\rho^{(f)}$ density of water, $K^{(s)}$ is the bulk modulus of the mineral grains, $K^{(f)}$ is the bulk modulus of water, β is the porosity, ς is the tortuosity, and K is the permeability.

Property	F	V_P	V_s	α_{0P}	α_{0S}
Units	MHz	m/s	m/s	m^{-1}	m^{-1}
Value	0.78	2540	1555	6	27
Error %	–	0.6	2.25	10	10

Table 7.2: Measured "dry" dynamic properties of the porous sample S082. V_p is the "dry" P-wave phase velocity, V_s is the "dry" S-wave phase velocity, α_{0P} is the P-wave attenuation of the "dry" sample, α_{0S} is the S-wave attenuation of the "dry" sample. The attenuations are given at the frequency 0.78 MHz.

pulse. The source is the same used in all experiments. The frequency bandwidth of the source is 0.2 to 1.2 MHz. The predominant wavelength in the fluid is 1.9 mm which is larger than the average grain size of 0.175 mm. Since the type of glass used to make the beads is of various quality, the density might vary slightly from batch to batch. A range of density values are given for soda-lime glass and a mean value is taken to be 2455 kg.m^{-3} and the error is taken as the difference between the mean and the extreme value. The bulk modulus of the beads is taken to be 43.7 GPa with an error of 5%. All the other parameters listed in table 7.1 are actual measurements in the laboratory.

7.3 Experimental procedure

A new experimental method of probing porous materials has been developed using a large area (10 cm×7.5 cm) ultrasonic transducer (see chapter 4) as an acoustic

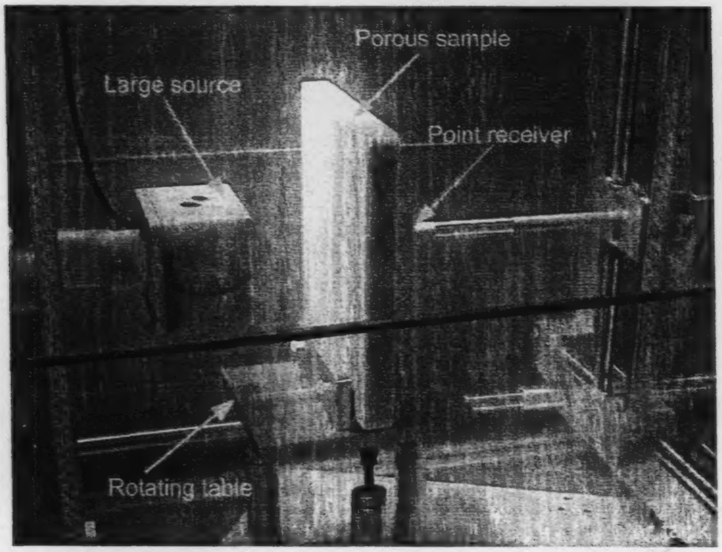

Figure 7.3: Wave transmission through a water-saturated synthetic porous plate using an acoustic scanner. A large source transducer is used to generate a nearly flat and large beam. The transmitted wave field is recorded by a near-point receiver.

source (Fig. 7.3). One major advantage of such a source is that the central amplitude of the generated bounded acoustic field remain nearly constant within the dimensions of the experiment. This simplifies the analysis and makes small events easily detectible. This method turns out to be very useful in detecting the slow compressional wave in fluid-saturated porous materials. The setup as described in figure 7.3 allows measurements of the three propagating modes within the water-saturated porous sample for a large range of angles of incidence. Both the large source and the near-point receiver remain fixed as the plate is rotated from -50° to +50° in steps of 1°. In this configuration the receiver always points to the centre of the source. The acoustic bounded pulse that reaches the point receiver of any wave mode emerges parallel to the incident one but shifted to the left (or the right) with a distance that depends on the velocity of the wave mode considered within the porous sample according to the Snell's Law of refraction. However the wave field of any transmitted wave mode will be spread near critical angles as all wave numbers present in the incident acoustic bounded pulse will be refracted at different angles. This is actually true only if the velocity of the wave mode is much higher than that of water. Because

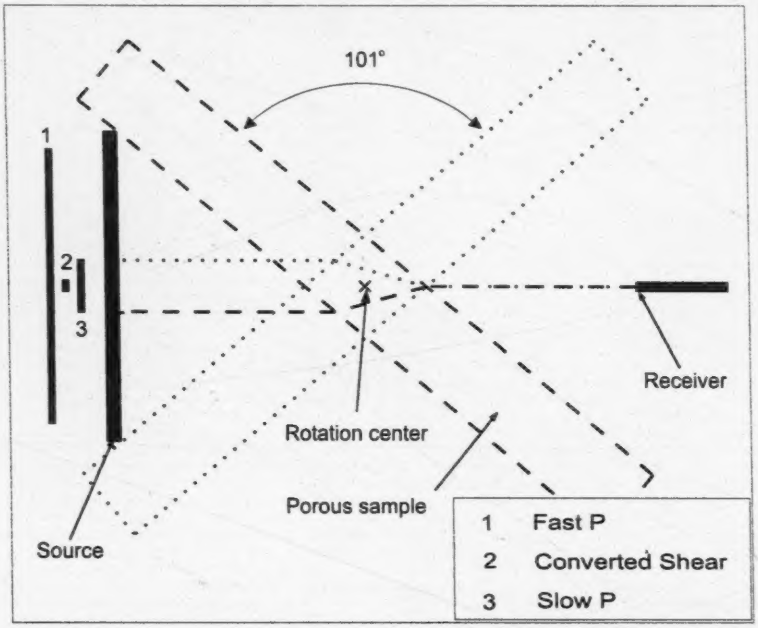

Figure 7.4: A cartoon of the transmission experiment showing the three wave modes. The angle of incidence changes as the porous sample rotates while the source and receiver remain constant. 1, 2, and 3 show the area where the rays originate for the fast P-wave, the S-wave, and the slow P-wave respectively. 1: Fast P-wave with velocity of 2500 m/s, and incidence angles of -30^o to +30^o. 2: Converted S-wave with a velocity of 1450 m/s, and incidence angles of -50^o to +50^o. 3: Slow P-wave with a velocity of 980 m/s, and incidence angles of -50^o to +50^o. The velocity in the water is 1490 m/s.

the source used here generates a large and flat bounded acoustic pulse, wave arrivals at the point receiver originate from a small area around the centre that depend on the velocity of the wave mode. For example if the velocity of a wave mode is equal to the velocity of the surrounding medium (here water) the arrival always originates from the centre of the source for all angles of incidence. As the velocity increases or decreases from that of water this area will increase. This is illustrated in figure 7.4 for three wave modes, a fast compressional wave (1: 2500 m/s angles -30^o to +30^o), a converted S-wave (2: 1450 m/s angles -50^o to +50^o), and a slow compressional wave (3: 980 m/s angles -50^o to +50^o). For a large number of incident angles the three wave modes originate from an area that has a constant amplitude within the dimensions of the experiment. This allows the attenuation of these waves to be considered without major correction such as geometrical spreading.

7.4 Experimental observations

Here observations of transmitted wave modes through the porous sample as recorded by the point receiver with the setup described in the previous section will be presented. Before pointing out the various arrivals, it is first convenient to show the arrival times at which various waves that propagate in the water, then through the water-saturated sample, and finally back in the water that would be detected at the point receiver. Three probable but hypothetical waves with velocities, faster, equal, and slower than that of water are considered. For simplicity the trajectories will be calculated using Snell's law. Consider a fast wave with velocity of 2500 m/s, a wave with velocity 1490 m/s equal to that of water, and finally a slow wave with a velocity of 980 m/s. The distances travelled are shown in figure 7.5 for a source-receiver distance of 17 cm. The total distance travelled in the water medium by each wave with the corresponding velocity is shown in panel *a*) for angles of incidence varying from -50^o to $+50^o$. This shows that the total distance travelled in the water for all three waves decreases as the angle of incidence increases (or decreases) from normal incidence as the sample is rotated. The second panel *b*) shows the distance in the sample as a function of angle of incidence. It shows clearly that the distance travelled by each wave in the sample increases for all angles of incidence that depart from normal incidence. Panel *c*) shows the overall distance travelled by each wave which again increases for all angles of incidence that depart from normal incidence except that of the wave which has the same velocity as that of water that remains constant for all angles of incidence. Therefore a wave with a velocity in the sample that is equal to that of water will appear at the same time regardless of the angle of incidence. Since the overall travel distance always increases with angle of incidence the arrival time for these waves will be progressively dominated by the travel distance in the sample.

If the velocity of the wave is lower than that of water then the arrival time will increase as the angle of incidence departs from the normal incidence and therefore this wave will show a curvature towards increasing arrival times relative to normal. On the other hand, if the velocity of a wave is greater than that of water then the

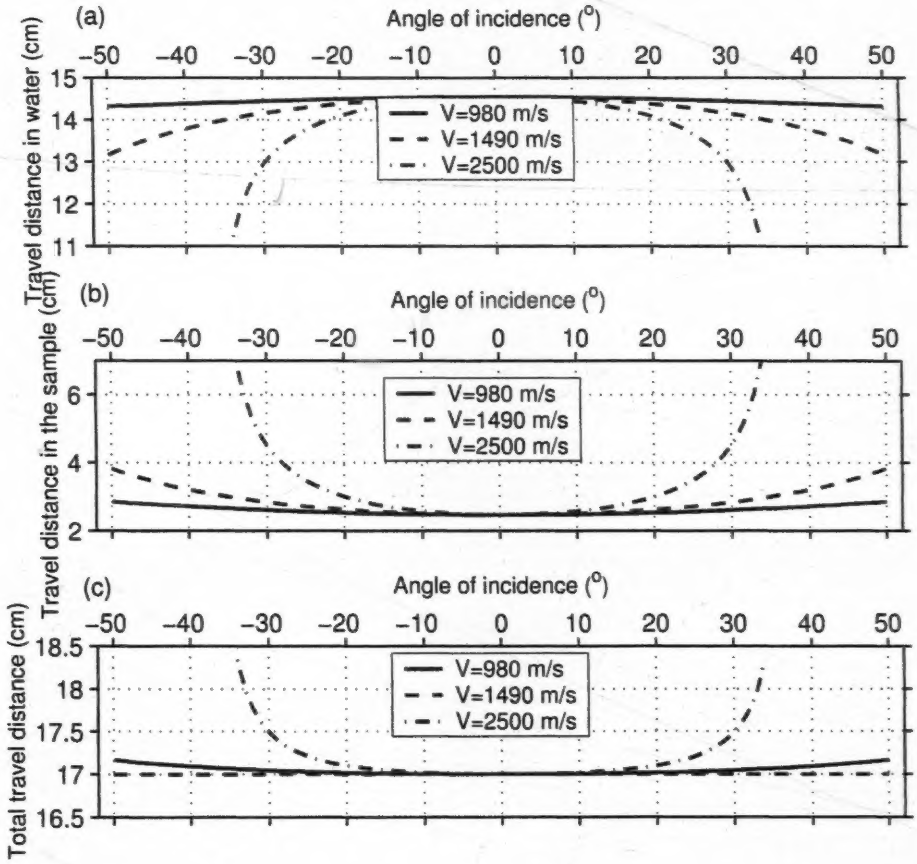

Figure 7.5: Travel distances and arrival times of the various waves that are transmitted through a thin water-saturated porous plate immersed in water. a) Total distance travelled in water. b) Distance travelled in the sample. c) Total distance travelled in the sample and in the water.

arrival time will decrease with increasing (or decreasing) angles of incidence; and consequently this wave will curve towards shorter arrival times. Therefore using the setup as described in the previous section various wave arrivals will be easily identifiable on the display of the recorded traces.

The waveforms recorded in the experiment of section 7.3 are displayed in figure 7.6. The recorded amplitudes by the point receiver are displayed with each trace normalized by its root mean square (RMS) amplitude. This helps to show better the

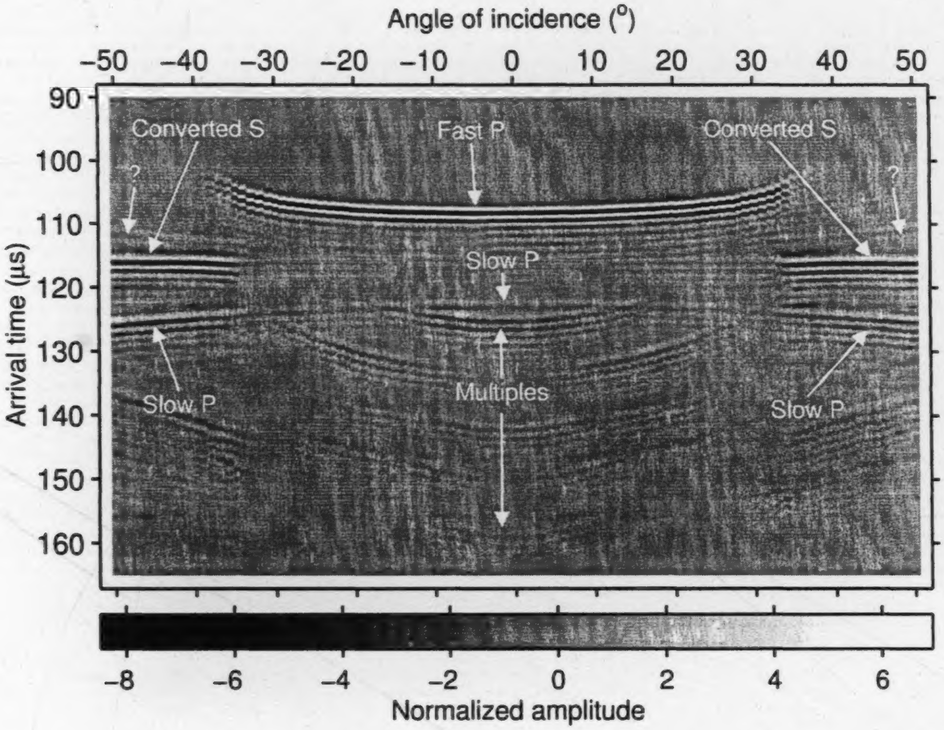

Figure 7.6: Observed transmitted bounded pulse through a thin water-saturated porous plate immersed in water. Each trace is normalized by its RMS amplitude. The amplitudes are true along the time axis. The unknown arrival labelled by a question mark could be interpreted as described in chapter 4 section 4.4.

wave field at large angles of incidence. In this display many wave modes are clearly distinguished. One event, labelled as slow P-wave, is curving towards increasing time and therefore its velocity within the sample must be less than that of water. This event is clearly the slow P-wave that is excited at the first boundary and then converted to a sound wave in the water at the second boundary. The event labelled converted S-wave is an S-wave excited at the first boundary and then converted at the second boundary back to a sound wave. This event is curving subtly towards increasing time suggesting that the velocity is less than but nearly that of water. The large amplitude event is the fast P-wave and is curving towards the decreasing time indicating its velocity is greater than that of water. The other events are mainly multiples of the fast P-wave. The multiple at about 135 μs appear only above 10^o of angle of incidence suggesting, but not confirmed, that it is a first order multiple that is converted as an S-wave at the first boundary and back to a P-wave at the second boundary. It is evident that beyond the P-wave critical angle (33.1^o) most of the transmitted energy is converted to the S and slow P waves. Despite the high attenuation of the slow P-wave it appears strong at all angles. Each trace is normalized by its RMS amplitude but no gain is applied along the time axis. This is in accordance with the illustrative example studied in chapter 5. Another event worth noting is that labelled with a question mark which curves upwards and therefore its velocity must be higher than that of water. The interpretation of this event could be the "porosity wave" predicted by de la Cruz/Spanos theory as reported in chapter 4 section 4.4. Its approximate velocity, picked from the observed data, is 1800 m/s.

7.5 Phase velocities of the observed waves

The bounded acoustic pulse is recorded after travelling through the water-saturated synthetic porous sample. The data shown in figure 7.6 will be used in this section to infer the measurement of the phase velocity and the attenuation of the fast P, the slow P, and the converted S waves. The arrival of each wave mode is isolated by a time window and used along with the source wavelet to calculate the phase velocity and attenuation according to the procedure described in sections 6.5 and 6.6. To calculate the phase velocities the travel distance must be known. For the fast P-wave the data used is at normal incidence and therefore the distance is simply the sample thickness. However for the slow P-wave the arrivals at low angles of incidence are highly contaminated by the first multiple of the fast P-wave. The converted S-wave is simply very weak at low angles. Therefore the far 11 traces (large angle of incidence) are used for both the slow P-wave and the S-wave where these transmitted events appear strong. The distances used are those leading to the least spreading of calculated velocities. The phase velocity of the fast P-wave is shown in figure 7.7 and calculated according to the procedure described in section 6.5. The phase velocities are 2730 ±20 m/s, 1485±15 m/s, and 1015±10 m/s, for the fast P-wave, the S-wave, and the slow P-wave respectively. These velocities are all given as the mean value at the peak frequency 0.78 MHz of the input signal. The results are shown in figures 7.7, 7.8, and 7.9. A summary is given in table 7.3.

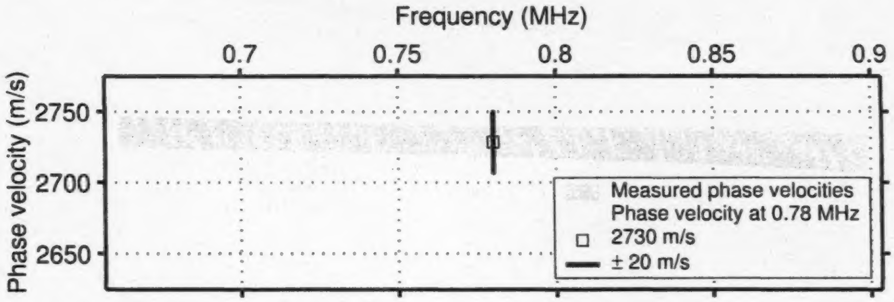

Figure 7.7: Measured phase velocity of the fast P-wave. A mean value of 2730±20 m/s is measured. The error is taken as the extremes of the results of 11 arrivals of the fast P-wave (shaded area).

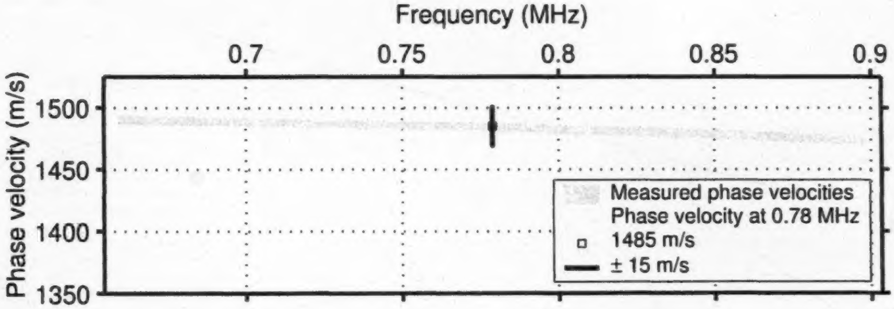

Figure 7.8: Measured phase velocity of the S-wave. A mean value of 1485±15 m/s is measured. The error is taken as the extremes of the results of 11 arrivals of the converted S-wave (shaded area).

Although the trends in these figures are suggestive of abnormal dispersion (i.e. velocities decreasing with frequency) the experimental error cannot prelude the cases of constant velocity or normal dispersion (i.e. velocities increasing with frequency).

Wave mode	Fast P	Slow P	Shear
Phase velocity (m/s)	2730 ± 20	1015 ± 10	1485 ± 15

Table 7.3: The measured phase velocities of the fast P, the slow P, and the converted S waves.

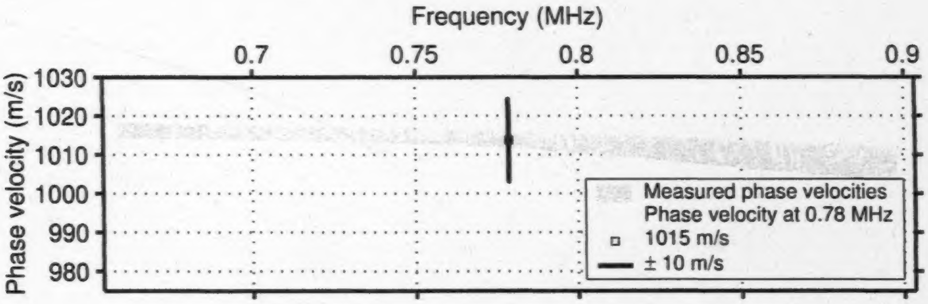

Figure 7.9: Measured phase velocity of the slow P-wave. A mean value of 1015±10 m/s is measured. The error is taken as the extremes of the results of 11 arrivals of the slow P-wave (shaded area).

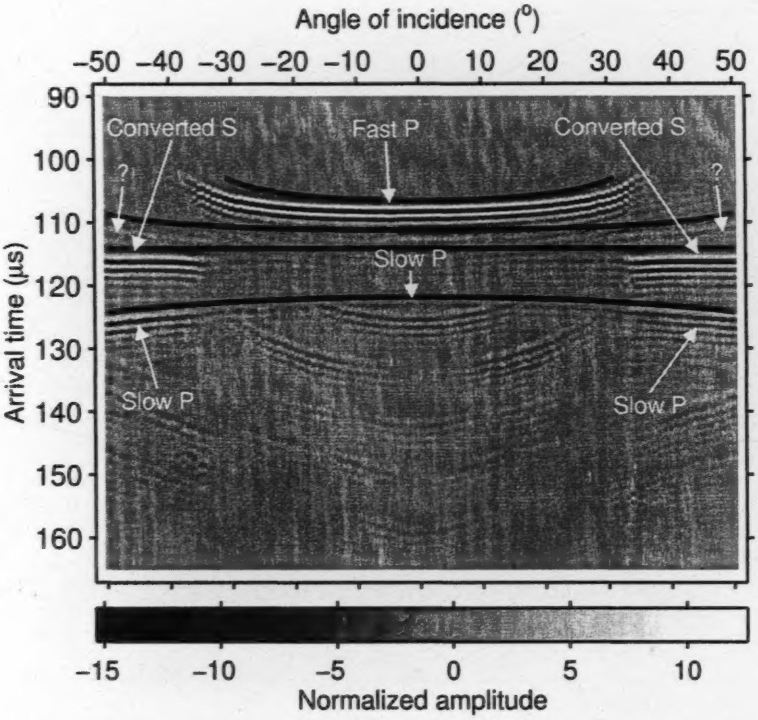

Figure 7.10: Calculated arrival times via Snell's law. The velocities of table 7.3 are used. The unknown arrival labelled by a question mark (approximately 1800 m/s) could be interpreted as described in chapter 4 section 4.4.

Alternatively, it is also convenient to show that the velocities of the observed wave modes can be approximated by using Move Out (MO) corrections based on Snell's law. The calculated travel times for the three wave modes are superimposed on the display of the recorded data (Fig. 7.10). The MO corrections are calculated according to the geometry of the experiment described by the schematic diagram given in figure 7.4. For each of the three events of interest, the fast P-wave, the S-wave, and the slow P-wave an MO correction is applied according to the velocity of each wave as given in table 7.3. The MO process is applied such that the travel time is corrected to become only that across the sample and at normal incidence. The result is shown in figure 7.11 where the three events are nearly flattened. However

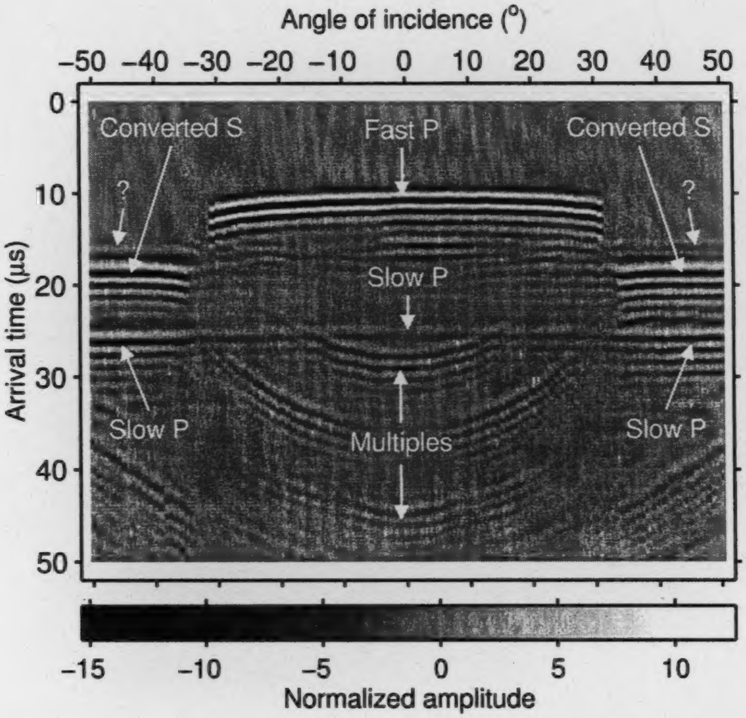

Figure 7.11: 4 main events, the fast P, the converted S, the slow P, and "the porosity wave labelled ?" corrected to normal incidence. The Move Out corrections were calculated with the measured velocities given in table 7.3 that are respectively 2730 m/s, 1485 m/s, 1015 m/s, and 1800 m/s for "the event labelled with a question mark".

the fast P-wave exhibits a curvature at high angles of incidence. This is normal according to the geometry of the problem. The centre of the wave field generated by the source evolves as it propagates as described in detail in chapter 3. The minimum travel distance in the present problem is 17 cm, which includes the travel distance both in the water medium and the water-saturated porous sample. At this distance the stable part of the bounded acoustic pulse is reduced and waves emanating from the parts far from the centre of the source have a different geometry which has not been taken into account in the calculation. However the fast P-wave arrivals in the central traces are nearly flat. These originate from the neighbourhood of the centre of the source and their geometrical path is close to that used to calculate the travel time curves.

7.6 Attenuations of the observed waves

The same data used for the phase velocity is used in the attenuation measurements for the three observed wave modes. The attenuation are measured according to the procedure described in sections 6.6. However it is important to note that in the small frequency range the attenuations will not exhibit the curvature that is typical of attenuation in porous media. Recall equation 6.30 the attenuation model described in section 6.6 chapter 6

$$Y(\omega) = \alpha_0 f^N (r_2 - r_1) + B \tag{7.1}$$

To use this equation either the data must be known in a wide range of frequencies including low frequencies or the exponent N must be given. If a linear model ($N = 1$) is assumed some of the attenuation is diluted in the intercept B and is not readily retrievable. Therefore one must know the exponent N in order to obtain an absolute measurement of attenuation from the observed data. At this stage not all parameters that are needed for modelling were measured. The dynamic mass transfer ρ_{12} can be inferred from the tortuosity, the porosity, and the fluid density. However the viscosity correction factor $F(\omega)$ is not known and can not be measured at this point. An alternative will be described below.

As pointed out earlier in section 4.9 chapter 4 ρ_{12} and $F(\omega)$ (and eventually shear viscosity η and permeability K) can be replaced if the phase velocity and the attenuation of the S-wave of the fluid-saturated porous medium are known. At present only the phase velocity of the S-wave is measured, not the attenuation. It cannot be measured directly as the model to apply is unknown. A similar problem holds for the measurement of the attenuation of the fast P and slow P waves. However within the range of frequency bandwidth present in the input signal these attenuations are varying linearly. A straight line fit will provide the attenuation for each of the three modes within an unknown constant. At this point a solution to the problem would be that shear attenuation that provides the attenuations of the three modes parallel to the measured ones and also the fast P and slow P wave velocities be in the measured range. Using the measured phase velocities and the attenuations (within a constant) of the fast P, the slow P, and the S waves it is possible to numerically calculate the attenuation of the S-wave that leads to the best fit of the observations. It is found that the attenuation of the slow P-wave is highly dependent on the S-wave velocity because the latter depends on ρ_{12} that in turn influences greatly the phase and attenuation of the slow P-wave. In table 7.4 the numerical results are calculated at the peak frequency 0.78 MHz. ρ_{12} and $F(\omega)$ are inferred and consequently Δ is calculated. Also ρ_{12} can be inferred from the tortuosity, the porosity, and the density of the fluid. Note that the velocity of the S-wave is given to more significant digits than reasonable in order to point out that the slow P-wave is highly influenced by a small change in the S-wave velocity, therefore in the ρ_{12} parameter.

Property	S velocity	S attenuation	ρ_{12}	$F(\omega)$	Δ
Units	m/s	m^{-1}	kg/m^3	–	μm
Value	1487.9	41.5	-187.5	$21.64 + i21.64$	10.8

Table 7.4: Inferred dynamic mass transfer ρ_{12}, the viscosity correction factor $F(\omega)$, and the characteristic length Δ at the frequency 0.78 MHz.

The observed attenuations are given in figures 7.12, 7.13, and 7.14 for the fast P, the converted S, and the slow P waves respectively. The calculated attenuation curves are overlayed. It is important to note here that the attenuation of the fast P and the S waves are highly influenced by the attenuation of the solid skeleton given in table 7.2. The influence of the shear and P-wave attenuation of the solid skeleton is described in section 4.8.

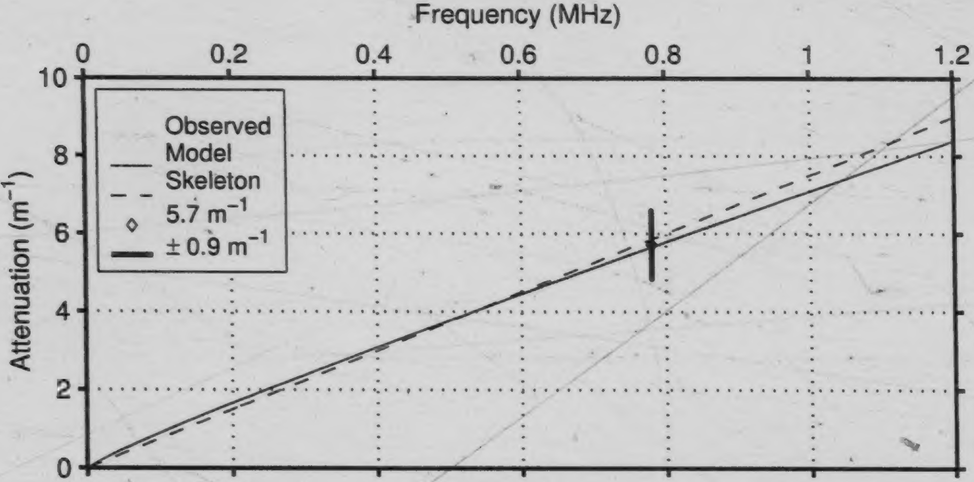

Figure 7.12: Measured attenuation of the fast P-wave. The observed attenuation (shaded area) is calculated with 11 fast P-wave arrivals. The attenuation at the peak frequency of the source wavelet is shown with an error bar of 6.5%.

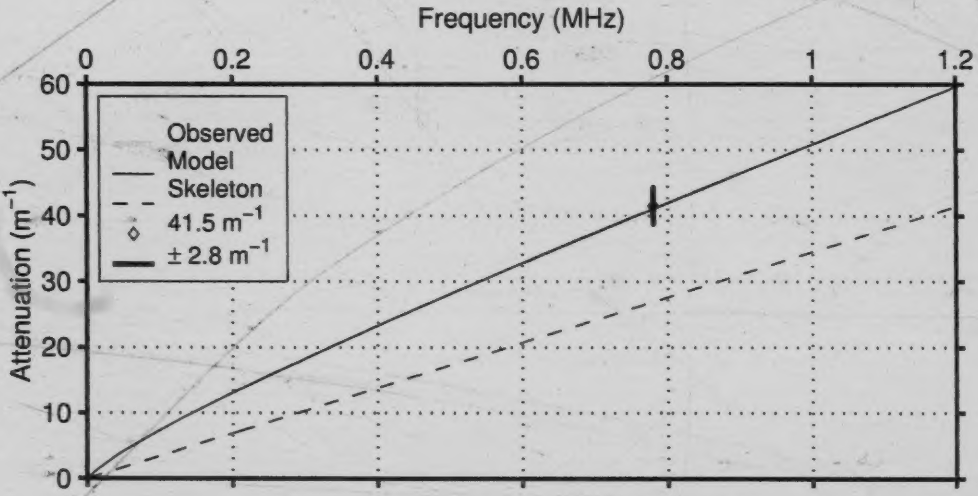

Figure 7.13: Measured attenuation of the S-wave. The observed attenuation (shaded area) is deduced from 11 converted S-wave arrivals at post S-critical angle of incidence. The attenuation at the peak frequency of the source wavelet (0.78 MHz) is shown with an error bar of 4.6%.

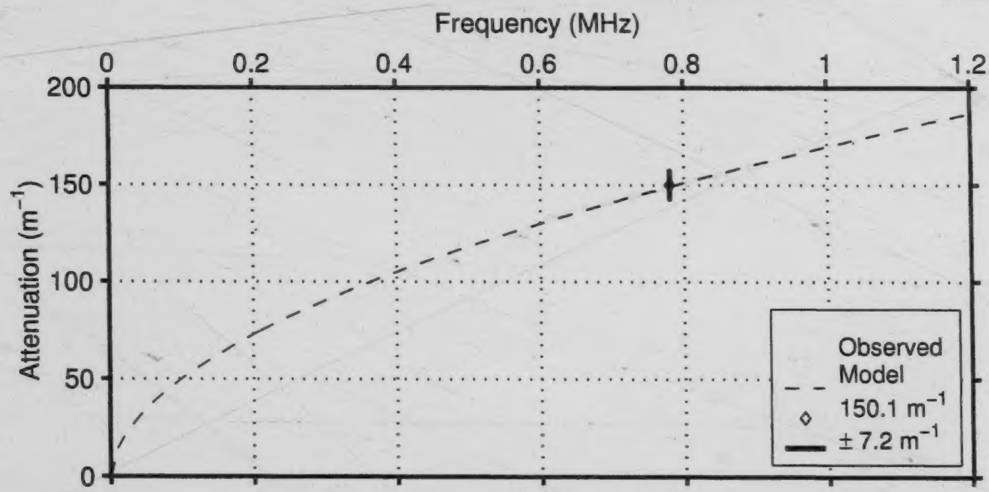

Figure 7.14: Measured attenuation of the slow P-wave. The observed attenuation (shaded area) is calculated with 11 slow P-wave arrivals. The attenuation at the peak frequency of the source wavelet (0.78 MHz) is shown with an error bar of 9.9%.

7.7 Conclusions

An experimental method that employs a large transducer to probe porous materials was developed. The large source and the point-receiver pair has successfully recorded the transmitted slow P-wave through a 2.46 cm thick water-saturated porous synthetic rock. This wave appeared strongly at all angles of incidence without amplification. The method does not require the receiver to move in search for detectible arrivals. The velocities and attenuations of the fast P, the slow P, and the converted S waves were successfully estimated. The arrival time for each wave is calculated and matches the observed recorded data. The overall attenuation of the converted S and fast P waves were highly influenced by the attenuation of the solid skeleton. As expected the slow P-wave is highly attenuated. All useful parameters needed for the modelling of wave propagation in the water-saturated porous material have been determined. Over the relatively narrow bandwidth of the experiments, it is difficult to see any dispersion (see figures 7.7, 7.8, and 7.9) let alone relate this dispersion to the attenuation.

Chapter 8

Reflectivity experiments from the interface between a fluid and a fluid-saturated thin porous plate

8.1 Introduction

As described in chapter 6 the elastic theory does not necessarily properly describe the reflectivity from fluid-saturated porous material interfaces due to both attenuation and the existence of a second P-wave.

In this chapter the results of the reflectivity experiments from a water and a water-saturated porous material interface that were conducted on a thin porous synthetic plate constructed from sintered soda-lime glass beads will be given. The reflectivity measurements are conducted using the same setup used in chapter 3 to measure reflectivity from a fluid and elastic solid interfaces. The author believes these are the first quantitative studies of reflectivity from a liquid-porous medium interface.

The thin porous sample labelled S082 is originally designed for transmission measurements as described in the previous chapter. Reflectivity measurements were also conducted on this sample. The large acoustic bounded pulse source and the near-point receiver were used in the experiments as for elastic media in chapter 3.

First a description of the synthetic porous sample will be given. It will be followed by the determination of all relevant parameters that are needed for modelling wave propagation in porous media. Then the reflectivity results from the interface between water and the water-saturated synthetic porous sample are presented with the corresponding calculated model.

8.2 Experimental reflectivity from water and a water-saturated thin porous synthetic sample

In this section a complete reflection experiment from an interface between water and a thin (2.46 cm), water-saturated porous plate, including identification of all possible converted waves present, will be discussed in details. Identification of these wave modes is important for two reasons. First, it can help us understand where the amplitude of the primary reflection may be disturbed by interfering arrivals. Second, the arrivals seen are to the best of the author's knowledge the only experimental observations of wave mode conversion between S and slow P waves. It turns out that this analysis is important to understand these data. Then the focus will be on the main reflection from the water and the water-saturated porous sample interface. The calculated plane wave and bounded acoustic pulse models will be compared to the experiments, this may be considered as a fundamental test of porous media theories.

The sample is immersed in water after being saturated by the same fluid under vacuum conditions. The same setup used to acquire reflectivity from water-elastic solid materials interfaces as described in chapter 3 is used here. The porous sample is described in detail in chapter 7. First a study of the observed wave events will be conducted according to simple ray theory and event travel times only.

A schematic of the reflectivity experimental setup is given in figure 8.1. The source was described in chapter 3. Energy arriving at the point receiver can be modelled by simple ray tracing. The two edges of the source (S1 and S2 in figure 8.1) act as diffraction source points, and as such, as individual sources. These edge diffraction events are clearly seen in the characterization images of chapter 3. It is found that the edge of the source labelled S1 in figure 8.1 plays a major role in the reflected events from the second boundary between the water-saturated sample and

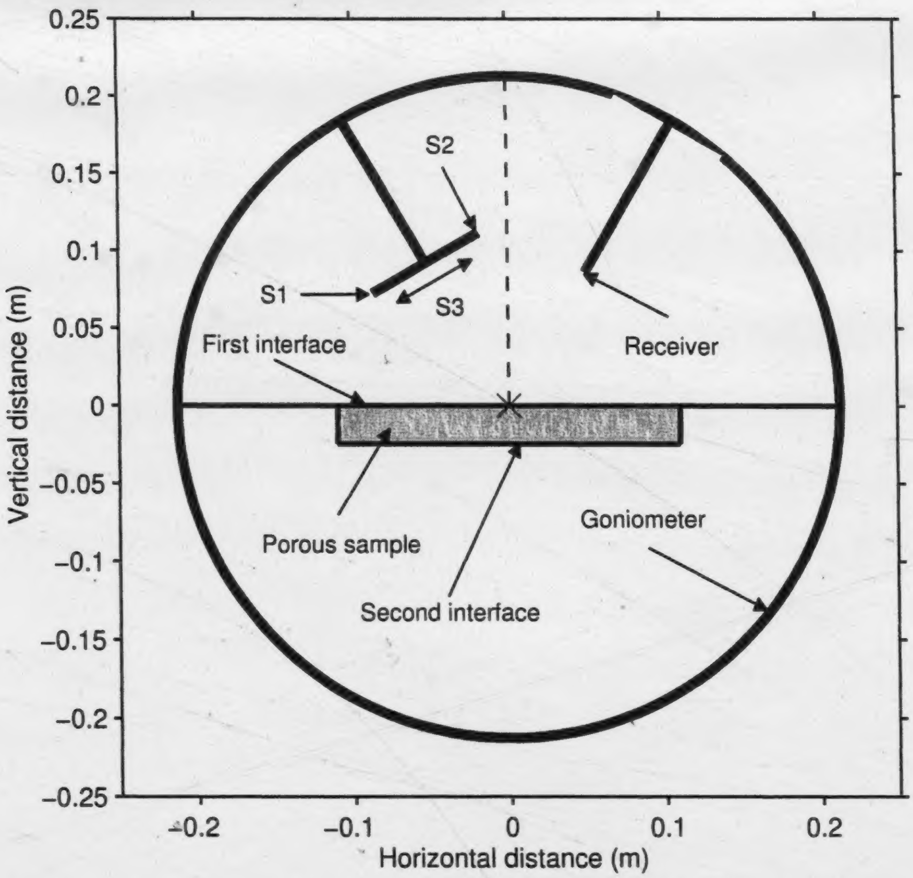

Figure 8.1: Setup diagram of the acoustic goniometer (to scale) for the reflectivity measurement. Using ray theory three possible sources can be considered. The edges of the source act as diffraction points denoted here as S1 and S2 and the flat portion of the source generates a flat acoustic bounded pulse. The porous sample is 2.46 cm thick.

the water medium. Because of geometry only one event emanating from the edge labelled S2 is seen. The central flat part of the source labelled S3 generates a nearly flat wave field and its propagation and reflection behaviour differs from the edges as the P-wave critical angle is approached.

This setup is used to acquire reflectivity at source-receiver angles varying from 12.5^o to 60^o. This range is limited by the physical aperture that the configuration

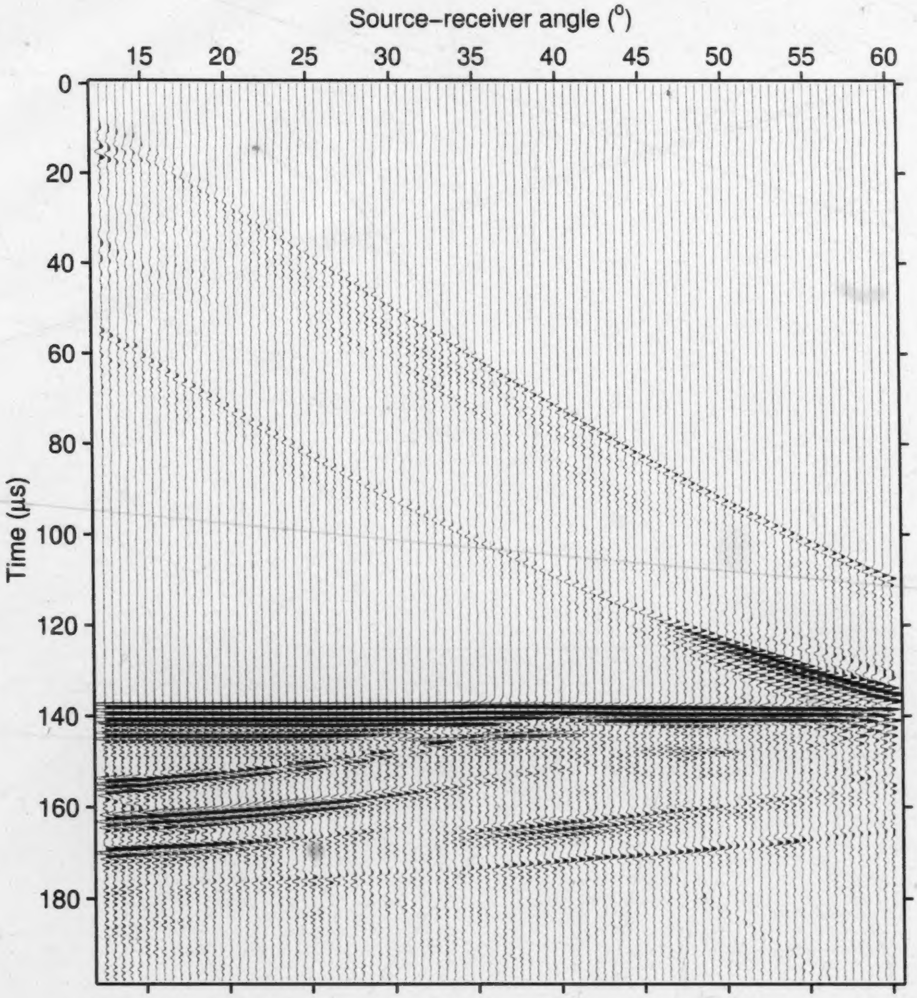

Figure 8.2: Uninterpreted observed data using the setup of figure 8.1.

allows. The uninterpreted observed data is shown in figure 8.2 as a variable area wiggle plot where a constant gain is applied and high amplitudes clipped in order to better visualize weak events. Interpreted data is shown in figures 8.3, 8.4, and 8.5. Several events are distinguishable in the display. For reference, the flat lying event beginning at 138 μs is the primary reflection of interest here. It is flat (i.e. at constant arrival time) as intended in the construction of the goniometer. A ray tracing code was written for this particular geometry in order to differentiate between these various observed events. In the previous chapter the three wave modes that can

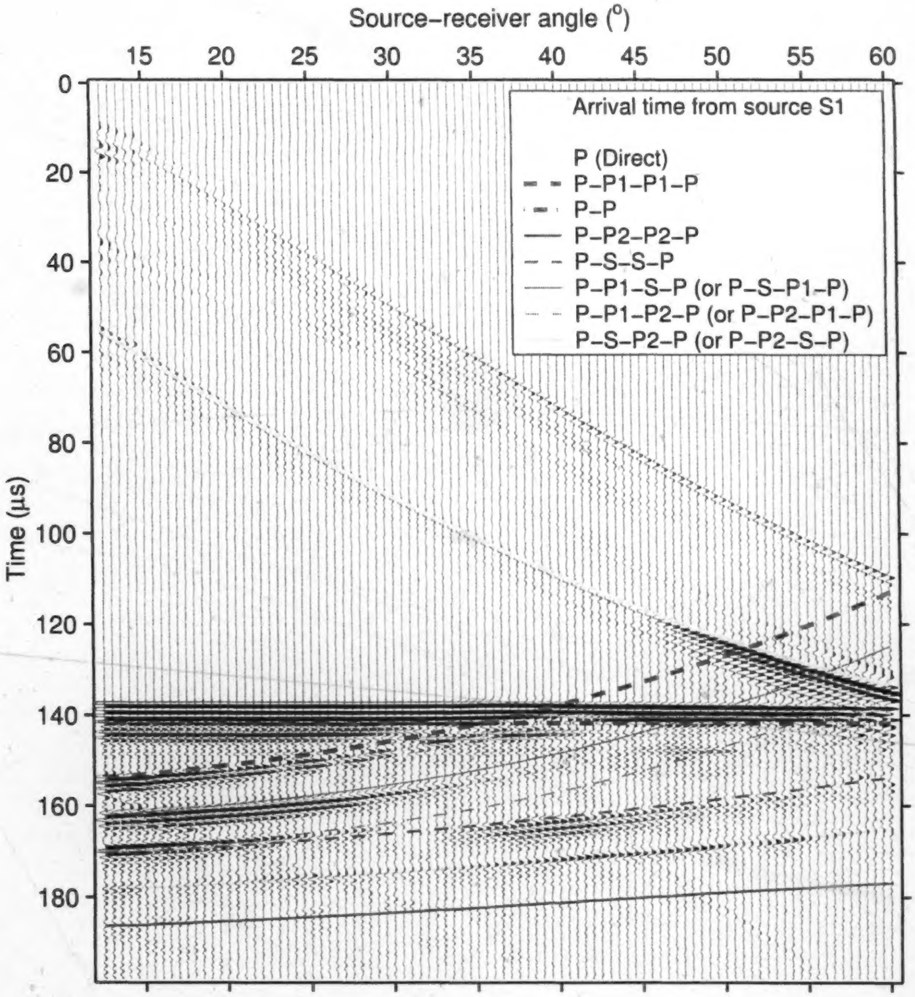

Figure 8.3: Observed data using the setup of figure 8.1. Overlayed curves are arrival time of various wave modes originated from the source edge only (S1 in figure 8.1). The trajectories are, P in water, P1 fast P in sample, P2 slow P-wave in sample, and S shear in sample. See text for details for each combination shown in the legend.

propagate in such a material were detected and the phase velocities measured in the transmission experiment. These velocities will be employed here in calculating arrival times to assist in identification of the various events present in the observations. Various combinations of wave arrivals that are converted at both interfaces of the water-saturated porous sample with the enveloping water medium will be considered.

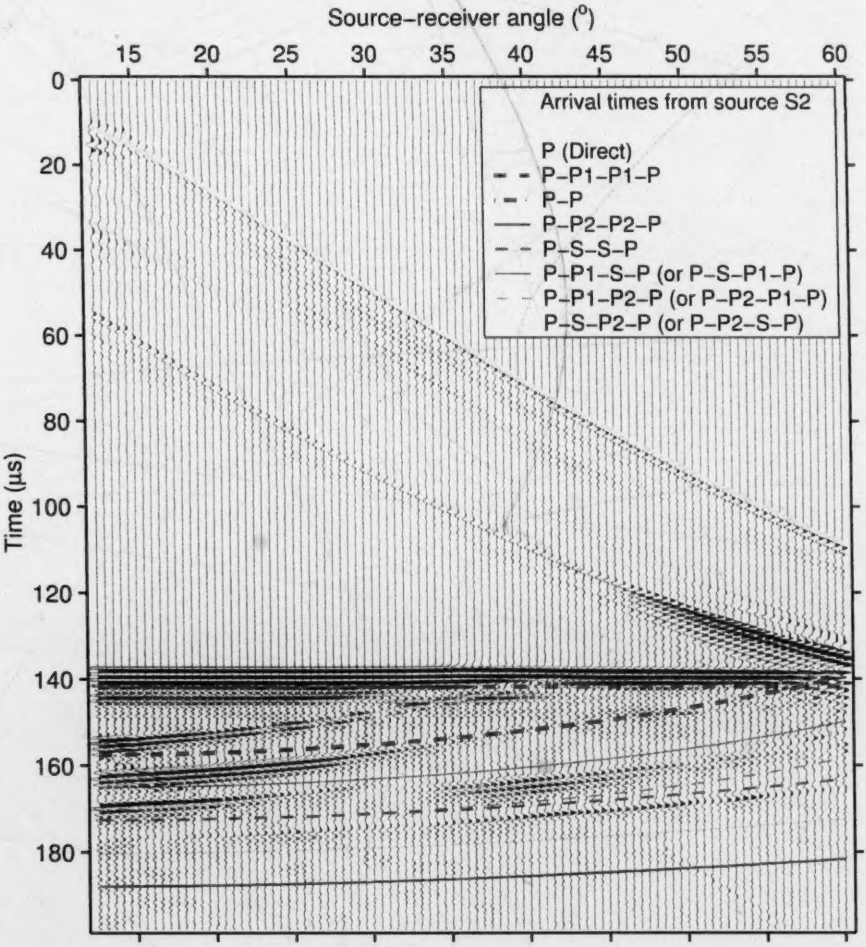

Figure 8.4: Observed data using the setup of figure 8.1. Overlayed curves are arrival time of various wave modes originated from the source edge (S2 in figure 8.1). The trajectories are, P in water, P1 fast P in sample, P2 slow P-wave in sample, and S shear in sample. The anticipated S2 arrivals are not seen due to the use of the highly directional source-receiver pair. See text for details for each combination shown in the legend.

Following the system used in global seismology to distinguish branches of ray paths, the portion of the path in the water medium of a wave either emanating from the source or reflected back to the receiver is denoted P. For example, the wave directly from the transmitter to the receiver is denoted "P" and that directly reflected

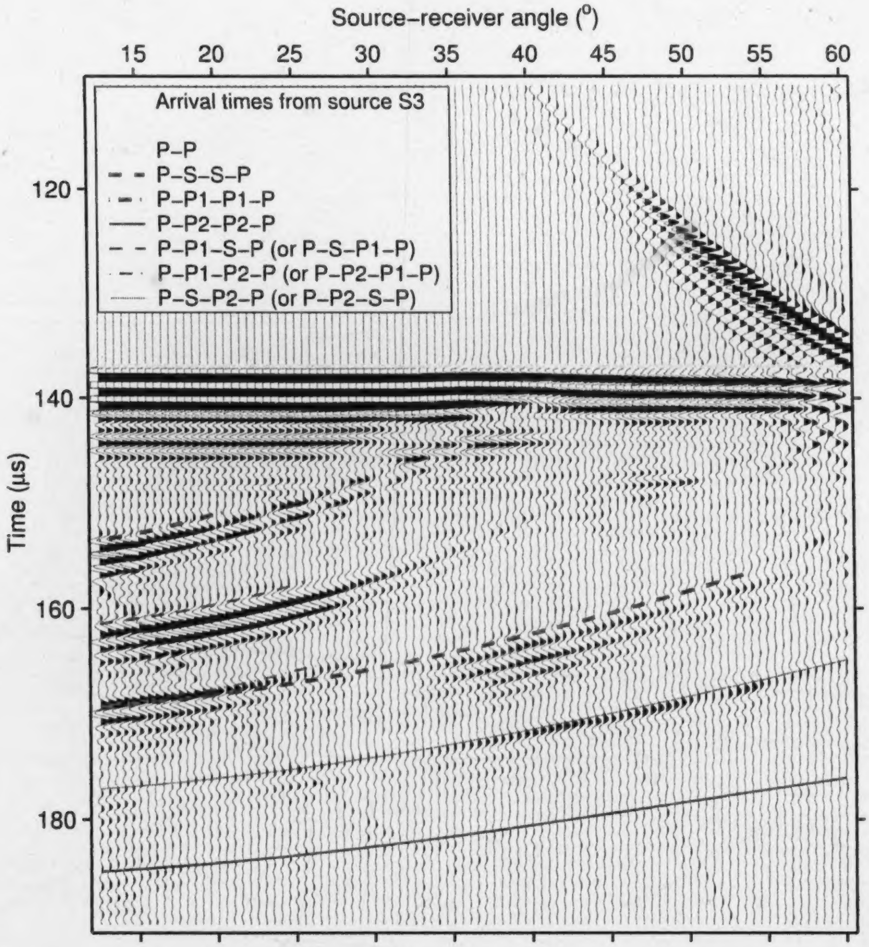

Figure 8.5: Observed data using the setup of figure 8.1. Overlayed curves are arrival time of various wave modes originated from the centre of the source (S3 in figure 8.1). The trajectories are, P in water, P1 fast P in sample, P2 slow P-wave in sample, and S shear in sample. See text for details for each combination shown in the legend.

as "P-P". The travel path within the sample is denoted first by the mode along the down-going path, and second for that along the up-going path with combinations P1-P1, P1-P2, P1-S, S-S, S-P2, and P2-P2 where P1 represents the fast P-wave, P2 the slow P-wave, and S the S-wave.

The results of the estimated arrival times from the edge of the source S1 to the receiver are overlayed on the observed data in figure 8.3. It is worthwhile reiterating that the fast P, the converted S, and the slow P wave speeds used in this analysis are 2730 m/s, 1485 m/s, and 1015 m/s respectively. The direct arrival (i.e. not reflected) is shown as P in the display. At large angles this wave interferes with the event of interest for the study of the variation of reflectivity with angle. The event denoted as P-P1-P1-P is the reflection of the fast P-wave at the second interface. This wave interferes with the primary reflection at approximately 40^o. Because of this interference the reflectivity is not expected to match the model beyond this angle perfectly. It is important to note that this interference problem would be even more severe for a narrower aperture transmitter.

The event denoted P-P is the reflection of the S1 diffracted wave from the first interface. This event is also flat in time and lags the primary reflection by 15 μs but is relatively very weak. Thankfully, this turns out not to be a problem in measuring the amplitudes of the main reflection at the first interface.

The events denoted as P-P1-S-P and P-S-P1-P are the converted P1 to S and S to P1 at the second interface. These events arrive simultaneously. Similarly the event denoted as P-P1-P2-P (or P-P2-P1-P) is a converted fast P1-wave to a slow P2-wave at the second interface. To the author's knowledge, this is the first documented observation of such mode conversions.

The event denoted by P-S-S-P is the converted shear mode and exhibits high energy at large angles as the theory suggested in chapter 4.

Another interesting event is that denoted as P-S-P2-P (or P-P2-S-P) which is a converted S-wave to a slow P-wave at the second interface. However this event interferes with the P-S-S-P event at low angles. The event P-P2-P2-P is the slow P-wave mode that is generated at the first interface but is highly attenuated as the distance travelled in the sample is large. However this event is very weak and does not show properly without substantially amplifying the data.

The results of the arrival times from the edge of the source S2 to the receiver are overlayed on the observed data in figure 8.4. Only the direct arrival shown as P in the display emanates from the edge of the source S2 and no other event matches the arrival times.

The bulk of the energy generated by the large source travels as a flat acoustic bounded pulse maintaining a stable amplitude at large distances as demonstrated in chapter 3. The events generated by rays originating from the central portion of the source labelled S3 in figure 8.1 are shown in figure 8.5. The main event of interest is the reflected wave P-P. The later events match and follow a pattern similar to that for S1 (Fig. 8.3). The range of angles at which these events appear decreases with increasing velocity. This display shows that the main energy of all events do indeed originate from the centre of the source.

The calculated travel time curves for all possible combinations of converted wave modes as given in figures 8.3, 8.4, and 8.5 completes the identification of all of the events. A summary is given in figure 8.6 where the time series are amplified. There are several events worth noting. There are two reflected P-waves (P-P) from the first interface originating from the edges of the source labelled S1 and S2. All other events are reflected from the second interface between the water-saturated porous sample and the water medium. We distinguish the reflected fast P-wave (P-P1-P1-P), the converted S from P1 at interface 2 (P-P1-S-P), the reflected converted S-wave, the converted S-wave to a slow P-wave at interface 2 (P-S-P2-P), a converted slow P-wave from the fast P-wave at interface 2 (P-P1-P2-P), and the reflected slow P-wave (highly attenuated, P-P2-P2-P). It is interesting to note that despite the high attenuation associated with the slow P-wave it is detected by the setup as three arrivals. The arrival P-P2-P2-P is similar to the transmitted P-P2-P already reported in the literature (Plona, 1980; Kedler and Smeulders, 1997) and analogous to that detected in the transmission experiment described in chapter 7. However this wave has not been reported as a reflected wave. Furthermore, two other modes of this wave are detected by the present experiment. First as a converted fast P-wave to a slow P-wave and as a converted S-wave to a slow P-wave. These two modes appear clearly in the observed data. In this highly porous material a large portion of the energy is converted to slow P-wave modes at both interfaces between the water medium and water-saturated porous material.

Now let us focus on the reflected event. The wave reflected from the first interface originates always from the centre of the source. This event is shown in figure 8.7 plot-

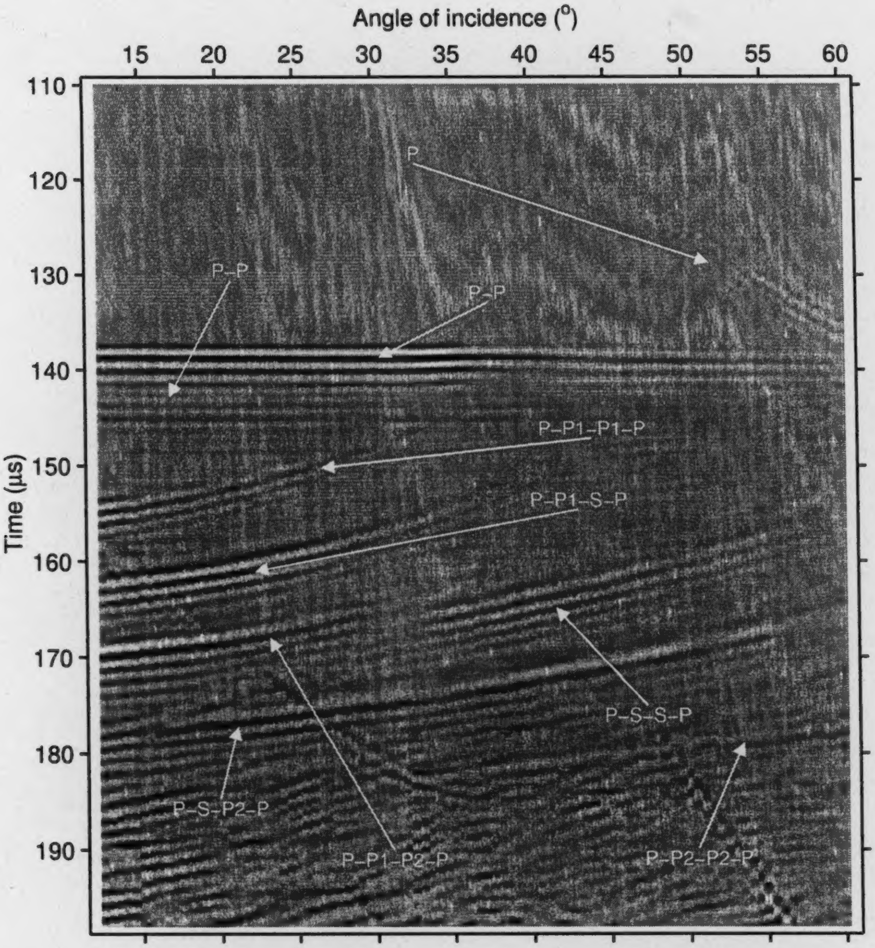

Figure 8.6: Identification of events detected by the reflectivity setup of figure 8.1. The type of waves are, P sound wave in water, P1 fast P-wave, P2 slow P-wave, and S S-wave. See text for various combination of ray paths.

ted in the true observed amplitudes. The data displays clearly the variation of amplitude with angle of incidence. However the data is contaminated at some angles by the P-P1-P1-P, the P-P1-S-P, and the direct wave modes as mentioned earlier (Fig. 8.3). The data is contaminated beyond approximately 40° angle of incidence. Therefore the observed reflectivity should not be expected to match the calculated models beyond this angle as the models do not incorporate the reflection from lower interface.

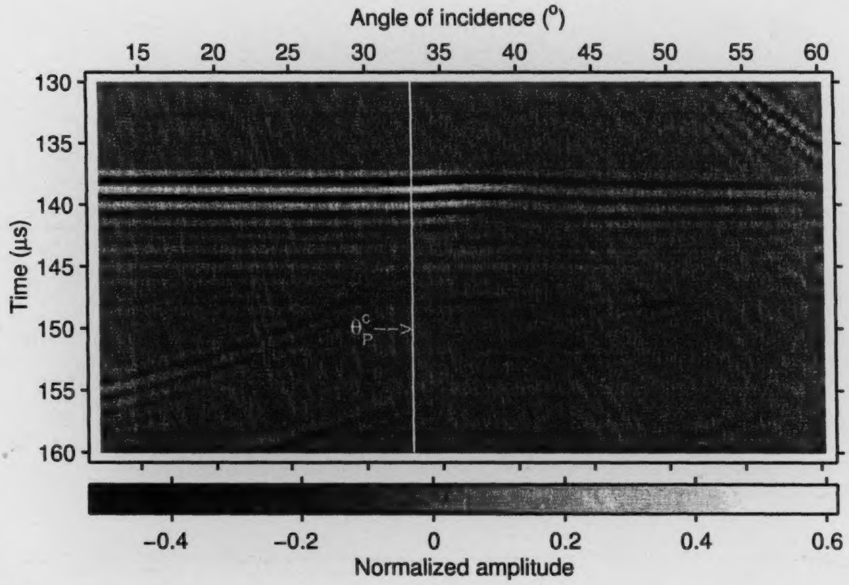

Figure 8.7: Displays of the recorded reflectivity from a water and a water-saturated porous plate normalized to the input signal.

The measured parameters given for the porous sample S082 (Tables: 7.1 and 7.2 chapter 7) are used to calculate both the reflectivity of a plane wave and of a bounded acoustic pulse in a manner similar to that in chapter 3 in elastic media. The results are shown in figure 8.8 where the maximum of the amplitude envelope calculated via Hilbert transform is used in the amplitude measurements. It is important to reiterate that the amplitudes in Figure 8.8 are normalized by the amplitude of the direct arrival recorded separately by setting the source and the receiver at a straight distance equal to the reflection path. Figure 8.9 displays the phase angles versus the angle of incidence of the observed and modelled reflectivity. The results agree well with each other.

The complete reflection-transmission experiment for the porous sample S082 studied here is given in figure 8.10 for plane waves where the wave fields are averaged over a small volume element of the saturated porous material. Using Zoeppritz's equations an elastic model is calculated for the water-saturated porous material characterized by the P and S wave velocities, 2730 m/s and 1485 m/s respectively, and is shown in figure 8.11. Evidently the two do not agree with each other for the energy

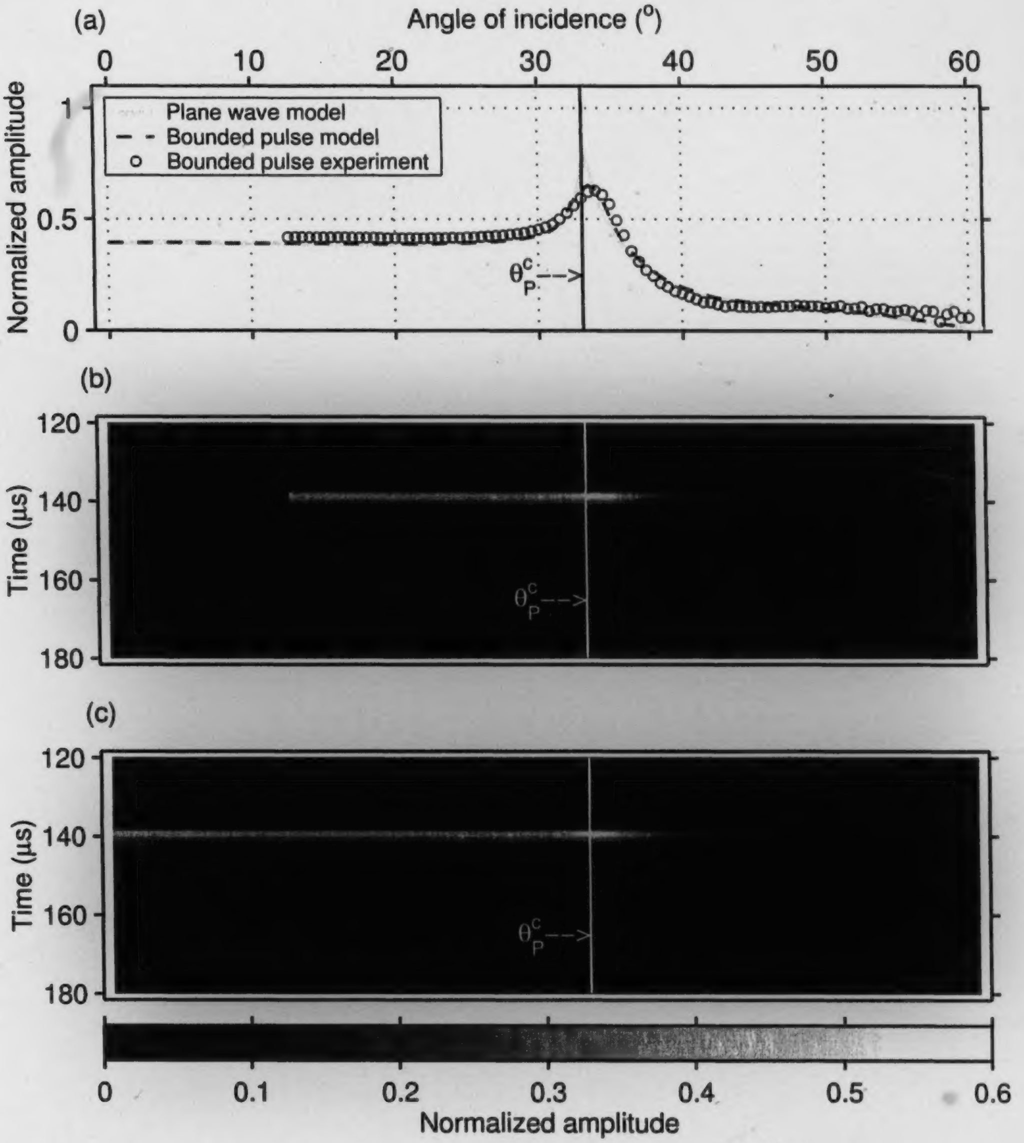

Figure 8.8: Reflectivity from water and a 2.46 cm thick porous synthetic sample saturated by water. a) The observed and modelled reflection coefficients. b) Observed amplitude envelope of the reflected wave. c) Modelled amplitude envelope of the reflected wave. The P-critical angle is calculated with Snell's law. There is no S-critical angle of incidence.

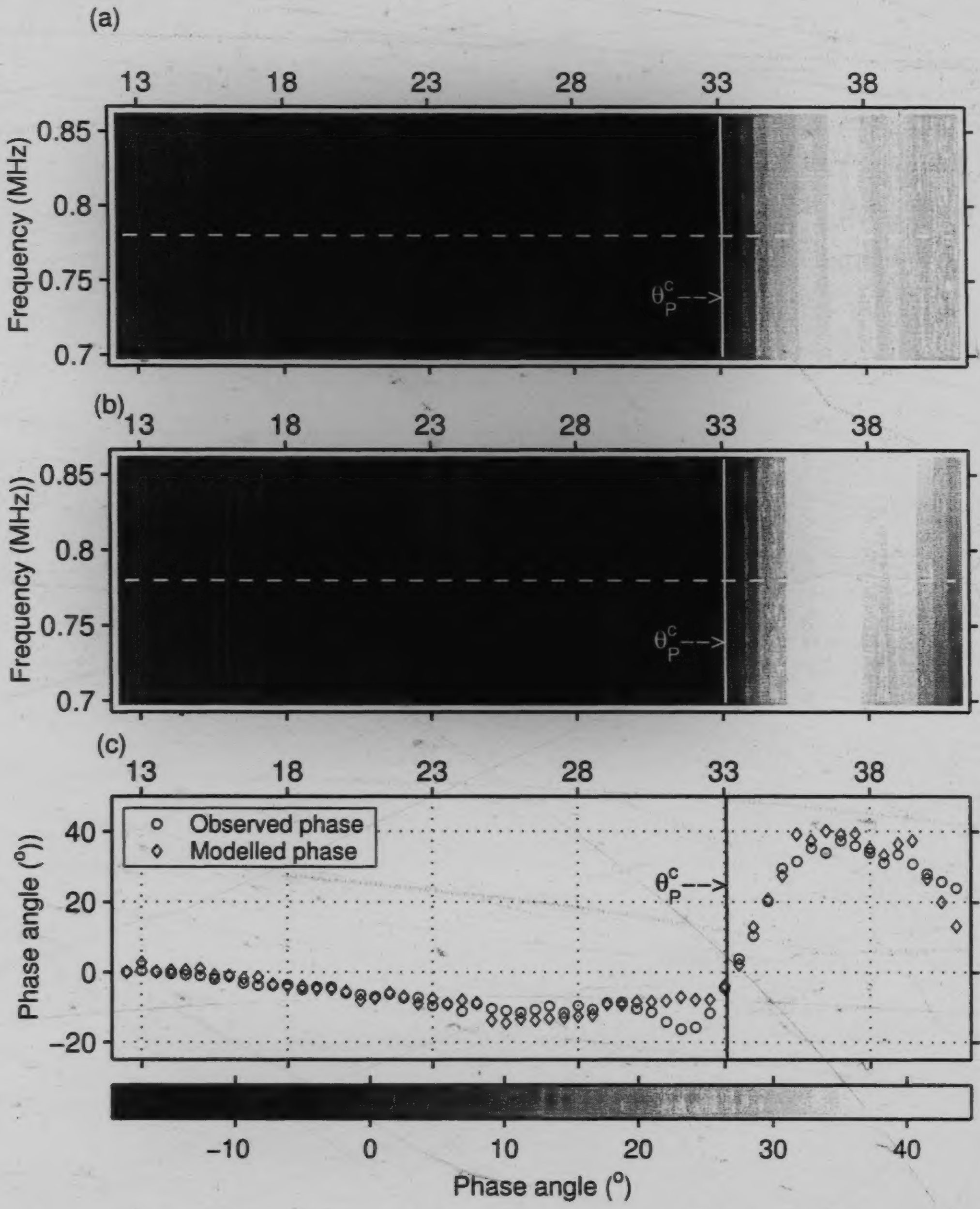

Figure 8.9: a) Phase angle of the observed reflectivity. b) Phase angle of the modelled reflectivity. c) The observed and modelled phase angle at 0.78 MHz. The dashed line shows the frequency of the phase angles displayed in panel c).

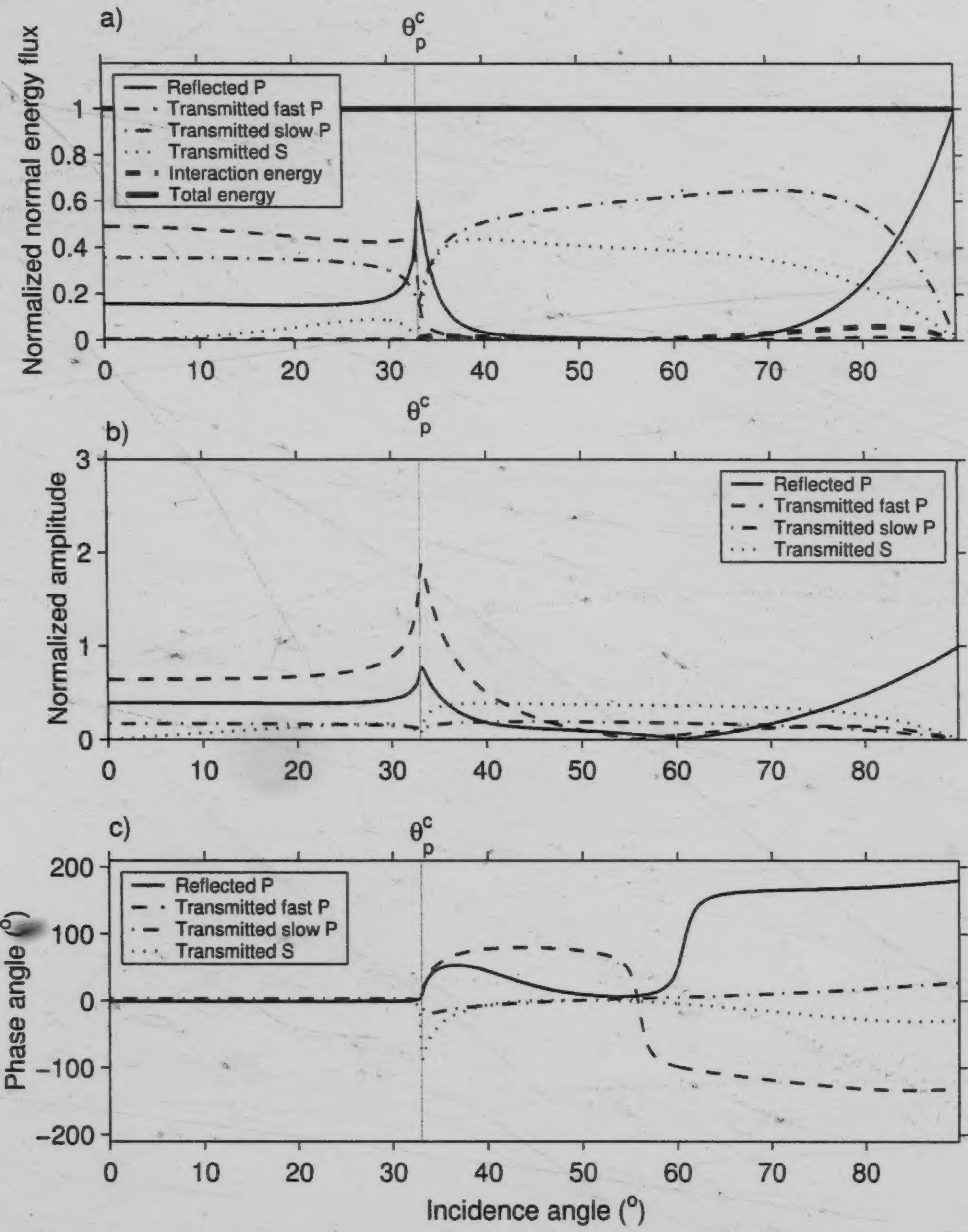

Figure 8.10: The reflectivity-transmission of the water-saturated porous material. The wave fields are averaged over a unit volume of the bulk material. a) Energy balance. b) Amplitudes. c) Phase angles.

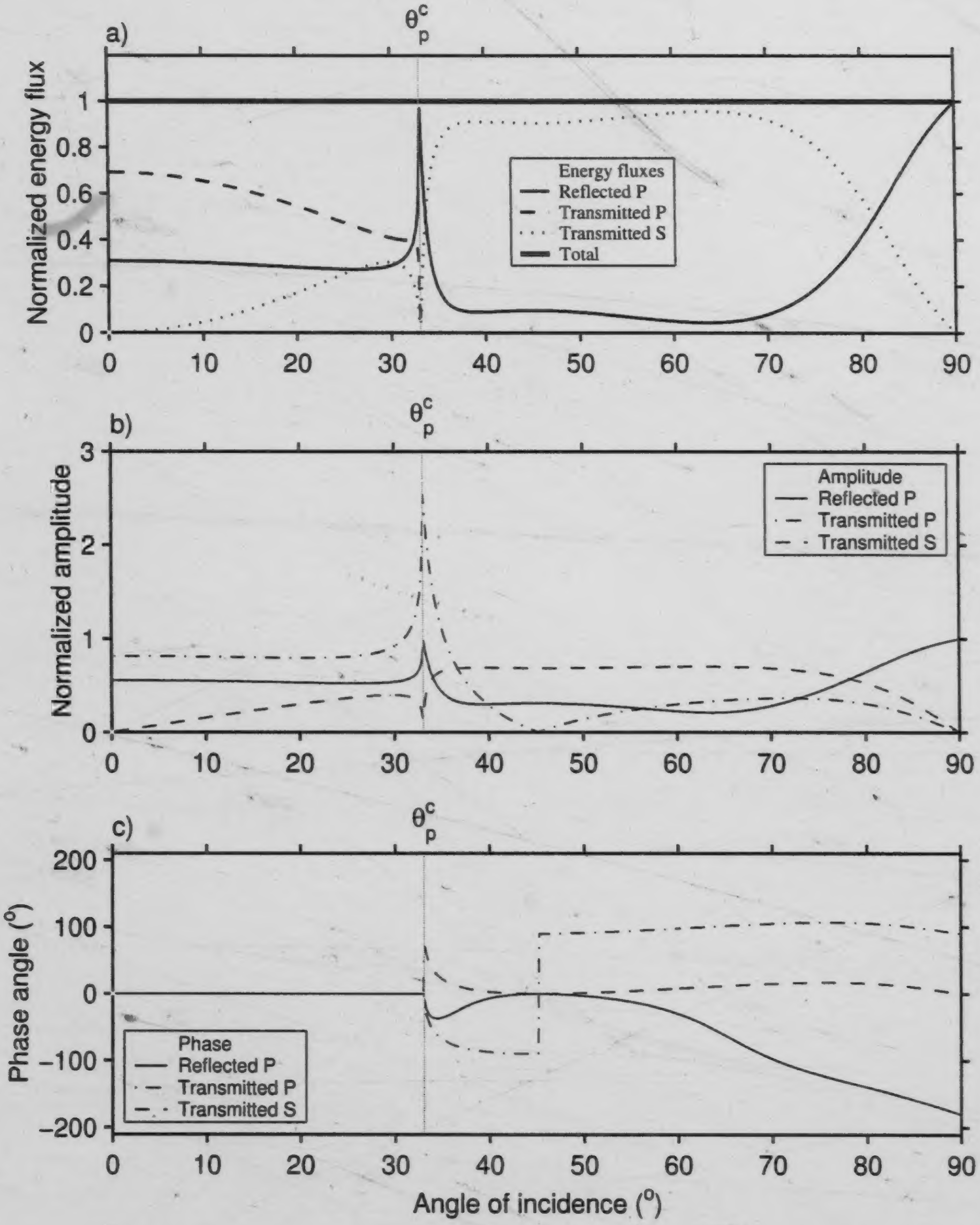

Figure 8.11: The reflectivity-transmission of an elastic medium replacing the water-saturated porous material. The P and S wave velocities are 2730 m/s and 1485 m/s respectively. a) Energy balance. b) Amplitudes. c) Phase angles.

balance of the boundary, the amplitudes, and the phase angles at the frequency of 0.78 MHz.

8.3 Discussion

In the light of the experimental results and the calculated models for the reflectivity from the porous sample S082 it appears that the reflectivity curve matches well the calculated one. This suggests that Biot and de la Cruz/Spanos theories appear both appropriately describe this type of highly porous and permeable material.

For this porous material it is found that

- The observed reflectivity matches well that predicted by modelling.
- The observed phase angle of the reflectivity matches well the modelled one.
- The measured phase velocities of the fast P, the slow P, and the converted S waves agree with calculations.
- The measured attenuations of the fast P, the slow P, and the converted S waves agree with calculations.
- First observation of a slow P-wave converted from a fast P-wave and from an S-wave.

8.4 Conclusions

Reflectivity experiments were conducted on a synthetic thin water-saturated porous plate. The results were compared to modelled reflectivity using measurements of all relevant parameters and a full wave propagation theory in porous media was employed. The results are very satisfactory for this sample. The experimental data obtained using the bounded acoustic pulse employed in this experiment matches closely the calculated bounded acoustic pulse model. The plane wave reflectivity is very close to the experiment except at the P-wave critical angle were the sharp change in reflectivity is smoothed in a manner similar to the observed reflectivity from water-elastic solid interfaces presented in chapter 2 and 3. It is found that large acoustic wave fields lead to closer results to plane wave solution.

It is also found that the Zoeppritz's equations (i.e. fully elastic) do not properly describe the observations in this frequency range. The experiments detected wave mode conversions from both the fast P and the S waves to a slow P-wave.

Chapter 9

Reflectivity from water and weakly consolidated water-saturated porous materials interfaces

9.1 Introduction

In this chapter results of the observed reflectivity curves from the boundary between water and water-saturated thick porous synthetic blocks will be presented. These samples exhibit a large permeability that varies between 4 D and 326 D. First a description of these samples will be given. These samples could not be characterized with the same level of confidence as the thin sample discussed in chapters 7 and 8 and as such are considered separately here. Further, there are some concerns that the sintering process in these thick samples is not homogeneous. The attenuation of the solid skeleton is further large and was difficult to estimate. Despite these deficiencies, the results are of interest and provide additional support to the observations of chapter 8.

The samples were designed to be 7 cm thick to avoid reflected arrivals from the second boundary between the material and the water. However the degree of sintering of the glass beads was not sufficient and consequently the attenuation of the solid skeletons does not allow enough energy to be transmitted for velocity and attenuation measurements. Smaller samples were cored from the original large samples in order to perform velocity and attenuation measurements but the results were not satisfactory. Consequently these samples will be treated with a different procedure than that used to study the thin porous plate presented in the previous chapters. The modelling procedure relies more on numerical calculations rather than measurements of all parameters. While the results of these measurements cannot be as definitive as those for the better characterized sample discussed in the previous chapters, the results are consistent with and supportive of the findings of chapter 8.

9.2 Porous synthetic samples

9.2.1 Sample construction

Synthetic porous sandstones were constructed by sintering glass beads with sizes ranging from 30 – 40 mesh to 170 – 325 mesh. The beads were commercial glass beads used commonly for sand blasting purposes. The beads are not sorted exactly and the sizes given by the manufacturer do not always match the actual mesh size as revealed by S.E.M photographs (Figs. 9.1 and 9.2). A graphite mold was used to construct the six porous samples used in this study by sintering glass beads in a programmable electric oven. The temperature increase with time curve was the same for all samples. The temperature was slowly raised from room temperature to 700°C. The duration of the process was approximately four hours. The oven then automatically shut down and was kept closed for about 20 hours in order to minimize residual stress that would build up if the cooling process is not slow enough. Uniform synthetic porous samples were obtained. The glass beads were not highly sintered and consequently the samples are very fragile. The benefit of this is that the samples are also highly compressible relative to the saturating water and this increases the slow P-wave effects.

All samples were 22 cm×22 cm and 7 cm thick except for one sample that is 2.46 cm thick that was studied in detail in chapters 7 and 8. The resulting porous synthetic sandstones were uniform with flat surfaces. The characteristics of the samples are given in table 9.1. The S.E.M photographs in figures 9.1 and 9.2 display the enlarged surface of each sample. These samples exhibit a wide range of bead sizes which do not always agree with the mesh sizes given in table 9.1 particularly sample S040 that shows beads as small as 20μm diameter.

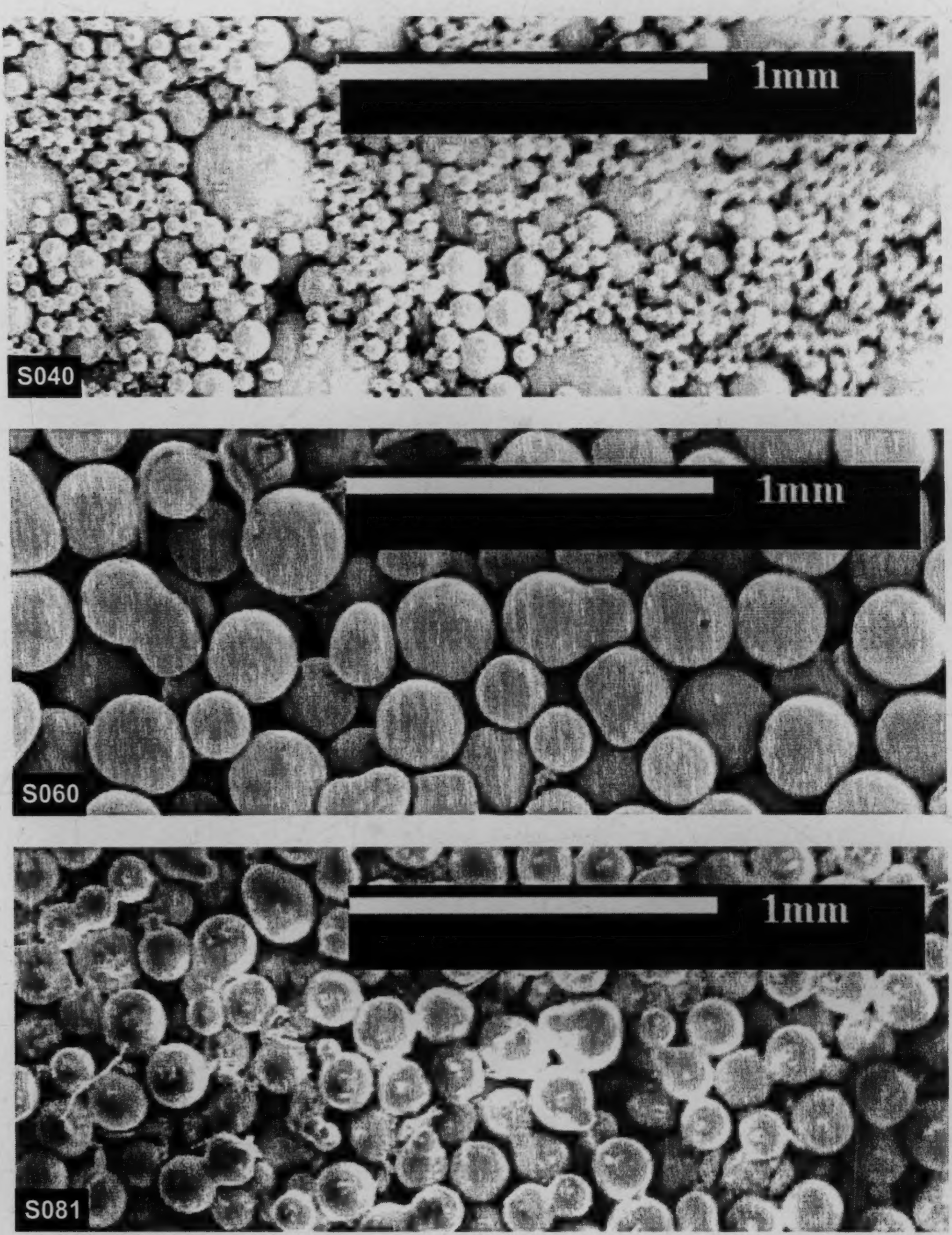

Figure 9.1: S.E.M photographs of the surface of the porous synthetic sandstones used in this study (Samples S040, S060, and S081).

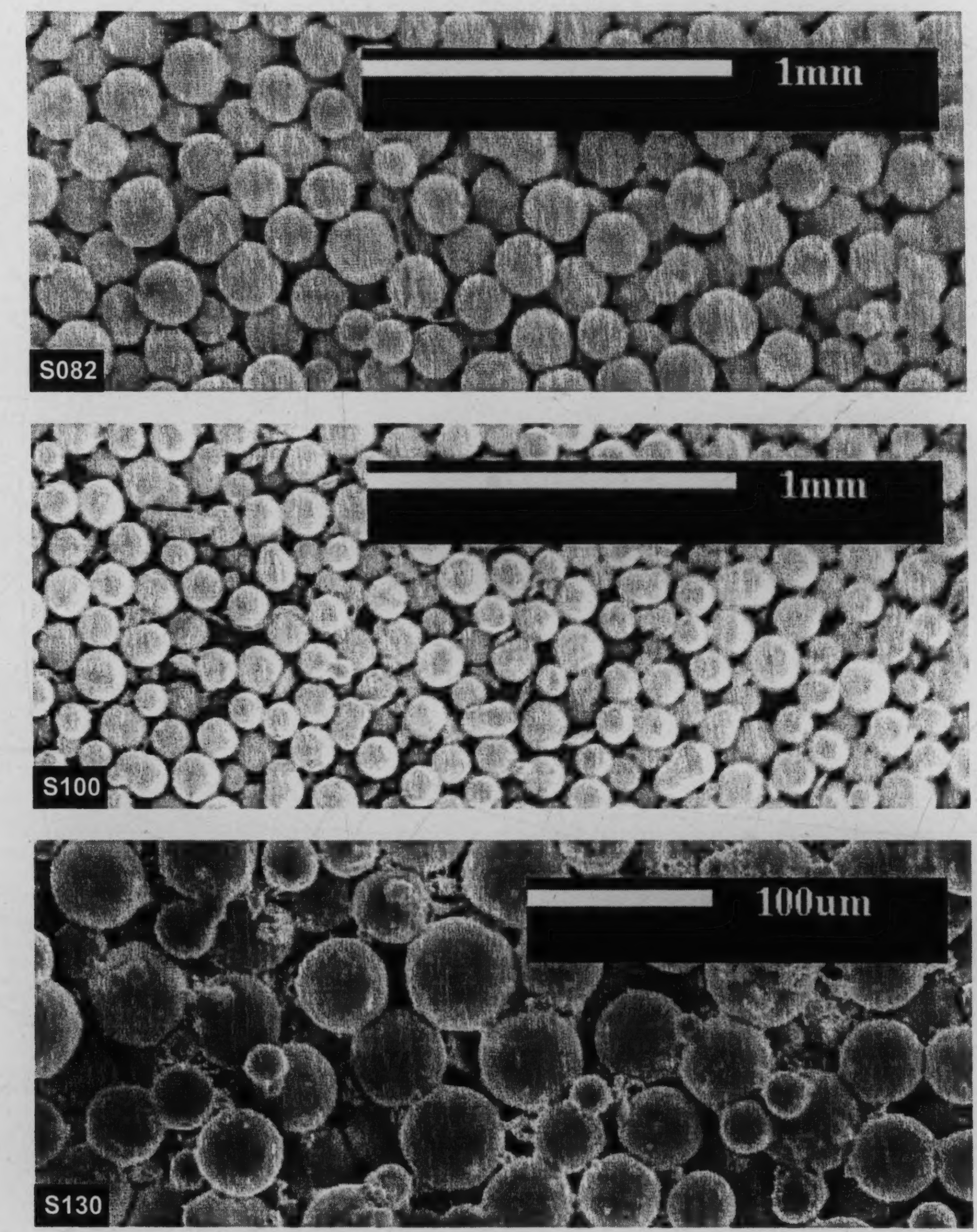

Figure 9.2: S.E.M photographs of the surface of the porous synthetic sandstones used in this study (Samples S082, S100, and S130).

Sample	Mesh	d_g	$\rho^{(s)}$	Length	Width	Thickness
	–	μm	$kg.m^{-3}$	cm	cm	cm
S040	30 – 40	425 – 600	2455 ± 35	22.4	22.4	7.03
S060	50 – 70	212 – 300	2455 ± 35	22.4	22.4	7.03
S081	70 – 100	150 – 212	2455 ± 35	22.4	22.4	7.03
S082	70 – 100	150 – 212	2455 ± 35	22.4	22.4	2.46
S100	100 – 170	90 – 150	2455 ± 35	22.4	22.4	7.03
S130	170 – 325	45 – 90	2455 ± 35	22.4	22.4	7.03

Table 9.1: Porous samples characteristics. Mesh size, grain diameter d_g, mineral grain density $\rho^{(s)}$, and dimensions of the sample.

9.2.2 Porosity measurements

The porosities were measured using water-saturated and "dry" weight measurements of the samples. The results are given in table 9.2. The porosity varies between 34% and 40%. Therefore the samples are very porous.

Sample	S040	S060	S081	S082	S100	S130
Porosity β	0.336	0.346	0.385	0.391	0.397	0.379
Error %	±2	±2	±2	±2	±2	±2

Table 9.2: Measured porosities of the porous synthetic samples used in this study.

9.2.3 Tortuosity measurements

The details of the electrical conductivity tortuosity measurements were given in chapter 6. An example of conductivity measurements is given in table 9.3 and in 9.4 for the porous sample S060.The tortuosity results for the samples given in table

V_{1s} (mV)	11.2	22.2	34.8	44.8	65.8	91.6	117.4	131.6	153.6
V_{2s} (mV)	14.2	27.8	43.6	56.0	82.2	124.4	146.2	164.4	192.2

Table 9.3: Measured electrical potentials for the saline solution.

V_{1p} (mV)	10.2	20.4	30.2	45.6	61.8	76.8	103.8	112.6	130.2
V_{2p} (mV)	55.0	108.6	161.4	242.2	330.0	407.0	532.2	596.2	688.6

Table 9.4: Measured electrical potentials for the porous sample S060 saturated with the same saline solution as that in table 9.3.

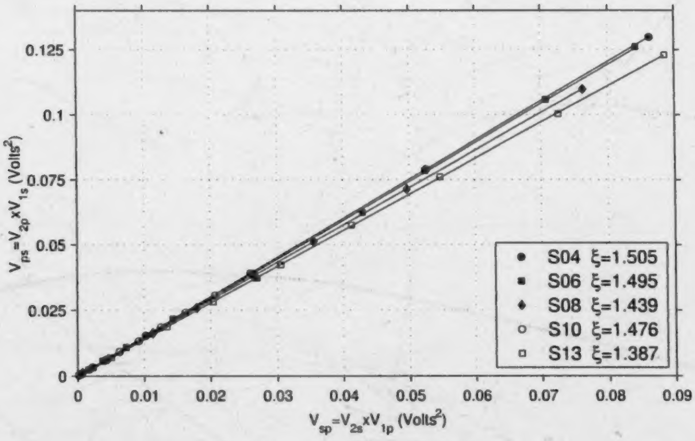

Figure 9.3: Tortuosity results for the porous samples described in table 9.1.

Sample	mesh	d_g	β	ς
	μm	–	–	–
S040	30 – 40	425 – 600	0.336	1.505
S060	50 – 70	212 – 300	0.346	1.495
S081	70 – 100	150 – 212	0.385	1.439
S082	70 – 100	150 – 212	0.391	1.439
S100	100 – 170	90 – 150	0.397	1.476
S130	170 – 325	45 – 90	0.379	1.387

Table 9.5: Porous samples characteristics, grain diameter d_g, porosity β, and measured tortuosity ς.

9.1 are shown in figure 9.3. These samples show very little variation in tortuosity (standard deviation: 0.026, mean: 1.468) as well as in porosity (standard deviation: 0.0254, mean: 0.3722). The results are summarized in table 9.5.

9.2.4 Permeability measurements

The details of the permeability measurement procedure were given in chapter 6. The permeability measurement results of the six synthetic porous samples are given in table 9.6. In the present study the permeability test is run with 6 cylindrical porous samples cored from the original samples. The results are shown in figure 9.4 and figure 9.5.

Sample	mesh –	d_g μm	β –	ρ kg/m^3	K D	K m$^2 \times 10^{-12}$
S040	30 – 40	425 – 600	0.336	2455	326	316
S060	50 – 70	212 – 300	0.346	2455	64	62
S081	70 – 100	150 – 212	0.385	2455	30	29
S082	70 – 100	150 – 212	0.391	2455	21	20
S100	100 – 170	90 – 150	0.397	2455	22	22
S130	170 – 325	45 – 90	0.379	2455	4	4

Table 9.6: Properties of the synthetic porous samples used in this study, grain diameter d_g, grain density ρ, porosity β, and measured permeability K in D and m^2.

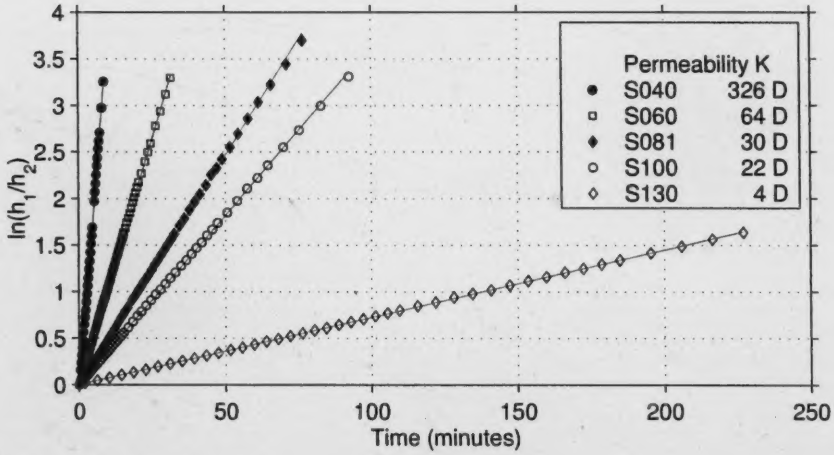

Figure 9.4: Measured permeability for the porous samples described in table 9.1.

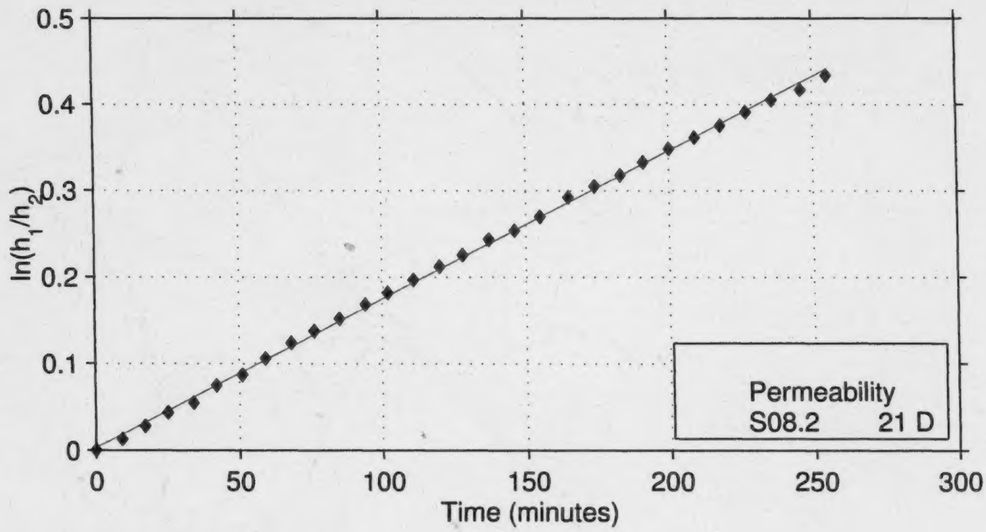

Figure 9.5: Measured permeability for the porous sample S082.

For the sake of comparison the permeability can also be expressed (Walsh and Brace, 1984) as follows

$$K = \left(\frac{1}{m}\right) \beta^3 \left(\frac{V}{A_s}\right)^2 \left(\frac{1}{\varsigma^2}\right) \tag{9.1}$$

where m is equal to 2 for circular tubes and equal to 3 for cracks. ς is the tortuosity and was described earlier. For the model above we have the porosity $\beta = 1 - \frac{\pi}{3\sqrt{(2)}}$ and the tortuosity $\varsigma = \frac{\pi}{3}$. The minimum diameter of the pores is $\frac{2\sqrt{3}-3}{6}$ of the diameter of the beads. The permeability is $K = \frac{81}{32\pi^4}\beta^3 d_g^2$ where d_g is the diameter of the grains. The results using equation 9.1 are close to those measured directly in the above experiment. Furthermore, these measurements agree with published results on similar glass bead sands (porosity: 0.40) (Gray, 1963).

9.2.5 Phase velocity and attenuation measurements of the solid skeleton

Attempts to measure the P and S phase velocity and attenuation on the air-saturated thick samples were not satisfactory. Unfortunately not enough wave energy was transmitted through due to large attenuations. It is possible that the samples are not uniformly sintered along the thickness length. The wave forms are greatly

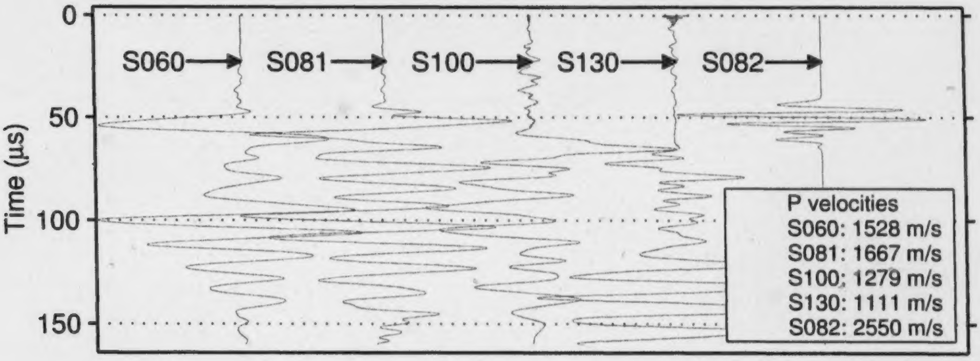

Figure 9.6: Transmission wave forms and estimated first arrival P-wave velocities of the "Dry" solid skeletons of the porous samples described in table 9.1. For display purposes the wave form of the thin sample S082 discussed in chapters 7 and 8 is stretched 4 times, therefore the reading of the vertical time for this wave form must be divided by 4.

distorted (Fig. 9.6) and the velocities are low confirming the low degree of sintering of the glass beads the samples were constructed with. The reflectivity measurements on these samples will rather be influenced by the near surface portion of the material than the deep part. The near surface of the solid skeleton exhibits higher stiffness than in the centre. Consequently the velocity at the near surface would be higher. Near surface core samples were taken from the original large ones to perform velocity and attenuation measurements. As the S.E.M. photographs revealed the pore and grain sizes vary quite significantly from one sample to the other. The grain sizes decrease in the order the samples were listed in table 9.1. The sample S040 displays a wide range of grain size diameters. Attempts to measure both phase velocities and attenuations on these samples were unsuccessful. The cored samples were too short and the surface could not be made perfectly parallel to allow precise measurements, furthermore a coupling agent had to be used to allow enough energy to be transmitted. This had influenced the measurements and particularly the attenuations. The P and S velocities were measured using two wave forms acquired on two samples with a small difference in thickness and the results are given in table 9.7 with uncertainties calculated assuming 0.25 mm uncertainty on the thickness measurements. These velocities will be used in the next section as a starting set in the numerical calculations.

Sample	V_p m/s	V_s m/s
S040	1980 ± 95	1050 ± 50
S060	2310 ± 190	1330 ± 110
S081	2290 ± 190	1765 ± 100
S100	1890 ± 260	1160 ± 160
S130	2140 ± 190	1600 ± 140

Table 9.7: Estimated P and S wave velocities on thin samples cored from the large original ones. The uncertainties were calculated using an error estimate of 0.25 mm in the measurements of the thickness of the samples.

9.3 Reflectivity observations and modelling

In this section the observed reflectivity curves from the thick water-saturated porous samples described in the previous section will be given along with the first attempt to calculate the corresponding models using the estimated parameters. The bounded acoustic pulse used in previous experiments is used to acquire reflectivity from the five thick synthetic water-saturated samples described in the previous section. The frequency of the source signal is in the range of 0.2 MHz to 1.2 MHz with the main peak at the frequency 0.78 MHz. The velocity in the water medium as measured during each experiment is 1490 m/s except during the experiment of the S130 sample where the measured velocity was 1475 m/s, probably due to changes in temperature and purity of the water. Therefore the wavelength in the water at the peak frequency of 0.78 MHz is 1.9 mm.

9.3.1 Numerical approach

Using the estimated velocities measured in the previous section a numerical approach is used to find the best set of parameters μ_M, A, Q, R, and Δ that leads to a good fit of the observed and the calculated reflectivities using the measured porosity. It was possible to find a set of parameters that produce a close model to the observed reflectivity curve for all samples except for sample S040, the most permeable one.

For this sample it was not possible to find a set of parameters μ_M, A, Q, R, and

Δ without adjusting the porosity from a measured value of 0.336 to a value of 0.435. It is interesting to point out that this sample is also the least uniform in terms of the consistency of bead sizes as indicated in the S.E.M. photographs of figures 9.1 and 9.2. It is unlikely that an error of 23% would have been made on the porosity measurement as it was performed twice with the same result found.

This suggests that the sample S040 was not completely under vacuum and may only have been partially saturated. An alternative probable scenario for this sample is a scattering problem since the size of the beads cover a large range of diamaters nearly from $\ll 10$ μm to $\gg 500$ μm. This sample exhibits small pores as well as large pores of various shapes (Fig. 9.1). This might indicate that this sample grossly violates the assumptions of the Biot and de la Cruz/Spanos theories considered here.

The parameters μ_M, A, Q, R, and Δ found by numerical calculations are listed in table 9.8 The velocities and attenuations deduced from the parameters of table 9.8 are given in table 9.9. Some of the velocities agree within the limits of the uncertainties with those measured via transmission tests whereas others (S081 and S130) do not. However, due to the small thickness and the precision on the flatness of the surfaces of the samples the measurements are not very reliable. A small variation in the thickness of 0.01 mm will change the velocity by 50 m/s. The unjacketed bulk modulus must be complex if estimated from the parameters A, Q, and R derived from the static experiments. This suggests that the "dry" bulk modulus K_M cannot be estimated from the velocity measurements and attenuations when the solid skeleton exhibits large attenuations that could be frequency dependent.

Sample	μ_M GPa	A GPa	Q GPa	R GPa	Δ μm
S040	$1.568 + i0.025$	$4.946 + i0.203$	$0.869 - i0.008$	$0.838 + i0.001$	50
S060	$3.752 + i0.177$	$3.584 + i0.182$	$1.086 - i0.006$	$0.636 + i0.001$	0.26
S081	$5.256 + i0.110$	$3.266 + i0.431$	$0.845 - i0.022$	$0.796 + i0.002$	0.15
S100	$4.717 + i0.168$	$2.881 + i0.149$	$0.897 - i0.010$	$0.790 + i0.001$	0.19
S130	$6.385 + i0.633$	$4.138 + i0.476$	$0.849 - i0.027$	$0.695 + i0.001$	0.16

Table 9.8: μ_M, A, Q, R, and Δ resulting from the numerical calculations to find the best set that leaded to a best match of the observed and calculated reflectivities.

Sample	V_p m/s	V_s m/s	α_{0P} s.m^{-1}	α_{0S} s.m^{-1}
S040	1990	930	59	53
S060	2180	1390	87	106
S081	2610	1665	65	40
S100	2455	1585	58	71
S130	2905	1840	123	169

Table 9.9: Calculated P and S wave velocities and attenuations using the parameters of table 9.8. A linear model is assumed for the attenuations.

9.3.2 Observed and modelled results

The results of the observed reflectivities, the plane wave models, and the bounded acoustic pulse models are shown in figures 9.7 through 9.11. The models were calculated using the numerical approach above and the estimated parameters given in table 9.8. The modelled results are close to the observed curves. However, not all the features that appeared in the observations were adequately matched, particularly beyond the P-wave critical angle of incidence where the phase angle changes with angle of incidence. It is important here to point out that the plane wave calculated reflectivity is also close to the bounded acoustic pulse models even at the P-wave critical angle of incidence. This is mainly due to the high P and S attenuations the solid skeletons of these samples exhibit. Indeed some tests were performed during the numerical approach described above and found that when the attenuations were not taken into account a sharp change in the plane wave reflectivity occurs at the P-critical angle of incidence.

9.4 Conclusions

The reflectivity responses from boundaries of water and water-saturated thick porous samples that exhibit high P and S attenuations of the solid skeleton and high range of permeabilities were acquired in laboratory experiments. Most of the parameters needed for modelling calculations were measured. However the velocities on the "dry" solid skeletons were not very accurate and the attenuations could not

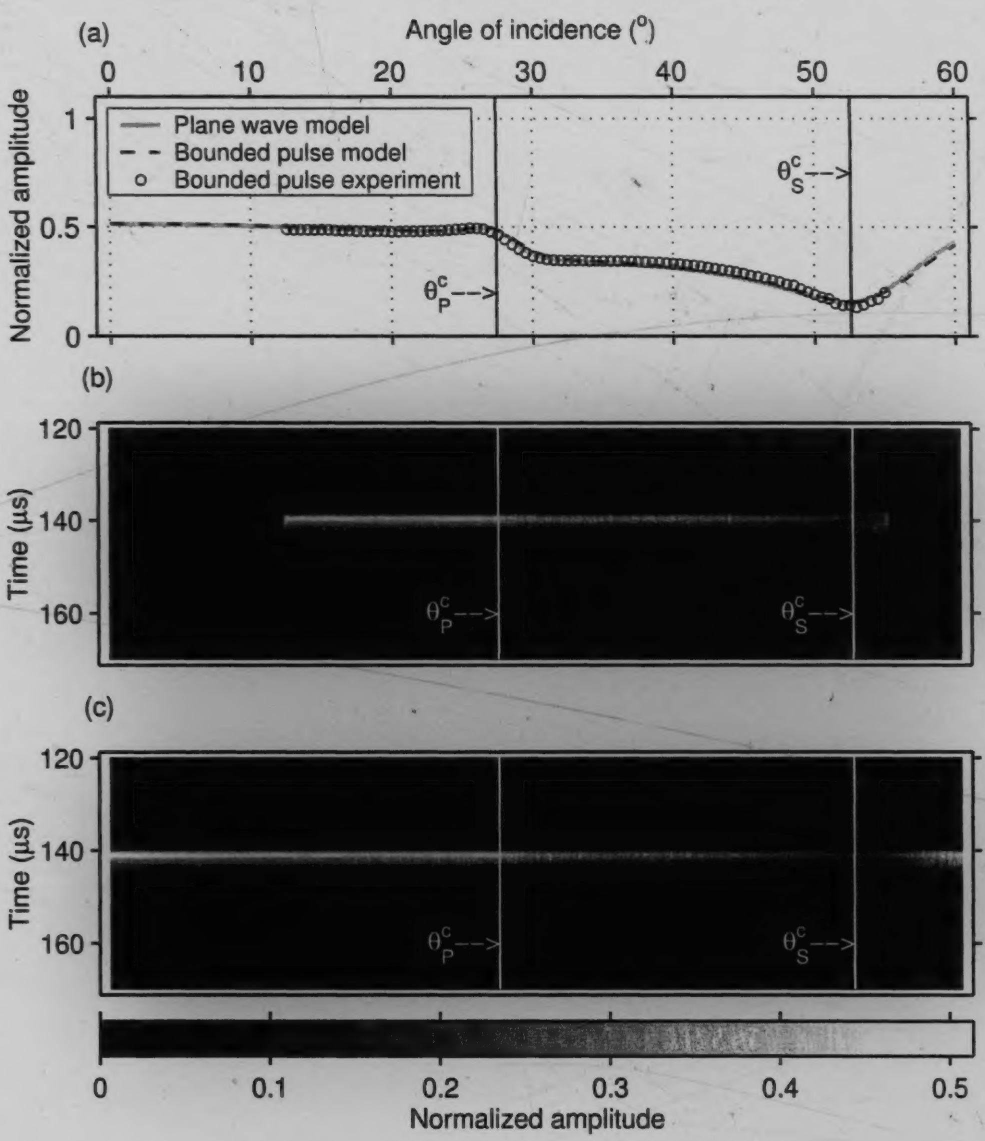

Figure 9.7: Observed and modelled reflectivity from a boundary between water and a water-saturated 7 cm thick synthetic porous plate. a) Measured, modelled, and plane wave reflectivity response. b) Observed maximum amplitude envelope. c) Modelled maximum amplitude envelope. Material labelled S130 with a permeability K=4 D.

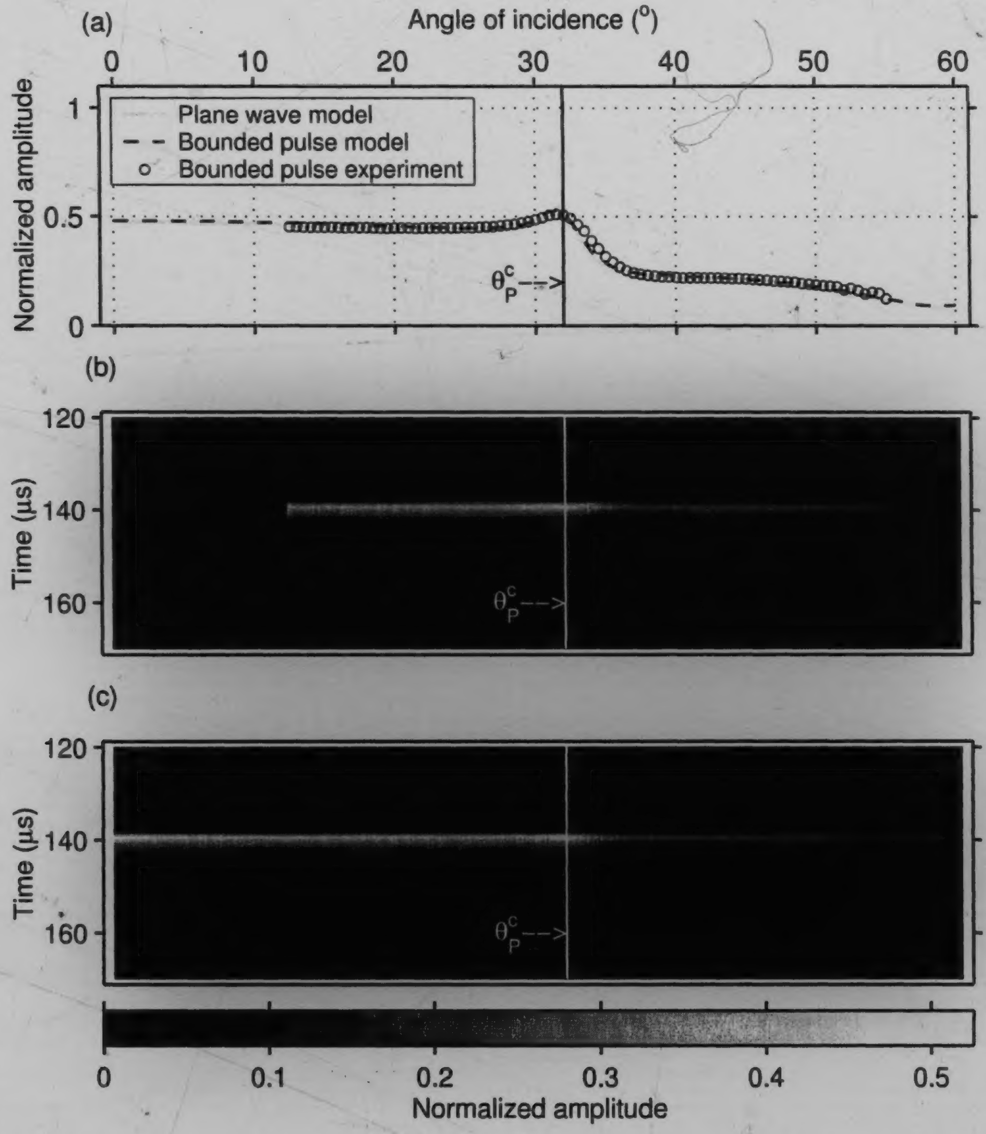

Figure 9.8: Observed and modelled reflectivity from a boundary between water and a water-saturated 7 cm thick synthetic porous plate. a) Measured, modelled, and plane wave reflectivity response. b) Observed maximum amplitude envelope. c) Modelled maximum amplitude envelope. Material labelled S100 with a permeability K=22 D.

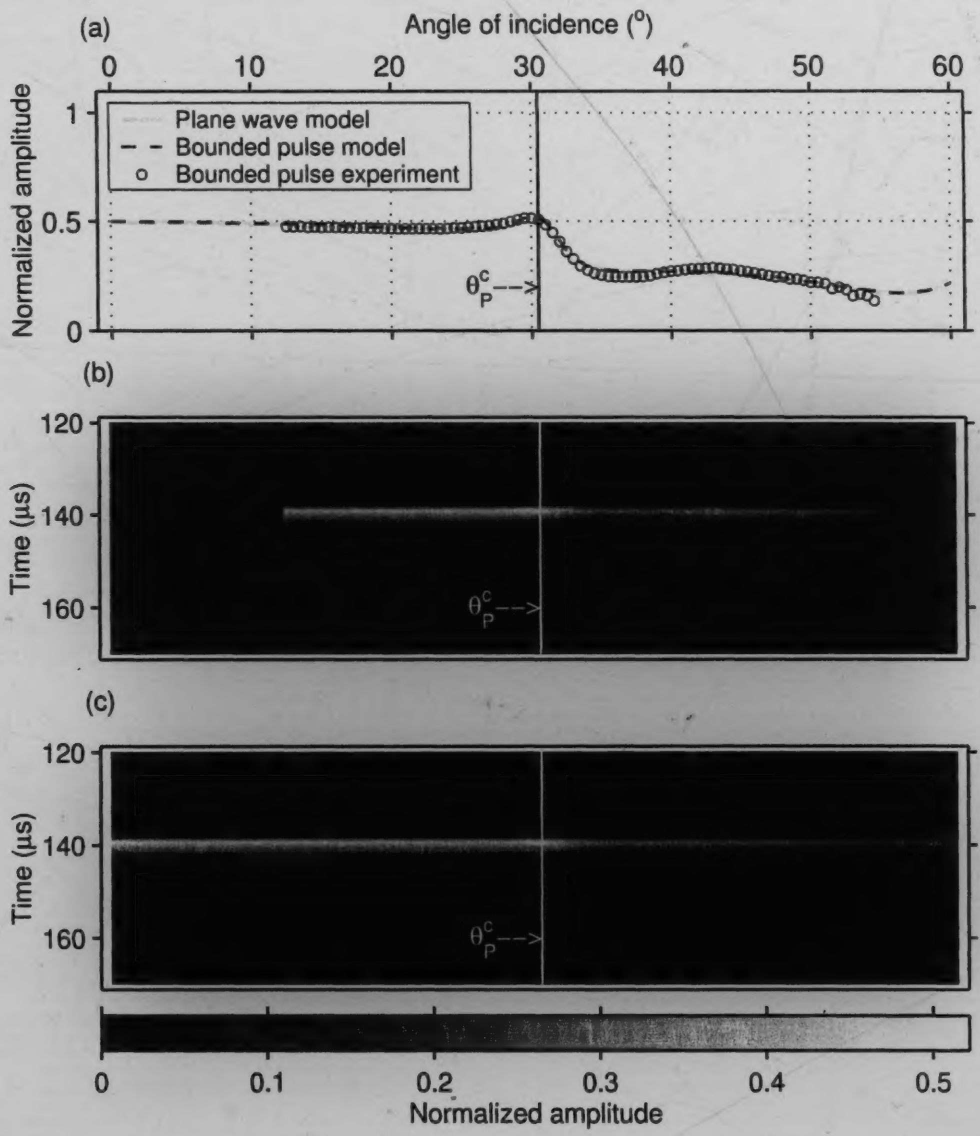

Figure 9.9: Observed and modelled reflectivity from a boundary between water and a water-saturated 7 cm thick synthetic porous plate. a) Measured, modelled, and plane wave reflectivity response. b) Observed maximum amplitude envelope. c) Modelled maximum amplitude envelope. Material labelled S081 with a permeability K=30 D.

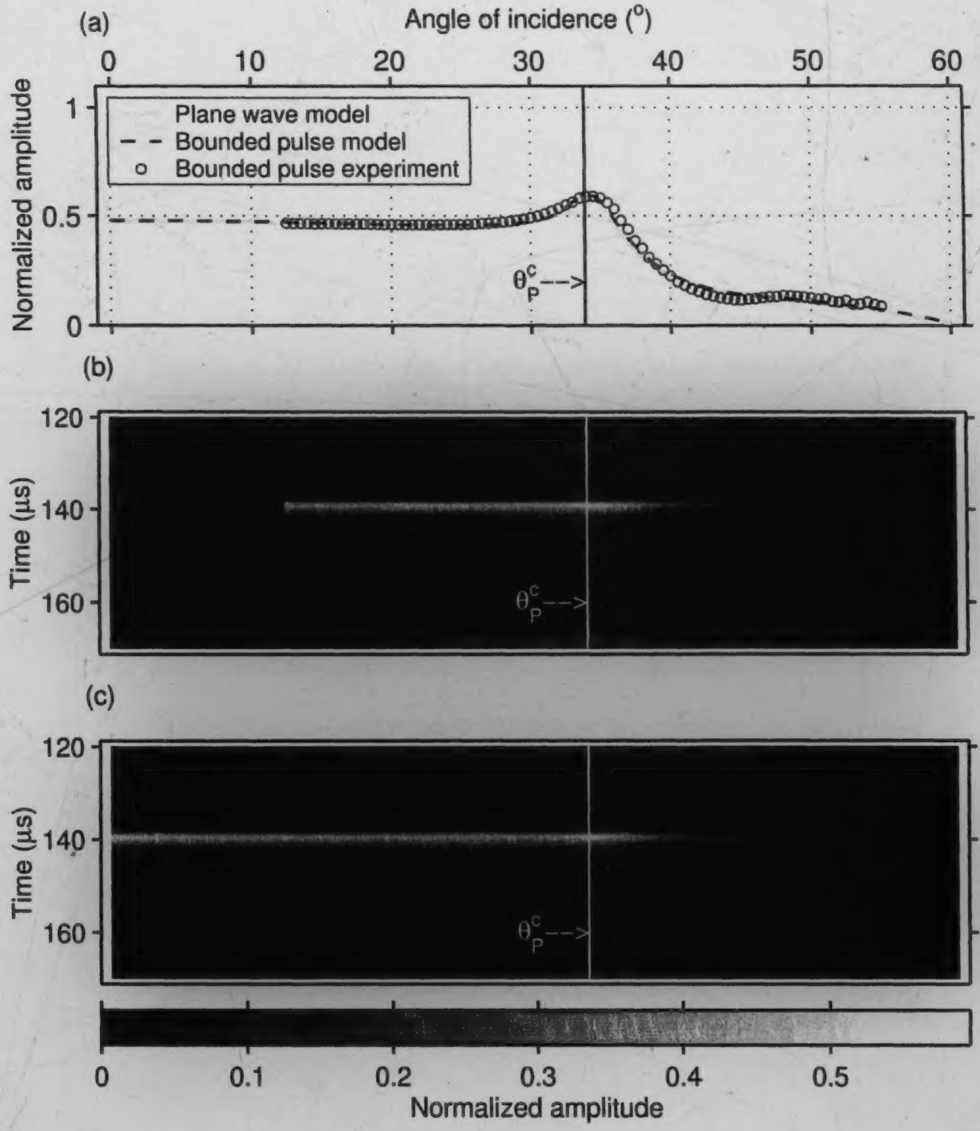

Figure 9.10: Observed and modelled reflectivity from a boundary between water and a water-saturated 7 cm thick synthetic porous plate. a) Measured, modelled, and plane wave reflectivity response. b) Observed maximum amplitude envelope. c) Modelled maximum amplitude envelope. Material labelled S060 with a permeability K=64 D.

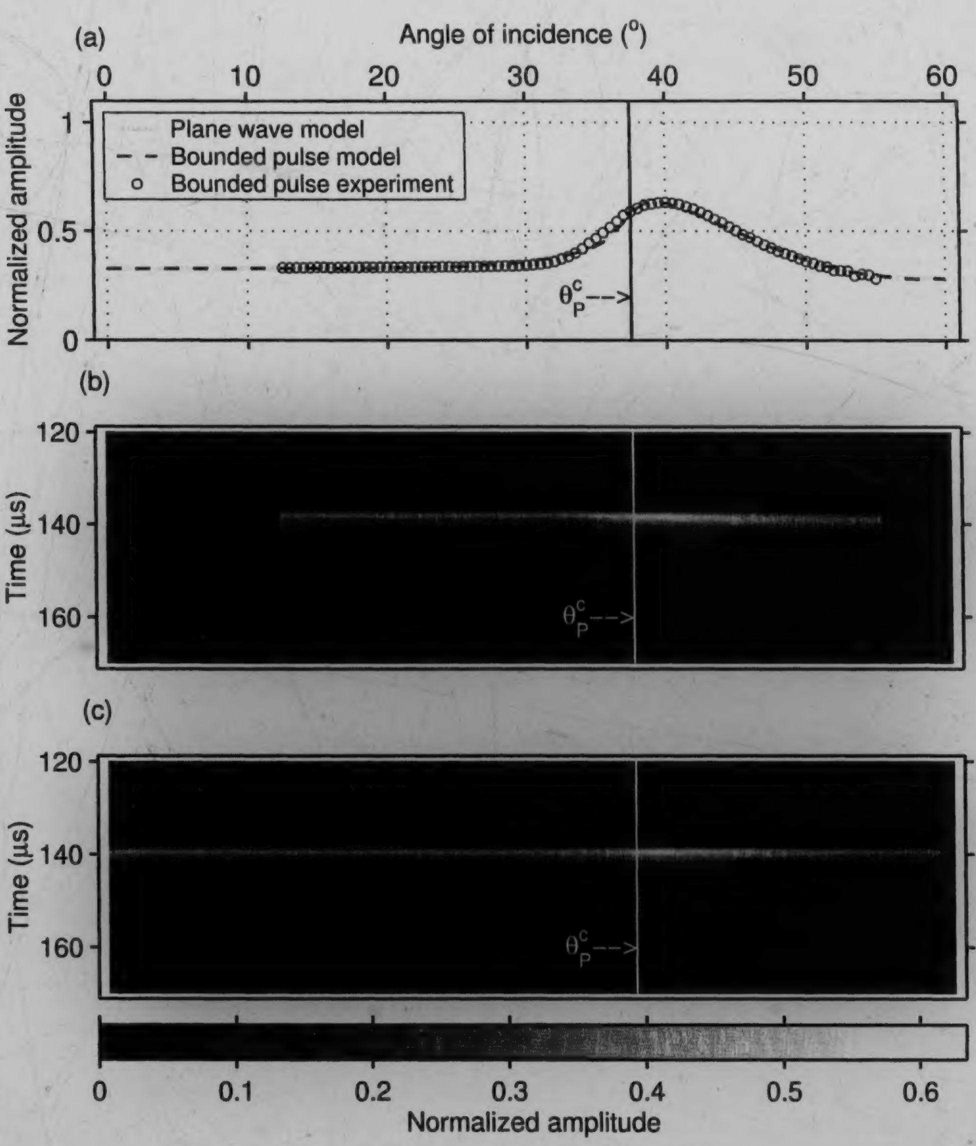

Figure 9.11: Observed and modelled reflectivity from a boundary between water and a water-saturated 7 cm thick synthetic porous plate. a) Measured, modelled, and plane wave reflectivity response. b) Observed maximum amplitude envelope. c) Modelled maximum amplitude envelope. Material labelled S040 with a permeability K=326 D.

be measured. A numerical approach is used to estimate the remaining parameters and a best fit of the reflectivity curves were estimated. The modelled curves describe well the observations despite that not all details that appear in the observations were matched by the models. It is also possible that the theories considered here do not hold for the porous sample S040 that exhibits large variation in pore and bead size diameters.

Chapter 10

Conclusions

In this thesis work, a complete experimental and modelling study of wave propagation, reflectivity, and transmission in porous materials was presented. A new ultrasonic reflectivity method of probing the mechanical properties of both elastic and poroelastic materials was developed. The first parts of the work describe an ultrasonic configuration consisting of a "large" transmitter, that simulates a plane wave response as much as possible, and a "small" point receiver that samples uniformly the resulting pulsed wave field.

The amplitude along the axis of propagation of the generated wave field by the large source remains nearly constant at large distances from the source. This makes many weak events detectible at large distances without major corrections to the measurements. The near-point receiver minimizes averaging of the wave field near the point of observation. The source and receiver were well characterized and calibrated on isotropic elastic solids.

The analysis was not able to fully use simple plane wave assumption, however, finite transducer effects needed to be accounted for. An exact expression of the source wave field is used in all modelling calculations. It is found that the reflection coefficient from a water-elastic solid interface experiences a large drop of amplitude. Many earlier authors attributed this to a leaky Rayleigh wave, but here an extensive numerical modelling has shown that the phase of the reflection coefficient is the only responsible for this phenomenon. This is supported mainly by

- Surface waves travelling in the elastic solid along the interface do exist at post P (and eventually S) critical angle of incidence but do not contribute to the energy balance of the boundary.

- A surface wave that would leak energy to the fluid medium above the solid will have a complex horizontal wave number, as considered in some literature, and would violate the boundary value problem that requires the horizontal wave number to be a real number only.
- Extensive modelling has shown that any reflection coefficient that exhibits large changes in the phase angle as a function of angle of incidence will produce similar effects in the reflectivity of bounded acoustic pulses.
- Any abrupt change in the reflection coefficient will be smoothed out in the reflectivity of bounded acoustic pulses even when the phase is null.

A comparison of two theories that attempt to describe waves in porous media was made. It is found that the Biot and de la Cruz/Spanos theories are nearly equivalent when water is the saturating fluid and if the unjacketed modulus is equal to the modulus of the solid minerals. In this case the compatibility condition $\delta_s K^{(f)} = \delta_f K^{(s)}$ is met. However it is important to note that the Biot theory does not account for dynamic porosity in contrast with the de la Cruz and Spanos theory. Furthermore if the fluid is replaced by one with a higher viscosity, substantial differences occur. This is particularly true for the slow P-wave phase velocity and attenuation. This viscosity effect will in turn affect any reflectivity and transmission partitioning of energy. However, the experiments in the thesis used water, a low viscosity fluid, and were unable to distinguish any differences between the two theories. It is also worth noting that the de la Cruz/Spanos theory predicts other processes that occur during wave propagation due to porosity and fluid pressure coupling.

The theories used in this thesis work were rewritten exclusively in terms of scalar and vector potentials. The analysis focussed on the interaction between the fluid and the solid skeleton for each wave mode that propagates in fluid-saturated porous materials. This is done through the complex number that relates the potentials in the fluid and the solid skeleton. It is also found that if the S-wave is well characterized by its phase velocity and attenuation the measurements of several parameters, the permeability K, the viscosity η, and more importantly the mass transfer ρ_{12} and the viscosity correction factor $F(\omega)$ are not required.

The calibrated source and receiver were first used in a series of transmission and reflectivity experiments in a number of water-saturated synthetic porous materials constructed of sintered glass beads. A complete transmission and reflection experiment was conducted on a thin synthetic porous plate. The source and receiver pair permitted a definitive observation of the slow P-wave that appeared strongly at all angles between -50^o and $+50^o$ angles of incidence. It was possible to measure accurately the velocities and attenuations of the fast P, the slow P, and the S waves. These observed velocities agreed well with those predicted using measurements of all relevant parameters in separate experiments.

A reflectivity experiment was also conducted on the same sample and several converted wave modes were observed. On this sample several measurements were performed of the observed wave modes mainly

- The phase velocity of the fast P, the slow P, and the S waves.
- The attenuations of the fast P, slow P, and S wave. However these measurements are not absolute and modelling was required in the final results. Moreover the P and S attenuations of the solid skeleton were found to contribute in part to the overall attenuations.

The observed data from the reflectivity experiment revealed the following mode conversions that to the author's knowledge have not previously been observed

- P-P1-P2-P: A converted fast P-wave to a slow P-wave at the second boundary.
- P-S-P2-P: A converted S-wave to a slow P-wave at the second boundary.
- P-P2-P2-P: A generated slow P-wave at the first boundary and reflected from the second boundary.

For this thin porous sample the theoretical calculations agree well with the observations of

- the phase velocities of all wave modes,
- the attenuations of all wave modes,
- the reflectivity curve,

- the phase angle of the reflected wave, and
- the calculated arrival times for all combination of wave conversions at the boundaries.

It is also possible that the "porosity wave" predicted by de la Cruz/Spanos theory was observed. However, this interpretation at present remains speculative and further modelling using theory that incorporates this additional mode is necessary to support this possibility.

It is worth reiterating that the use of purely elastic solutions, as is assumed in geophysical field studies which explore for hydrocarbons, cannot explain the observed reflectivity curves.

Reflectivity experiments were also conducted on weakly sintered synthetic glass bead thick samples. The large attenuation of both P and S waves of the solid skeleton influence the overall reflectivity responses. These samples exhibit a wide range of permeability and pore size and could not be characterized to the same level of confidence as with the thin sample. It is found that the theory agrees quite well with the experiments but subtle changes in the observed reflectivity were not featured by the calculations particularly at post P-wave critical angle of incidence. Some of the discrepancies in the sample with the largest beads may be due to either errors in the determination of porosity or in violation of the underlying assumption the sample is homogeneous at the scale of wavelengths used. However, the major conclusion of this thesis is that the Biot and de la Cruz/Spanos theories appear to adequately describe the reflectivity of the interface between a low viscosity liquid and a high porosity saturated porous medium.

It is also found that the reflectivity calculated from Zoeppritz's equations does not agree with that calculated from the porous media theory. This might have an implication in AVO analysis at least in any laboratory physical modelling of reflectivity and transmission in fluid-saturated porous materials.

As future work it would be interesting to conduct the same experiments with the source and receiver developed in this study by replacing the low viscosity fluid (water) by a high viscosity fluid (e.g. glycerol) and test the differences the calculations have revealed between the Biot and de la Cruz/Spanos theories. Another simple experiment is to construct small samples then saturate them with a high viscosity fluid and conduct velocity and attenuation measurements to test both theories at various frequency bandwidths.

What would be the response at low frequencies? Do Zoeppritz's equations approximate well reflectivity from fluid-saturated porous materials? To help answer these questions it would be interesting to calculate the response of a simple layered porous medium with various properties and saturated with various fluids using the equations of wave propagation in porous media. This would lead to an AVO analysis on the calculated models that would be compared to that calculated through Zoeppritz's equations and related approximations.

Appendix A

Acoustic beam with a cosine taper

For purposes of modelling, the edges of a bounded acoustic beam can be modulated in different ways. One of them is to modulate the bounded acoustic beam with cosine ramps at the edges. This is just an example that is used in the text to show the removal of the ringing effect in the Fourier domain. Envisage a monochromatic beam (frequency ω) travelling at an angle α with respect to the z axis (Fig. 2.1). Let $F(x)$ be of the form

$$F(x) = \begin{cases} 0 & : \quad x < -b \\ \frac{1}{2}(\cos[k_0(x+a)] + 1) & : \quad -b \leq x < -a \\ 1 & : \quad -a \leq x \leq a \\ \frac{1}{2}(\cos[k_0(x-a)] + 1) & : \quad b \geq x > a \\ 0 & : \quad x > b \end{cases} \tag{A.1}$$

then we can write

$$\Phi_1(k_x) = \frac{1}{2}\int_a^b (\cos[k_0(x-a)] + 1)e^{-i(k_{\alpha x}-k_x)x}dx \tag{A.2}$$

$$\Phi_2(k_x) = \int_{-a}^{a} e^{i(k_{\alpha x}-k_x)x}dx \tag{A.3}$$

$$\Phi_3(k_x) = \frac{1}{2}\int_a^b (\cos[k_0(x-a)] + 1)e^{i(k_{\alpha x}-k_x)x}dx \tag{A.4}$$

To evaluate equation A.2 and equation A.4 let $y = x - a$ and $m = k_{\alpha x} - k_x$. We have

$$\Phi_1(m) = \frac{1}{2}e^{-ima}\int_0^{b-a} \cos(k_0 y)e^{-imy}dy + \frac{1}{2}e^{-ima}\int_0^{b-a} e^{-imy}dy \tag{A.5}$$

The first term of equation A.5 can be rewritten as

$$\Phi_{11}(m) = \frac{1}{2}e^{-ima}\int_0^{b-a}\cos(k_0 y)\cos(my)dy - \frac{i}{2}e^{-ima}\int_0^{b-a}\cos(k_0 y)\sin(my)dy \tag{A.6}$$

Equation A.6 is evaluated using table of integrals (Dwight, 1964). Here we assume that $m \neq \pm k_0$. The case where this condition is not met will be given later.

$$\begin{aligned}\Phi_{11}(m) \;=\;& \frac{1}{2}e^{-ima}\left[\frac{\sin([(k_0 - m)(b-a)]}{2(k_0 - m)} + \frac{\sin[(k_0 + m)(b-a)]}{2(k_0 + m)}\right] - \\ & \frac{i}{2}e^{-ima}\left[\frac{\cos[(m - k_0)(b-a)]}{2(m - k_0)} + \frac{\cos[(m + k_0)(b-a)]}{2(m + k_0)}\right] - \\ & \frac{i}{2}e^{-ima}\left[\frac{1}{2(m - k_0)} + \frac{1}{2(m + k_0)}\right]\end{aligned} \tag{A.7}$$

Equation A.7 can be rewritten as

$$\Phi_{11}(m) = \frac{im}{2(k_0^2 - m^2)}\left(e^{-imb} + e^{-ima}\right) \tag{A.8}$$

The second term of equation A.5 leads

$$\Phi_{12}(m) = \frac{i}{2m}\left(e^{-imb} - e^{-ima}\right) \tag{A.9}$$

We also have

$$\Phi_3(m) = \frac{1}{2}e^{ima}\int_0^{b-a}\cos(k_0 y)e^{imy}dy + \frac{1}{2}e^{ima}\int_0^{b-a}e^{imy}dy \tag{A.10}$$

The first term of equation A.10 can be rewritten as

$$\Phi_{31}(m) = \frac{1}{2}e^{ima}\int_0^{b-a}\cos(k_0 y)\cos(my)dy + \frac{i}{2}e^{ima}\int_0^{b-a}\cos(k_0 y)\sin(my)dy \tag{A.11}$$

Equation A.11 is evaluated using table of integrals (Dwight, 1964)

$$\begin{aligned}\Phi_{31}(m) \;=\;& \frac{1}{2}e^{ima}\left[\frac{\sin[(k_0 - m)(b-a)]}{2(k_0 - m)} + \frac{\sin[(k_0 + m)(b-a)]}{2(k_0 + m)}\right] - \\ & \frac{i}{2}e^{ima}\left[\frac{\cos[(m - k_0)(b-a)]}{2(m - k_0)} + \frac{\cos[(m + k_0)(b-a)]}{2(m + k_0)}\right] + \\ & \frac{i}{2}e^{ima}\left[\frac{1}{2(m - k_0)} + \frac{1}{2(m + k_0)}\right]\end{aligned} \tag{A.12}$$

Equation A.12 can be rewritten as

$$\Phi_{31}(m) = -\frac{im}{2(k_0^2 - m^2)}\left(e^{imb} + e^{ima}\right) \tag{A.13}$$

The second term of equation A.10 leads

$$\Phi_{32}(m) = -\frac{i}{2m}\left(e^{imb} - e^{ima}\right) \tag{A.14}$$

Equation A.3 leads to

$$\Phi_2(m) = \frac{2\sin(ma)}{m} \tag{A.15}$$

Gathering equations A.8, A.9, A.13, A.14, and A.15 we get

$$\Phi(m) = \frac{k_0^2}{2\pi(k_0^2 - m^2)m}\left[\sin(mb) + \sin(ma)\right] \tag{A.16}$$

replacing m by its value we have

$$\Phi(k_x) = k_0^2 \frac{\sin\left[(k_{\alpha x} - k_x)b\right] + \sin\left[(k_{\alpha x} - k_x)a\right]}{2\pi(k_{\alpha x} - k_x)\left[k_0^2 - (k_{\alpha x} - k_x)^2\right]} \tag{A.17}$$

when $k_{\alpha x} - k_x \neq \pm k_0$. In the case where $k_{\alpha x} - k_x = \pm k_0$ the integration of equations A.5, A.11, and equation A.3 leads to

$$\Phi(\pm k_0) = \frac{\cos(k_0 a)}{4k_0} + \frac{\sin(k_0 a)}{\pi k_0} \tag{A.18}$$

which completes the description of the known field on the $z = 0$ plane in the Fourier domain. Equation A.18 is also the limiting case of equation A.17, thus equation A.17 is valid for all k_x.

$$\Phi(k_x) = \frac{k_0^2}{2\pi\left[k_0^2 - (k_{\alpha x} - k_x)^2\right]} \frac{\sin\left[(k_{\alpha x} - k_x)b\right] + \sin\left[(k_{\alpha x} - k_x)a\right]}{(k_{\alpha x} - k_x)} \tag{A.19}$$

Appendix B

Review of the Biot theory

B.1 Introduction

A review of the original work of Biot (1956a; 1956b) will be given here. These papers contain several typographical errors that we hope to correct here. The derived equations of motion and solutions are the most used in the literature for wave propagation in porous media. The equations of motion governing the wave propagation in porous materials saturated with a single fluid were derived in (Biot, 1956a; Biot, 1956b). A review of this theory will be given along with the experimental determination of the different parameters involved (Biot and Willis, 1957). In the following the superscripts $^{(s)}$ and $^{(f)}$ will denote the solid skeleton (solid frame) and the fluid components respectively. A repetitive index implies a summation over the index. Using the fact that there exists a potential energy Biot derived the stress-strain relations

$$\sigma_{ij} = 2\mu_M e_{ij} + (Ae_{ll} + Q\epsilon_{kk})\,\delta_{ij} \tag{B.1}$$

$$s = Qe_{ll} + R\epsilon_{kk} \tag{B.2}$$

where δ_{ij} is 1 if $i = j$ and is 0 if $i \neq j$. σ_{ij} are the stress components acting on the solid portion of a unit volume element of the aggregate. s is stress acting by the fluid portion on the wall of the considered element. e_{ll} and ϵ_{ll} are the divergences of the displacement $\vec{u}^{(s)}$ of the solid and the displacement $\vec{u}^{(f)}$ of the fluid respectively. The above equations describe the stresses in the solid and in the fluid in a small unit volume of the aggregate, that is a two phase material, composed of a porous solid skeleton and a fluid that completely saturates the void volume within the solid skeleton. The stresses in the solid and the fluid are linked together by the parameters Q and R. As the wave propagates through the element the solid skeleton and the fluid interact with each other. For example as the volume element compresses the pore pressure increases and a portion of the fluid flows out of the element. As the fluid flows out viscous friction occurs. There is a great dependence between the solid and the fluid through inertia and viscous flow, flow that is highly dependent on frequency. The strain relations are given by

$$e_{ij} = \frac{1}{2}\left(u_{i,j}^{(s)} + u_{j,i}^{(s)}\right) \tag{B.3}$$

$$\epsilon_{ij} = \frac{1}{2}\left(u_{i,j}^{(f)} + u_{j,i}^{(f)}\right) \tag{B.4}$$

where i, j means the derivative of the i^{th} component with respect to the j^{th} direction. μ_M is the shear modulus of the solid skeleton.

B.2 Determination of Biot parameters

The coefficients Q, R, A, and μ_M can be determined experimentally (Biot and Willis, 1957). The shear modulus of the solid skeleton μ_M can be measured directly. The other parameters can be derived from experimental tests using the stress-strain relations given in equations B.1 through B.4. A review of the methodology of Biot and willis (1957) will be given below.

B.2.1 Jacketed compressibility test

A fluid-saturated specimen of the solid material is enclosed in a thin impervious jacket (Fig. B.1). The specimen is then subjected to a confining pressure P_c and the pore pressure is kept constant by allowing fluid flow through an opening to the atmosphere. The dilatation of the specimen e_{ii} is measured and the bulk modulus K_M of the solid skeleton (solid frame) is then given by

$$K_M = -\frac{P_c}{e_{ii}} \tag{B.5}$$

In this case the total fluid pressure is applied to the total external surface of the specimen. Thus the fluid pressure (confining pressure P_c) is equal (with a negative sign) to the average principal stresses σ_{ii}. The pore pressure remains constant. Thus

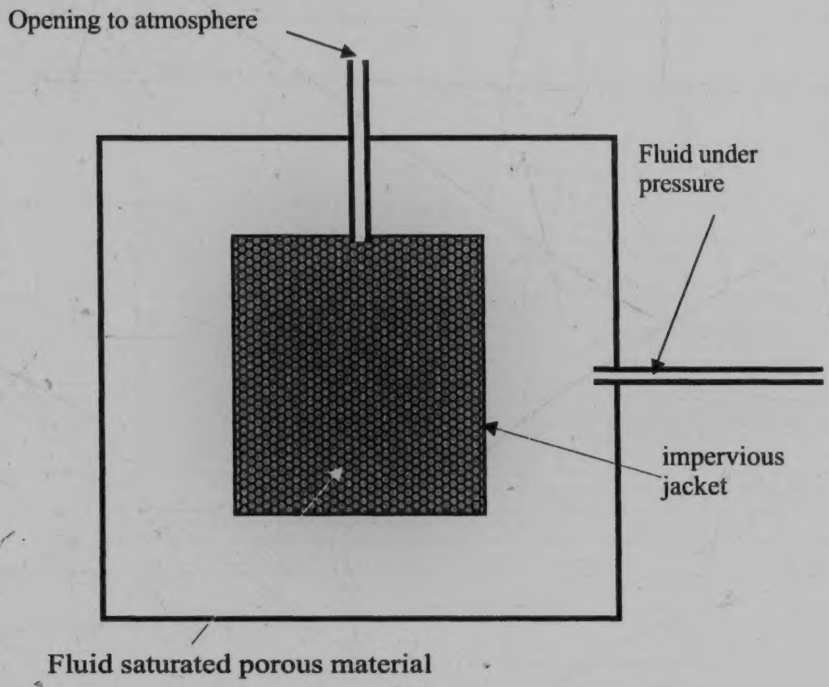

Figure B.1: Jacketed compressibility test setup.

we have

$$\frac{1}{3}\sigma_{ii} = -P_c \tag{B.6}$$

Equations B.1 and B.2 yield in this case

$$\begin{aligned} 0 &= Qe_{ii} + R\epsilon_{ii} && \text{(B.7)} \\ \frac{1}{3}\sigma_{ii} &= \left(\frac{2}{3}\mu_M + A\right) e_{ii} + Q\epsilon_{ii} && \text{(B.8)} \end{aligned}$$

Equations B.7 and B.8 yield

$$-\frac{P_c}{e_{ii}} = \frac{2}{3}\mu_M + A - \frac{Q^2}{R} \tag{B.9}$$

Using equation B.5 in equation B.9 we get

$$K_M = \frac{2}{3}\mu_M + A - \frac{Q^2}{R} \tag{B.10}$$

We can see here that $A - \frac{Q^2}{R}$ plays the role of the Lamé constant for the solid skeleton in the presence of the fluid.

B.2.2 Unjacketed compressibility test

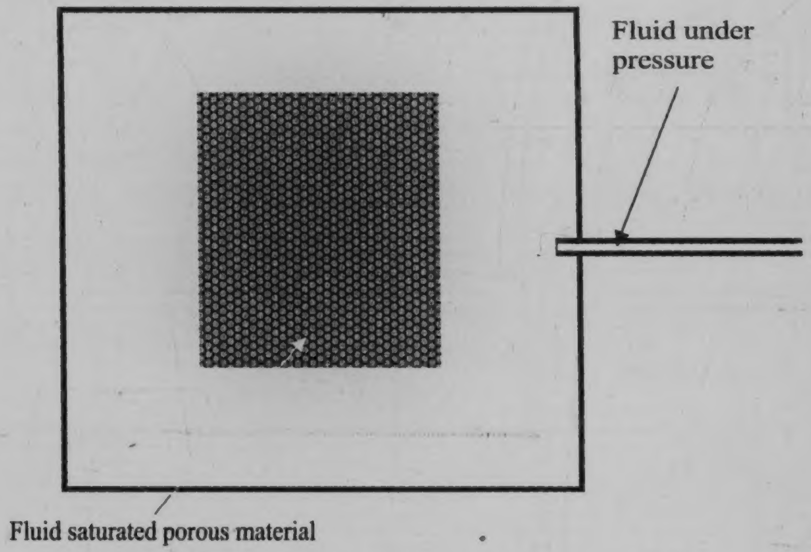

Figure B.2: Unjacketed compressibility test setup.

In this test a fluid-saturated specimen of the porous material but with no impervious jacket is placed in a same fluid and a confining pressure is applied (Fig. B.2). The dilatation e_{ii} of the specimen is measured and an unjacketed bulk modulus K_{un} is determined by

$$K_{un} = -\frac{P_c}{e_{ii}} \tag{B.11}$$

In this test the confining fluid pressure P_c acts on both the solid and the fluid on each surface of the specimen. Thus we have

$$\frac{1}{3}\sigma_{ii} = -(1-\beta)P_c \tag{B.12}$$

and equation B.1 and B.2 yield in this case

$$\begin{aligned} -\beta P_c &= Q e_{ii} + R\epsilon_{ii} && \text{(B.13)} \\ \frac{1}{3}\sigma_{ii} &= \left(\frac{2}{3}\mu_M + A\right) e_{ii} + Q\epsilon_{ii} && \text{(B.14)} \end{aligned}$$

Combining equations B.12 through B.14 we get

$$\left(1 - \beta\frac{(R+Q)}{R}\right) K_{un} = \left(\frac{2}{3}\mu_M + A\right) - \frac{Q^2}{R} \tag{B.15}$$

To completely describe the system in the unjacketed compressibility test we will consider the volume of fluid which enters the pores of the specimen that is $\beta(e_{ii} - \epsilon_{ii})$. The coefficient of fluid content γ is defined a

$$\gamma = \frac{\beta(e_{ii} - \epsilon_{ii})}{P_c} \tag{B.16}$$

Using equation B.16 in equation B.11 yields

$$\epsilon_{ii} = -\frac{\gamma}{\beta} P_c - \frac{P_c}{K_{un}} \tag{B.17}$$

which combined with equation B.13 yields

$$\beta(R + Q) + \left(R\gamma - \beta^2\right) K_{un} = 0 \tag{B.18}$$

Solving equation B.10, B.15, and B.18 for A, Q, and R we explicitly get

$$\begin{aligned}
R &= \frac{\beta^2 K_{un}^2}{(K_{un} + \gamma K_{un}^2 - K_M)} && \text{(B.19)}\\
Q &= \frac{\beta K_{un}\,(K_{un} - K_{un}\beta - K_M)}{(K_{un} + \gamma K_{un}^2 - K_M)} && \text{(B.20)}\\
A &= \frac{(K_{un} - K_{un}\beta - K_M)^2}{(K_{un} + \gamma K_{un}^2 - K_M)} + K_M - \frac{2}{3}\mu_M && \text{(B.21)}
\end{aligned}$$

To derive R, Q, and A from the above equations we need to measure the unjacketed bulk modulus K_M of the solid skeleton, the shear modulus μ_M, the porosity β, and the coefficient of fluid content γ. The above equations can be rewritten as

$$\begin{aligned}
M &= \frac{\beta K_{un}}{(K_{un} + \gamma K_{un}^2 - K_M)} && \text{(B.22)}\\
R &= M\beta K_{un} && \text{(B.23)}\\
Q &= M\,(K_{un} - K_{un}\beta - K_M) && \text{(B.24)}\\
A &= \frac{Q^2}{R} + K_M - \frac{2}{3}\mu_M && \text{(B.25)}
\end{aligned}$$

These equations show the interdependence of the solid skeleton and the fluid. A plays the role of the Lamé constant. If the fluid is not present then $A = K_M - \frac{2}{3}\mu_M$ which is the Lamé constant of the solid skeleton in the absence of the fluid. If the solid is non-porous ($\beta = 0$) then A is simply the Lamé constant of the solid. The coefficient of fluid content γ has to be measured to complete the set of parameters that describe the porous medium.

B.2.3 Determination of the coefficient of fluid content

A fluid-saturated specimen of the porous material with no impervious jacket is placed in a closed chamber. The same fluid is then injected into the chamber. The volume of the injected fluid per unit pressure is the sum of the solid (mineral) compressibility, the volume of fluid that entered the pores γ and a fixed quantity θ that depends on the elastic properties of the fluid in the chamber. The injected fluid volume is then given by

$$V_1 = \frac{1}{K_{un}} + \gamma + \theta \tag{B.26}$$

where $K^{(s)}$ is the bulk modulus of the solid material (mineral). The specimen is then removed from the chamber and its volume replaced by fluid. The volume of injected fluid is then measured. In this case it is given by

$$V_2 = \theta + \frac{1}{K^{(f)}} \tag{B.27}$$

where $K^{(f)}$ is the bulk modulus of the fluid. From equations B.26 and B.27 we derive the volume difference

$$\Delta V = \frac{1}{K_{un}} + \gamma - \frac{1}{K^f} \tag{B.28}$$

Thus the coefficient of fluid content is given by

$$\gamma = \Delta V - \frac{1}{K_{un}} + \frac{1}{K^{(f)}} \tag{B.29}$$

If the solid skeleton is composed of an isotropic and homogeneous solid material the fluid content may be determined directly from the compressibility of the fluid $K^{(f)}$ and that of the mineral grains $K^{(s)}$. If we consider the unjacketed test the porosity does not vary when a confining pressure is applied and the bulk modulus of the solid skeleton K_{un} is equal to the bulk modulus of the mineral grains $K^{(s)}$. In this case the dilatation of the fluid is

$$\epsilon_{ii} = -\frac{P_c}{K^{(f)}} \tag{B.30}$$

Then the fluid content γ is given by

$$\gamma = \beta \left(\frac{1}{K^{(f)}} - \frac{1}{K^{(s)}} \right) \tag{B.31}$$

and equations B.22 through B.25 will hold with $K_{un} = K^{(s)}$.

B.3 Wave propagation

B.3.1 Equations of motion

Let a solid porous material saturated with a single fluid be homogeneous and isotropic with a uniform porosity. The wavelength is assumed to be larger than a small unit volume element of the aggregate, that is the volume of the solid skeleton and its fluid content. The wave field is averaged over the unit volume considered. Any wavelength that is close or smaller then the unit volume will produce scattering, a phenomenon that is not considered here but may act on at least one of the samples studied in chapter 9. Thus the wavelength must be larger than the pore size. As an acoustic wave propagates through the medium flow of the fluid in and out of the considered element occurs. The flow is supposed to be of Poiseuille type. Therefore the frequency limit is set to the frequency at which Poiseuille flow breaks down. This frequency limit is extended to that limited by the wavelength in the Biot (1956b). The frequency limitation will be discussed later. The kinetic energy T is written in the following form

$$\begin{aligned} T &= \frac{1}{2}\rho_{11}\left[\left(\dot{u}_x^{(s)}\right)^2 + \left(\dot{u}_y^{(s)}\right)^2 + \left(\dot{u}_z^{(s)}\right)^2\right] + \\ &\quad \rho_{12}\left[\dot{u}_x^{(s)}\dot{u}_x^{(f)} + \dot{u}_y^{(s)}\dot{u}_y^{(f)} + \dot{u}_z^{(s)}\dot{u}_z^{(f)}\right] + \\ &\quad \frac{1}{2}\rho_{22}\left[\left(\dot{u}_x^{(f)}\right)^2 + \left(\dot{u}_y^{(f)}\right)^2 + \left(\dot{u}_z^{(f)}\right)^2\right] \end{aligned} \tag{B.32}$$

where $\dot{u}_x$ denotes the derivative of the $\hat{x}$ component of the displacement with respect to time. A dissipation function D, written in a quadratic form, that vanishes when there is no relative motion between the solid and the fluid is used. It is given by

$$D = \frac{1}{2}b\left[\left(\dot{u}_x^{(s)} - \dot{u}_x^{(f)}\right)^2 + \left(\dot{u}_y^{(s)} - \dot{u}_y^{(f)}\right)^2 + \left(\dot{u}_z^{(s)} - \dot{u}_z^{(f)}\right)^2\right] \tag{B.33}$$

where b is related to Darcy's permeability K, the porosity of the material β, and the viscosity of the fluid η by

$$b = \frac{\eta\beta^2}{K} \tag{B.34}$$

ρ_{11} and ρ_{22} are the dynamic mass coefficients

$$\rho_{11} = (1-\beta)\rho^{(s)} - \rho_{12} \tag{B.35}$$

$$\rho_{22} = \beta\rho^{(f)} - \rho_{12} \tag{B.36}$$

where $\rho^{(s)}$ is the density of the solid material, $\rho^{(f)}$ is the density of the fluid, and ρ_{12} is the additional mass coupling induced mutually on the solid and the fluid. The total mass ρ is then

$$\rho = \rho_{11} + \rho_{22} + 2\rho_{12} \tag{B.37}$$

which is simply

$$\rho = (1-\beta)\rho^{(s)} + \beta\rho^{(f)} \tag{B.38}$$

The mutually induced mass couples the solid and the fluid through the kinetic energy equation B.32. This mass enters in the cross terms between the solid and the fluid displacements. Consider the $\hat{x}$ direction. The total force due to the stress acting on the solid $q_x^{(s)}$ and that acting on the fluid $q_x^{(f)}$ in a volume element are derived from Lagrange's equations

$$\begin{aligned} \frac{\partial}{\partial t}\left(\frac{\partial T}{\partial \dot{u}_x^{(s)}}\right) + \frac{\partial D}{\partial \dot{u}_x^{(s)}} &= q_x^{(s)} && \text{(B.39)} \\ \frac{\partial}{\partial t}\left(\frac{\partial T}{\partial \dot{u}_x^{(f)}}\right) + \frac{\partial D}{\partial \dot{u}_x^{(f)}} &= q_x^{(f)} && \text{(B.40)} \end{aligned}$$

In the $\hat{x}$ direction these forces are given by

$$\begin{aligned} q_x^{(s)} &= \frac{\partial \sigma_x}{\partial x} + \frac{\partial \sigma_y}{\partial y} + \frac{\partial \sigma_z}{\partial z} && \text{(B.41)} \\ q_x^{(f)} &= \frac{\partial s}{\partial x} && \text{(B.42)} \end{aligned}$$

Using equations B.1, B.2, B.32, and B.33 in equations B.39 through B.42 the wave equations of motion in porous media are

$$\begin{aligned} \mu_M \nabla^2 \vec{u}^{(s)} + \vec{\nabla}\left[(A+\mu_M)\vec{\nabla}\cdot\vec{u}^{(s)} + Q\vec{\nabla}\cdot\vec{u}^{(f)}\right] &= \frac{\partial^2}{\partial t^2}\left(\rho_{11}\vec{u}^{(s)} + \rho_{12}\vec{u}^{(f)}\right) + \\ &\quad\; b\frac{\partial}{\partial t}\left(\vec{u}^{(s)} - \vec{u}^{(f)}\right) && \text{(B.43)} \\ \vec{\nabla}\left[Q\vec{\nabla}\cdot\vec{u}^{(s)} + R\vec{\nabla}\cdot\vec{u}^{(f)}\right] &= \frac{\partial^2}{\partial t^2}\left(\rho_{12}\vec{u}^{(s)} + \rho_{22}\vec{u}^{(f)}\right) \\ &\quad\; b\frac{\partial}{\partial t}\left(\vec{u}^{(s)} - \vec{u}^{(f)}\right) && \text{(B.44)} \end{aligned}$$

which can be rewritten as

$$\begin{aligned}\mu_M \nabla^2 \vec{u}^{(s)} + \vec{\nabla}\left[(A+\mu_M)\vec{\nabla}\cdot\vec{u}^{(s)} + Q\vec{\nabla}\cdot\vec{u}^{(f)}\right] &= (1-\beta)\rho^{(s)}\frac{\partial^2}{\partial t^2}\vec{u}^{(s)} - \\ &\quad \rho_{12}\frac{\partial^2}{\partial t^2}\left(\vec{u}^{(s)}-\vec{u}^{(f)}\right) + \frac{\eta\beta^2}{K}\frac{\partial}{\partial t}\left(\vec{u}^{(s)}-\vec{u}^{(f)}\right) \qquad \text{(B.45)}\\ \vec{\nabla}\left[Q\vec{\nabla}\cdot\vec{u}^{(s)} + R\vec{\nabla}\cdot\vec{u}^{(f)}\right] &= \beta\rho^{(f)}\frac{\partial^2}{\partial t^2}\vec{u}^{(f)} + \rho_{12}\frac{\partial^2}{\partial t^2}\left(\vec{u}^{(s)}-\vec{u}^{(f)}\right) - \\ &\quad \frac{\eta\beta^2}{K}\frac{\partial}{\partial t}\left(\vec{u}^{(s)}-\vec{u}^{(f)}\right) \qquad \text{(B.46)}\end{aligned}$$

These equations are the coupled equations of motions that describe wave propagation in porous media. Now we will look at the derivation of the different wave modes that could propagate in such media.

B.3.2 Longitudinal waves

Let $\varepsilon^{(s)} = \vec{\nabla}\cdot\vec{u}^{(s)}$ and $\varepsilon^{(f)} = \vec{\nabla}\cdot\vec{u}^{(f)}$. To investigate the propagation of only longitudinal waves we apply the divergence operator (the divergence of a rotational wave field will be zero) to the equations B.45 and B.46. These equations reduce to

$$\begin{aligned}\nabla^2\left[(A+2\mu_M)\varepsilon^{(s)} + Q\varepsilon^{(f)}\right] &= (1-\beta)\rho^{(s)}\frac{\partial^2}{\partial t^2}\varepsilon^{(s)} - \rho_{12}\frac{\partial^2}{\partial t^2}\left(\varepsilon^{(s)}-\varepsilon^{(f)}\right) + \\ &\quad \frac{\eta\beta^2}{K}\frac{\partial}{\partial t}\left(\varepsilon^{(s)}-\varepsilon^{(f)}\right) \qquad \text{(B.47)}\\ \nabla^2\left[Q\varepsilon^{(s)} + R\varepsilon^{(f)}\right] &= \beta\rho^{(f)}\frac{\partial^2}{\partial t^2}\varepsilon^{(f)} + \rho_{12}\frac{\partial^2}{\partial t^2}\left(\varepsilon^{(s)}-\varepsilon^{(f)}\right) - \\ &\quad \frac{\eta\beta^2}{K}\frac{\partial}{\partial t}\left(\varepsilon^{(s)}-\varepsilon^{(f)}\right) \qquad \text{(B.48)}\end{aligned}$$

In the coupled equations B.47 and B.48 only the divergences of the wave field are present. Thus these equations of motion govern the propagation of longitudinal waves in a fluid-saturated porous medium. Now consider a longitudinal plane wave propagating in the $\vec{x}$ direction

$$\vec{u}^{(s)} = C^{(s)}\vec{k}e^{i\left(\omega t-\vec{k}\cdot\vec{x}\right)} \qquad \text{(B.49)}$$

$$\vec{u}^{(f)} = C^{(f)}\vec{k}e^{i\left(\omega t-\vec{k}\cdot\vec{x}\right)} \qquad \text{(B.50)}$$

where $C^{(s)}$ and $C^{(f)}$ are the maximum amplitudes of the wave in the solid and the fluid respectively. In general, the wave number $\vec{k}$ is complex to account for attenuation. $\vec{x}$ is the position vector, ω is the angular frequency, and i is the $\sqrt{-1}$. Using the solutions of the form given by B.49 and B.50 in B.47 and B.48 we get

$$\begin{aligned}
\left[k^2\left(A+2\mu_M\right)-\omega^2\left(1-\beta\right)\rho^{(s)}+\omega^2\rho_{12}+i\omega\frac{\eta\beta^2}{K}\right]\varepsilon^{(s)}+& \\
\left[k^2Q-\omega^2\rho_{12}-i\omega\frac{\eta\beta^2}{K}\right]\varepsilon^{(f)} &= 0 \qquad \text{(B.51)}\\
\left[k^2Q-\omega^2\rho_{12}-i\omega\frac{\eta\beta^2}{K}\right]\varepsilon^{(s)}+& \\
\left[k^2R+\omega^2\rho_{12}-\omega^2\beta\rho^{(f)}+i\omega\frac{\eta\beta^2}{K}\right]\varepsilon^{(f)} &= 0 \qquad \text{(B.52)}
\end{aligned}$$

In order for the equations B.51 and B.52 to hold the determinant of the coefficients must vanish. This leads to the following frequency equation

$$ak^4+bk^2+c=0 \qquad \text{(B.53)}$$

where a, b, and c are given by

$$\begin{aligned}
a &= R\left(A+2\mu_M\right)-Q^2 \qquad \text{(B.54)}\\
b &= \left(A+2\mu_M\right)\left(\omega\rho_{12}-\omega\beta\rho^{(f)}+i\frac{\eta\beta^2}{K}\right)\omega+ \\
&\quad \left(R+2Q\right)\left(\omega\rho_{12}+i\frac{\eta\beta^2}{K}\right)\omega-R\left(1-\beta\right)\rho^{(s)}\omega^2 \qquad \text{(B.55)}\\
c &= \left[\left(1-\beta\right)\beta\rho^{(f)}\rho^{(s)}-\rho_{12}\rho\right]\omega^4-i\rho\frac{\eta\beta^2}{K}\omega^3 \qquad \text{(B.56)}
\end{aligned}$$

Equation B.53 admits two physical solutions, thus two longitudinal waves can propagate. The real and the imaginary parts of the two roots k_1 and k_2 of equation B.53 provide the velocity and the attenuation for each wave. The higher velocity wave and the lower velocity wave are referred to as the fast P and slow P waves respectively.

B.3.3 Rotational waves

To consider only rotational waves we apply the curl operator (the curl of a longitudinal wave field is zero) to equations B.45 and B.46. Let $\vec{\Omega}^{(s)}=\vec{\nabla}\times\vec{u}^{(s)}$ and

$\vec{\Omega}^{(f)} = \vec{\nabla} \times \vec{u}^{(f)}$ then equations B.45 and B.46 lead to

$$\begin{aligned}(1-\beta)\rho^{(s)}\frac{\partial^2}{\partial t^2}\vec{\Omega}^{(s)} - \rho_{12}\frac{\partial^2}{\partial t^2}\left(\vec{\Omega}^{(s)} - \vec{\Omega}^{(f)}\right) + & \\ \frac{\eta\beta^2}{K}\frac{\partial}{\partial t}\left(\vec{\Omega}^{(s)} - \vec{\Omega}^{(f)}\right) &= \mu_M \nabla^2 \vec{\Omega}^{(s)} \qquad \text{(B.57)}\\ \beta\rho^{(f)}\frac{\partial^2}{\partial t^2}\vec{\Omega}^{(f)} + \rho_{12}\frac{\partial^2}{\partial t^2}\left(\vec{\Omega}^{(s)} - \vec{\Omega}^{(f)}\right) - & \\ \frac{\eta\beta^2}{K}\frac{\partial}{\partial t}\left(\vec{\Omega}^{(s)} - \vec{\Omega}^{(f)}\right) &= 0 \qquad \text{(B.58)}\end{aligned}$$

These coupled two equations, B.57 and B.58 govern the propagation of rotational waves in a fluid-saturated porous medium. Now consider a rotational plane wave propagating in the direction $\vec{x}$

$$\vec{u}^{(s)} = \vec{C}^{(s)} e^{i\left(\omega t - \vec{k}\cdot\vec{x}\right)} \qquad \text{(B.59)}$$

$$\vec{u}^{(f)} = \vec{C}^{(f)} e^{i\left(\omega t - \vec{k}\cdot\vec{x}\right)} \qquad \text{(B.60)}$$

where $\vec{D}^{(s)} \cdot \vec{k} = 0$ and $\vec{D}^{(f)} \cdot \vec{k} = 0$. Using solutions B.59 and B.60 in B.57 and B.58 we get

$$\begin{aligned}\left[k^2\mu_M - (1-\beta)\,\rho^{(s)}\omega^2 + \rho_{12}\omega^2 + i\omega\frac{\eta\beta^2}{K}\right]\vec{\Omega}^{(s)} - & \\ \left[\rho_{12}\omega^2 + i\omega\frac{\eta\beta^2}{K}\right]\vec{\Omega}^{(f)} &= 0 \qquad \text{(B.61)}\\ \left[\rho_{12}\omega + i\frac{\eta\beta^2}{K}\right]\vec{\Omega}^{(s)} + \left[\beta\rho^{(f)}\omega - \rho_{12}\omega - i\frac{\eta\beta^2}{K}\right]\vec{\Omega}^{(f)} &= 0 \qquad \text{(B.62)}\end{aligned}$$

In order for the equations B.61 and B.62 to hold the determinant must vanish. We get the frequency equation

$$\begin{aligned}k^2\mu_M\left(\beta\rho^{(f)}\omega - \rho_{12}\omega - i\frac{\eta\beta^2}{K}\right) - \rho^{(s)}\rho^{(f)}\beta\,(1-\beta)\,\omega^3 + & \\ \beta\rho^{(f)}\left(\rho_{12}\omega + i\frac{\eta\beta^2}{K}\right)\omega^2 &= 0 \qquad \text{(B.63)}\end{aligned}$$

Equation B.63 admits one physical solution, thus only one rotational wave can propagate. The real and imaginary parts of the root k provide respectively the phase velocity and the attenuation of the wave. This root is

$$k = \left[\frac{\rho^{(s)}\rho^{(f)}\beta\,(1-\beta)\,\omega^3 - \beta\rho^{(f)}\left(\rho_{12}\omega + i\frac{\eta\beta^2}{K}\right)\omega^2}{\mu_M\left(\beta\rho^{(f)}\omega - \rho_{12}\omega - i\frac{\eta\beta^2}{K}\right)}\right]^{\frac{1}{2}} \qquad \text{(B.64)}$$

B.3.4 Frequency limitations

It is necessary to determine the frequency limit for the validity of the theory. The upper frequency limit is at a bound where the wavelength is close to the pore size. Generally however this frequency bound is lower. It is set at the frequency where Poiseuille flow breaks down. This frequency limit is given by

$$f_{\lim} = \frac{\pi\eta}{4\rho^{(f)}d^2} \tag{B.65}$$

where d is the diameter of the pores, η the viscosity, and $\rho^{(f)}$ the fluid density. To set the frequency limit according to the pore size a complex correction factor must be applied to the coefficient b in equations B.45 and B.46 to allow for flow that deviates from Poiseuille flow to be taken into account (Biot, 1956b). This correction factor is based on, the shape and geometry of the porous medium pores, and on the fluid flow conditions. It is derived in detail in Biot (1956b). This correction factor $F(\kappa)$ is

$$F(\kappa) = \frac{\kappa^2 T(\kappa)}{4(\kappa + 2iT(\kappa))} \tag{B.66}$$

where κ is

$$\kappa = a\sqrt{\frac{\omega\rho^{(f)}}{\eta}} \tag{B.67}$$

and $T(\kappa)$ is given by

$$T(\kappa) = \frac{ber'(\kappa) + ibei'(\kappa)}{ber(\kappa) + ibei(\kappa)} \tag{B.68}$$

Bei.m where a is a length that is characteristic of the size and geometry of the pores and $'$ denotes the first derivative with respect to κ. For circular pores it is equal to the radius whereas in the case of slits of opening a_1 it is given by $a = \frac{2}{3}a_1$. With the correction factor $F(\kappa)$ multiplying b the upper frequency limit is extended to the wavelength close to the diameter of the pores. The *ber* and *bei* are the Kelvin functions that are

$$ber(\kappa) = \sum_{j=0}^{\infty} \frac{(-1)^j \kappa^{4j}}{2^{4j}(2j!)^2} \tag{B.69}$$

$$bei(\kappa) = \sum_{j=0}^{\infty} \frac{(-1)^j \kappa^{2+4j}}{(2^{2+4j}[(2j+1)!]^2} \tag{B.70}$$

The *ber* and *bei* functions are given in figure B.3 and the correction factor $F(\kappa)$ is given in figure B.4. The presently reviewed Biot theory was extended by the

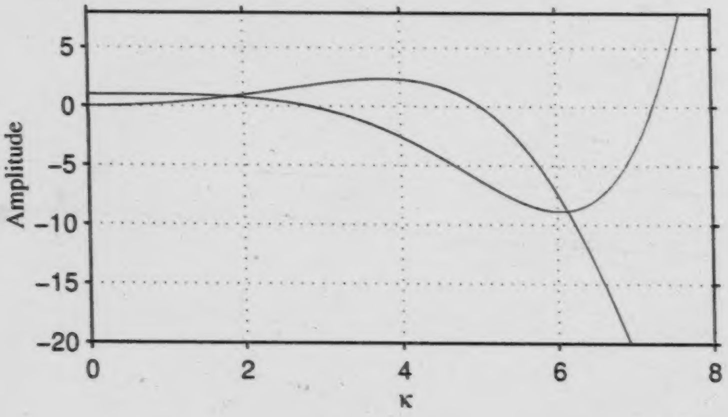

Figure B.3: *ber* and *bei* functions. They oscillate with increasing amplitudes.

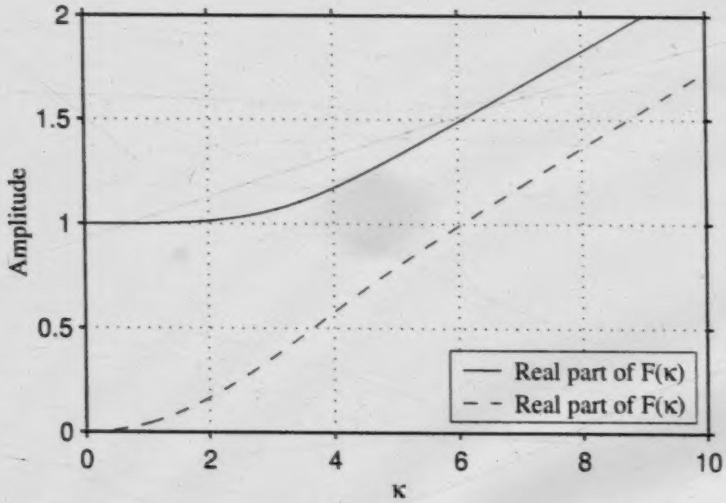

Figure B.4: The real and imaginary parts of the viscosity correction factor $F(\kappa)$. At large κ the curves tend to straight lines.

same author to include anisotropic media, viscoelastic media, and solid (skeleton) dissipation (Biot, 1962a; Biot, 1962b). This new approach led to a new set of parameters, the same set of parameters as describe above with a difference that they are now complex to account for various energy losses. These energy losses are those such as physical-chemical phenomena, inter-granular effects, cracks, relaxation effects due to bulk viscosity, and other effects mentioned in Biot (1962a; 1962b).

The evaluation of these various effects is beyond the experimental objectives of this study. We will only take into account an approximation of the dissipation intrinsic to the solid skeleton. A linear viscoelastic model will be assumed for these losses.

Appendix C

Review of the de la Cruz/Spanos theory

C.1 Wave propagation

Here a summary of the theory developed by de la Cruz and Spanos will be given here. The details of the theory can be found in de la Cruz and Spanos (1985; 1989b). The theory is derived first from the microscopic wave equations that govern wave propagation separately in the fluid and in the solid. In the fluid the equation of motion is given by

$$\frac{\partial}{\partial t}\left(\rho^{(f)} v_i^{(f)}\right) = \partial_k \left(p^{(f)} f \delta_{ik} + \rho^{(f)} v_i^{(f)} v_k^{(f)} - \sigma_{ik}^{(f)}\right) = 0 \tag{C.1}$$

where $v^{(f)}$ is the particle velocity, $\rho^{(f)}$ is the fluid density, $p^{(f)}$ is the fluid pressure, δ_{ik} is the Kroenecker delta, and $\sigma_{ij}^{(f)}$ is the stress in the fluid. The stress is given by

$$\sigma_{ij}^{(f)} = \eta \left(v_{i,k}^{(f)} + v_{k,i}^{(f)} - \frac{2}{3} v_{l,l}^{(f)} \delta_{ik} \right) \tag{C.2}$$

where η is the fluid shear viscosity and i, k is the derivative of the i^{th} component with respect to the k^{th} component. A repeated index implies summation. The continuity equation in the fluid is defined as

$$\frac{\partial \rho^{(f)}}{\partial t} + \vec{\nabla} \cdot (\rho^{(f)} \vec{v}^{(f)}) = 0 \tag{C.3}$$

In the solid wave propagation is governed by the equation of motion

$$\rho^{(s)} \frac{\partial^2 u_i^{(s)}}{\partial t^2} = \frac{\partial \sigma_{ik}^{(s)}}{\partial x_k} \tag{C.4}$$

where $\rho^{(s)}$ is the density of the solid, $u^{(s)}$ is the particle displacement in the solid, $\sigma_{ik}^{(s)}$ are the stress components in the solid. The stress is given by

$$\sigma_{ik}^{(s)} = K^{(s)} u_{ll}^{(s)} \delta_{ik} + 2\mu_s \left(u_{ik}^{(s)} - \frac{1}{3} u_{ll}^{(s)} \delta_{ik} \right) \tag{C.5}$$

where $K^{(s)}$ and μ_s are the bulk modulus and the shear modulus of the solid mineral respectively and

$$u_{ik}^{(s)} = \frac{1}{2} \left(u_{i,k}^{(s)} + u_{k,i}^{(s)} \right) \tag{C.6}$$

The fluid and the solid see each other only through the boundary conditions at the fluid-solid boundary. These boundary conditions are

$$\begin{aligned} \vec{v}^{(f)} &= \frac{\partial \vec{u}^{(s)}}{\partial t} && \text{(C.7)} \\ \sigma_{ik}^{(s)} n_k &= -p^{(f)} n_i + \sigma_{ik}^{(f)} n_k && \text{(C.8)} \\ & && \text{(C.9)} \end{aligned}$$

where $\vec{n}$ is the unit vector normal to the boundary. The transition from the microscopic scale to the macroscopic scale equations was based on the averaging theorems of Slattery (1969) and Whitaker (1969) which are given by

$$\begin{aligned} \int_V \partial_i G_f dV &= \partial_i \int_V G_f dV + \int_{A_{fs}} G_f n_i dA && \text{(C.10)} \\ \int_V \partial_t G_f dV &= \partial_t \int_V G_f dV - \int_{A_{fs}} G_f \vec{v} \cdot \vec{n} dA && \text{(C.11)} \\ & && \text{(C.12)} \end{aligned}$$

where A_{fs} is surface of the interfaces between the solid and the fluid, $\vec{v}$ is the particle velocity of the solid-fluid element, and $\vec{n}$ is the unit vector normal to the fluid-solid interface of the element considered. These theorems link the averages of the space and time derivatives to the derivatives of averages. G_f is the physical quantity being averaged. Applying the above theorems to the fluid and solid microscopic scale equations the following equations of motion were derived

$$\begin{aligned} \rho^{(s)} \frac{\partial^2 \vec{u}^{(s)}}{\partial t^2} = \frac{\beta_0}{(1-\beta_0)} \frac{K^{(s)}}{\rho^{(f)} V^2} \vec{\nabla} p^{(f)} + \mu_s \nabla^2 \vec{u}^{(s)} + & \qquad \text{(C.13)} \\ \left(K^{(s)} + \frac{1}{3}\mu_s \right) \vec{\nabla}(\nabla \cdot \vec{u}^{(s)}) + \frac{\beta_0}{(1-\beta_0)} K^{(s)} \vec{\nabla}(\nabla \cdot \vec{u}^{(f)}) + \frac{\eta}{K} \frac{\beta_0^2}{1-\beta_0} \frac{\partial}{\partial t} \left(\vec{u}^{(f)} - \vec{u}^{(s)} \right) & \end{aligned}$$

$$\rho^{(s)}\frac{\partial^2\vec{u}^{(f)}}{\partial t^2} = -\vec{\nabla}p^{(f)} + \eta\left(\frac{1}{3}\vec{\nabla}(\nabla\cdot\vec{v}^{(f)} + \nabla^2\vec{v}^{(f)}\right)) - \frac{\eta\beta_0}{K}\frac{\partial}{\partial t}\left(\vec{u}^{(f)} - \vec{u}^{(s)}\right) \quad \text{(C.14)}$$

where K is the permeability, β_0 is the porosity, and $p^{(f)}$ given by

$$p^{(f)} = -\frac{Q}{\beta_0}\vec{\nabla}\cdot\vec{u}^{(s)} - \frac{R}{\beta_0}\vec{\nabla}\cdot\vec{u}^{(f)} \quad \text{(C.15)}$$

where Q and R are the equivalent of the Biot parameters. The details of the derivation can be found in de la Cruz and Spanos (1985).

In a later paper de la Cruz et al. (1989b) have incorporated the term involving the relative acceleration that is the ρ_{12} term in Biot theory and introduced the dilation parameters δ_s and δ_f leading to a new set of equations

$$\begin{aligned}
(1-\beta_0)\,K^{(s)}\vec{\nabla}\left(\vec{\nabla}\cdot\vec{u}^{(s)}\right) - K^{(s)}\vec{\nabla}\beta + (1-\beta_0)\mu_s\left[\nabla^2\vec{u}^{(s)} + \frac{1}{3}\vec{\nabla}\left(\vec{\nabla}\cdot\vec{u}^{(s)}\right)\right] &= \\
(1-\beta_0)\rho^{(s)}\frac{\partial^2}{\partial t^2}\vec{u}^{(s)} - \rho_{12}\frac{\partial^2}{\partial t^2}\left(\vec{u}^{(s)} - \vec{u}^{(f)}\right) + \frac{\eta\beta_0^2}{K}\frac{\partial}{\partial t}\left(\vec{u}^{(s)} - \vec{u}^{(f)}\right) & \quad \text{(C.16)} \\
-\beta_0\vec{\nabla}p^{(f)} + \beta_0\eta\frac{\partial}{\partial t}\left[\nabla^2\vec{u}^{(f)} + \frac{1}{3}\vec{\nabla}\left(\vec{\nabla}\cdot\vec{u}^{(f)}\right)\right] &= \\
\beta_0\rho^{(f)}\frac{\partial^2}{\partial t^2}\vec{u}^{(f)} + \rho_{12}\frac{\partial^2}{\partial t^2}\left(\vec{u}^{(s)} - \vec{u}^{(f)}\right) - \frac{\eta\beta_0^2}{K}\frac{\partial}{\partial t}\left(\vec{u}^{(s)} - \vec{u}^{(f)}\right) & \quad \text{(C.17)} \\
\frac{1}{K^{(f)}}\frac{\partial p^{(f)}}{\partial t} = -\vec{\nabla}\cdot\frac{\partial\vec{u}^{(f)}}{\partial t} - \frac{1}{\beta_0}\frac{\partial\beta}{\partial t} & \quad \text{(C.18)} \\
\frac{\partial\beta}{\partial t} = \delta_s\vec{\nabla}\cdot\frac{\partial\vec{u}^{(s)}}{\partial t} - \delta_f\vec{\nabla}\cdot\frac{\partial\vec{u}^{(f)}}{\partial t} & \quad \text{(C.19)}
\end{aligned}$$

Equations C.16 through C.19 can be combined to

$$\begin{aligned}
(1-\beta_0)\mu_s\nabla^2\vec{u}^{(s)} + \left[(1-\beta_0)\left(K^{(s)} + \frac{1}{3}\mu_s\right) - \delta_s K^{(s)}\right]\vec{\nabla}\left(\vec{\nabla}\cdot\vec{u}^{(s)}\right) & \\
+\delta_f K^{(s)}\vec{\nabla}\left(\vec{\nabla}\cdot\vec{u}^{(f)}\right) &= \\
(1-\beta_0)\rho^{(s)}\frac{\partial^2}{\partial t^2}\vec{u}^{(s)} - \rho_{12}\frac{\partial^2}{\partial t^2}\left(\vec{u}^{(s)} - \vec{u}^{(f)}\right) + \frac{\eta\beta_0^2}{K}\frac{\partial}{\partial t}\left(\vec{u}^{(s)} - \vec{u}^{(f)}\right) & \quad \text{(C.20)} \\
K^{(f)}\delta_s\vec{\nabla}\left(\vec{\nabla}\cdot\vec{u}^{(s)}\right) + K^{(f)}\left(\beta_0 - \delta_f\right)\vec{\nabla}\left(\vec{\nabla}\cdot\vec{u}^{(f)}\right) + & \\
\beta_0\eta\frac{\partial}{\partial t}\left[\nabla^2\vec{u}^{(f)} + \frac{1}{3}\vec{\nabla}\left(\vec{\nabla}\cdot\vec{u}^{(f)}\right)\right] &= \\
\beta_0\rho^{(f)}\frac{\partial^2}{\partial t^2}\vec{u}^{(f)} + \rho_{12}\frac{\partial^2}{\partial t^2}\left(\vec{u}^{(s)} - \vec{u}^{(f)}\right) - \frac{\eta\beta_0^2}{K}\frac{\partial}{\partial t}\left(\vec{u}^{(s)} - \vec{u}^{(f)}\right) & \quad \text{(C.21)}
\end{aligned}$$

In a later paper Hickey et al. (1995) have incorporated the bulk viscosity, and introduced the macroscopic shear modulus of the frame μ_M that is present in the Biot theory. A new set of equations were then given

$$\begin{aligned}\mu_M\nabla^2\vec{u}^{(s)} + \left[(1-\beta_0)\left[K^{(s)} + \frac{1}{3(1-\beta_0)}\mu_M\right] - \delta_s K^{(s)}\right]\vec{\nabla}\left(\vec{\nabla}\cdot\vec{u}^{(s)}\right)& \\ +\delta_f K^{(s)}\vec{\nabla}\left(\vec{\nabla}\cdot\vec{u}^{(f)}\right) &= \\ (1-\beta_0)\rho^{(s)}\frac{\partial^2}{\partial t^2}\vec{u}^{(s)} - \rho_{12}\frac{\partial^2}{\partial t^2}\left(\vec{u}^{(s)}-\vec{u}^{(f)}\right) + \frac{\eta\beta_0^2}{K}\frac{\partial}{\partial t}\left(\vec{u}^{(s)}-\vec{u}^{(f)}\right)&\end{aligned} \tag{C.22}$$

$$\begin{aligned}K^{(f)}\delta_s\vec{\nabla}\left(\vec{\nabla}\cdot\vec{u}^{(s)}\right) + K^{(f)}\left(\beta_0-\delta_f\right)\vec{\nabla}\left(\vec{\nabla}\cdot\vec{u}^{(f)}\right) +& \\ (1-\beta_0)\eta\left[\frac{\mu_M}{(1-\beta_0)\mu_s} - 1\right]\frac{\partial}{\partial t}\left[\nabla^2\vec{u}^{(s)} + \frac{1}{3}\vec{\nabla}\left(\vec{\nabla}\cdot\vec{u}^{(s)}\right)\right] +& \\ \beta_0\eta\frac{\partial}{\partial t}\left[\nabla^2\vec{u}^{(f)} + \left(\frac{\xi_f}{\eta}+\frac{1}{3}\right)\vec{\nabla}\left(\vec{\nabla}\cdot\vec{u}^{(f)}\right)\right] + \xi_f\vec{\nabla}\frac{\partial\beta}{\partial t} &= \\ \beta_0\rho^{(f)}\frac{\partial^2}{\partial t^2}\vec{u}^{(f)} + \rho_{12}\frac{\partial^2}{\partial t^2}\left(\vec{u}^{(s)}-\vec{u}^{(f)}\right) - \frac{\eta\beta_0^2}{K}\frac{\partial}{\partial t}\left(\vec{u}^{(s)}-\vec{u}^{(f)}\right)&\end{aligned} \tag{C.23}$$

which can be rewritten as

$$\begin{aligned}\mu_M\nabla^2\vec{u}^{(s)} + \left[(1-\beta_0)\left[K^{(s)} + \frac{1}{3(1-\beta_0)}\mu_M\right] - \delta_s K^{(s)}\right]\vec{\nabla}\left(\vec{\nabla}\cdot\vec{u}^{(s)}\right)& \\ +\delta_f K^{(s)}\vec{\nabla}\left(\vec{\nabla}\cdot\vec{u}^{(f)}\right) &= \\ (1-\beta_0)\rho^{(s)}\frac{\partial^2}{\partial t^2}\vec{u}^{(s)} - \rho_{12}\frac{\partial^2}{\partial t^2}\left(\vec{u}^{(s)}-\vec{u}^{(f)}\right) + \frac{\eta\beta_0^2}{K}\frac{\partial}{\partial t}\left(\vec{u}^{(s)}-\vec{u}^{(f)}\right)&\end{aligned} \tag{C.24}$$

$$\begin{aligned}K^{(f)}\delta_s\vec{\nabla}\left(\vec{\nabla}\cdot\vec{u}^{(s)}\right) + K^{(f)}\left(\beta_0-\delta_f\right)\vec{\nabla}\left(\vec{\nabla}\cdot\vec{u}^{(f)}\right) +& \\ (1-\beta_0)\eta\left[\frac{\mu_M}{(1-\beta_0)\mu_s} - 1\right]\frac{\partial}{\partial t}\left[\nabla^2\vec{u}^{(s)} + \frac{1}{3}\vec{\nabla}\left(\vec{\nabla}\cdot\vec{u}^{(s)}\right)\right] +& \\ \beta_0\eta\frac{\partial}{\partial t}\left[\nabla^2\vec{u}^{(f)} + \frac{1}{3}\vec{\nabla}\left(\vec{\nabla}\cdot\vec{u}^{(f)}\right)\right] +& \\ \xi_f\frac{\partial}{\partial t}\left[\delta_s\vec{\nabla}\left(\vec{\nabla}\cdot\vec{u}^{(s)}\right) + \left(\beta_0-\delta_f\right)\vec{\nabla}\left(\vec{\nabla}\cdot\vec{u}^{(f)}\right)\right] &= \\ \beta_0\rho^{(f)}\frac{\partial^2}{\partial t^2}\vec{u}^{(f)} + \rho_{12}\frac{\partial^2}{\partial t^2}\left(\vec{u}^{(s)}-\vec{u}^{(f)}\right) - \frac{\eta\beta_0^2}{K}\frac{\partial}{\partial t}\left(\vec{u}^{(s)}-\vec{u}^{(f)}\right)&\end{aligned} \tag{C.25}$$

C.2 de la Cruz/Spanos parameters

All parameters for this theory can be determined in standard laboratory experiments as mentioned earlier. ρ_{12} can be determined in the same way as for the Biot theory. The last two parameters, the dilation parameters δ_s and δ_f for the solid and the fluid respectively must be determined. This can be done in laboratory measurement tests as given in Hickey et al. (1995). Below a review of the work of Hickey et al. (1995) will be given. Recall the equations of continuity, pressure, and porosity that were used in the derivation of the equations of motion in section C.1 as given in Hickey et al. (1995). These equations will be used in the compressibility tests to determine the dilation parameters δ_s and δ_f. As mentioned earlier the thermal coupling is neglected. Again since this theory uses the change in porosity, we distinguish between unperturbed porosity and the perturbed porosity by using the symbols β_0 and β respectively. The equations of continuity are given by

$$\frac{\rho^{(s)} - \rho_0^{(s)}}{\rho_0^{(s)}} - \frac{\beta - \beta_0}{1 - \beta_0} + \vec{\nabla} \cdot \vec{u}^{(s)} = 0 \tag{C.26}$$

$$\frac{1}{\rho_0^{(f)}} \frac{\partial}{\partial t} \rho^{(f)} + \frac{1}{\beta_0} \frac{\partial}{\partial t} \beta + \vec{\nabla} \cdot \vec{v}^{(f)} = 0 \tag{C.27}$$

the pressure equations are

$$\frac{1}{K^{(s)}} (p^{(s)} - p_0) - \frac{\beta - \beta_0}{1 - \beta_0} + \vec{\nabla} \cdot \vec{u}^{(s)} = 0 \tag{C.28}$$

$$\frac{1}{K^{(f)}} \frac{\partial p^{(f)}}{\partial t} + \frac{1}{\beta_0} \frac{\partial \beta}{\partial t} + \vec{\nabla} \cdot \vec{v}^{(f)} = 0 \tag{C.29}$$

and the porosity equation is

$$\frac{\partial \beta}{\partial t} = \delta_s \vec{\nabla} \cdot \vec{v}^{(s)} - \delta_f \vec{\nabla} \cdot \vec{v}^{(f)} \tag{C.30}$$

Eliminating $\vec{\nabla} \cdot \vec{u^{(s)}}$ and $\vec{\nabla} \cdot \vec{u^{(f)}}$ in equations C.26-C.30 we get

$$\rho^{(s)} - \rho_0^{(s)} = \frac{\rho^{(s)}}{K^{(s)}} (p^{(s)} - p_0^{(s)}) \tag{C.31}$$

$$\beta - \beta_0 = \frac{\delta_f}{K^{(f)} \left[\beta_0 (1 - \beta_0) - \delta_f (1 - \beta_0) - \delta_s \beta_0\right]} (p^{(f)} - p_0) - \frac{\delta_s}{K^{(s)} \left[\beta_0 (1 - \beta_0) - \delta_f (1 - \beta_0) - \delta_s \beta_0\right]} (p^{(s)} - p_0) \tag{C.32}$$

The total confining pressure is

$$p = \beta p^{(f)} + (1 - \beta) p^{(s)} \tag{C.33}$$

which can be rewritten to the first order as

$$p - p_0 = \beta_0 (p^{(f)} - p_0) + (1 - \beta_0)(p^{(s)} - p_0) \tag{C.34}$$

C.2.1 Drained compressibility tests

A drained compressibility test can be achieved using the setup used for the Biot theory for the jacketed compressibility test given in figure B.1. Under a change of confining pressure the mass of the solid is conserved and the fluid pressure $p^{(f)}$ is kept constant. The bulk modulus for this process is defined as

$$\frac{1}{K_{bc}} = -\frac{1}{V_0}\left(\frac{\Delta V}{\Delta p}\right)_{p^{(f)}=p_0} \tag{C.35}$$

where $\Delta V = V - V_0$ is the change of volume of the sample, V_0 is the initial volume of the sample, Δp is the change in confining pressure. Equation C.35 can be rewritten as

$$\frac{1}{K_{bc}} = \frac{1}{(1-\beta_0)\rho_0^{(s)}}\left(\frac{\partial\left[(1-\beta)\rho^{(s)}\right]}{\partial p}\right)_{p^{(f)}=p_0} \tag{C.36}$$

Using equations C.31, C.32, and C.34 equation C.36 can be rewritten to the first order as

$$K_{bc} = K^{(s)}\frac{\beta_0(1-\beta_0) - \delta_f(1-\beta_0) - \delta_s\beta_0}{\beta_0 - \delta_f} \tag{C.37}$$

In this test setup another measurement can be done by keeping the confining pressure constant and changing the pore pressure. The bulk modulus K_{bp} of this process is commonly called the pseudo-bulk modulus. It is defined as

$$\frac{1}{K_{bp}} = -\frac{1}{V_0}\left(\frac{\Delta V}{\Delta p^{(f)}}\right)_{p=p_0} \tag{C.38}$$

which can be rewritten as

$$\frac{1}{K_{bp}} = \frac{-1}{(1-\beta_0)\rho_0^{(s)}}\left(\frac{\partial\left[(1-\beta)\rho^{(s)}\right]}{\partial p^{(f)}}\right)_{p=p_0} \tag{C.39}$$

Using equations C.31, C.32, C.34, and C.36 equation C.39 can be rewritten to the first order as

$$\frac{1}{K_{bp}} = \frac{1}{K_{bc}} - \frac{1}{K^{(s)}} + \frac{\delta_f K^{(s)} - \delta_s K^{(f)}}{K^{(s)}K^{(f)}\left(\beta_0(1-\beta_0) - (1-\beta_0)\delta_f - \beta_0\delta_s\right)} \tag{C.40}$$

C.2.2 A continuous family of compressibilities

A family of compressibilities is defined by the degree at which the fluid is allowed to flow out of the sample during compression. This is defined as

$$\frac{1}{K_\theta(\theta)} = -\frac{1}{V_0}\left(\frac{\Delta V}{\Delta p}\right)_{\theta=constant} \tag{C.41}$$

where ΔV is the volume change of the sample, Δp is the pressure change, and θ defined as

$$\theta = \frac{p^{(f)} - p_0}{p - p_0} \tag{C.42}$$

and kept constant during the measurements. This equation can be rewritten as

$$\frac{1}{K_\theta(\theta)} = \frac{1}{(1-\beta_0)\rho_0^{(s)}} \frac{d\left[(1-\beta)\rho^{(s)}\right]}{dp} \tag{C.43}$$

Using equations C.31, C.32, and C.33 in equation C.43 we obtain

$$\frac{1}{K_\theta(\theta)} = \frac{1}{K_{bc}} - \frac{1}{K_{bp}}\theta \tag{C.44}$$

This way one can perform a series of compressibility tests keeping θ constant near a given value, say almost drained tests and determine from the slope and intercept of equation C.44 the moduli K_{bc} and K_{bp} that are necessary to determine δ_f and δ_s. The dilation parameters δ_s and δ_f are given by

$$\delta_f = \beta_0 \left[\frac{K_f(K_{bc} - \beta_0 K_{bp})}{\beta_0 K_{bp}(K^{(s)} - K^{(f)}) + K^{(f)} K_{bc}}\right] \tag{C.45}$$

$$\delta_s = \beta_0 \left[\frac{K_{bp}\left[(1-\beta_0)K^{(s)} - K_{bc}\right]}{\beta_0 K_{bp}(K^{(s)} - K^{(f)}) + K^{(f)} K_{bc}}\right] \tag{C.46}$$

Therefore a measurement of the drained bulk moduli K_{bc} and K_{bp} allows the determination of the dilation parameter δ_f and δ_s.

C.2.3 Coefficient of fluid content

The coefficient of fluid content γ as defined in the Biot theory in appendix B is not needed in the present theory but is useful for the comparison of the two theories. In the present theory this coefficient can be defined, during an unjacketed compressibility test, as

$$\gamma = \frac{1}{V_0}\left(\frac{\Delta V_f}{\Delta p}\right)_{\theta=1} \tag{C.47}$$

where $\Delta V^{(f)}$ is the volume of the fluid that enters the pores of the sample, and θ is as defined in equation C.42. The change in confining pressure Δp is equal to the change in pore pressure $\Delta p^{(f)}$. Therefore

$$\Delta V^{(f)} = \beta_0(V - V_0) + V_0(\beta - \beta_0) + V_0^{(f)}\Delta P^{(f)} \tag{C.48}$$

where $V^{(f)}$ is the final volume of fluid in the pores and V is the final volume of the sample. Accordingly $V_0^{(f)}$ is the initial volume of fluid in the pores and V_0 is the initial volume of the sample. $\Delta p^{(f)}$ is the change in the pore pressure. Using equation C.48 in equation C.47 and using C.41 for $\theta = 1$ we get

$$\gamma = \frac{\beta_0}{K^{(f)} K_\theta(1)} + \frac{\beta - \beta_0}{p - p_0} \tag{C.49}$$

and using equations C.32 and C.33 in equation C.49 one obtains

$$\gamma = \beta_0 \left[\frac{1}{K^{(f)}} - \frac{1}{K_\theta(1)} \right] + (1 - \beta_0) \left[\frac{1}{K^{(s)}} - \frac{1}{K_\theta(1)} \right] \tag{C.50}$$

References

Aki, K., and Richards, P. G., 1980, Quantitative seismology: W. H. Freeman and Co.

Arntsen, B., and Carcione, J. M. J., 2001, Numerical simulation of the biot slow wave in water-saturated nivelsteiner sandstone: Geophysics, **66(3)**, 890–896.

Auld, B. A., 1973, Acoustic fields and waves in solids:, volume I John Wiley & sons, New York, London, Sydney, Toronto.

Beamish, J. R., Hikata, A., and Elbaum, C., 1983, Sound velocity in helium-filled porous vycor glass: Physical Review B.

Becker, F. L., and Richardson, R. L., 1971, Influence of material properties on rayleigh critical-angle reflectivity: Journal of the Acoustical Society of America, **51(5-Part 2)**, 1609–1617.

Bedford, A., and Drumheller, D. S., 2000, Introduction to elastic wave propagation: John Wiley and Sons, Inc.

Bertoni, H. L., and Tamir, T., 1973, Unified theory of rayleigh-angle phenomena for acoustic beams at liquid-solid interfaces: Applied Physics, **2**, 157–172.

Bhatia, A. B., and Singh, R. N., 1986, Sound propagation, *in* Brewer, D. F., Ed., Mechanics of Deformable Media: University of Sussex press, 158–167.

Biot, M. A., and Willis, D. G., 1957, The elastic coefficients of the theory of consolidation: Journal of Applied Mechanics, **24**, 594–601.

Biot, M. A., 1956a, Theory of propagation of elastic waves in a fluid-saturated pourous solid. i low-frequency range: Journal of the Acoustical Society of America, **28-2**, 168–178.

—— 1956b, Theory of propagation of elastic waves in a fluid-saturated pourous solid. ii low-frequency range: Journal of the Acoustical Society of America, **28-2**, 179–191.

Biot, M. A., 1962a, Generalized theory of acoustic propagation in porous dissipative media: Journal of the Acoustical Society of America, **33-4**, 1482–1498.

—— 1962b, Mechanics of deformation and acoustic propagation in porous media: Journal of Applied Physics, **34-9**, 1254–1264.

Borcherdt, R. D., 1977, Reflection and refraction of type-ii s waves in elastic and anelastic media: Bulletin of the Seismological Society of America, **67-1**, 43–67.

Borcherdt, R. D., 1982, Reflection-refraction of general p-and type-i s-waves in elastic and anelastic solids: Geophys. J. R. astr. Soc., **70**, 621–638.

Bouzidi, Y., and Schmitt, D. R., 2000, Laboratory calibration of amplitude variation with angle using acoustic goniometer: Expanded abstracts: Society of Exploration Geophysics, **70**, 210–213.

Bouzidi, Y., Schmitt, D. R., Burwash, R. A., and Kanasewich, E. R., 2002, Depth migration of deep seismic reflection profiles: crustal thickness variations in alberta: Canadian Journal of Earth Sciences, **39**, 331–350.

Breazeale, M. A., and Adler, L., 1974, Reflection of agaussian ultrasonic beam from a liquid-solid interface: Journal of the Acoustical Society of America, **56(3)**, 866–872.

Breazeale, M. A., Adler, L., and Scott, G. W., 1977, Interaction of ultrasonic waves incident at the rayleigh angle onto a liquid-solid interface: Journal of the Acoustical Society of America, **48(2)**, 530–537.

Brekhovskikh, L. C., 1960, Waves in layered media, *in* Beyer, R. T., Ed., Applied mathematics and mechanics: Academic press, New York, London, 100–122.

Clearbout, J. F., 1985, Imaging the earth's interior: Blackwell Scientific Publications, Oxford, London, Edinburgh, Boston, Palo Alto, Victoria.

Courtney, R. C., and Mayer, L. A., 1993, Calculation of acoustic parameters by filter-correlation method: Journal of the Acoustical Society of America, **93(2)**, 1145–1154.

de la Cruz, V., and Spanos, T. J. T., 1985, Seismic wave propagation in a porous medium: Geophysics, **50**, 1556–1565.

de la Cruz, V., and Spanos, T. J. T., 1989a, Seismic boundary conditions for porous media: Journal of Geophical Research, **94 (B3)**, 3025–3029.

—— 1989b, Thermomechanical coupling seismic wave propagation in a porous medium: Journal of Geophical Research, **94 (B1)**, 637–642.

de la Cruz, V., j[] Hube, and Spanos, T. J. T., 1992, Reflection and transmission of seismic waves at the boundaries of porous media: Wave motion, **16**, 323–338.

de la Cruz, V., Sahay, P. N., and Spanos, T. J. T., 1993, Thermodynamics of porous media: Proceedings of the Royal Society of London, series A, **443**, 247–255.

Denneman, A. I. M., Drijkoningen, G. G., Smeulders, D. M. J., and Wapenaar, K., 2002, Reflection and transmission of waves at a fluid/porous-medium interface: Geophysics, **67(1)**, 282–291.

Deresiewicz, H., and Skalak, R., 1963, On uniqueness in dynamic poroelasticity: Bulletin of the Seismological Society of America, **53-4**, 783–788.

Diachok, O. I., and Mayer, W. G., 1970, Conical reflection of ultrasound from liquid-solid interface: Journal of the Acoustical Society of America, **47(1-Part 2)**, 155–157.

Dvorkin, J., and Nur, A. M., 2000a, Dynamic poroelasticity: A unified model with the squirt and the biot mechanisms:, *in* Seismic and acoustic velocities in reservoir rocks Soc. of Expl. Geophys., 19, 44–53.

—— 2000b, The squirt-flow mechanism: Macroscopic description:, *in* Seismic and acoustic velocities in reservoir rocks Soc. of Expl. Geophys., 19, 54–64.

Dvorkin, J., Mavko, G., and Nur, A. M., 2000, Squirt flow in fully saturated rocks:, *in* Seismic and acoustic velocities in reservoir rocks Soc. of Expl. Geophys., 19, 65–75.

Dwight, H. B., 1964, Tables of integrals and other mathematical data: The MacMillan Company.

Dziewonski, A. M., and Hales, A. L., 1972, Numerical analysis of dispersed seismic waves, *in* Bolt, A. [illegible]., Ed., Methods in computational physics: Academic press, New York, London, 39–85.

Ewing, W. M., Jardetzky, W. S., and Press, F., 1957, Elastic waves in layered media, *in* Shrock, R. R., Ed., International Series in the Earth Sciences: McGraw Hill, New York,Toronto, London, 31–33.

Frenkel, J., 1944, On the theory of seismic and seismoelectric phenomena in moist soils: Journal of Physics U.S.S.R., **8**, 230.

Geerits, T. W., and Kelder, O., 1997, Acoustic wave propagation through porous media: Theory and experiments: Journal of the Acoustical Society of America, **102(2)**, 2495–2510.

Goos, F., and Hänchen, H., 1947, Ein neuer und fundamentaler versuch zur totalreflexion: Ann. Physik, **6**, 333–346.

Gray, D. E., 1963, Mechanics, *in* Lindsay, R. B., Ed., American Institute of Physics Handbook: McGraw-Hill Book Company, Inc., 194–196.

Guéguen, Y., and Palciauskas, V., 1994, Introduction to the physics of rocks: Princton University Press, Princeton, New Jersey.

Guo-Zhen, Z., Xi-Fu, Z., and Hong-Zhi, G., 2001, Experimental study of nonspecular reflected acoustic field on a water-fspm interface: Cninese Journal of Geophysics.

Gurevich, B., and Schoenberg, M., 1999, Interface conditions for biot's equations of poroelasticity: Journal of the Acoustical Society of America, **102(3)**, 1480–1484.

Hickey, C. J., and Sabatier, J. M., 1997, Choosing biot parameters for modeling water-saturated sand: Journal of the Acoustical Society of America, **105(5)**, 2585–2589.

Hickey, C. J., Eastwood, J. E., and Spanos, T. J. T., 1991, Seismic wave propagation in oil sands: AOSTRA Journal of research, **7**, 67–81.

Hickey, C. J., Spanos, J. T., and de la Cruz, V., 1995, Deformation parameters of permeable media: Geophysical Journal International, **121**, 359–370.

Horowitz, B. R., and Tamir, T., 1971, Lateral displacement of a light beam at a dielectric interface: Journal of the optical soceity of America, **61(5)**, 586–594.

Johnson, D. L., and Kojima, H., 1994, Probing porous-media with 1^{st} and 2^{nd} sound. ii. acoustic properties of water-saturated porous-media: Journal of Applied physics, **76(1)**, 115–125.

Johnson, D. L., Plona, T. J., and Scala, C., 1982, Tortuosity and acoustic slow waves: Physical Review Letters, American Physical Society, **49-25**, 1840–1845.

Johnson, D. L., Koplik, T. J., and Dashen, R., 1987, Theory of dynamic permeability and tortuosity in fluid-saturated porous media: Journal of Fluid Mechanics, **176**, 379–402.

Kedler, O., and Smeulders, D. M. J., 1997, Observation of the biot slow wave in water-saturated nivelsteiner sandstone: Geophysics, **62(6)**, 1794–1796.

King, M. S., and Marsden, J. R., 2002, Velocity dispersion between ultrasonic and seismic frequencies in brine-saturated reservoir sandstones: Velocity dispersion between ultrasonic and seismic frequencies in brine-saturated reservoir sandstones:, Soc. of Expl. Geophys., Geophysics, 254–258.

Litovitz, T. A., 1960, Non-crystalline solids Wiley, New York, p 252.

Morse, R. W., 1952, Acoustic propagation in granular media: Journal of the Acoustical Society of America, **24**, 696–700.

Neubauer, W. G., and Dragonette, L. R., 1974, Measurement of rayleigh phase velocity and estimates of shear speed by schlieren visualization: Journal of Applied Physics, **45(2)**, 618–622.

Ngoc, T. D. K., and Mayer, W. G., 1980, Numerical integration method for reflected beam profiles near rayleigh angle: Journal of the Acoustical Society of America, **67(4)**, 1149–1152.

O'Connell, R. G., and Budiansky, B., 1977, Viscoelastic properties of fluid-saturated cracked solids: Journal of Geophical Research, **82(36)**, 5719–5735.

O'Connell, R. G., and Budiansky, B., 1978, Measures of dissipation in viscoelastic media: Geophical Research Letters, **5(1)**, 5–8.

Plona, T. J., 1980, Observation of a second bulk compressional wave in a porous medium at ultrasonic frequencies: Applied Physics Letters, **36**, 259–261.

Quan, Y., and Harris, J. M., 1997, Seismic attenuation tomography using the frequency shift method: Geophysics, **62(2)**, 895–905.

Santos, J. E., Corbero, J. M., Ravazzoli, C. L., and Hensley, J. L., 1992, Reflection and transmission coefficients in fluid-saturated porous media: Journal of the Acoustical Society of America, **91 (4)**, 1911–1923.

Schmidt, H. D., and Jensen, F. B., 1985, Full wave solution for propagation in multilayered viscoelastic media with application to gaussian beam reflection at a fluid-solid interfaces: Journal of the Acoustical Society of America, **77(3)**, 813–824.

Schoch, A., 1950, Schallrelexion, schallbrechung und schallbeugung: Ergebnisse Der Exakten Naturwissenschaften, **23**, 127–234.

Schoch, A., 1952a, Der schallbeugung durch platten: Acustica, **2(1)**.

—— 1952b, Seitliche versetzung eines total reflektierten strahles bei ultraschallwellen: Acustica, **2(17)**.

Shuey, R. T., 1985, A simplification of the zoeppritz-equations: A simplification of the zoeppritz-equations:, Society of Exploration Geophysicists, Geophysics, 609–614.

Slattery, J. C., 1969, Single-phase flow through porous media: J. Am. Inst. Chem. Eng., **15**, 866–872.

Spanos, J. T., 2001, The thermodynamics of porous media: Chapman & Hall\CRC.

Stoll, R. D., and Kan, T. K., 1981, Reflection of acoustic waves at water-sediment interface: Journal of the Acoustical Society of America, **70(1)**, 149–156.

Tamir, T., and Bertoni, H. L., 1973, Lateral displacement of optical beams at multilayered and periodic structures: Journal of the optical society of America, **61(10)**, 1397–1413.

Walsh, J. B., and Brace, W. F., 1984, The effect of pressure on porosity and the transport properties of rock: Journal of Geophysical Research.

Warner, K., and Beamish, J. R., 1988, Ultrasonic measurement of the surface area of porous materials: Journal of Applied Physics.

Warner, K., and Beamish, J. R., 1994, Frequency dependence of sound propagation in superfluid-filled porous media: Physical review B.

Whitaker, S., 1969, Advances in the theory of fluid motion in porous media: Ind. Eng. Chem.

Wu, K., Xue, Q., and Adler, L., 1990, Reflection and transmission of elastic waves from a fluid-saturated porous solid boundary: Journal of the Acoustical Society of America, **87(6)**, 2349–2358.

Wylie, C. R., 1961, Advanced engineering mathematics: McGraw-Hill Book Company.

Zoeppritz, K., 1919, Erdbebenwellen vii. viib. ber reflexion und durchgang seismischer wellen durch unstetigkeitsflchen. nachrichten der kniglichen gesellschaft der wissenschaften zu gttingen: Mathematisch-physikalische Klasse, pages 66–84.